RUHR-UNIVERSITÄT BOCHUM

Static, cyclic and dynamic properties of granular materials

Debdeep Sarkar

75

Debdeep Sarkar

Debdeep Sarkar

Influence of particle characteristics on the behaviour of granular materials under static, cyclic and dynamic loading

Bochum 2022   Heft 75

Influence of particle characteristics on the behaviour of granular materials under static, cyclic and dynamic loading

Dissertation

as a requirement of the degree of
Doktor-Ingenieur (Dr.-Ing.)

at the Faculty of
Civil and Environmental Engineering
Ruhr-Universität Bochum

submitted by
Debdeep Sarkar
from Serampore, West Bengal, India

Reviewers:
Prof. Dr.-Ing. habil. Torsten Wichtmann (Ruhr-Universität Bochum, Germany)
Prof. Dr.-Ing. habil. Ivo Herle (Technische Universität Dresden, Germany)
Prof. Md. Mizanur Rahman (University of South Australia, Australia)

Bochum, 2022

Preface of the editor

Beside density and stress the mechanical behaviour of granular soils under monotonic, cyclic and dynamic loading depends on the characteristics of the grains, i.e. their size, size distribution (grading), shape, surface roughness and mineralogy. Previous studies on the influence of grain shape in the literature led to contradictory results, possibly due to the use of materials with different grain size distribution curves. A systematic experimental investigation on the combined influence of grain shape and grading on the response of granular materials to monotonic, cyclic and dynamic loading was missing so far. It was thus the objective of the present dissertation of Debdeep Sarkar.

Debdeep Sarkar has performed a large number of high-quality laboratory tests, including index tests, direct shear tests, monotonic and cyclic triaxial tests with drained or undrained conditions, resonant column tests and wave velocity measurements. In these experiments he used three granular materials with significantly different grain shape (glass beads, natural sand, crushed glass), which were each prepared with two specific grain size distribution curves having the same mean grain size but different uniformity coefficients. Each of these six materials was tested at different densities and stress states.

Debdeep Sarkar thoroughly analyses and quantifies the influence of grain shape and grading on various soil properties derived from the tests, like the maximum and minimum void ratios, shear strength, critical state, liquefaction resistance, shear wave velocity or stiffness and damping at small to intermediate strains. The dependence of the parameters of various empirical equations describing these properties as well as the material constants of the elastoplastic SANISAND model on the grain characteristics is also studied. The experimental observations under monotonic loading are qualitatively corroborated by the results of discrete element simulations considering grain shape by a simplified approach.

The thesis of Debdeep Sarkar clearly demonstrates that the influences of grading and grain shape interact with each other and should not be treated independently, which partially explains contradicting tendencies in the literature. The research work of Debdeep Sarkar represents a valuable contribution to a better understanding of the influence of particle characteristics on the mechanical behaviour of granular soils, which may lead to more reliable estimates of their properties in future, particularly with respect to the resistance against liquefaction under earthquake loading.

Bochum, November 2022   Prof. Dr.-Ing. habil Torsten Wichtmann

This work is dedicated to my beloved
parents, my lovely supportive wife Bidisha, and
my favorite football club Manchester United F. C.

Acknowledgements

Abstract

Dynamic motions may be a result of natural (e.g. earthquakes, volcanoes, tsunami, etc.) or man-made (traffic, machine drilling, blasting, etc.) activities. Certain soils do not have the capacity to resist strong dynamic motions and have been observed to lose a part of their strength and stiffness, leading to significant damages such as differential settlements, tilting of buildings and bridges and in worst cases, collapse of structures. Particle characteristics such as grain size, gradation, mineralogy, fines content (i.e. particles smaller than 0.063 mm in size) and grain shape play an important role in determining the mechanical behavior of granular soils. However, relatively few systematic studies on the influence of the particle characteristics, particularly grain shape, on the monotonic behavior of granular soils up to the steady state, the cyclic liquefaction behavior as well as stiffness and damping at small to intermediate strains of granular soils can be found in literature.

In this study, the influence of various particle characteristics such as the grain size, gradation and shape on the inherent, static, cyclic and dynamic behavior of granular materials is investigated. Besides the grain shape, the study assesses the influence of the grain size parameters (mean grain size d_{50} and uniformity coefficient C_u) on the limit void ratios of granular soils. In addition, a series of monotonic triaxial tests under various boundary conditions (e.g. effective stresses, void ratios and drained/undrained conditions) were performed on three materials having vastly different grain shapes (glass beads, natural sand, crushed glass) but a similar d_{50} and C_u with the aim to quantify the impact of grain shape on various soil properties such as peak friction, steady state friction and dilatancy angles as well as the critical state line in the void ratio versus effective mean stress plane. The study was extended to cyclic undrained triaxial tests using a second gradation for each material to assess the combined influence of grain shape and gradation on liquefaction resistance. The small- and intermediate strain properties of the various materials were also investigated in resonant column tests under torsional or axial mode of vibration. The impact of grain shape and gradation on the various fitting parameters of existing analytical models for shear stiffness and modulus degradation characterization was assessed. Recommendations regarding the choice of suitable grain shape parameters to characterize shear wave velocities in granular soils were provided.

The experimental results were then briefly discussed in the framework of micromechanics, where the discrete element method (DEM) was used to simulate granular packings of different particle shapes subjected to monotonic drained and undrained loading. In addi-

tion, the influence of grain shape on various fitting parameters in a popular elastoplastic constitutive model (SANISAND) was investigated. Finally, a simple example of ground response analysis was studied to evaluate soil responses under a pre-defined earthquake in ground with different particle characteristics.

Zusammenfassung

Dynamische Beanspruchungen können das Ergebnis natürlicher (z.B. Erdbeben, Vulkane, Tsunami etc.) oder vom Menschen verursachter Aktivitäten (Verkehr, Bohr- und Sprengarbeiten etc.) sein. Bestimmte Böden sind nicht in der Lage, starken dynamischen Einwirkungen zu widerstehen, und verlieren einen Teil ihrer Festigkeit und Steifigkeit. Erhebliche Schäden wie Setzungsunterschiede, eine Schiefstellung von Gebäuden und Brücken und im schlimmsten Fall der Einsturz von Bauwerken können dadurch verursacht werden. Partikeleigenschaften wie Korngröße, Korngrößenverteilung, Mineralogie, Feinkorngehalt (d.h. Partikel mit einer Größe von weniger als 0,063 mm) und Kornform spielen hierbei eine wichtige Rolle und beeinflussen das mechanische Verhalten der Böden. In der Literatur finden sich jedoch nur relativ wenige systematische Untersuchungen zum Einfluss der Partikeleigenschaften granularer Böden, insbesondere der Kornform, auf das monotone Verhalten bis zum kritischen Zustand, das Verflüssigungsverhalten bei zyklischer Beanspruchung sowie die Steifigkeit und Dämpfung bei kleinen bis mittleren Dehnungen.

In dieser Arbeit wird der Einfluss verschiedener Partikeleigenschaften wie Korngröße, Korngrößenverteilung und Kornform auf das inhärente, statische, zyklische und dynamische Verhalten granularer Materialien untersucht. Neben der Kornform wird der Einfluss der Korngrößenparameter (mittlerer Korndurchmesser d_{50} und Ungleichformigkeitszahl C_u) auf die Lagerungsdichte (lockerste und dichteste Lagerung) von granularen Böden untersucht. Darüber hinaus wurde eine Reihe von monotonen Triaxialversuchen unter verschiedenen Randbedingungen (z.B. effektive Spannungen, Lagerungsdichte und drainierte/undrainierte Bedingungen) an drei Materialien mit sehr unterschiedlichen Kornformen (Glaskugeln, natürlicher Sand, gebrochenes Glas), aber einem ähnlichen d_{50} und C_u durchgeführt, um den Einfluss der Kornform auf verschiedene Bodeneigenschaften wie den Peakreibungswinkel, den Reibungswinkel im kritischen Zustand und den Dilatanzwinkel zu quantifizieren sowie die kritische Zustandslinie (critical state line) im Druck-Porenzahl-Diagramm zu bestimmen. Die Studie wurde unter Verwendung einer zweiten Korngrößenverteilung für jedes Material auf zyklische undrainierte Triaxialversuche erweitert, um den kombinierten Einfluss von Kornform und Korngrößenverteilung auf der Verflüssigungswiderstand zu bewerten. Die dynamischen Eigenschaften der verschiedenen Materialien bei kleinen bis mittleren Dehnungen wurden in Resonanzsäulenversuchen unter Torsions- oder Axialschwingungen untersucht. Die Auswirkungen von Kornform und Korngrößenverteilung auf die verschiedenen Anpassungsparameter bestehender analytis-

cher Modelle zur Beschreibung der Schubsteifigkeit und dessen Degradation mit steigender Scherdehnung wurden analysiert. Es wurden Empfehlungen für die Wahl geeigneter Kornformparameter zur Charakterisierung von Scherwellen geschwindigkeiten in granularen Böden gegeben.

Die experimentellen Ergebnisse wurden anschließend im Kontext der Mikromechanik diskutiert, wobei die Diskrete-Elemente-Methode (DEM) verwendet wurde, um granulare Packungen mit unterschiedlichen Kornformen zu simulieren, die einer monotonen drainierten oder undrainierten Belastung unterzogen wurden. Darüber hinaus wurde der Einfluss der Kornform auf die verschiedenen Materialkonstanten eines bekannten gängigen elastoplastischen konstitutiven Modells (SANISAND) untersucht. Schließlich wurde ein einfaches Beispiel einer Bodenreaktionsanalyse untersucht, um die Bodenbewegungen bei einem vordefinierten Erdbeben in einem Boden mit unterschiedlichen Partikeleigenschaften zu beurteilen.

Contents

Nomenclature

q Deviatoric stress

$p^{'}$ Mean effective stress

ϵ_v Volumetric strain

$\epsilon_1, \varepsilon_1$ Axial strain

ϵ_2, ϵ_3 Lateral strains

u Pore water pressure or back pressure

e Void ratio

e_i Initial void ratio typically after sample preparation

e_0 Void ratio at the end of consolidation

e_{ss}, e_{cs} Void ratio at steady or critical state

τ, e_{c0} Critical void ratio corresponding to an effective stress $p^{'} = 1$ kPa

λ Slope of the critical state line in the $e - p^{'}$ diagram

α, ζ Fitting parameter to account for the curvature of the critical state line

p_a Atmospheric pressure (normally considered as 100 kPa)

$p^{'}_{ss}$ Mean effective stress at the steady state

ϕ_p Peak friction angle

ϕ_{cs} Critical- or steady-state friction angle

ψ Dilation angle

e_{max}, e_{min} Maximum and minimum void ratio of soils respectively

G_s, G_m, G_g Specific gravity of the soil/material/glass beads

CSR Cyclic stress ratio

CRR Cyclic resistance ratio

N_c Number of cycles to initial liquefaction

E Young's Modulus

σ Axial stress

τ Shear stress

γ Shear strain

γ^{ampl} Shear strain amplitude

ν Poisson's ratio

G Shear modulus

M Constrained modulus

G_0, G_{max} Initial shear modulus at small strain

E_{max} Initial elastic modulus at small strain

M_{max} Initial constrained modulus at small strain

$G(\gamma)/G_{max}$ Shear modulus degradation ratio

$E(\epsilon)/E_{max}$ Elastic modulus degradation ratio

G_{sec} Secant shear modulus

ρ Regularity factor

D, D_{min} Damping ratio and minimum damping respectively

D_{max} Maximum damping ratio

r_{cir}, r_{ins} Smallest circumscribing and largest inscribing circles inside a particle respectively

S_A Area sphericity

S_D Diameter sphericity

S_P Perimeter sphericity

S, S_C Circle ratio sphericity

S_{WL} Width to length ratio sphericity

d_{50}, D_{50} Mean grain size

C_u Uniformity coefficient

d_{50}, D_{50} Mean grain size

R, R_w Grain roundness

I_D Relative density

v_s Shear wave velocity

v_p Primary wave velocity

A, C, d, x, n Various fitting parameters related to small-strain shear or elastic modulus determination

γ_r Reference shear strain where $G/G_{max} = 0.5$

ϵ_r Reference axial strain where $E/E_{max} = 0.5$

α Fitting parameter for the shear modulus degradation curve

$C_1, C_2, M, N, \Omega, \Gamma$ Various fitting parameters for describing damping ratio profile at intermediate shear strain

Ar Aspect ratio

Cir Circularity

$Comp$ Compactness

So Solidity

Cv Concavity

Cx Convexity

MR Mod Ratio

RF R-Factor

$Rect$ Rectangularity

t Time

J, J_0, J_L Polar moment of inertia of the sample, the bottom and top parts of the resonant column device respectively

L Specimen length

H/D Specimen height (H) to diameter (D or D_s) ratio

D_c Specimen diameter after consolidation

f, f_r Frequency/Resonant frequency respectively

L Specimen length

E_{50}^{ref} Secant primary triaxial loading stiffness

ΔV_m Volume change due to membrane penetration

V_0 Initial volume of the specimen

E_m, t_m Elastic modulus and thickness of the membrane

σ_3' Effective principle stress in the lateral direction

M Slope of the steady state line (q/p')

I_R Relative density index

CG Abbreviation for crushed glass

$Rhein$ Abbreviation for Rhein sand

CG Abbreviation for round glass

a, b Certain fitting parameters for the $CSR - N$ relationship

M_w Moment magnitude of an earthquake

I Inclination of the trendline in the $CRR - I_D$ curves

$\bar{x}, d_{i,avg}$ Averaged value of the fitting parameters x and d (also denoted as $\bar{d}$

S_u Grain shape uniformity coefficient obtained from the shape distribution curves d

S_{50} Mean grain shape from the shape distribution curves d

k_n, k_s Normal and tangential stiffnesses respectively

μ, μ_i, μ_f Friction coefficients, typically at beginning and end of sample preparation using the DEM

F_n, F_t Normal and tangential contact forces

CN Mechanical coordination number

CN_0 Coordination number

N_0, N_1 Number of particles with zero and one contacts respectively

M_c Slope of the critical state line (equivalent to M) as defined in SANISAND

$M_{e/c}$ Ratio of the critical state slopes under extension and compression regime

m Tangent of half the opening angle of the yield surface

G_0^{el} Dimensionless shear stiffness parameter

h_0 Positive material constant 1 to define the hardening modulus

c_h Positive material constant 2 to define the hardening modulus

n_b Material constant to calculate the stress image on the boundary surface

A_0 Dilatancy material constant

n_d Material constant to calculate the stress image on the boundary surface

z_{max} Maximum value that z can attain

c_z Control of the evolution of z

SI Sensitivity index

1 Introduction

1.1 Background

Dynamic loading may be caused by man-made or natural sources. Man-made dynamic loadings include those originating from machine foundations, drilling, explosions/blastings or may also result from operation of very heavy or unbalanced machinery, mining, construction (such as pile driving, deep dynamic compaction, etc.) and heavy traffic. One of the most common examples of natural dynamic events are earthquakes. An earthquake may be described as the ground motions resulting from a sudden slip on a fault or from volcanic activities, or any sudden stress changes in the earth crust.

The destructive effects of dynamic ground motions are multifarious, some of which are landslides, tsunamis and forest fires. Some of the damages caused by earthquakes and repetitive dynamic motions are shown in Fig. 1.1. In view of this, two important phenomena require attention: the amplification of ground shaking, and liquefaction (Towhata 2008). In the event of ground shaking, the major issues that arise are:

- Amplification of motion in soft alluvial deposits.

- Permanent/residual deformation of earth structures.

- Landslides.

- Dynamic soil-structure interaction.

It is important to note that liquefaction may not only be a direct consequence of earthquakes. Take for example, the loosely deposited sand dumps in the former open pit mines in the Lusatian lignite fields in Eastern Germany, which occasionally liquefied without the occurence of an earthquake. The reason for liquefaction was found to be a re-increase in the water table since the termination of the ground water pumping at the end of active mining in the 1990s in combination with the loose collapsible state of the sandy dumps. The triggers were found to be earth construction works or other dynamic works in the vicinity. The following problems are widely encountered during soil liquefaction:
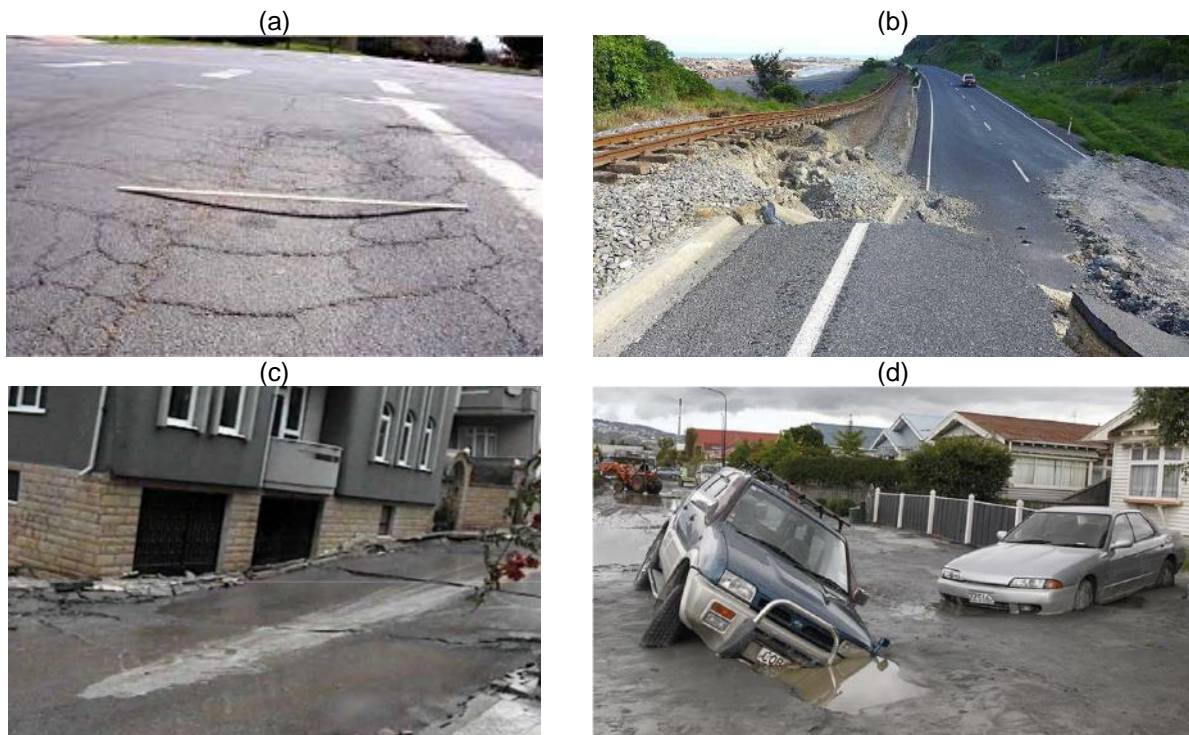
Figure 1.1: Damages due to dynamic events such as traffic loadings and earthquakes: (a) rutting due to repeated vehicle loads (after Calvarano et al. 2017), (b) ground settlement due to the Kaikoura 2016 earthquake (accessed from: stuff.co.nz), (c) differential settlement underneath buildings in Christchurch (accessed from: theconstructor.org), and (d) liquefaction of soils, a direct consequence of the Christchurch (2011) earthquake (accessed from: stuff.co.nz)

- Loss of bearing capacity.

- Boiling of sand and water.

- Lateral flow of ground.

- Uncertainties related to soil-structure interaction.

All of these situations are responsible for significant economic damages, therefore efforts have been made in the past few decades to understand and minimize their detrimental effects. One of the major aims of geotechnical earthquake engineering is to predict the magnitude of the ground motions which are expected to occur for a specific earthquake so that engineers can take this additional information into consideration while designing structures. This is termed as ground response analysis. The resulting dynamic stresses and strains due to ground motions are usually recorded for evaluation of liquefaction hazards. Since the early 1900s, seismologists and geotechnical engineers have worked towards the development of empirical methods based on the characteristics of recorded earthquakes

to chart predictive relationships to assess both ground motion and liquefaction analysis. However, much work remains to be done in this aspect since soil properties vary from place to place which means ground response analyses must be carried out in a site-specific way.

1.2 Basic definitions

This section introduces some of the most important terminologies that are frequently used throughout the course of the thesis. Focus is laid in particular on the established concepts that are used in studies relating to liquefaction of soils (both under monotonic and cyclic loading) and other dynamic properties.

1.2.1 Liquefaction susceptibility

In 1920, Hazen was the first who used the term 'liquefy' in the context of soil mechanics to denote the phenomenon of liquefaction. A more general definition of liquefaction was given by Castro & Poulos (1977), where they stated it as "a phenomenon wherein a saturated sand loses a large percentage of its shear resistance (due to static or to cyclic loading) and flows in a manner resembling a liquid until the shear stress acting on the mass is as low as its reduced shear resistance". Indeed, liquefaction occurs when a mass of saturated/partially saturated cohesionless soil loses strength due to the generation of excess pore water pressure, resulting in large deformations. Liquefaction may result in landslides, lateral soil spreading, large settlements and tilting of buildings, and failure of waterfront retaining structures. Some of the popular cases of natural disasters caused by liquefaction are Niigata and Alaska (1964), San Fernando Dam failure (1971), and the Loma Prieta (1989) and Kobe (1995) earthquakes.

Studies have reported two different types of liquefaction mechanisms due to application of dynamic loading: flow liquefaction and cyclic mobility. Static liquefaction or static instability refers to the undrained deviatoric strain softening behavior observed in monotonic undrained tests (refer Fig. 1.2a). Under cyclic undrained loading, the material might display a flow type of behavior characterized by a sudden large deformation, mostly in extension. This is characterized by a sudden loss of mean effective stress and a significant increase in pore water pressure (Fig. 1.2b). Additionally, cyclic liquefaction can occur either as cyclic mobility or instability. In these conditions, the soil shows deviatoric strain softening response due to a series of cyclic stress pulses and rapid generation of excess pore water pressure, although the initial deformations are not as high as in the case of

flow liquefaction (Fig. 1.2c). Cyclic mobility is generally encountered in fine-grained soils as well as medium dense to dense sands, where overlapping butterfly-shaped loops in the effective stress path are evident.
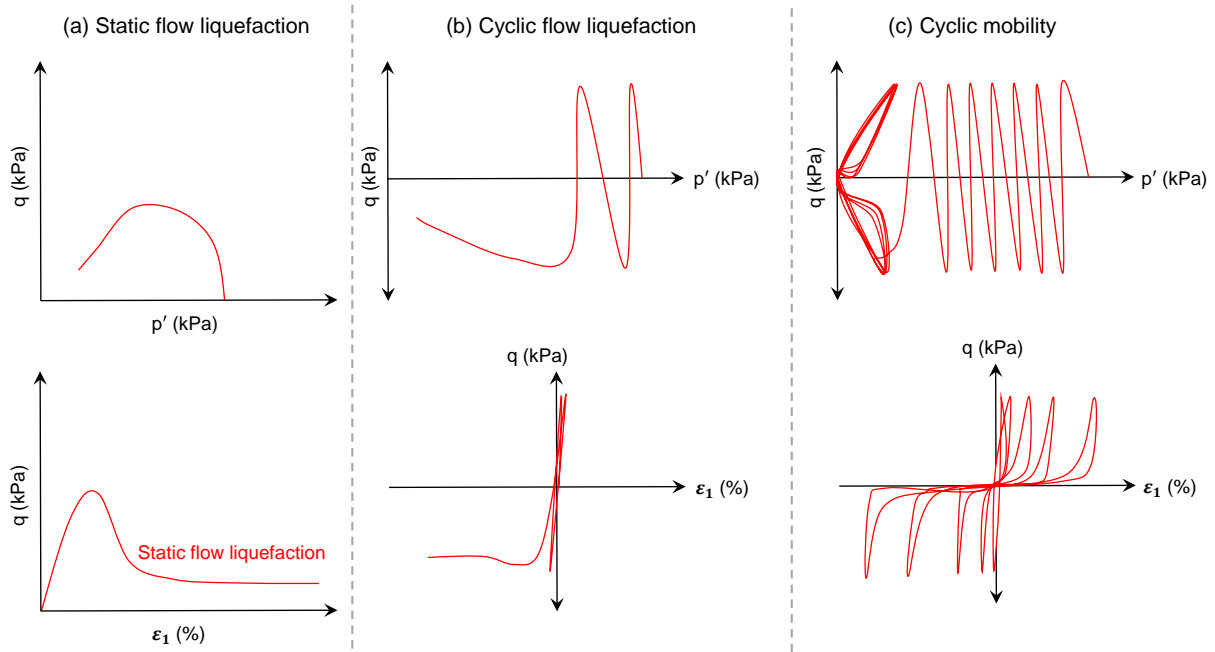
Figure 1.2: Schematic representation of different forms of liquefaction encountered under static and cyclic undrained loading

There have been significant advances in the past decades to understand the effect of various uncertainties not only related to earthquakes, but also soil characteristics and boundary conditions which play an important role on the instability and liquefaction susceptibility of soils. In granular materials, the mechanical properties are primarily governed by the grain-to-grain contacts, particle characteristics and particle rearrangement. For static and cyclic liquefaction of soils, the following sub-section discusses some important terminologies which will be used throughout in the course of this research.

1.2.2 Concept of steady state / critical state

The term 'steady state' (or critical state) was first coined by Casagrande in 1936, and was modified by Roscoe et al. (1958) to denote a state in which soil continuously deforms at constant stress and constant void ratio. This state is considered the ultimate state which soils reach once sheared. Castro (1969) modified the definition of steady state as the state at which the soil mass is continuously deforming at constant volume, constant normal

effective stress, constant shear stress and constant velocity. This can be mathematically represented as shown in Eq. (1.1):

$$dq = 0, dp^{'} = 0, d\epsilon_v = 0, du = 0 \text{ while } |d\epsilon_q| \neq 0 \tag{1.1}$$

Although some literatures report that the steady state and the critical state are not the same (Alarcon-Guzman et al. 1988; Konrad 1990), most studies conclude similarity between them (Casagrande 1975; Poulos 1981; Been & Jefferies 1985; Sladen et al. 1985; Verdugo & Ishihara 1996; Yamamuro & Lade 1998; Thevanayagam 1998). Casagrande (1975) separated these two terms by stating that critical state applies only to drained tests while steady state is used in the interpretation of undrained shear test results; however recently, through a compilation of several past studies, Kang et al. (2019) demonstrated a negligible difference between the steady state and critical state. Therefore, in light of these findings, the steady state and the critical state are considered the same throughout the present work.

Steady state line

As noted in the previous section, steady state refers to the final state of the soil undergoing continuous shear deformation at constant volume. Therefore, the void ratio remains constant irrespective of the magnitude of shear deformation. The final void ratio of the soil at such a state is termed as the steady state void ratio e_{ss}. The steady state has two aspects: the first is a locus or line in deviatoric shear stress q-mean effective stress $p^{'}$ plane (Fig. 1.3a), and the second is a line in the void ratio e-mean effective stress $p^{'}$ space (Fig. 1.3b). The steady state line (SSL) in $q - p^{'}$ plane is a straight line passing through the origin with a constant slope. In $e - \log p^{'}$ space, the SSL is treated conventionally as a straight line (after Schofield & Wroth 1968), which is denoted by Eq. (1.2). In other words, it denotes that the critical void ratio e decreases as the logarithm of the effective stress increases.

$$e_{ss} = \tau - \lambda \log \left(\frac{p^{'}_{ss}}{p_a} \right) \tag{1.2}$$

$p^{'}_{ss}$ and p_a denote the mean effective stress at the steady state and the atmospheric pressure respectively, whereas τ and λ denote the intercept and slope of the SSL (together termed as the steady state line parameters), and are intrinsic soil properties which can
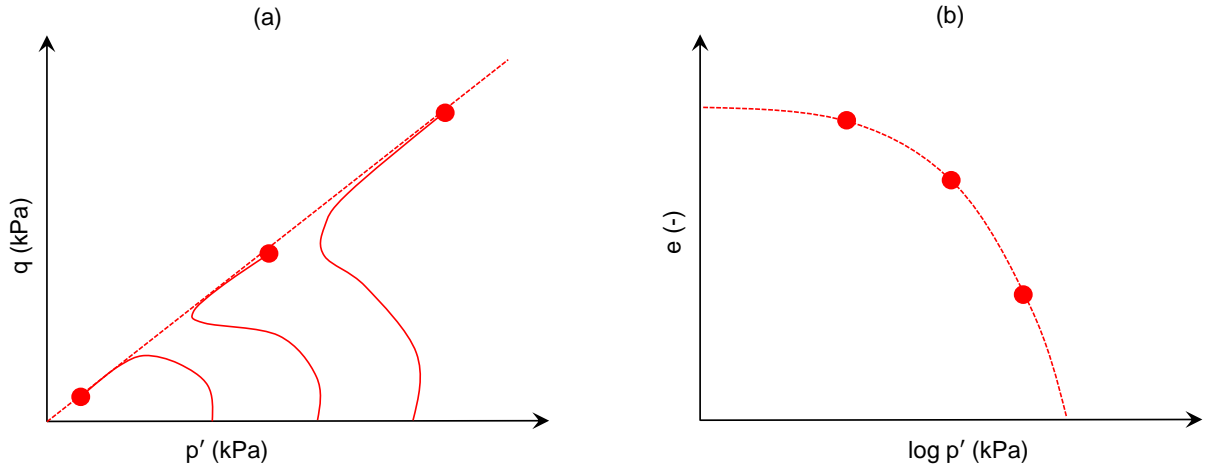
Figure 1.3: Schematic representation of the steady state / critical state in both (a) $q - p'$ and (b) $e - p'$ diagrams

be determined through experiments. In recent years, there have been certain arguments against adopting a linear expression for the SSL (Verdugo & Ishihara 1996; Thevanayagam et al. 2002; Rahman 2009). Certain triaxial test results on sand show that the SSL may be better approximated as a curve instead of a straight line, especially for low confining stresses. In light of this, Li & Wang (1998) suggested the exponential form of Eq. (1.3):

$$e_{ss} = \tau - \lambda \left(\frac{p'_{ss}}{p_a} \right)^{\alpha} \tag{1.3}$$

Therein α is a fitting parameter which can be assumed as 0.6 for sands and sand-fines mixtures (Yang & Wei 2012).

Quasi-steady state and phase transformation

Granular materials gain shear strength through interparticle sliding friction caused by the interlocking between individual particles due to the particle shape and surface roughness. The peak friction angle ϕ_p is typically achieved at the point where the shear strength of a granular material reaches the peak. Furthermore, under drained conditions, a dense material undergoes initial densification followed by dilation at larger strains causing a volume increase. For loose samples under drained conditions, contraction occurs leading to a volume decrease (densification) till reaching the critical state void ratio. In undrained tests, a quasi-steady state (QSS) or a phase transformation (PT) point may be encountered

as shown in Fig. 1.4. Contrary to reports by Zhang & Garga (1997), the QSS is widely considered to be a real material behavior rather than a test-induced or device-dependent phenomenon. With a further increase in axial strain, there are three possibilities: flow, partial flow and no flow behavior. For a sample undergoing flow liquefaction, the deviatoric stress continues to decrease after attaining a maximum till a steady state is achieved. However, for a sample undergoing partial liquefaction, the deviator stress increases after the QSS gradually till reaching the steady state. For no flow conditions, the existence of a phase transformation (PT) point may be noted, where a switch from contractive to dilative tendency may be encountered (Ishihara 1993; Nguyen et al. 2018). Generally, the PT phenomenon is encountered when the material is in a dense state (Li & Dafalias 2000). In general, flow behavior is noted for loose specimens whereas medium dense to dense specimens are expected to show no flow behavior.
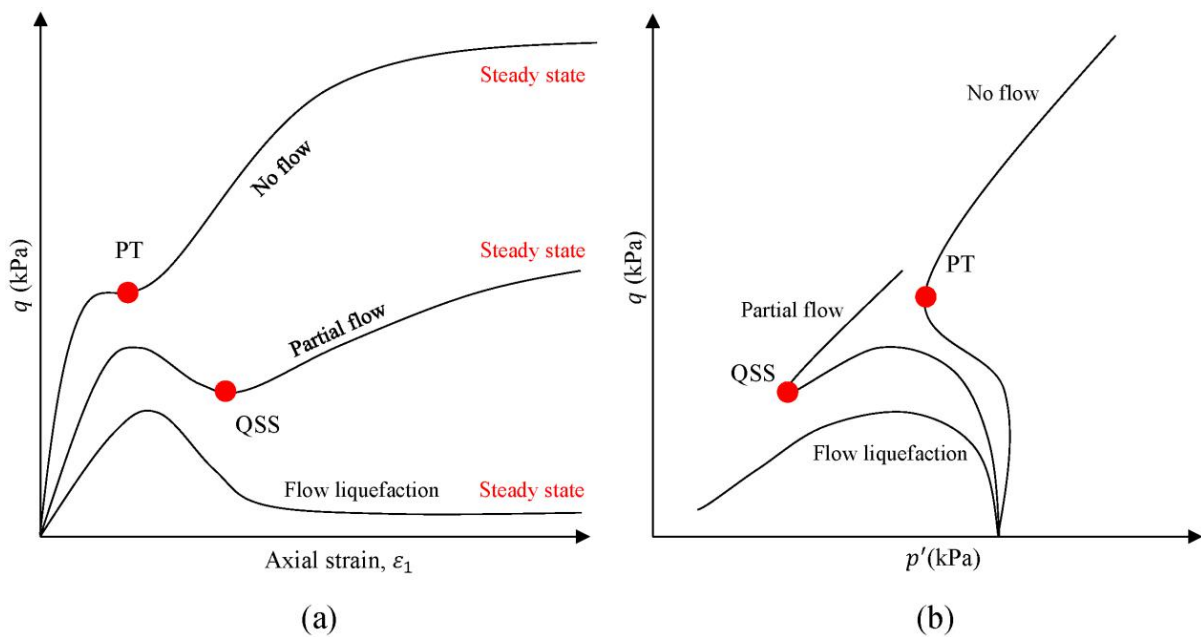
Figure 1.4: Concept of quasi-steady state (QSS) and phase transformation (PT) from (a) $q - \varepsilon_1$ and (b) $q - p'$ curves (modified after Zhang & Garga 1997 and Yang & Dai 2011)

1.2.3 Cyclic stress ratio (CSR) and cyclic resistance ratio (CRR)

When subjected to cyclic loads, saturated samples develop excess pore water pressure, which results in a decrease in the mean effective stress. After a certain number of cycles, the magnitude of the excess pore water pressure becomes equal to the total stress, as a

result of which the effective stress drops to zero. At this point, the sample starts showing large deformations since the shear strength of the specimen has been reduced to zero, i.e. the sample has liquefied. The amplitude of the cyclic deviatoric stress q^{ampl} that the specimen is subjected to divided by twice the effective confining stress p_0' is termed as the cyclic stress ratio CSR imposed on the specimen, while the number of cycles N_c needed to achieve zero effective stress denotes the number of cycles to liquefaction. Some studies use a certain strain criterion, e.g. reaching a double amplitude of 5% axial strain in extension and compression, in conjunction with the zero effective stress condition to denote failure. Plotting the results of various tests in terms of their CSRs against the corresponding N_c on a semi-logarithmic scale yields a unique relationship describing the liquefaction resistance (see Fig. 1.5). The cyclic resistance ratio (CRR) corresponding to an equivalent earthquake loading of a certain magnitude (e.g. M_w=7.5) is denoted as the value of the CSR from the above mentioned curve read at a certain N_c ($N_c = 15$ for example).
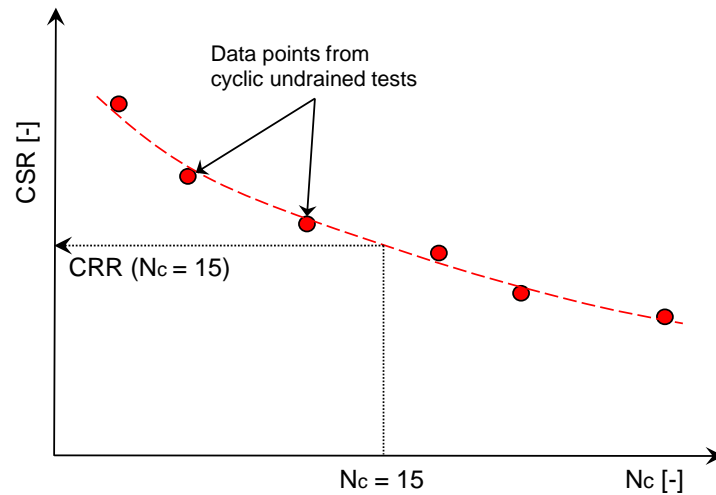
Figure 1.5: Schematic representation of the critical stress ratio (CSR) and critical resistance ratio (CRR) considering $N_c = 15$

1.2.4 Stiffness and damping in soils

The stiffness of a material indicates it's ability to resist deformation once a certain stress/load is applied on it. A material develops a certain stress and strain once an external load is applied on it. In mathematical terms, the ratio of the stress (force per unit area) to the strain (deformation per unit length) is referred to as the material stiffness.

When considering a soil specimen under one-directional axial loading, the ratio of the axial stress σ to the corresponding axial strain ε is denoted as the Young's modulus E (see Eq. 1.4a). If the load is torsional in nature, i.e. acts laterally in the form of a torque, the ratio of the generated shear stress τ to the corresponding shear strain γ denotes the shear modulus G (Eq. 1.4b).

$$E = \frac{\sigma}{\varepsilon} \tag{1.4a}$$

$$G = \frac{\tau}{\gamma} \tag{1.4b}$$

In a perfectly elastic medium, stress waves generated from an earthquake or other dynamic sources are expected to travel indefinitely without any change in the amplitude. However, in reality, this is not the case: the amplitudes attenuate with distance. This can be attributed to two factors:

Material damping

A part of the plastic energy of a travelling wave is converted to heat energy. Thus, this conversion of energy culminates in a reduction in the mechanical amplitude. Viscous damping is often used to represent this dissipation of elastic energy (Kramer 1996).

Radiation damping

In addition to the loss of energy caused due to material damping, a reduction in the specific energy (elastic energy per unit volume) due to increase in volume over which the waves are travelling is referred to as the radiation damping. This can also be illustrated by an example of an earthquake: at the epi-center of an earthquake, stress waves travel outward in all directions, and over time, the specific energy decreases since the wavefronts are spherical and cover a wider volume of the material. This mode of damping is also termed as geometric attenuation.

Determination of dynamic properties of soils

To determine dynamic properties of soils at various strain levels, there are two possibilities: in-situ measurement and laboratory testing. For in-situ tests, some of the most common

measurements are the geo-physical tests, which includes Seismic Reflection Test, Seismic Refraction Test, Suspension Logging Test, Steady-State-Vibration Test, Spectral Analysis of Surface Waves Test, Up-/Down-hole Test and Cross-Hole Test (Ishihara 1996; Kramer 1996; Reynolds 2011). Most of these tests are used worldwide for site exploration by practicing engineers. To measure dynamic properties in the laboratory, Resonant Column (RC) test, Ultrasonic Pulse Test, Piezoelectric Bender/Extender Elements Test, Cyclic Triaxial Test, Cyclic Simple Shear Test and Cyclic Torsional Test are of significance (Kramer 1996; Clayton 2011).
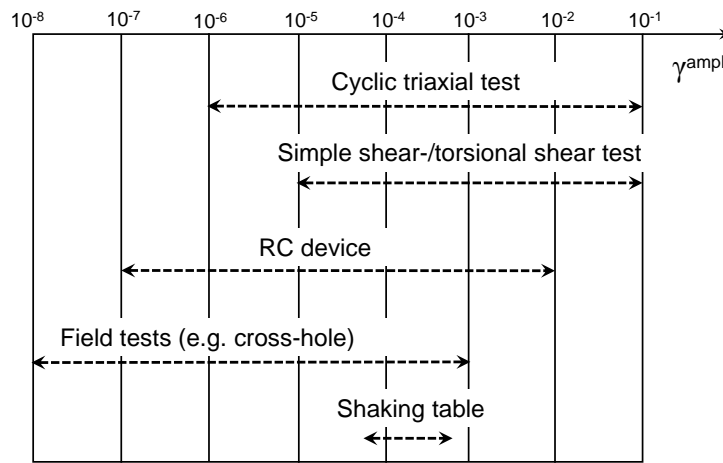
Figure 1.6: Typical ranges of shear strain amplitude γ^{ampl} for different types of tests (after Wichtmann 2005)

Furthermore, different tests measure soil dynamic properties at various strain levels: the resonant column test is suitable for determination of the properties in the range of small to medium strain levels (i.e. $10^{-4}\%$ to $10^{-1}\%$), whereas cyclic simple shear, cyclic torsional and cyclic triaxial tests are generally suitable for the evaluation of large strain dynamic properties (i.e. $> 10^{-1}\%$). The typical strain ranges corresponding to the various tests are summed up in Fig. 1.6. For certain strain magnitudes different test types can be applied. For example, at strains of 10^{-5} (or $10^{-3}\%$), the dynamic properties may be estimated using the RC device and cyclic triaxial devices in the laboratory, or through conducting field tests (like cross-hole tests).

In general, it is widely accepted that as the level of strain increases, the damping ratio D also increases while all stiffness moduli (G, E and constrained modulus M) decrease continuously (Goudarzy 2015; Goudarzy et al. 2018; Payan 2017). At very small strains, however, the stiffnesses are constant and take their maximum values as G_{max}, E_{max} and M_{max}. The variation of G and D with respect to the shear strain γ is shown in Fig.
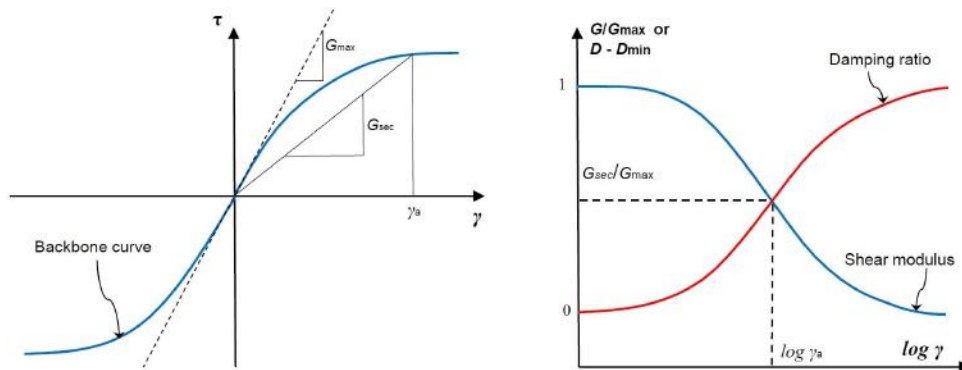
Figure 1.7: Definition of small-strain shear modulus and variations of shear modulus and damping ratio with shear strain (after Kramer 1996)

1.7. The modulus degradation at a certain shear strain is often quantified by the ratio G/G_{max}. Hence, the maximum value of this ratio is always 1, and with increasing strains, the ratio decreases due to decreasing G. The damping ratio at very low strains is very small and denoted as D_{min}.

1.3 Motivation and objectives of the present study

From past experiences, it is known that local soil conditions determine the nature and extent of damages due to dynamic ground motions. Amongst them, granular soils have significantly gained attention owing to their widespread appearance in nature. The mechanical behavior of granular soils has been a long standing interest in the scientific community, particularly because of their practical importance coupled with difficulties in the determination of grain contact properties in micromechanical investigations (Yang & Luo 2015). Based on the numerous earthquakes and dynamic motions that occur on a regular basis the magnitude of damages is different for different locations. For an earthquake of a similar magnitude on the Richter scale, certain places encounter larger damages while others remain practically unharmed. One of the prinicipal causes of this difference in soil behavior is varying particle characteristics as well as other boundary conditions such as the level of ground water, the possibility of drainage and relative density.

The physical properties of granular soils are dependent on various factors: the grain shape, size, gradation, mineralogy as well as fines content. Grain size and gradation can be readily determined in a standard geotechnical laboratory using a standard sieve analysis, while the determination of grain shape has always proven to be challenging which is why no

available standard specifies methods for its determination. Therefore, the majority of studies have described grain shape qualitatively, for example, as angular or round grains based on certain charts (e.g. Krumbein & Sloss 1963). However, recent computational approaches (e.g. Sukumaran & Ashmawy 2001; Rasband 2004; Landini 2008; Zheng & Hryciw 2015) have made it possible to characterize grain shape quantitatively.

In the last few decades, the influence of grain shape on soil properties has significantly gained attention (e.g. Santamarina & Cho 2004; Cho et al. 2006; Bui 2009; Cavarretta 2009). Alongside, the number of questions and uncertainities with respect to the influence of grain shape and size has also grown. For example, there have been several disagreements over the influence of mean grain size d_{50} on the limit void ratios in granular soils with some studies suggesting a significant influence (Kolbuszewski & Frederick 1963) contrary to others (Kabai 1968; Youd 1973; Zheng & Hryciw 2016). In particular, for sand-fines mixtures, the influence of grain shapes (of both sand and fines) on the limiting void ratios is an emerging field of research with only a handful of studies (e.g. Chang et al. 2015; Sarkar et al. 2020).

With respect to the static soil properties, i.e. the mechanical behaviour under monotonic loading, certain researchers have investigated the influence of grain size (Islam et al. 2011; Wang et al. 2013), fines content (Phan et al. 2016; Thevanayagam 1998) and mineral characteristics (Zhao & Liu 2018). A few studies have investigated the mobilization of the friction angles at the undrained peak shear resistance and steady state (Olson & Mattson 2008; Santamarina & Cho 2004), fabric (Been & Jefferies 1985), interparticle friction (Thornton 2000); however, studies on the influence of grain shape are quite rare. Only a handful of studies in the recent decade may be found on this aspect, e.g. Yang & Luo (2015), Altuhafi et al. (2016), and Alshibli & Cil (2018). Nevertheless, the variation of peak friction and dilation angles or steady state parameters (including steady state friction angle) with varying grain shape are unclear. Regarding the effect of grain shape on cyclic liquefaction susceptibility, only a couple of studies can be found in the present decade, e.g. Wei & Yang (2014), Keramatikerman & Chegenizadeh (2017) and Wei et al. (2020) demonstrating the lack of studies considering these aspects. In the field of small strain dynamic properties of granular soils, some researchers have recently proposed certain empirical models to account for the particle characteristics (e.g. Senetakis et al. 2012 and Payan et al. 2016); however, no studies were performed under intermediate strain ranges to account for the modulus degradation curve and damping ratio.

Therefore to sum up, limited studies can be encountered in literature dealing with the influence of grain characteristics (grain size, gradation and shape) on the static, cyclic and

dynamic behaviour of granular soils. Considering the importance of these properties for a ground response analysis or the evaluation of the liquefaction risk during earthquakes or due to man-made dynamic sources, the objective of this thesis is a comprehensive experimental study on the influence of particle characteristics on the mechanical behavior of granular materials.
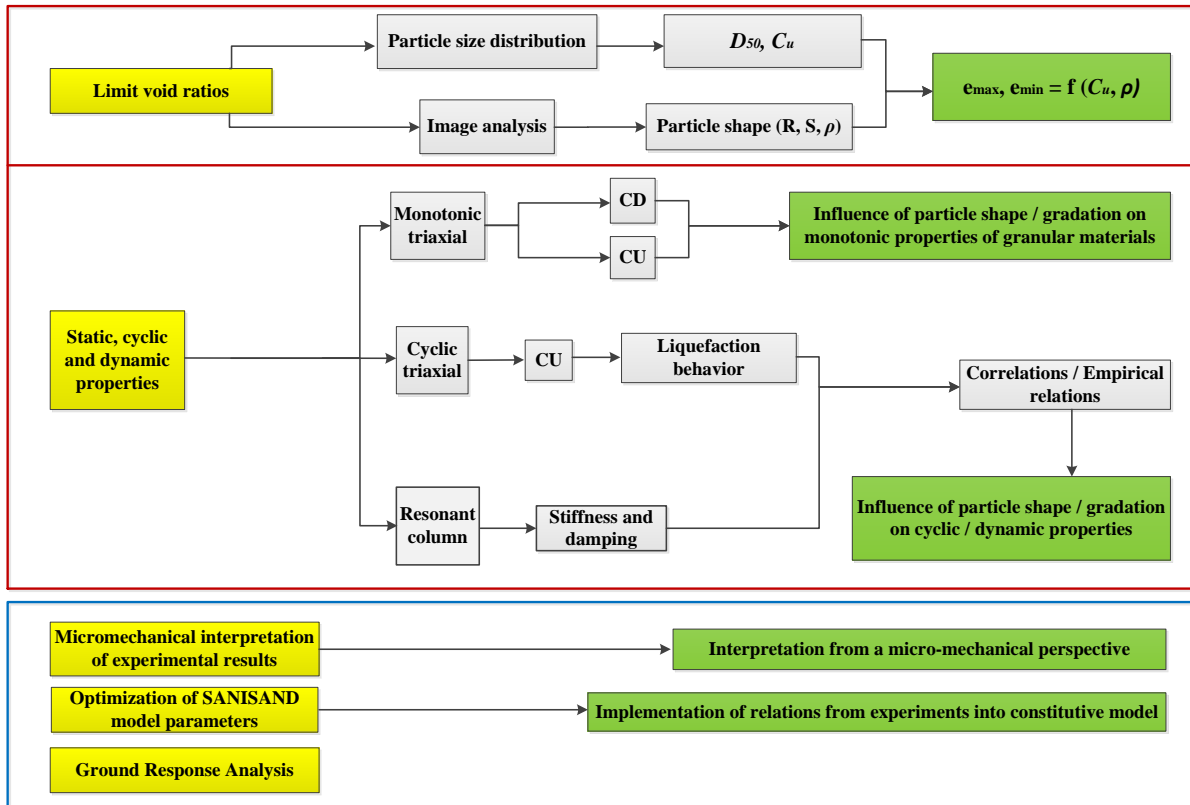
Figure 1.8: The complete work packages dealt with in the present study

To achieve the above objectives, the present work is divided roughly into three work packages (denoted as WP) represented in Fig. 1.8. The first work package deals with a new set of empirical equations to characterize the limit void ratios e_{max} and e_{min} of granular materials considering both the influences of grain shape and grain size. The second work package forms the backbone of the research as it includes various laboratory studies using monotonic and cyclic triaxial tests along with resonant column tests. Various aspects of the influence of grain shape, size and gradation on the behavior of granular materials under monotonic, cyclic and dynamic loading are brought forward. The third work package interprets the experimental findings from a micromechanical and continuum perspective. At the end, the experimental data will be used to study the influence of grain

shape through simulating the ground deformation responses under a certain pre-defined dynamic motion representating an earthquake.

1.4 Contents of the thesis

This thesis consists of eight chapters, the contents of which may be summarized as follows:

- *Chapter 1* introduces the topic, briefly provides the motivation, objectives and lists the organization of this thesis.

- *Chapter 2* presents a comprehensive literature review on the state-of-the-art studies in the field of particle shape characterization as well as introduces previous studies investigating the influence of different factors and boundary conditions on the properties of soils incorporating small to large strains.

- *Chapter 3* presents methods for the characterization of grain shape of granular materials using image analysis procedures. The effect of particle shape and size on the limit void ratios e_{max} and e_{min} is studied based on own experimental data and data from the literature. The dependencies are described by a mathematical model.

- *Chapter 4* presents the laboratory devices that were used for the experiments along with a description of their operation and calibration procedures.

- *Chapter 5* studies the monotonic and cyclic characteristics of granular materials. The effects of particle shape and gradation on the various soil properties such as shear strength, peak friction, dilation and steady state angle are discussed. Results from cyclic undrained triaxial tests to investigate the influence of grain shape and gradation on the liquefaction behavior of granular soils are also presented.

- *Chapter 6* shows the results for the influence of grain size, shape and gradation on the shear modulus and damping of granular materials at small to intermediate strains through an extensive experimental study using the resonant column device. Additionally, recommendations to quantify grain shape in a more holistic way for characterizing the shear wave velocity of granular materials was provided.

- *Chapter 7* discusses in brief the micromechanics of granular materials using discrete element modeling. Furthermore, recommendations to consider the influence of grain shape on the material constants of the elastoplastic SANISAND model were provided. Ground response analyses were also carried out to study soil deformations under pre-defined earthquakes in ground with different particle characteristics.

- *Chapter 8* summarizes the results from the research as well as provides some recommendations for future studies.

2 State-of-the-art review

The current state-of-the-art review considers the relevant and most current research concerning the effect of particle characteristics on the behavior of granular soils. It summarizes and critically analyzes the experimental and computational approaches to determine and describe the particle characteristics. Additionally, based on the literature review the need of further research is outlined, which motivated the research presented in subsequent chapters.

2.1 Physical and mechanical characteristics of particles: an overview

The formation of sands is a geological process which takes place over thousands of years. The process of weathering of intact rock is complex and varies depending upon the climate of the region, which leads to various soils with different mineralogical composition. In general, sands constitute a unique mixture of mineral particles and voids filled mainly with air and water. In terms of mineralogy of the grains, quartz dominates along with small percentages of other minerals such as feldspar, muscovite, chlorite, magnetite, epidote, etc. Some sands are rich in carbonate. Such types of soils have a significant proportion of sediment fabric of biogenic origin caused due to wave induced accumulations of sediment (sand to boulder in size) deposited on shores (Short 2005). Such types of sands may be encountered in tropical or temperate beaches where a source of carbonate-producing detritus exists, explaining their widespread prevalence on coral reefs and tidal flats.

The most important processes that impart particle characteristics may again be subdivided based on the grain sizes. For small grains and clay minerals, the effect of chemical and biological weathering is significant. The disintegration of soil/rock under such effects occurs fastest under hot and humid climates. An excess of water may lead to leaching of important clay nutrients and may form acidic soils. In marshy regions having a poor drainage, the chemical mineralogy is dominated by organic matter. For large grains, the

size and shape is strongly affected by the process of solidification in igneous rocks (Smalley 1966). The older a sand, the higher the probability of it to be rounded since the sand grains have been subjected to mechanical and chemical weathering for a longer duration. In addition, with increasing angularity of the grains, the susceptibility of particle breakage increases. Through the process of water and wind erosion, sand grains are known to be transported over large distances in rivers, which would cause the surfaces to get smoother with lesser irregularities, imparting a rounded shape. Such rounded grains are common in desert regions and can be found commercially, especially in sand-mining regions. One well-known example is the Ottawa sand, found in the sand-mining pits of Ottawa, Illinois. Angular sands are commonly used for blasting (used to smoothen various surfaces under high pressures). However, it is important to note that various sands, having various shapes, sizes and mineralogy, exhibit different intrinsic mechanical properties.

The three most important parameters to describe particle characteristics in engineering practice are mineralogy, particle size and particle shape. In the following sections, the influence of particle mineralogy and size are summed up briefly, preceding an exhaustive review of studies on the influence of particle morphology which forms the core of the present research.

2.1.1 Particle size and size distribution

Particle size is an important parameter influencing the behavior of individual particles and the whole packing. The inter-particle friction between two glass spheres increases with an increase in the sphere size (Skinner 1969) as larger particles may contain a higher degree of internal flaws which may also lead to an increase in the degree of crushability and a lower strength (Bui 2009).

It is well established that particle size gradation strongly influences the limit void ratios (Cho et al. 2006; Sarkar et al. 2019a). A well graded material (with a higher uniformity coefficient) is expected to show lower void ratio limits and a smaller difference between the maximum and minimum void ratios than a poorly graded material. However, for sand-silt mixtures, a higher disparity exists in particle size, where the mean size of the host material may exceed the mean size of the fines by 6.5 times. In such cases, the soil skeleton may be more compressible at a certain percentage of fines by weight (called the threshold fines content) than at any other percentage. The limit void ratios at such fine content attain their minimum values, after which an increase in fine content leads to an

increase in the void ratios. A detailed discussion on the influence of the grain size on the static, cyclic and dynamic soil properties is carried out at a later stage.

2.1.2 Particle mineralogy

One of the most important properties of a soil is it's mineral content. Properties such as the specific gravity, Young's modulus, shear modulus and the Poisson's ratio are affected by mineralogy (Terzaghi et al. 1996; Mitchell & Soga 2005). Generally speaking, a higher value of elastic modulus implies that the soil has a lower compressibility, and can sustain larger contact pressure, and hence, a larger load bearing capacity than a soil with a low elastic modulus. As stated before, the main constituent of most sand grains is quartz, which is a mineral composed of silicon and oxygen atoms in a continuous framework of SiO_4 bearing a tetrahedral shape, chemically represented as SiO_2.

In marine environments, sediments can be widely divided into three subgroups: lithogenous, hydrogenous and biogenous sediments (Noorany 1989). The mineral constituent of carbonate sands are however different, since they are formed through the calcareous skeletal remains of corals, shells of mollusks and algae. Carbonate sands mostly contain hollow particles and have a rough exterior texture leading to higher particle crushing. In terms of chemical composition, some sands may also contain traces of phosphorus coming from the bones and teeth of marine organisms.

In addition, the mineral content of soils is directly responsible for influencing surface properties such as adsorption/absorption, and electro-chemical bonding leading to various contact patterns such as face-to-face or edge-to-edge (noticeable in clays). Strictly speaking, granular materials like sand and non-plastic silt are mostly inert in nature. Some researchers (e.g. Bowden & Tabor 1950; Horn & Deere 1962; Koerner 1970) have also suggested that mineral composition can also affect the inter-particle friction coefficient.

2.1.3 Particle shape: various morphology descriptors

There are different methods for the descriptive and quantitative representation of particle shape (ISO-9276 6). To incorporate every aspect of external morphology, Barrett (1980) stated three *independent* aspects to define particle shape: form, roundness and surface texture (Fig. 2.1). Considering a 2D projection obtained when particles are dropped onto a horizontal surface, the form is considered to be a property representative of the macro

scale geometrical proportions of the particle. It is often represented in terms of sphericity, which measures the degree of similarity between a particle and a sphere. In the medium scale, roundness measures the shape of the particle asperities. As a micro scale descriptor, surface texture or surface roughness is a measure of the roughness that is superimposed on both corners and edges between corners.
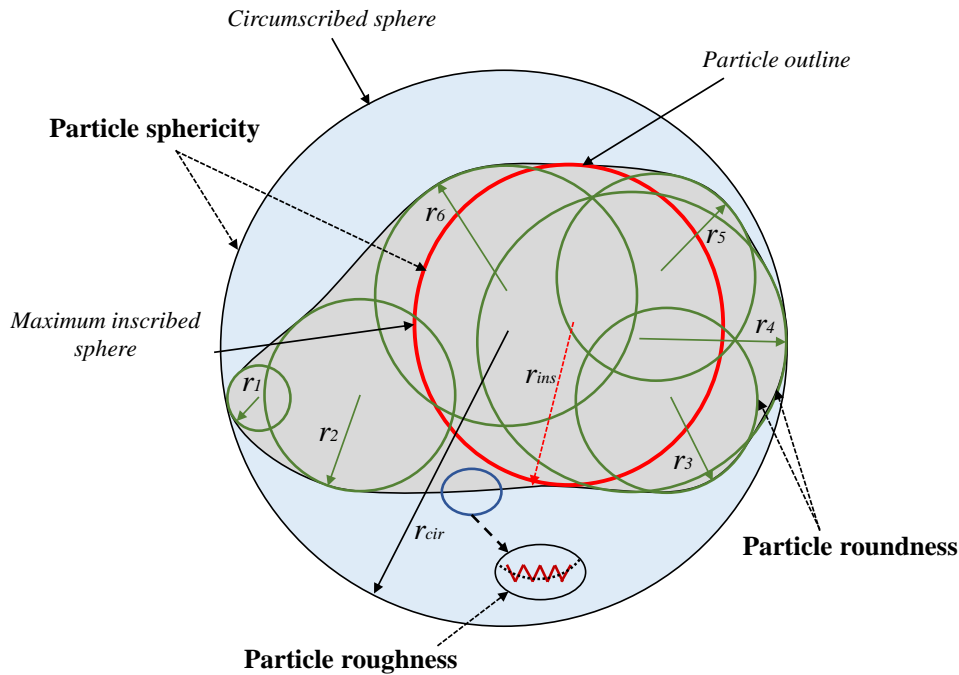
Figure 2.1: Particle shape terminology (form, roundness and roughness) defined by and modified after Barrett (1980)

Characterization of particle form

The first systematic approach to shape analysis was forwarded by Wadell during the early 1930s in his work on problems of sedimentation. As pointed out by Wadell (1932), the behavior of a particle in a suspension could be characterized by the ratio of the surface area of a sphere having the same volume as the particle (*ses*), to the actual surface area of the particle (*asp*). This ratio was termed as the degree of true sphericity (Ψ), and mathematically represented as:

$$\Psi = \frac{ses}{asp} \tag{2.1}$$

Wadell (1933) also introduced another 2D descriptor, termed as the degree of circularity, which is the ratio of the circumference of a circle having the same projected area as the particle, to the actual perimeter of the particle. In a later study, Wadell (1935) introduced the 2D degree of sphericity (S_w) as:

$$S_w = \frac{d}{d_{c,min}} \qquad (2.2)$$

where d is the diameter of the circle with an area A equal to the area of projection on the plane of the largest and intermediate particle diameters (L and I respectively) with the smallest diameter (S) perpendicular to the plane, and $d_{c,min}$ is the diameter of the smallest circumscribed circle. He further showed that for all shapes with a flatness ratio (S/I) greater than 0.25, the absolute scatter between the two degrees of sphericity ($\Psi - S_w$) was in the range of 0.01-0.08, which increased dramatically for flatter shapes (e.g. for $S/I \leq 0.25$). Owing to problems in measuring surface area of a particle, it is easier to calculate the ratio of the volume of a particle to the volume of the circumscribing sphere, the cube root of which yields the operational sphericity (Wadell 1933). Assuming a triaxial ellipsoid with three diameters, Krumbein (1941) modified the definition of operational sphericity (Ψ_0) as:

$$\Psi_0 = \sqrt[3]{\frac{(\pi/6) \times L \times I \times S}{(\pi/6) \times L^3}} = \sqrt[3]{\frac{I \times S}{L^2}} \qquad (2.3)$$

Rittenhouse (1943) proposed a visual but approximate method for estimating 2D sphericity. A reference chart was prepared by making enlarged camera lucida drawings of a large number of sand grains (Fig. 2.2). For computation of sphericity in the reference charts, the Wadell (1935) method was used. For visual determination of particle sphericity, individual grains were magnified and compared with the reference chart.

Corey (1949) hypothesized that a particle will generally fall with the largest projected area normal to the direction of fall. He reasoned that flatness is a significant shape factor and combined the flatness ratios S/L and S/I to define the Corey shape factor (CSF):

$$CSF = \sqrt{\frac{S \times S}{L \times I}} = \frac{S}{\sqrt{L \times I}} \qquad (2.4)$$

In other words, CSF is also the square root of the ratio between the cross section of the maximum inscribed sphere and the maximum projected area of a particle, and can be considered as a sphericity index. At the same time, Aschenbrenner (1956) argued that
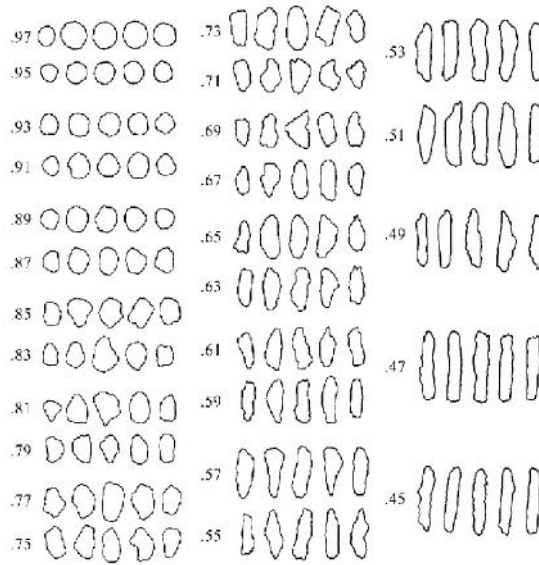
Figure 2.2: Visual chart for determination of 2D particle sphericity (after Rittenhouse 1943)

sedimentary sand grains do not have smooth surfaces like an ellipsoid and suggested considering particle shape as a solid with 14 faces (tetradecahedron). Furthermore, applying the concept of true sphericity as given by Wadell (1932), Aschenbrenner (1956) proposed working sphericity (Ψ_w):

$$\Psi_w = 12.8 \frac{\sqrt[3]{p^2 q}}{1 + p(1 + q) + 6\sqrt{1 + p^2(1 + q^2)}} \tag{2.5}$$

where p is the ratio of the smallest to the intermediate diameter (S/I) and q is the ratio of the intermediate to the largest diameter (I/L).

According to Sneed & Folk (1958), the drag force on an ellipsoid is proportional to the maximum projected area as the ellipsoid has a tendency to orient itself with the maximum projected area normal to the direction of motion. With this reasoning, they introduced the maximum projected sphericity (Ψ_p), which is defined as the cubic root of the ratio between the projected area of the inscribing sphere and the maximum projected area of a particle:

$$\Psi_p = \sqrt[3]{\frac{S^2}{L \times I}} \tag{2.6}$$

As evident from the above discussion, there are many different definitions of sphericity based on various theoretical considerations and specifications of their definition. Mitchell

& Soga (2005) and Zheng & Hryciw (2015) summarized the five most popular definitions of sphericity as follows:

- Area sphericity

$$S_A = \frac{A_s}{A_{cir}} \tag{2.7}$$

- Diameter sphericity

$$S_D = \frac{D_c}{D_{cir}} \tag{2.8}$$

- Circle ratio sphericity

$$S_C = \frac{D_{ins}}{D_{cir}} \tag{2.9}$$

- Perimeter sphericity

$$S_P = \frac{P_c}{P_s} \tag{2.10}$$

- Width to length ratio sphericity

$$S_{WL} = \frac{d_2}{d_1} \tag{2.11}$$

A_s and A_{cir} are the projected area of the soil particle and the area of the minimum circumscribing circle respectively; D_c, D_{ins} and D_{cir} represent the diameter of a circle having the same projected area as the particle, the diameter of the largest inscribing circle and the diameter of the minimum circumscribing circle respectively; P_c and P_s are the perimeter of a circle having the same projected area as the particle and the perimeter of the particle respectively; and d_1 and d_2 are the length and width of a particle respectively.

Characterization of particle roundness

Wadell (1932) pointed out that while sphericity is essentially a 3D particle property, roundness can only be measured in a single plane. According to him, a corner may be defined as any single part of the projected outline of a particle which has a radius of curvature r less than or equal to the radius r_{ins} of the maximum circle inscribed within the given projected outline. Extending this concept for all the corners inside the particle on a particular plane, Wadell defined the degree of roundness R_w as the arithmetic mean of the roundness of the individual corners in that plane, divided by r_{ins} defined mathematically as:

$$R_w = \frac{\sum_{i=1}^{N} \frac{r_i}{N}}{r_{ins}} \tag{2.12}$$

where N represents the number of corners of radius r_i, with $0 \leq r_i \leq r_{ins}$. Wadell's concept of 2D roundness was based on the theory that particles align on a horizontal surface in such a manner so that the maximum projected areas are visible for imaging. However, one major drawback of this definition of roundness was that it is a scale dependent parameter and varies with image magnification (Cavarretta 2009). On the contrary, Lees (1964) disagreed with Wadell's definition of roundness stating that it might not be applicable to crushed rock particles. He postulated a non-empirical method for determining the angularity of particles, considering the three main characteristics of angularity:

1. The degree of acuteness, which is the angle existing between the considered faces, measured in the plane of normal to these faces,

2. The relative projection, which is the projection of the tip of the corner from and relative to the size of the largest internal spherical mass of the particle, and

3. The number of angular corners.

A term, the angularity number, was suggested based on the angles subtended at corners by the particle:

$$Angularity\ number = \sum \frac{(180 - \alpha) \times x}{R} \tag{2.13}$$

where R is the radius of the largest inscribed circle, x is the distance between a corner tip and the center of the largest inscribed circle, and α is the angle at the corresponding corner. A practical difficulty of the method suggested by Lees (1964) is the determination of the center of the largest inscribed circle (Bui 2009).

Mandelbrot (1977) and Vallejo (1996) used fractal dimension to describe particle outlines. Glass beads, Ottawa and Pittsburgh sands were photographed by a 35 mm camera attached to a microscope, and an image analyzer and digitizer (for converting analog images into digital ones) was employed to obtain geometric information (area, perimeter, diameter, aspect ratio and fractal dimension).

However, it is argued by Sukumaran & Ashmawy (2001) that fractal analysis often fails to distinguish between particles of vastly different shapes. Also, it was noticed that large changes in particle morphology were reflected by small changes in fractal dimensions. To overcome this shortcoming, shape and angularity factors (analogous to Wadell's sphericity and roundness), were proposed for quantifying numerically a 2D projection of a particle. It was also shown that the shape and angularity factors provided independent measures of particle shape and angularity.

A mathematical descriptive technique based on Fourier analysis for characterizing 2D particle shape was forwarded by Ehrlich & Weinberg (1970). They estimated grain shape through an expansion of the periphery radius as a function of angle about the grain's center of gravity. The radius $R(\theta)$ is given by:

$$R(\theta) = R_0 + \sum_{n=1}^{\infty} R_n \, cos(n\theta - \phi_n) \tag{2.14}$$

In the above expression, θ is defined as the polar angle measured from an arbitrary reference line, R_0 is equivalent to the average radius of the grain in the given plane, R_n and n represent the harmonic amplitude and harmonic order respectively, while ϕ_n denotes the phase angle. However, one major drawback of this method was encountered with highly irregular particles, where the particle profile doubles back upon itself causing the radius to intersect the outline twice.

Visual methods for particle characterization

Wadell (1932) proposed a chart based on a visual examination of sand particles picked from different grade sizes of grains of St. Peter sandstone and enlarged to approximately the same size, as can be seen from Fig. 2.3. The values provided below the images are defined as *Roundness/Sphericity*. This method was completely based on eye estimation causing a higher probability of human errors. However, the first systematic and generalized attempt at classification of particles in terms of particle form can be traced back to the mid 1930s, where Zingg (1935) proposed a chart (Fig. 2.4) dividing particles into four categories: disc (oblate), spheroid, blade and roller (prolate), based on elongation (I/L) and flatness (S/I) of a particle. Although straightforward, the chart suffers from a major disadvantage while characterizing natural sand particles as the resulting diagram is overpopulated in sectors I, II and IV of the chart for values of I/L and S/I higher than 2/3.

Considering a particle to be a triaxial ellipsoid with long intermediate and short diameters denoted as a, b and c respectively, Krumbein (1941) presented a new expression for sphericity, termed intercept sphericity, defined as:

$$\Psi_i = \sqrt[3]{\frac{bc}{a^2}} \tag{2.15}$$

Adopting Zingg's chart for form characterization, a new chart combining the existing Zingg's chart and the chart based on intercept sphericity, was proposed as shown in
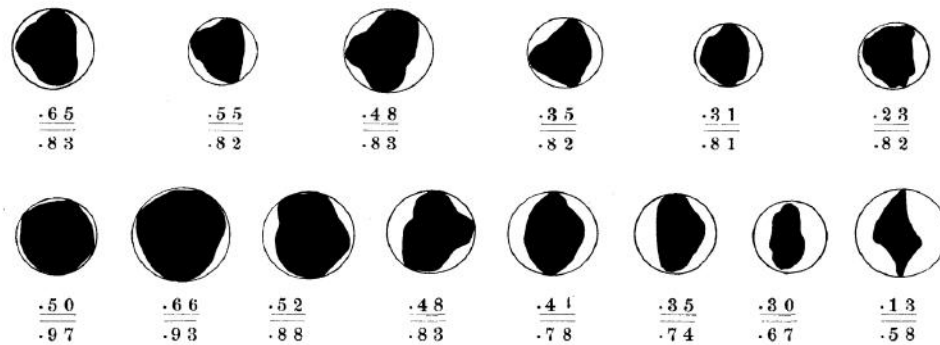
Figure 2.3: Visual chart for determination of particle form (after Wadell 1932): values for each geometry are represented as roundness over sphericity
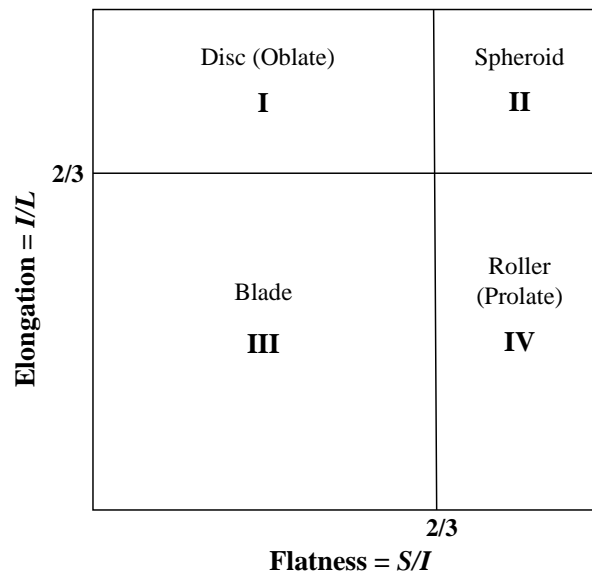
Figure 2.4: Classification of particle form, modified after Zingg (1935)

Fig. 2.5. Although the concept of intercept sphericity is not in terms with the true sphericity, this method has the added advantage of showing how different forms may have the same value of sphericity. As noted by Krumbein & Sloss (1963), the line representing an intercept sphericity of 0.5 sweeps through three classes: disc, blade and roller. However, Powers (1953) claimed that the visual method of Krumbein (1941) was slow and that the roundness class intervals were too small to be of significance. Six roundness classes between 0.12 and 1 (see Table 2.1) to determine roundness depending on either low or high values of sphericity were proposed: very angular, angular, sub-angular, sub-rounded, rounded and well rounded.

Table 2.1: Roundness classification chart suggested by Powers (1953)

Grade terms	Class intervals	Geometric means
Very angular	0.12-0.17	0.14
Angular	0.17-0.25	0.21
Sub-angular	0.25-0.35	0.30
Sub-rounded	0.35-0.49	0.41
Rounded	0.49-0.70	0.59
Well rounded	0.70-1.00	0.84

Sneed & Folk (1958) criticized the original Zingg's chart stating that it was inadequate for any detailed description of form since the chart had only four highly disproportionate classes. Consequently, they suggested using a triangular chart for form classification (Fig. 2.6). As pointed out by Cavarretta (2009), one major disadvantage of the Sneed and Folk chart is the inability to distinguish blade from roller like particles in a material having a high concentration of both types of particles.

Down the years, Krumbein & Sloss (1963) proposed a classical chart (Fig. 2.7) with intervals of 0.2 incorporating both particle sphericity and roundness, and which has far reaching consequences in studies relating to particle shape. Although the exact procedure for the preparation of this chart was not discussed, the sphericity was reported to be related to the proportion between length and breadth of the projected sections while roundness was based on the curvatures formed by the outlines. Cavarretta (2009) inferred that their definition might have been based on the circle ratio sphericity (also termed *irregularity*), which as noted earlier, is the ratio between the diameter of the largest inscribed circle to the diameter of the smallest circumscribed circle of the particle.

In recent years, Altuhafi et al. (2013) used 36 sands to characterize particle shape using angularity ratio (AR), sphericity (S) and convexity (C_x) to represent particle shape. With the QICPIC system, these three shape measurements were calculated, which prevented any scale dependent calculation, that is used in the evaluation of roundness. In agreement with the analysis of Powers' chart, angular particles generally had the lowest combined values of convexity and sphericity, whereas rounded particles had the highest. Empirical, graphical relationships between the values of convexity and sphericity and the qualitative shape measures (i.e. angular, subangular, subrounded, and rounded) were also developed. In addition, Altuhafi et al. (2016) proposed a parameter based on the sphericity, angularity and convexity of materials and denoted it as $SAGI$ which was able to locate the position of a material in 3-D space of AR, C_x and S. A smaller $SAGI$ ($SAGI$ <10) refers to

a rounded material, whereas a $SAGI$ greater than 12 would represent an angular material.
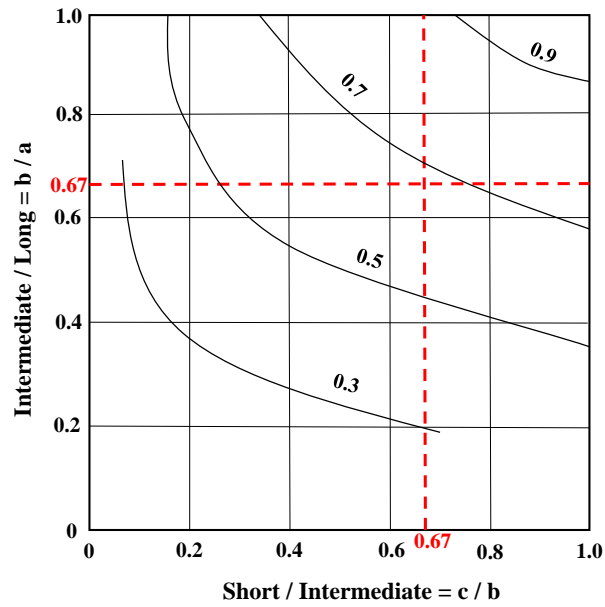
Figure 2.5: Classification of particle form suggested by Krumbein (1941): red dashed lines denote the classification borders as defined in the original Zingg's chart
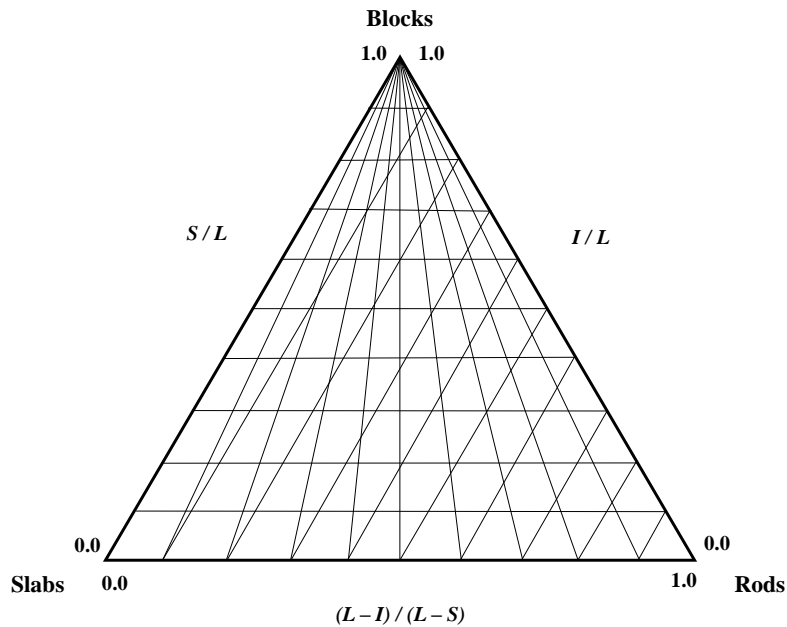
Figure 2.6: Triangular chart for form classification, adopted and redrawn after Sneed & Folk (1958)
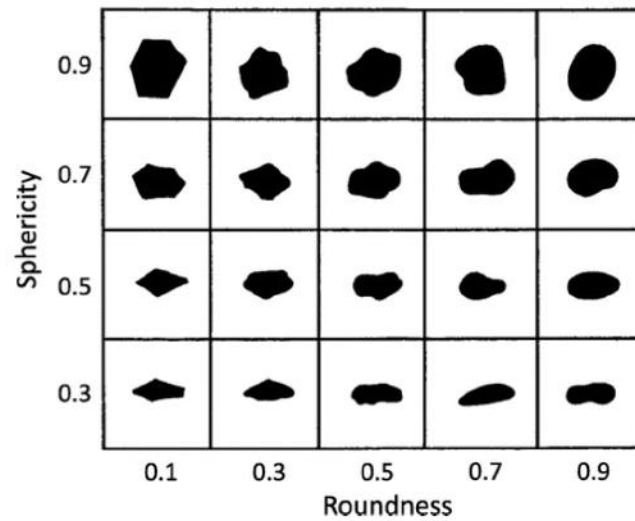
Figure 2.7: Visual chart for obtaining sphericity and roundness, after Krumbein & Sloss (1963)

Recent computational approaches to characterize grain shape

To simplify efforts in obtaining shape parameters, Zheng & Hryciw (2015) through computational geometry, developed methods for determination of soil particle sphericity, roundness and surface roughness. The digitization of Wadell's roundness was not an easy task as it called for a removal of the roughness and the particle's corners needed to be fitted with appropriate circles. The accuracy of the computational algorithm developed was verified with an excellent match with manually calculated results as well as the results of Krumbein & Sloss (1963). However, for image analysis, images with a minimum of 200 pixels per circumscribing circle diameter are required for accurate results.

Druckerey et al. (2016) developed a computer code to analyze 3D images of granular materials to measure particle lengths, volume, surface area, global centroid location and orientation using high resolution synchrotron micro-computed tomography (SMT) to quantify individual particle morphology including contact location and orientation. The major drawback however, was that for images with a high file size and a high number of particles, the computational time was considerably large - requiring over 70 GB RAM and 4-5 hours of computing time.

Furthermore, Zhou et al. (2018) developed a spherical harmonic analysis to reconstruct a 3D realistic surface of the sand particles based on X-ray micro-computed tomographic images collected from a series of image-processing techniques. As particle shape descriptors, three dimensional sphericity and roundness were used. Based on the analysis, their

methods proved to be efficient in capturing the 3D morphology, and the authors have kept the door open for more sophisticated and accurate discrete-element modeling in future.

Particle surface roughness

While sphericity and roundness are particle measurements in the macro and medium scale, particle surface texture is a measurement in the micro scale. Bhushan (2001) states that "the surfaces contain irregularities of various orders ranging from shape deviations to irregularities of the order of interatomic distances". Therefore it can be concluded that every surface has certain indentations no matter how smooth it may apparently seem to the naked eye. Furthermore, Bhushan (2001) categorizes surface texture into four distinctive regions: (1) roughness (nano and micro-scale roughness), (2) waviness (macro-roughness), (3) lay and (4) flaws. Since any natural surface can be defined through many scales, measurement of surface indentations can be therefore directly attributed to the sensitivity of the measuring device.

In one of the early attempts at understanding particle roughness, Richardson (1961) noticed that some natural surface profiles are self similar over a broad range of scales, meaning that the surfaces seem repetitive under different scales of magnification. A relationship was proposed between the length λ of the reference step of the measurement and the length of the profile $P(\lambda)$ as a set of points on the log-log plot. The slope of the line fitting the experimental data was observed to be nearly constant for λ varying over a broad range of scales. The slope of the constant line was $(1\text{-}D_{F_{ID}})$, with $D_{F_{ID}}$ representing the 2D fractal dimension of the surface.

Later, in an attempt to measuring the fractal dimension of a fractured surface, Friel & Pande (1993) stated that the fractal dimension of a self-similar surface can be represented as:

$$S(\eta^2) = \log C - [(D_s - 2)/2] \times \log \eta^2 \tag{2.16}$$

$$Slope = (D_s - 2)/2 \tag{2.17}$$

where $S(\eta^2)$ refers to the surface area at scale η (same as λ), D_s refers to the fractal dimension, and C is a constant. In general, for a geometrical entity (defined by the length of a profile or area of a surface) M_{ge} with n number of dimensions, the expression of the

fractal dimension $D_{F_{nD}}$ of a self-similar geometric entity can be derived as the slope of the line $\log\left[M_{ge}(\lambda^n)\right], \log(\lambda^n)$ (Cavarretta 2009):

$$D_{F_{nD}} = n \times (slope) + n \tag{2.18}$$

In the scope of the present work, surface roughness is not taken into consideration: therefore a detailed state-of-the-art is not presented. As a reference, some other relevant suggested studies relating to particle roughness are Greenwood & Williamson (1966), Greenwood & Tripp (1967), Whitehouse & Archard (1970), Stremler (1982), Mate (2008), Cavarretta (2009), Cavarretta et al. (2010), Cavarretta & O'Sullivan (2012) and Yang et al. (2016).

2.2 Influence of particle characteristics on the limit void ratios

2.2.1 Influence of the particle size and gradation

The influence of the grain size on the maximum and minimum void ratios (e_{max} and e_{min} respectively) has been a point of investigation since the early 1930s. Burmister (1938) reported that when the range of particle sizes is larger, the density increases and, consequently, the void ratios are lower. One major drawback of the work was that the methods employed for obtaining the maximum density values did not provide an adequate measure for maximum density (Youd 1973). Later, in the 1960s, Kolbuszewski & Frederick (1963) demonstrated that the density limits of sands increase with increasing particle size although insufficient data was provided to back up their claim.

Kabai (1968) showed that a good correlation existed between maximum and minimum densities determined in the laboratory and the uniformity coefficient for Danube river sands. The minimum density was measured by pouring sand into a mold through a funnel, whereas maximum densities were obtained by compaction tests similar to standard compaction procedure (ASTM-D1557 07). The major drawback of their method was the limited accuracy of the maximum density while the effect of particle shape was totally ignored.

In one of the more well-known studies, Youd (1973) found that the influence of the mean grain size on the limit void ratios was negligible although larger grain sizes had slightly

lower void ratios, which was also in agreement with the findings of Cubrinovski & Ishihara (2002). They reported a significant influence of C_u where well-graded sands had smaller void ratios than uniformly graded ones. In addition, they proposed curves based on grain roundness and gradation as reference for determining e_{max} and e_{min} for clean sands (refer Fig. 2.8).
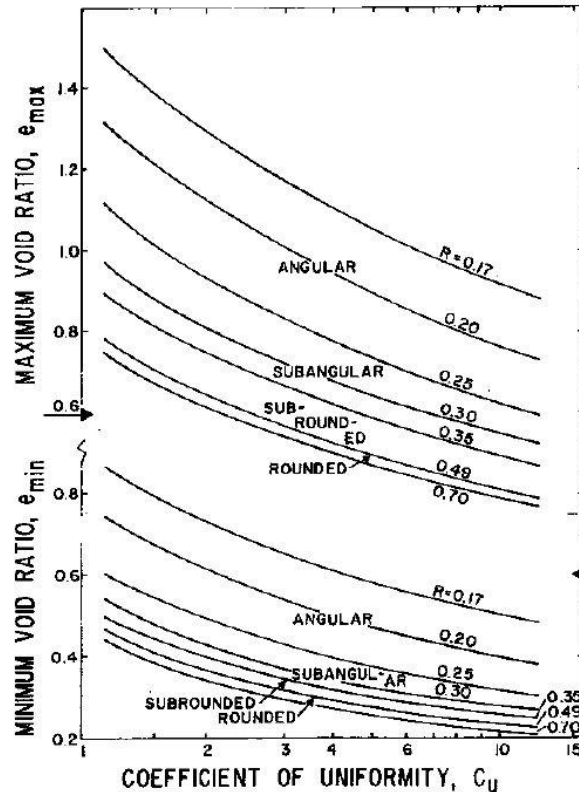
Figure 2.8: Generalized curves for estimating limit void ratios from gradational and particle roundness for clean sands (after Youd 1973)

Miura et al. (1997) examined the physical properties of sands and classified them further into primary and secondary properties, with the primary properties representing the permanent properties of soil grains such as mineralogy, shape, density and size distribution. Experiments were carried out in an attempt to study the relationships between primary and the index properties of sands. They concluded the following: e_{max}, e_{min} decrease with increasing d_{50} or C_u (Fig. 2.9a,b), the difference between the limiting void ratios ($e_{max} - e_{min}$) decreases with d_{50} but not with C_u (Fig. 2.9c), $e_{max} - e_{min}$ increases with increasing angularity and the angle of repose is independent of both d_{50} and C_u.

In recent studies, Zheng & Hryciw (2016) confirmed the findings of Youd (1973) and proposed equations to predict the limit void ratios for granular soils considering C_u as the
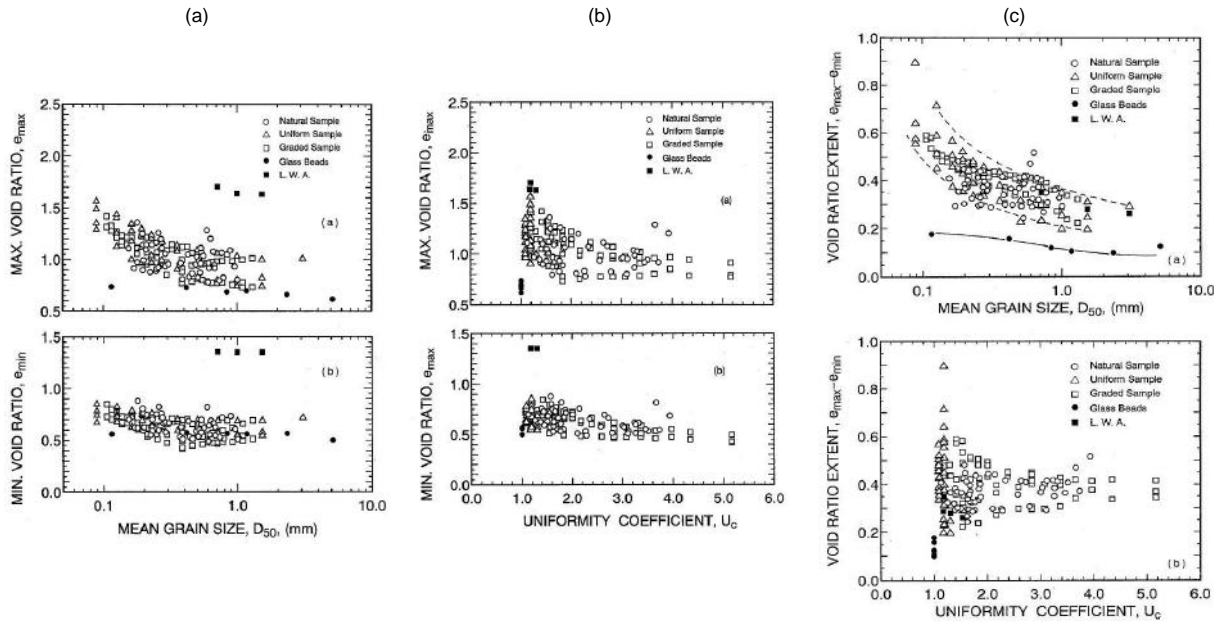
Figure 2.9: Variation of limit void ratios of clean sands with particle gradational characteristics after Miura et al. (1997)

relevant grain size parameter. They proposed the following equations for e_{max} and e_{min} using roundness R, sphericity S, uniformity coefficient C_u and reference void ratios $e_{max}°$ and $e_{min}°$ for glass beads having $R = S = C_u = 1$ respectively:

$$e_{max} = R^{-0.20} S^{-0.25} C_u^{-0.10} e_{max}° \tag{2.19}$$

$$e_{min} = R^{-0.15} S^{-0.25} C_u^{-0.15} e_{min}° \tag{2.20}$$

2.2.2 Influence of the particle shape

The first document which attempts to classify soil grains based on particle roundness can be traced back to Russell & Taylor (1937). Through visual examination and comparison with reference photographs, they proposed five classes for shape, varying from angular to well rounded. A tendency for the larger grains to possess both higher sphericity values and a higher degree of roundness was reported. In terms of mineralogy, a decreasing roundness was observed for minerals having a higher degree of quartz. A couple of decades later, Kolbuszewski & Frederick (1963) demonstrated that the density limits of sands increase with increasing particle size and decrease with increasing angularity. Using the

tipping method (Kolbuszewski 1948), the minimum void ratios were obtained, whereas
the maximum void ratios were determined by depositing sand in a vacuum.

One of the classical attempts at characterizing the limit void ratios using both the particle
shape and size was done following procedures listed in ASTM-D2049 (69) by Youd (1973)
through a comprehensive laboratory program. The results indicated that particle mean
size has no effect on the limit void ratios unlike the uniformity coefficient and roundness,
an increase in each of which causes a decrease in the limiting void ratios. However, the
influence of particle sphericity was not taken into consideration in the analysis.

Yasin & Safiullah (2003) used sphericity, elongation and flakiness as particle characteristics
to investigate the strength and volume change behavior of sands. Surprisingly, the sands
with higher sphericity were found to show higher void ratios than angular ones, contrary
to Youd (1973) and Miura et al. (1997).

One of the most comprehensive discussions highlighting the importance of the role of
particle shape on soil mechanical properties and the need for its characterization was
delivered by Santamarina & Cho (2004). In addition to particle shape characterized by
roundness and sphericity, roughness was also identified as another influencing parameter
in affecting mechanical behavior of soils. Besides, a comprehensive discussion on the effect
of particle shape on certain parameters (oedometric stiffness, small strain stiffness, critical
state, dilation and peak friction angle, monotonic and cyclic liquefaction) was provided.
Through a continuation of the work, Cho et al. (2006) carried out a comprehensive and
extensive study to rigorously investigate the effect of particle shape on the limit void
ratios (refer Fig. 2.10), critical state friction angle, intercept and slope of the critical state
line using a huge database compiled from literature. A new parameter called regularity,
which considers both the effect of roundness and sphericity, was introduced: a decrease in
regularity leads to an increase in the limit void ratios and the void ratio interval, decrease
in the small strain stiffness but increased sensitivity to the state of stress, increase in the
critical state angle, intercept and the slope of the critical state line. This study is one of
the most comprehensive ones to investigate the various aspects of particle shape in detail.

A decreasing non-linear variation of the limit void ratios with increasing particle roundness
was suggested by Rousé et al. (2008) although the parameter sphericity was not used (ref.
Fig. 2.11). In recent years, Altuhafi et al. (2016) evaluated the effect of size, shape, and
mineralogy on the mechanical behavior of sands using a compiled database of 25 sands
and encountered a decreasing trend of the limit void ratios with increasing aspect ratio
(AR), convexity (Cx) and sphericity (S). Furthermore, a new parameter $(SAGI)$ which
considers the effects of AR, Cx and S was proposed, which takes a higher value for
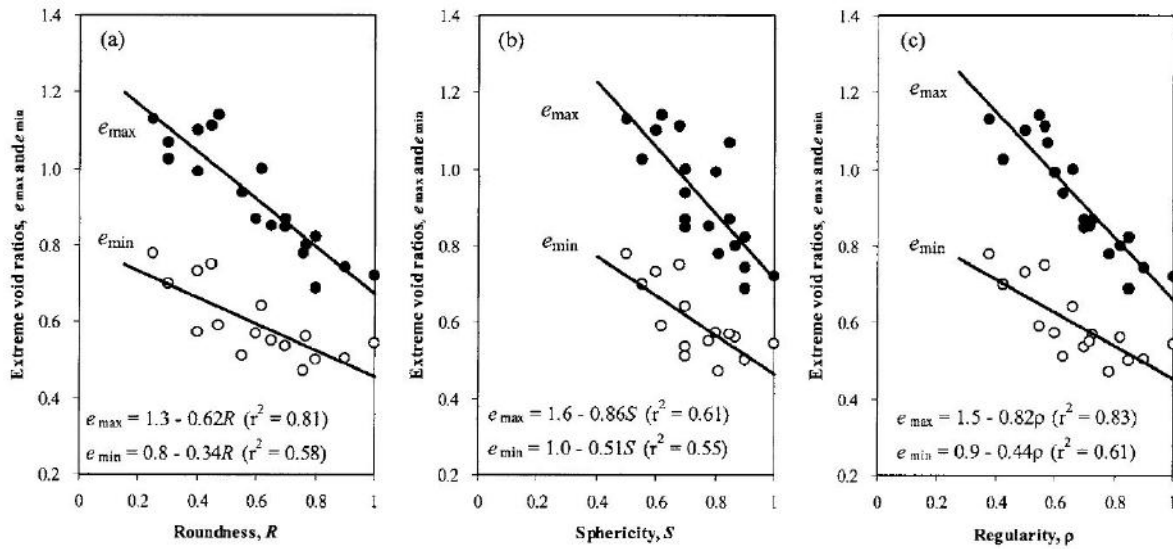
Figure 2.10: Effect of grain shape descriptors (a) Roundness R, (b) Sphericity S and (c) Regularity ρ on extreme void ratios (after Cho et al. 2006)

angular materials. Zheng & Hryciw (2016) formulated new equations (Eqs. 2.19 and 2.20) incorporating the influence of grain roundness and sphericity to characterize granular soils, where they claimed the superiority of their model in comparison to the model using only roundness presented by Youd (1973).

2.3 Mechanical characteristics of soils

In this section, a comprehensive discussion on the effect of particle size, mineralogy and shape on the engineering properties of granular materials follows. The subsections are divided into three parts - static (monotonic) tests, cyclic tests and small-strain dynamic characteristics.

2.3.1 Static and intrinsic properties of granular materials

2.3.1.1 Effect of particle size

One of the earliest studies that deals with the effect of particle size and grading on the shearing behavior of granular materials may be found in Kirkpatrick (1965). Through a series of drained triaxial tests on sand and glass beads, the shear strength of the granular
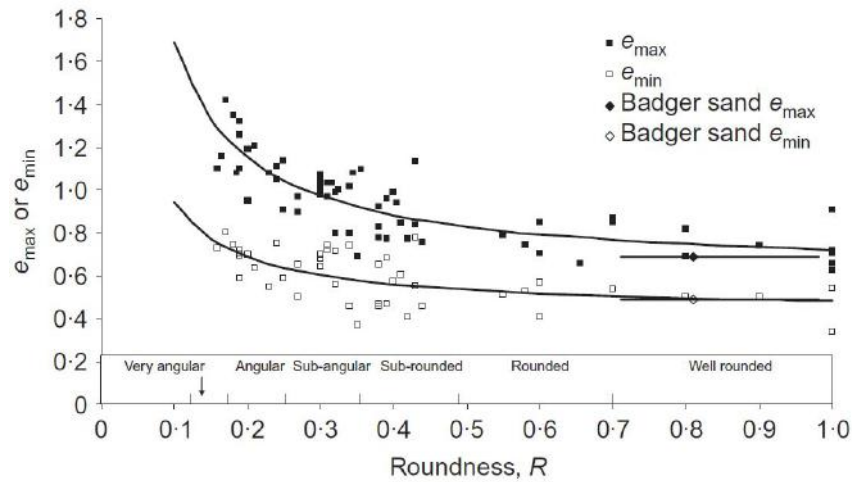
Figure 2.11: Influence of roundness R on extreme void ratios of granular soils (after Rousé et al. 2008)

materials was found to be independent of particle size and grading. On the contrary, an increase in the shear strength with an increase in the average particle diameter and a decrease in the uniformity coefficient C_u was found by Wang et al. (2013) on accumulated soils (rock-soil debris deposit), similar to the results of Kolbuszewski & Frederick (1963) and Zolkov & Wiseman (1965). The results also fit the observations of Kokusho et al. (2004) who reported similar findings from their monotonic tests on two different granular soils with three different gradations. Similar observations were made in Islam et al. (2011). Therefore, it can be concluded that the peak shear strength and friction angle are found to generally increase with increasing d_{50}.

In recent years, Islam et al. (2011) found an increase in the shear strength as well as the angle of internal friction of soils with increasing gradation (C_u) on their tests encompassing 8 uniformly distributed samples and 2 well-graded sands. In a later study, Harehdasht et al. (2017) examined the potential influence of particle-size distribution on stress-dilatancy behavior of granular materials from the results of 35 conventional drained triaxial compression tests. They found that the shear strength and dilatancy of the various tested materials were independent of C_u but decreased with increasing mean particle size (d_{50}), which was in contrast to the findings of Wen et al. (2018), who found an opposite trend through discrete element method (DEM) simulations under biaxial testing conditions. Later, Zhou et al. (2017) found an increase in the maximum friction angles for a higher C_u through DEM simulations. To conclude, the influence of C_u on the sand

behavior under monotonic loading and particularly shear strength remains unclear and needs further investigations.

2.3.1.2 Effect of particle mineralogy

From past experiences, it is widely known that the properties of granular soils having different mineralogy (such as carbonate soils) are vastly different from siliceous ones. Generally, calcareous carbonate sands are softer than quartz-dominated ones (Agarwal et al. 1977). The strength of such carbonate sands may increase with a certain amount of cementation. Agarwal et al. (1977) reported that for carbonate contents higher than 45% and at higher normal stresses, particle breakage accelerated. The low yield strength of carbonate sands was further confirmed by Hyodo et al. (1996) where it was noted that the isotropic yield strength for calcareous based sands was 300 kPa while it was 10 MPa for Toyoura sand, a quartz based sand.

Brandes (2011) found larger peak friction angles for carbonate sands compared to quartz based sands due to the different volume change tendencies resulting from different mineralogy; however, at larger stresses, friction angles decreased owing to significant breakage. Based on a series of monotonic triaxial tests, Hassanlourad et al. (2014) also concluded larger shear strengths of carbonate sands compared to quartz based sands. The strain softening behavior of such sands was found to be more pronounced than in case of quartz based sands. Furthermore, the effect of soil density on carbonate sands was less pronounced as the discrepancies between effective stress paths of dense and loose samples of carbonate sand was less than that for Firoozkooh quartz sand. Similar to Brandes (2011), a higher friction angle (by approxmiately 5°) was also noted for the carbonate sands.

2.3.1.3 Effect of particle shape

Particle shape significantly affects the shear strength of granular materials. A look at literature demonstrates that granular materials with spherical particles usually have a smaller angle of repose and reduced shear strength as compared to non-spherical particles due to the presence of rotation and lack of interlocking between particles (Rothenburg & Bathurst 1992), although no concrete evidence of the same was augmented by experimental studies until the early 2000s. Rousé et al. (2008) suggested a linear increase of the friction angle for increasing angularity, similar to the observations of Yasin & Safiullah (2003) and Cho et al. (2006). Yang & Wei (2012) may be one of the firsts to carry out comprehensive experiments to study the influence of grain shape. They carried out a series of

undrained triaxial tests on mixtures of uniform quartz sands (Toyoura and Fujian sands) and non-plastic fines (angular crushed silica and round glass beads). Besides the shape of host material, the shape of fines was found to affect the critical state friction angle. A small amount of angular silica within the host soil increased the critical state friction angle while an addition of fine round glass reversed the trend (refer Fig. 2.12). In addition, collapsibility (i.e. strain softening due to flow liquefaction) was also related to particle shape, with rounded materials showing a higher degree of collapsibility. They concluded that in binary mixtures composed of both rounded host and fine material, the preferred motion is rolling which yields an unstable microstructure unlike angular host and fines, which yielded a stable microstructure due to interlocking which prevents rolling. Shin & Santamarina (2013) used mixtures of round Ottawa 20-30 sand and angular blasting sand to demonstrate that an increase in the angularity of particles implied an increase in void ratio, small-strain shear modulus, oedometric compressibility and friction angle, and a decrease in the lateral stress coefficient. The presence of angular particles caused a decrease in the particle mobility thus increasing interlocking although preventing the formation of densely packed sands, consequently leading to a higher friction angle. In the field of beach sediment dynamics, Stark et al. (2014) demonstrated that elliptic, platy particles showed high internal friction angles ($41° - 49°$) in direct shear tests, whereas a round to angular gravel had a lower friction angle ($33°$). Similar observations were also reported by Abbireddy & Clayton (2015) and Keramatikerman & Chegenizadeh (2017) through triaxial compression tests using various materials with different degrees of angularity.

The dominant role of grain shape against grain hardness in static liquefaction of sand-fines mixtures was demonstrated through a series of strain-controlled tests by Wei & Yang (2014). Round fines were found to increase the liquefaction potential while the opposite trend was observed when adding angular fines (Yang & Wei 2012). For mixtures containing rounded materials with a large size difference between the coarse and fine grains, the grains favored rolling motion yielding an unstable microstructure, thus causing stick-slip hysteresis response in the $q - p'$ curves. A notable reduction in the steady state friction angle was observed with increasing the amount of rounded fines. In a later study investigating the influence of the relative size and shape effects of the silt grain matrix within the sand on static liquefaction, Monkul et al. (2017) observed that the static liquefaction potential increased with a decrease in the uniformity coefficient and with a decrease in the mean grain diameter ratio ($d_{50,sand}/d_{50,silt}$). Contrary to the findings of Yang & Wei (2012), the angular TT silt caused more metastable contacts in the specimen than the sub-rounded SI silt, as a result of which, the specimens with TT silt liquefied easier than the ones with SI silt.

Using three types of sand, natural, crushed and mixed (50% natural+50% crushed), the effect of particle shape on monotonic liquefaction was investigated through triaxial compression tests by Keramatikerman & Chegenizadeh (2017) where a decrease in strength was encountered as the values of particle shape descriptors (i.e. roundness, sphericity and regularity) increased. In addition, soil with higher rounded particles tended to liquefy earlier, an observation which was similar to some previous reports although the influence of grain size was not considered. In recent studies, Cherif Taiba et al. (2018) investigated the effects of particle shape on the shear response of different categories of sand-silt mixtures under static triaxial loading conditions. At low silt contents, the angular host materials showed significantly higher values of undrained shear strength while, at fines greater than 40%, the rounded host materials displayed a higher undrained strength. Additionally, the combined roundness and sphericity of the sand-silt mixtures was suggested as the decisive shape descriptors, instead of using individual shapes for either sand or silt.
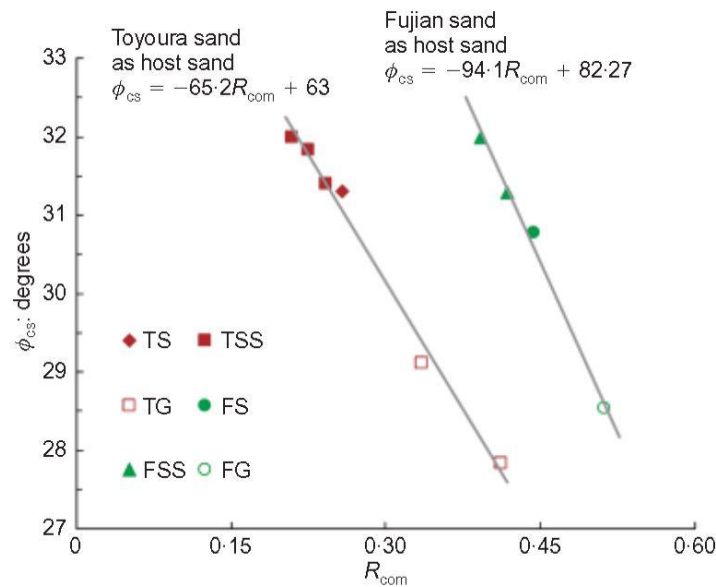
Figure 2.12: Variation of the steady state friction angle with combined roundness (overall roundness of mixture by weighted mass of host and fines) after Yang & Wei (2012). TS, TSS, TG, FS, FSS and FG refers to clean Toyoura sand, Toyoura sand with crushed silica and with glass beads, clean Fujian sand, Fujian sand with crushed silica and with glass beads respectively

2.3.2 Cyclic properties of granular materials

One of the most important characteristics of soils in geotechnical earthquake engineering is it's liquefaction resistance, i.e. the ability of the soil to resist dynamic loads without

showing a significant build-up of excess pore water pressure accompanied by a relevant loss in the shear strength. While the influence of certain factors such as the cell pressure (Castro & Poulos 1977; Seed 1981; Amini & Qi 2000; Hyodo et al. 2002; Bray et al. 2005; Rangasamy et al. 2010), degree of saturation and back pressure (Sherif et al. 1977; Yoshimi et al. 1989; Xia & Hu 1991; Yang et al. 2004), sample size (Wong et al. 1975; Campanella & Lim 1981), strain rate/frequency (Tatsuoka et al. 1986; Yamamuro & Lade 1993; Zhang 1994) and end constraints such as lubricated end platens (Vernese & Lee 1977; Tatsuoka et al. 1984; Tatsuoka et al. 1986) have been investigated and studied in great detail over the last 50 years, only few studies exist which deal with the influence of grain size and gradation, mineralogy and grain shape on the liquefaction resistance of granular soils.

2.3.2.1 Effect of particle size and gradation

A majority of the studies focus on the differences between sand and gravelly soils. Wong et al. (1975) showed that the liquefaction resistance of poorly graded gravelly soils was larger than that of sand possibly partially due to artificial effects of membrane compliance in large scale undrained cyclic triaxial tests. Similar observations were encountered in later studies by Tanaka et al. (1987) and Evans & Zhou (1995). Investigations by Vaid et al. (1990) showed that at lower densities, poorly graded water-deposited sands had lower cyclic strengths than well-graded ones, whereas the trend reversed at higher densities. Their study pointed out two factors: both the gradation and density affect the liquefaction resistance of sands.

2.3.2.2 Effect of particle mineralogy

Based on past experiences, although carbonate sands have a lower hardness than quartz sands, loose carbonate sands are shown to have a larger cyclic resistance as compared to loose quartz sands at similar stress conditions (Chen 1985; Hyodo et al. 1996; Morioka & Nicholson 2000; Nicholson 2006). Further confirming the above observations, Brandes (2011), Sandoval & Pando (2012) and Hassanlourad et al. (2014) reported that the cyclic liquefaction resistance of calcareous sands was higher than that of quartz sands. This could have resulted from the differences in grain shape and gradation. However, due to particle crushing, the undrained cyclic strength of such sands was found to decrease with increasing initial static deviator stress.

2.3.2.3 Effect of particle shape

Kokusho et al. (2004) and Kokusho (2007) investigated the influence of the uniformity coefficient C_u on the liquefaction resistance of six sands of medium density ($I_D = 0.50$). The tested sands could be grouped into two different geological origins: river and decomposed granite soils. The relatively round river sand was found to show a higher cyclic liquefaction resistance (defined as the number of cycles needed for a double strain amplitude of 5%) compared to the angular granite (Fig. 2.13a). In a similar way, the results of Hara et al. (2004) (see Fig. 2.13b) indicated that the grain shape along with the gradation dominates the cyclic resistance of sands although the authors failed to recognize this in their studies. Unfortunately, till date, the combined influence of grain shape and gradation on the liquefaction resistance of sands has not been sufficiently studied, which constitutes one of the major objectives of this research.
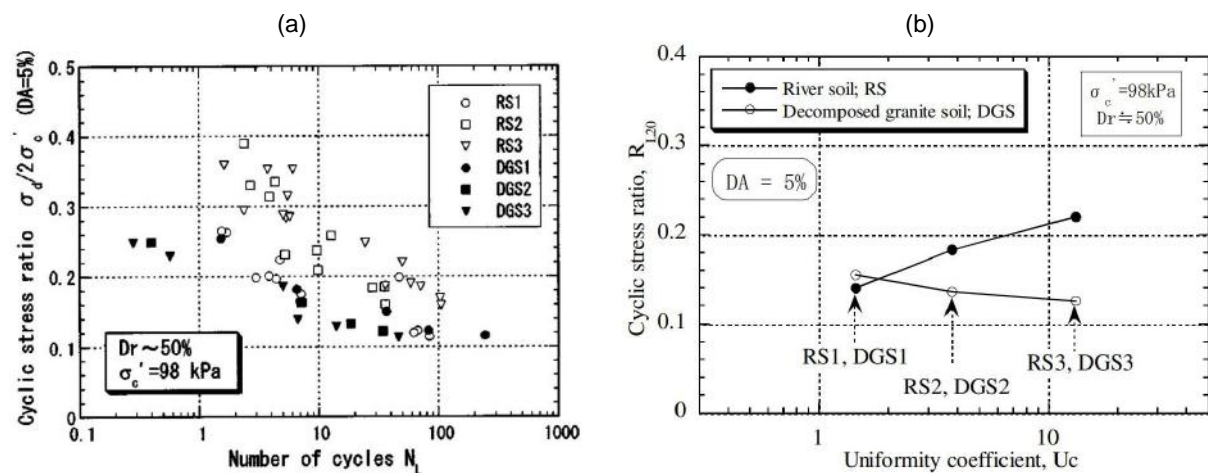
Figure 2.13: Relationship between cyclic stress ratio for 5% double amplitude strain and (a) the number of loading cycles and (b) uniformity coefficient for a medium dense sample ($I_D = 50\%$) under mean effective stress of 98 kPa after Hara et al. (2004). RS and DGS refers to rounded river and angular granite sands respectively, while the numbers denote different gradations

2.3.3 Dynamic small/intermediate strain properties of granular soils

The key soil dynamic parameters considered during seismic analysis of geo-structures are the shear wave velocity (v_s), primary wave velocity (v_p), shear modulus ($G = \rho v_s^2$), elastic / Young's modulus ($E = \rho v_p^2$), constrained elastic modulus (M), Poisson's ratio (ν) and the damping ratio (D). To assess the stress-strain response of soils and facilitate reliable

predictions of deformation under static and dynamic loadings, the small-strain dynamic properties as well as the stiffness degradation behaviour of geo-materials with increasing strain level must be determined correctly. In general, the dynamic properties of soils are influenced by certain factors, such as the void ratio / relative density, confining pressure, degree of saturation, mineralogy, plasticity properties, grain size characteristics, particle shape, over-consolidation ratio, stress history, loading frequency, inherent anisotropy and stress anisotropy (Hardin & Richart 1963; Hardin & Black 1968; Hardin & Black 1969; Chung et al. 1984; Nakagawa et al. 1997; Cho & Santamarina 2001; Cho et al. 2006; Wichtmann & Triantafyllidis 2009; Wichtmann & Triantafyllidis 2010; Senetakis et al. 2012; Payan 2017). Based on strain level, they can be further divided into two parts, which are discussed separately in the following.

2.3.3.1 Small-strain range ($\gamma < 10^{-5}$)

i) Effect of void ratio and confining pressure

The first documented studies on the determination of small-strain shear and elastic modulus date back to the 1960s (Hardin & Richart 1963; Hardin 1965; Hardin & Black 1968; Hardin & Black 1969; Drnevich 1967; Drnevich et al. 1967; Drnevich & Richart 1970). These studies identified the void ratio, confining pressure, over-consolidation ratio, soil structure, gradation, grain shape and mineralogy to affect the small-strain stiffness of soils. Using the RC device, Hardin & Richart (1963) obtained the shear wave velocity of sandy soils under isotropic stress conditions. They identified the void ratio and confining pressure as the two most significant factors which determine shear wave velocity. As years progressed, a host of researchers including (but not limited to) Hardin & Black (1968), Hardin & Black (1969), Hardin & Drnevich (1972a), Hardin & Drnevich (1972b), Sherif & Ishibashi (1976), Hardin (1978), Iwasaki et al. (1978), Kokusho (1980), Chung et al. (1984), Yu & Richart (1984), Seed et al. (1986), Saxena & Reddy (1989), Jamiolkowski et al. (1991), Ishihara (1996), Stokoe et al. (1999), Wichtmann & Triantafyllidis (2009) and Senetakis et al. (2012) used experimental data to formulate empirical models for the estimation of the small-strain shear modulus of sands. The generally used form is denoted by Eq. 2.21:

$$G_{max} = A\,f(e) \left(\frac{p^{'}}{p_a}\right)^n \tag{2.21}$$

where $f(e)$ is the void ratio function, p' is the mean effective stress, p_a is the atmospheric pressure (used as a reference for normalization purposes) and A and n are the model parameters to be determined experimentally. The expression determining the influence of p' has remained unchanged ever since, while different researchers have proposed various void ratio functions. Hardin & Richart (1963) suggested the void ratio function $f(e)$ as:

$$f(e) = \frac{(2.17 - e)^2}{1 + e} \quad \text{(for rounded materials)} \tag{2.22a}$$

$$f(e) = \frac{(2.97 - e)^2}{1 + e} \quad \text{(for angular materials)} \tag{2.22b}$$

Saxena & Reddy (1989) used another void ratio function (Eq. 2.23).

$$f(e) = \frac{1}{0.3 + 0.7e^2} \tag{2.23}$$

Based on experimental results, Jamiolkowski et al. (1991) suggested a power function (Eq. 2.24) for the variation of G_{max} with e:

$$f(e) = e^{-d} = e^{-1.3} \tag{2.24}$$

Previous studies have proposed a great number of empirical expressions bearing the general form of Eq. 2.21 based on experiments on different sands. Some of these studies are listed in Table 2.2. However, considering the significant scatter in the predicted values, it is clear that other factors such as mineralogy, fines content, grain size and shape and stress path affect G_{max} in soils.

Table 2.2: Existing empirical G_{max} expressions proposed in the literature

Reference	Name of sand	A (MPa)	$f(e)$	n
Hardin & Richart (1963)	Rounded Ottawa sand	70	$\frac{(2.17-e)^2}{1+e}$	0.50
	Angular crushed quartz sand	33	$\frac{(2.97-e)^2}{1+e}$	0.50
Iwasaki et al. (1978)	Different gradations of clean sand	51.7	$\frac{(2.17-e)^2}{1+e}$	0.38
Kokusho (1980)	Toyoura sand	84	$\frac{(2.17-e)^2}{1+e}$	0.50

Table 2.2 continued from previous page

Reference	Name of sand	A (MPa)	$f(e)$	n
Yu & Richart (1984)	Three types of clean sand	70	$\frac{(2.17-e)^2}{1+e}$	0.50
Chung et al. (1984)	Monterey No. 1 sand	52.3	$\frac{1}{0.3+0.7e^2}$	0.48
Saxena & Reddy (1989)	Monterey No. 1 sand	42.8	$\frac{1}{0.3+0.7e^2}$	0.57
Bellotti et al. (1996)	Quartz sand	72.4	$e^{-1.3}$	0.45
	Carbonate sand	70.8	$e^{-1.3}$	0.62
Goudarzy et al. (2014)	Glass beads	–	$e^{-3.98}$	0.40

Based on the limited literature available on E_{max}, the influence of the isotropic confining pressure was believed to have almost the same effect on the small-strain Young's modulus as on the small-strain shear modulus (Hardin & Richart 1963). Using a free-free RC device capable of both torsional and compressional modes of excitations in order to measure the small-strain shear and Young's moduli of Ottawa sand specimens subjected to isotropic confinement, the curves of unconstrained primary wave velocities were found to be parallel to those of the shear wave velocities confirming the above hypothesis. Therefore, a similar expression as G_{max} was forwarded for E_{max} albeit a different set of fitting parameters C and α (Lee 1993; Saxena & Reddy 1989; Menq 2003).

$$E_{max} = C\,f(e)\left(\frac{p^{'}}{p_a}\right)^{\alpha} \tag{2.25}$$

On their experiments on three sands (Toyoura, Fujian and Leighton Buzzard), Gu et al. (2013) observed that the void ratio dependence was larger for G compared to the constrained modulus M. Also, the stress exponent (n) for G was found to increase with increasing void ratio e, but a reverse trend was observed for M. Furthermore, the Poisson's ratio decreased with decreasing e and increasing $p^{'}$, and lay generally in the range of 0.18-0.32. Empirical equations (Eq. 2.26) were further proposed to link ν with G and M:

$$\nu = 0.620 \cdot G^{-0.200} \tag{2.26a}$$

$$\nu = 0.846 \cdot M^{-0.216} \tag{2.26b}$$

Similar to the G_{max} model, several void ratio functions were proposed in literature for E_{max}; however, the most common ones are the Hardin & Black (1966) and Jamiolkowski et al. (1991) models, the form of which was already shown previously.

ii) Effect of particle size and gradation

Some significant differences were encountered in the fitting parameters of the empirical equations for various sands with different particle characteristics after considering the influence of e and p', which result from the effects of the so-called 'minor' factors such as particle gradation, mineralogy and shape. Using results from different experiments in Japan, Ishihara (1996) stated that for small-strain shear modulus of sands and gravels at 100 kPa confining pressure, C_u and d_{50}, along with grain shape play a significant role. Furthermore, G_{max} of gravels was reported to be higher than that of sands, which would imply significant influence of the grain size.

The first concrete evidence to demonstrate the influence of C_u on small-strain stiffness may be encountered in Iwasaki & Tatsuoka (1977). For a constant e and p', G_{max} and E_{max} of sands were found to increase with decreasing C_u. Wichtmann & Triantafyllidis (2009) performed 163 RC tests on a host of 25 quartz sands with varied particle size distributions. Their results confirmed the observations of Iwasaki & Tatsuoka (1977) and later, aligned with those of Giang et al. (2017), where for a constant void ratio G_{max} was found to significantly decrease with increasing C_u (see Fig. 2.14a). Other studies (Senetakis et al. 2012; Yang & Gu 2013; Payan et al. 2016) also reported similar observations.

From results of tests performed on Denver sand, Chang & Ko (1982) confirmed that small-strain shear modulus of sand specimens is primarily a function of C_u with very little influence of d_{50}, contrary to the observations of Nakagawa et al. (1997), who found that at a specific void ratio, the shear wave velocity v_s increased slightly with increase in d_{50}, consequently signifying an increase in G_{max} with increasing d_{50}. On the other hand, Chang & Ko (1982) reported that for gravelly soils, the influence of d_{50} was found to be larger than that of C_u, an observation shared by Hardin & Kalinski (2005). Other studies suggesting an increase in G_{max} with increasing d_{50} are Lontou & Nikolopoulou (2004) and Sharifipour et al. (2004).

Performing tests on several gradations of river sands, Menq (2003) and Menq & Stokoe (2003) showed an almost constant magnitude of the small-strain shear modulus of sands with increasing d_{50} for a certain e and p'. However, contrary to previous reports, higher G
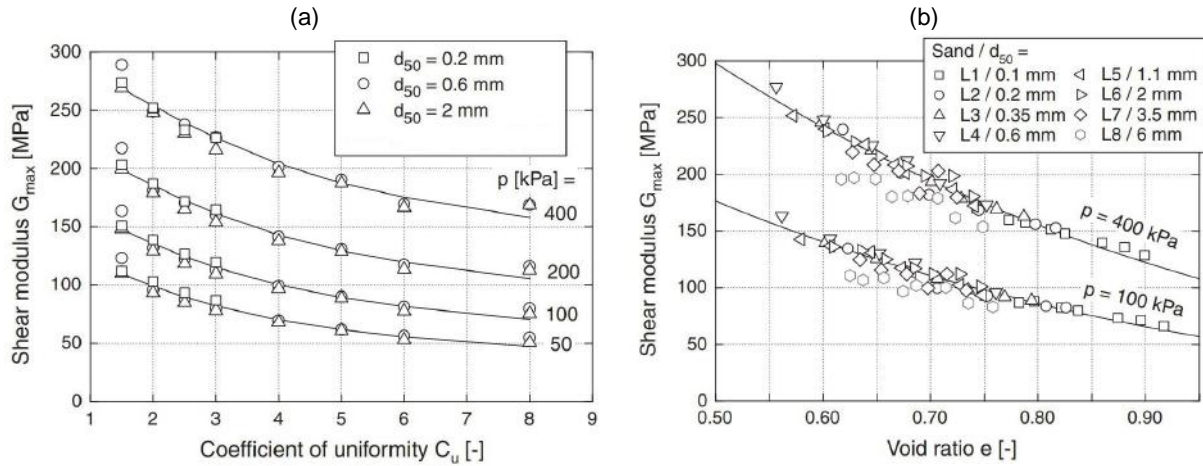
Figure 2.14: (a) Variation of shear modulus G_{max} at $e = 0.55$ as a function of C_u for different pressures (after Wichtmann & Triantafyllidis 2009); (b) comparing the negligible influence of d_{50} for two different pressures and a similar $C_u = 1.5$ (after Wichtmann & Triantafyllidis 2009)

values were reported for larger values of C_u at similar relative densities. The influence of mean grain size d_{50} on G_{max} was concluded as negligible based on RC experiments ($C_u <$ 1.8; $0.16 \leq d_{50} \leq 0.32$ mm). Similar observations were also reported by Bartake & Singh (2007), Patel et al. (2008), Wichtmann & Triantafyllidis (2009) (Fig. 2.14b), Senetakis et al. (2012) and Yang & Gu (2013).

Enomoto (2016) conducted a series of drained triaxial compression tests to evaluate the effects of grading and particle characteristics on the small-strain elastic stiffness of a wide variety of granular materials. From the results, it was concluded that the quasi-elastic modulus for the vertical loading direction was independent of maximum and mean particle diameters. Also, a decrease in the values of elastic modulus was noted with an increase in the uniformity coefficient. While previous researches (Saxena & Reddy 1989; Menq 2003; Wichtmann & Triantafyllidis 2009; Wichtmann & Triantafyllidis 2010) have attempted to correlate C and α in Eq. 2.25 primarily to the C_u and d_{50}, the effects of particle angularity and fines content were unclear. While a decrease in G_{max} with increasing C_u is clear, the influence of d_{50} remains unclear from the contrasting findings reported above.

iii) Effect of particle mineralogy and surface roughness

As already mentioned before, carbonate sands are highly angular in nature, however, they undergo severe breakage at higher confinement pressures unlike siliceous sands. Therefore, the small-strain dynamic properties of such sands are also a point of interest. There are

very few studies which explore the small- and intermediate strain properties of such sands. One study by Brandes (2011) using a cyclic triaxial device equipped with bender elements demonstrated that the shear wave velocities in carbonate sands are higher than those in quartz sands at comparable normal stresses, while shear modulus and damping were larger for quartz sands at strain levels between 0.05 and 1%. The differences in the behavior between the two types of sands were attributed to contrasts in grain geometry, hardness, gradation and the amount of intraparticle voids.

In recent studies, He et al. (2017) and He et al. (2019) tested two carbonate sands from Western Australia and the Philippines using piezoelectric elements to study the elastic modulus, shear modulus and the Poisson's ratio. He et al. (2017) also used flexural resonant column tests to investigate the dynamic behavior of carbonate sands. The sensitivity of carbonate sands to pressure was in general less pronounced than in case of quartz sands. The flexural damping in the range of small to medium strains was higher for carbonate sands in comparison to quartz sands. Although in the range of pressures tested the grain breakage was small, it was found that the typical empirical equations to predict the stiffnesses of quartz sands were not able to capture the corresponding values for carbonate sands. A new model which ignores the intra-particle voids in the calculation of global void ratio was found to yield satisfactory results as against quartz sands.

One of the first experimental studies to investigate the influence of surface roughness on the small-strain properties of granular materials can be found in Santamarina & Cascante (1998) who employed high-tolerance steel spheres subjected to successive cleaning and corrosion stages using a host of chemical agents to vary surface roughness via the formation of rust. Cylindrical specimens of these materials were tested in a resonant column device. The small-strain shear modulus and thus shear wave velocity were found least for the material with the most roughened surface, while damping became stress-independent with increasing roughness. In recent years, Otsubo et al. (2015) also found a reduction in shear wave velocity for roughened spherical materials compared to smooth particles. Furthermore, Otsubo & O'Sullivan (2018) tested cylindrical samples of four glass beads, three of which were mechanically roughened by a milling procedure to obtain varying degrees of roughness, in a triaxial cell equipped with piezoelectric elements (shear plates) at the end caps. They obtained lower values of primary and shear wave velocities along with a higher value of the stress exponent n for the roughened beads.

iv) Effect of particle shape

Limited studies in the literature investigated the effect of particle shape. In fact, the fitting parameters A (for G_{max}), C (for E_{max}) and n were regarded as being of minor importance and linked to the effect of particle gradation and shape (Iwasaki & Tatsuoka 1977; Menq 2003; Menq & Stokoe 2003; Hardin & Kalinski 2005; Wichtmann & Triantafyllidis 2009; Senetakis et al. 2012). The effect of particle shape was considered by Hardin & Richart (1963) through using different values of the fitting parameters of their empirical equation (e.g. 2.17 and 2.97 for round and angular sands, see Eq. 2.22), although a detailed study with a host of particle shapes was not performed.

Some of the studies focussing on particle shape were done by Lo Presti et al. (1997) and Bui (2009), who conducted RC tests on sands with variable particle shapes subjected to different isotropic confining pressures up to 600 kPa. It was observed that at the same e and p', the rounded materials generally had a higher stiffness than angular materials, and n was found to be higher for angular particles than for rounded ones (Bui 2009). In a separate study using an odometric cell equipped with bender elements, Cho et al. (2006) attempted to quantify the strong influence of the particle shape on A, C and n. The significance of particle shape on the small-strain damping ratio of sands in shear was further highlighted by Senetakis et al. (2012) who observed a more pronounced decrease in the damping ratio for angular to sub-angular particles (quarry quartz sands) as against sub-rounded or rounded natural sands. Furthermore, they suggested G_{max} models in these two categories depending on the general shape of the sand particles: quarry quartz (angular / sub-angular) or natural quartz (sub-rounded / rounded) sands. Recently, Payan et al. (2016) performed a comprehensive study through a set of torsional resonant column tests on sands with a variety of grain shapes under confining pressures ranging from 50 kPa to 800 kPa. In their study, the maximum value of strain for G_{max} was $10^{-3}\%$. To predict G_{max}, a new model, which incorporates the effect of C_u and particle shape in terms of regularity (ρ) was proposed (Eq. 2.27).

$$G_{max} = (84\, C_u^{-0.14}\, \rho^{0.68}) \times e^{-1.29} \times \left(\frac{p'}{p_a}\right)^{(C_u^{0.12})\,(-0.23\rho+0.59)} \tag{2.27}$$

For otherwise similar boundary conditions (same C_u, p' and e), sands with round grains (having a higher ρ) show larger G_{max} and consequently, v_s. The influence of particle characteristics on E_{max} was also presented, and captured through the expression Eq. 2.28. Also, since very few studies have dealt with the influence of particle shape and size

on Poisson's ratio (ν), Payan (2017) extended their study in this direction as well through Eq. 2.29. The predictions from their models against ρ following Eqs. 2.27, 2.28 and 2.29 for a void ratio $e = 0.6$ and $p' = 100$ kPa are shown in Fig. 2.15.

$$E_{max} = 245 \left(C_u^{-0.09} \, \rho^{0.82} \right) \times e^{-1.32} \times \left(\frac{p'}{p_a} \right)^{(C_u^{0.11})\,(-0.44\rho+0.66)} \tag{2.28}$$

$$\nu = 0.47 \left(C_u^{0.19} \, \rho^{0.56} \right) \times \left(\frac{p'}{p_a} \right)^{(0.1C_u^{0.1})\,(3.14-9.15\rho)} \tag{2.29}$$
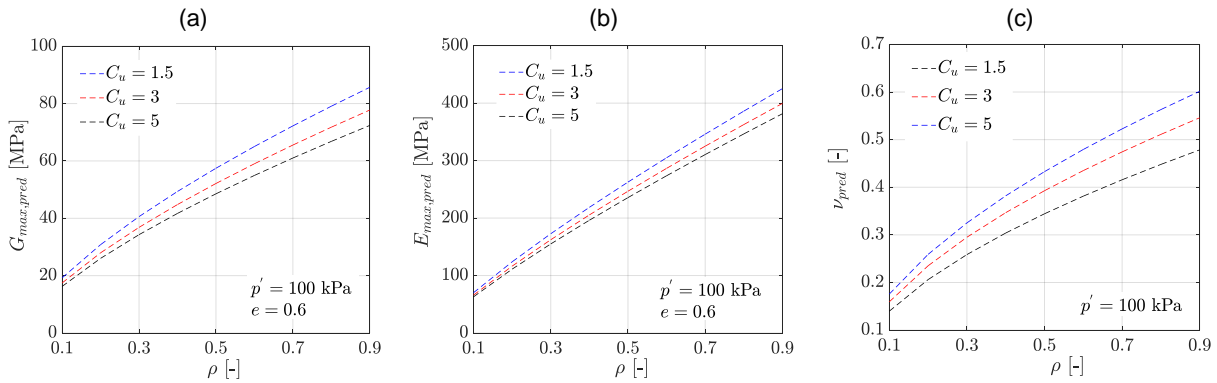
Figure 2.15: Predicted G_{max}, E_{max} and ν profiles against ρ considering $e = 0.6$ and $p' = 100$ kPa following the model of Payan (2017)

Giang et al. (2017) investigated the small-strain shear modulus (G_{max}) for calcareous sands against typical silica sand (Mol sand), where G_{max} values from angular calcareous sands were found to be higher than those of the naturally sub-rounded silica sand, starkly contrasting the observations of Lo Presti et al. (1997) and Bui (2009). One reason for this observation could be using sands constituted of a different mineral composition. Adopting a similar approach, Liu & Yang (2018) encountered a similar experience, where under similar boundary conditions, angular sands exhibited higher values of shear wave velocities at similar void ratios than those with rounded grains contradicting the findings of Payan et al. (2016).

2.3.3.2 Intermediate-strain range ($10^{-5} \leq \gamma \leq 10^{-3}$)

For the intermediate strain regime, Hardin & Drnevich (1972a) developed a well-known empirical relationship to predict the shear modulus degradation (G/G_{max}) with respect to the shear strain:

$$\frac{G}{G_{max}} = \frac{1}{1 + \frac{\gamma}{\gamma_r}} \tag{2.30}$$

where γ refers to the shear strain and γ_r denotes the reference shear strain, which is the shear strain at $G/G_{max} = 0.50$. A disadvantage of this formulation as argued by Zhang et al. (2005) is the poor fit to experimental data since only one curve fitting parameter in the form of γ_r is employed. Therefore, hyperbolic models employing two fitting parameters (γ_r and α) were suggested in Stokoe et al. (1999):

$$\frac{G}{G_{max}} = \frac{1}{1 + (\frac{\gamma}{\gamma_r})^\alpha} \tag{2.31}$$

Empirical relationships have been also developed to characterize damping ratio with respect to shear strain. Hardin & Drnevich (1972b) proposed Eq. 2.32 to estimate damping ratio based on the maximum damping ratio D_{max}, assumed to be 33% for sands.

$$\frac{D(\gamma)}{D_{max}} = \frac{\frac{\gamma}{\gamma_r}}{1 + \frac{\gamma}{\gamma_r}} \tag{2.32}$$

Another method to calculate damping ratio may be found in Uchida et al. (1980) which describes $D(\gamma)$ as a function of $G(\gamma)/G_{max}$. Through compiling various data, Zhang et al. (2005) formulated Eq. 2.33 with constants C_1 and C_2:

$$D(\gamma) - D_{min} = C_1 \left[\frac{G(\gamma)}{G_{max}}\right]^2 - C_2 \left[\frac{G(\gamma)}{G_{max}}\right] + (C_2 - C_1) \tag{2.33}$$

In recent years, Goudarzy et al. (2018) proposed Eq. 2.34 for the damping ratio of granular soils, which describes D as a function of γ_r and D_{min} with fitting parameters M and N:

$$\frac{D(\gamma)}{D_{min}} = M \left(\frac{\frac{\gamma}{\gamma_r}}{1 + \frac{\gamma}{\gamma_r}}\right)^N + 1 \tag{2.34}$$

Wichtmann & Triantafyllidis (2013) stated that the modulus degradation was not affected by the d_{50}, while for a certain shear strain amplitude, the G/G_{max} significantly decreased with increasing C_u. Also, damping was found to be almost independent of the grain size parameters. However, all the tests were performed with sub-angular sands, and therefore, the influence of grain shape was not explicitly investigated. Thus till date, there are practically no studies which deal with the influence of grain shape on the shear / elastic modulus degradation of sands under varying shear/axial strains, and therefore, further investigations are needed.

2.4 Summarizing and highlighting existing research gaps

The previous sections have demonstrated that particle morphology significantly affects the material behavior under monotonic, cyclic and dynamic loading, which is of significant practical relevance in the context of geotechnical earthquake engineering and particularly liquefaction risk estimation. Based on the review of the existing studies, the shortcomings and open questions are summarized below:

1. Quite different grain shape descriptors have been proposed in the literature. Some of them are suitable for describing grain shapes in the macro scale (e.g. sphericity), some in the medium scale (e.g. roundness) whereas certain descriptors characterize the micro scale surface properties (e.g. roughness). Some studies used one or more of these morphological parameters to investigate the effects of grain shape on certain intrinsic, static and dynamic properties of granular materials, although a lot of uncertainties regarding some of these tendencies remain because several studies came to contradicting results, due to which the influence of particle morphology has always remained a focal point for ongoing investigations.

2. Knowing the maximum and minimum void ratios or densities is necessary to judge the density state of a granular soil in situ. It is well acknowledged that grain shape strongly influences these limit void ratios. However, no established empirical equations to estimate e_{min} and e_{max} considering grain shape have been established so far, which could be used for estimates of the limit values if laboratory data is not available. Furthermore, the combined influence of grain size, gradation and shape is not sufficiently studied.

3. Although well acknowledged, studies highlighting the impact of grain shape on the drained and undrained monotonic response of granular materials are rare, and are often focused on the peak and steady state friction angles. The variation of the steady / critical state parameters with grain shape has not been studied thoroughly, leading to uncertain input parameters in estimating constitutive model parameters for numerical simulations.

4. From several studies with undrained cyclic tests, higher liquefaction resistance is reported for increasing d_{50} and C_u, while only a few studies reported an opposite trend. Some studies have also suggested that the influence of gradation on the liquefaction resistance depends on relative density. The apparent ambiguity in observations however has not been investigated considering the contribution of the grain shape.

In other words, there are no studies which demonstrate the combined influence of particle gradation and shape on the liquefaction susceptibility of granular soils.

5. While the literature is quite consistent regarding the influence of the uniformity coefficient C_u on the small-strain shear modulus G_{max} of granular soils, the influence of the mean grain size d_{50} remains debatable, with experimental evidences supporting both the increase or decrease of G_{max} with increasing d_{50}. Furthermore, experimental investigations on the influence of grain shape, size and gradation on the intermediate strain properties of granular soils, i.e. damping and modulus degradation and increase of damping with increasing strain amplitude are extremely rare and thus the effect is not well-understood.

The aim of the present research is to systematically deal with each of the above mentioned shortcomings or gaps to improve the current state-of-the-art understanding of the role of grain morphology, size and gradation with respect to the static, cyclic and dynamic behavior of granular soils.

3 Characterizing particle morphology and its effect on index properties of granular materials

3.1 Introduction

The main purpose of this chapter is to introduce the various methods for obtaining grain images, for converting raw images to machine-readable format as well as evaluating the particle shape of granular materials applied in this research.

3.2 Different particle morphology descriptors

While roundness (R) and sphericity (S) are the most widely used shape descriptors, there are other descriptors as well, e.g. aspect ratio, circularity and so on (Cox & Budhu 2008). In the present research, overall 16 different morphology descriptors (in the medium and macroscale) were employed which are listed below:

(1) **Roundness (R):** This denotes the ratio of the average value of the radii (r_i) of all corners (N in number) to the radius of the maximum inscribed circle r_{ins} (refer to Eq. 2.12 and Fig. 3.1a).

(2) **Area sphericity (S_A):** This denotes the ratio of the area of the grain A_s to the area of the minimum circumscribing circle A_{cir} (Fig. 3.1b).

(3) **Diameter sphericity (S_D):** Diameter sphericity (Fig. 3.1c) is calculated as the ratio of the diameter of a circle having the same projected area as the particle (D_c) to the diameter of the minimum circumscribing circle (D_{cir}).

(4) Circle ratio sphericity (S_c): Being by far the most popular definition of sphericity, it denotes the ratio of the diameter of the maximum inscribed circle D_{ins} to the diameter of the maximum circumscribed circle D_{cir} as evident in Fig. 3.1d.

(5) Perimeter sphericity (S_P): The ratio of the perimeter of a circle having the same projected area as the particle P_c to the perimeter of the particle P_s (refer Fig. 3.1e).

(6) Width-to-length ratio sphericity (S_{wl}): The ratio of the Feret breadth B to the length L is termed as the width-to-length ratio sphericity, also shown in Fig. 3.1f.

(7) Regularity factor (ρ): Used in Chapters 3 and 4 of this study, ρ denotes the average of R and S_c.

(8) Aspect ratio (Ar): Ar denotes the ratio of L to B, thereby being the complementary value of S_{wl}.

(9) Circularity (Cir): As shown in Fig. 3.1g, Cir denotes the ratio of the area of the grain A_S to the area of a circle with the same perimeter as the grain ($A_{cir,P}$).

(10) Compactness ($Comp$): The ratio of the diameter of a circle having the same area as the grain ($D_{cir,a}$) to the Feret maximum length L is the compactness, denoted as $Comp$ (see Fig. 3.1h).

(11) Solidity (So): The ratio of the grain projected area A_s to the area of the convex hull A_{CH} is termed solidity So, as schematically shown in Fig. 3.1i.

(12) Concavity (Cv): The difference between the area of the convex hull A_{CH} and the projected area of the grain A_s gives the value of the concavity Cv.

(13) Convexity (Cx): The ratio of the perimeter of the convex hull P_{CH} to the perimeter of the grain P_s is the convexity Cx (refer to Fig. 3.1i).

(14) Mod-Ratio (MR): The diameter of the maximum inscribed circle $D_{ins} = 2r_{ins}$ to the Feret length L (see Fig. 3.1j) denotes the MR.
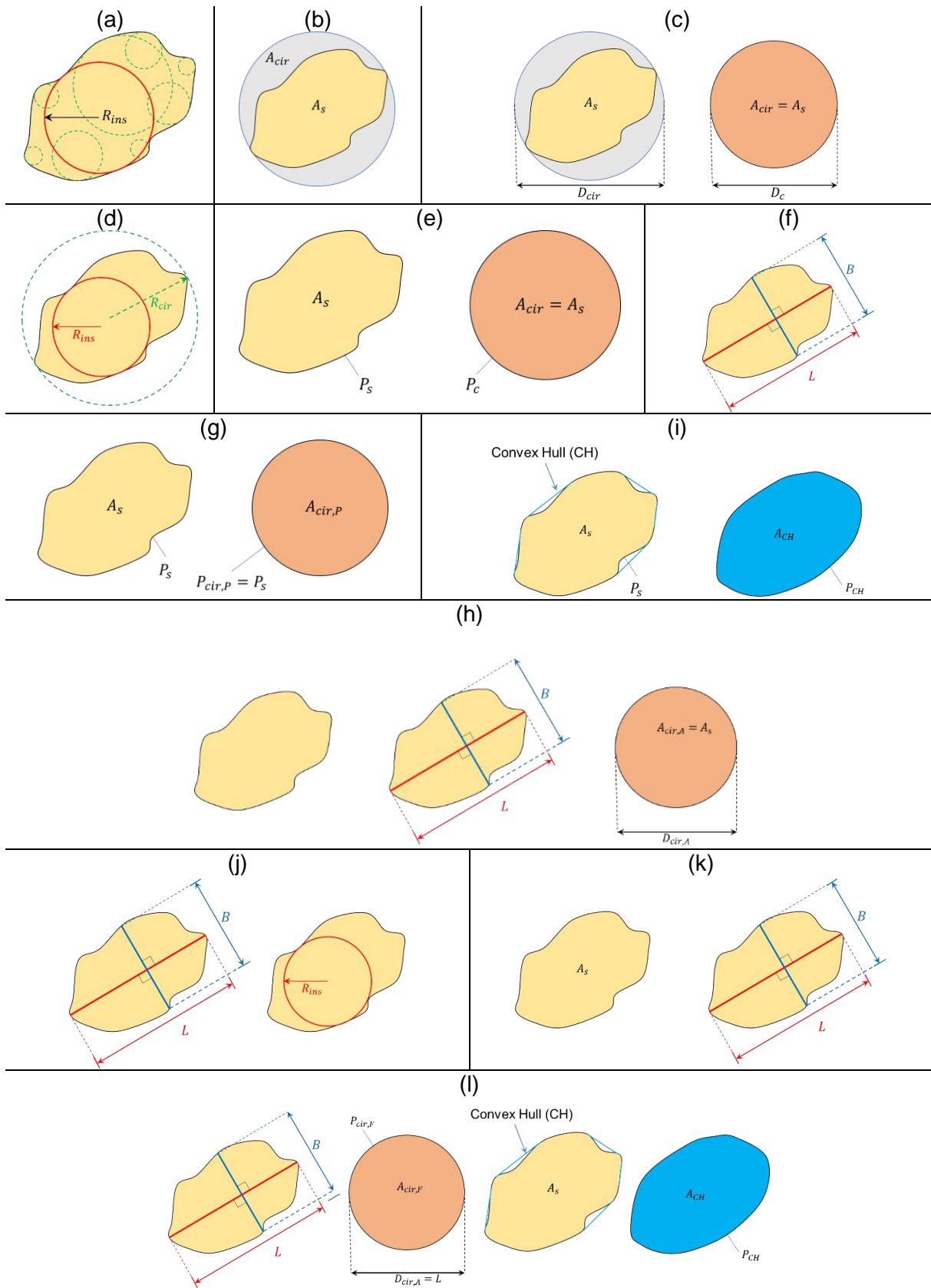
Figure 3.1: Schematic representations of the various grain shape descriptors used in this study

(15) R-Factor (RF): The ratio of the perimeter of the convex hull P_{CH} to the Feret diameter L times π represents the RF of the grains. It can be seen pictorially in Fig. 3.1l.

(16) Rectangularity ($Rect$): The ratio of the area of the grain A_s and the theoretical rectangle created by the Feret lengths L and B gives the $Rect$ (refer Fig. 3.1k).

Out of these 16 shape parameters, the meso/medium scale parameters which denote a measurement incorporating the various indentations and corners of the grain are the roundness, solidity, concavity and convexity. The other 12 parameters denote the grain shape in the macro scale.

3.3 Obtaining individual grain images

Depending on their genesis and transportation history, granular materials generally have different grain shapes. For the analysis of grain shape sharp high quality images of the grains are needed. In the upcoming sub-sections, two methods to obtain these images that were used in the course of the present study are explained along with a discussion of their advantages and disadvantages.

3.3.1 Microscope

High-quality images of grains were taken using a microscope (*Leica S6D* - available at the Faculty of Mechanical Engineering, Ruhr-Universität Bochum, see Fig. 3.2). The maximum possible magnification is 80. Therefore, sharp images were possible only for grain sizes devoid of fines, i.e. sizes smaller than 0.063 mm. To ensure that the images are obtained with sufficient brightness, an in-built light was provided as can be seen from Fig. 3.2a. Backgrounds of white and black color could be used. The choice depends on the color of the sand: if the sand grains were of a darker shade, a white background would be more suitable, while for grains having a lighter shade, a black background could be used.

3.3.2 Scanner

The scanner used in the present research was the CanoScan 9000F (Fig. 3.3). The maximum resolution of the images possible with the scanner was 4800 dpi although the level of magnification was not as large as in case of the microscope. A blue filter was selected as the background to enhance the quality of images, and ease the image processing and further
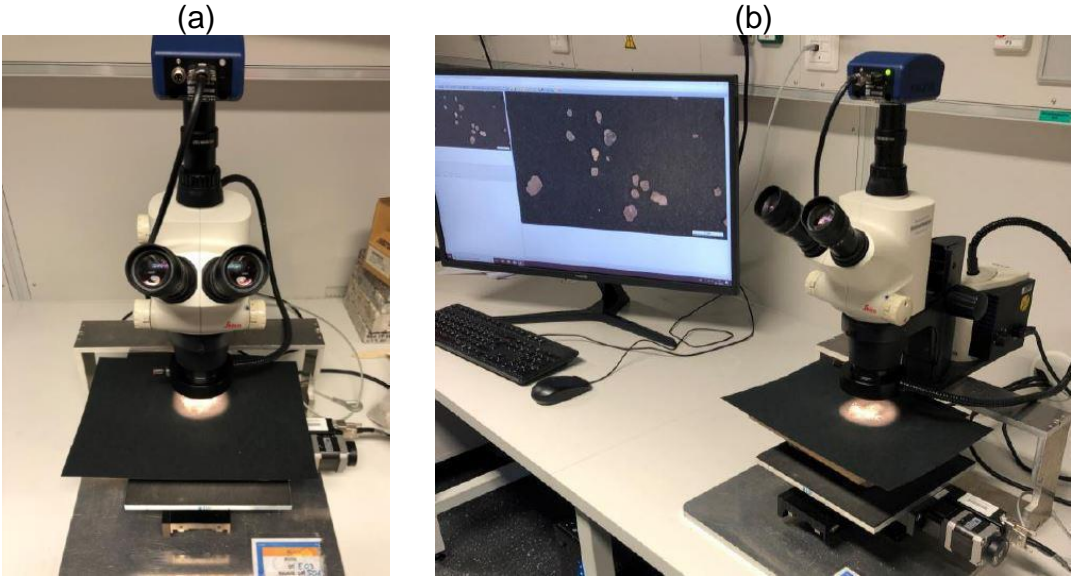
Figure 3.2: The microscope used for taking grain images: (a) front view, (b) the PC connected to the microscope for visualization and processing

analysis. Based on experience, adopting the blue background eliminates the possibility of reflection during the scanning process.
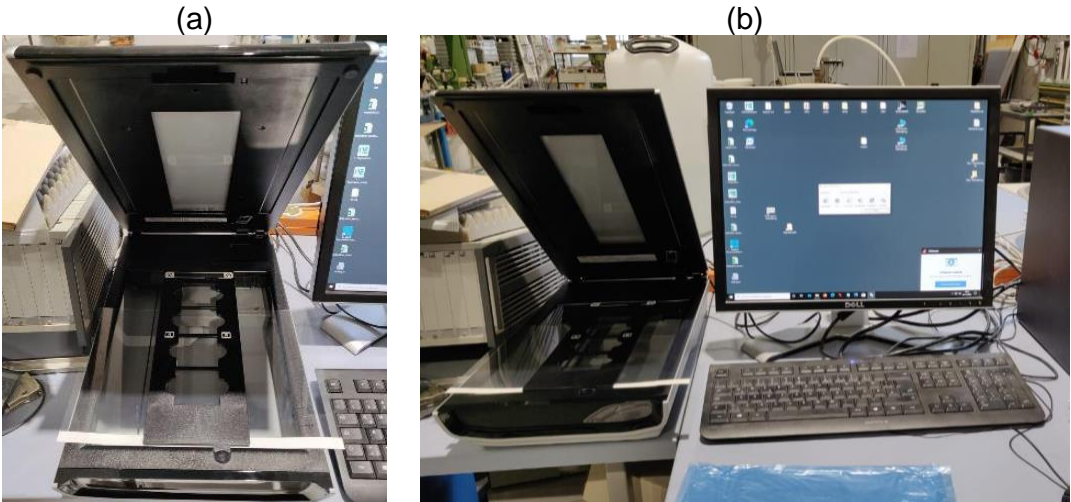
Figure 3.3: The scanner used for taking grain images: (a) front view, (b) the PC connected to the scanner for visualization and processing

3.3.3 Comparison between the images obtained via microscope and scanner

There are both advantages as well as disadvantages of procuring images via these two methods. In case of the microscope, the biggest advantage is that images of individual grains can be taken at a larger magnification of up to 80 times. Thus, the quality of images is comparatively better than that of images obtained via the scanner. However, since the focus is only on a very small area containing very few grains, a large number of photos are required to obtain a sufficiently large number of grain images for a reliable shape estimation using image analysis. Therefore, obtaining grain images with a microscope is time consuming. Furthermore, adjusting the background light can be problematic since a wrong choice of background and wrong alignment of the light could lead to shadows which interferes in the image analysis procedures.

In case of the scanner, the biggest advantage is that problems with the background light are totally eliminated, while at the same time, a significantly larger number of grains are captured within a very short time. The most important disadvantage arises from the limited magnification: for fine grained soils, the grain shapes determined with the scanner are not very reliable due to the lower magnification.

3.4 Determination of particle morphology utilizing image analysis procedures

3.4.1 Image processing using ImageJ

The image analysis was done using ImageJ, which is a public domain Java image processing and analysis program inspired by NIH Image for the Macintosh. It runs either as an online applet or as a downloadable application on any computer which supports Java. Downloadable distributions are available for Windows, Mac OS X and Linux. It can display, edit, analyze, process, save and print 8-bit, 16-bit and 32-bit images. Also, the software can read image formats such as JPG, TIFF and PNG. Further details about the software may be found in Ferreira & Rasband (2012).

In the current application, the images for the materials were obtained in JPG format. ImageJ has a host of various useful functions, some of which are contrast manipulation, sharpening, smoothening, edge detection and median filtering (Kumara et al. 2012). The

Figure 3.4: Flowchart describing the process of image processing

first step is to convert the raw image obtained to a binary form through the command '*Make Binary*', where the background is represented as white and the individual grains are denoted as black. It is imperative to convert the images into binary form so as to facilitate the application of other necessary functions needed for obtaining higher clarity of grain images - '*Erode*', '*Dilate*', '*Open*', '*Close*', '*Median*' and '*Fill holes*'. '*Erode*' removes additional pixels from the edge of black objects whereas *Dilate* adds pixels to the edges of black objects in order to obtain a smooth boundary. The function '*Open*' and '*Close*' are mutually complimentary to each other: '*Open*' performs an erosion operation followed by dilation whereas '*Close*' does the reverse. Since the microscopic raw images obtained may have some light reflections, certain spots may not be converted to black even after binarizing. This is in particular profound in most black objects. Therefore, these spots are represented as white pixels in the binary image. Hence to fill holes, '*Fill Holes*' is used to eliminate these white spots. The image processing process may be best decribed using the flowchart shown in Fig. 3.4.

To demonstrate the procedure by an example, a raw image of a few crushed glass particles taken with the microscope is used. The procedure is illustrated in Fig. 3.5. The first step is to adjust the brightness and contrast to show the grains with a different color than the background. This allows a clear distinction between them, which would enable the software to identify grain corners. After this operation is successfully accomplished, the image is converted to the binary format using the command '*Make Binary*'. The final procedure is to remove the various noises using the command '*Median*' which reduces noise by replacing each pixel with the median of the neighboring pixel values. The resulting image can be used for grain shape quantification using either ImageJ or MATLAB.

3.4.2 Image analysis using ImageJ and MATLAB approaches

To minimize human effort and errors during the determination of grain shape, various programs are available to process and analyze grain images captured using scanner or microscope. One such popular software, ImageJ (Rasband 2004), is widely used in grain shape analysis (Cox & Budhu 2008; Igathinathane et al. 2008; Fonseca et al. 2012; Rodriguez et al. 2012; Kumara et al. 2012; Wichtmann et al. 2019a). Two different methods
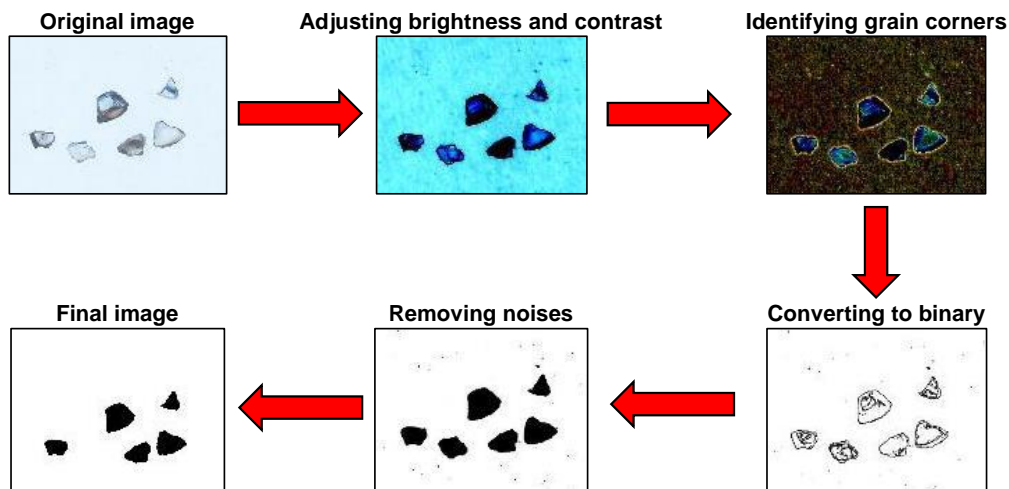
Figure 3.5: Conversion of raw image obtained from microscope to the binary image used for shape quantification

to process the images were used - the first one uses a built-in plugin of ImageJ, named *Particles*8 (henceforth referred to as ImageJ approach), while the second method applies the approach formulated by Zheng & Hryciw (2015) in MATLAB (referred to as MATLAB approach), which will be also further used in the upcoming chapters in this thesis. Raw images were taken using the microscope/scanner, and were converted to binary machine-readable format, after which the grain shape parameters were obtained using the two approaches (Particles8 and MATLAB).

Brief working principle of ImageJ

The plugin *Particles*8 available in ImageJ is able to analyze various binary shapes. The perimeter and area are measured from the centers of the boundary pixels of a particle, i.e. the length of the 8-neighbours chain code, called the Freeman algorithm (Freeman 1961). The program initially detects the first pixel of a particle by moving horizontally through the lines of the binary image. The determination of the area and the perimeter is done by starting from this pixel counterclockwise by scanning the adjacent eight pixels for other pixels belonging to the contour. Thus the algorithm circulates the entire particles until the contour is mapped with a closed chain of pixels. However, the plugin assumes square pixels with the aspect ratio of the capturing device set to 1:1.

Working principle of MATLAB

For the approach using MATLAB, the area and perimeter of the grains can be easily determined using the image−processing package from MathWorks (MathWorks 2014). To compute the minimum circumscribing circle, the maximum inscribed circle, and the particle length and width, the outline of a particle is discretized. The minimum number of outer points that will bound all of the others is determined, and the points, which are farthest from each other, define the diameter of a trial circle. If a point is found to be outside this circle, the new trial circle is redrawn using the third point additionally, thereby yielding the minimum circumscribing circle. The maximum inscribed circle is determined using an Euclidean map, further details of which may be found in Zheng & Hryciw (2015). To calculate the length and width, trial rectangular boxes circumscribing the outer points of the particle are conceptualized, and the box displaying the largest single dimension defines both the length and width of the particle. For further details, the reader is advised to consult Zheng & Hryciw (2015).

3.4.3 Validation of the results obtained from the two approaches

Krumbein & Sloss (1963) proposed a classical chart (see Fig. 2.7) with intervals of 0.2 incorporating both particle sphericity and roundness, and which has been frequently used in literature to determine particle shape. Although the exact procedure for the preparation of this chart was not discussed in the original publication, the sphericity was reported to be related to the proportion between length and breadth of the projected sections while roundness was based on the curvatures formed by the outlines. Cavarretta (2009) inferred that their definition might have been based on the circle-ratio sphericity. Therefore, this definition of sphericity was used as a basis of comparison between the results from ImageJ and MATLAB. To validate the results of the roundness and the sphericity obtained from the two approaches, four extreme shapes at the four corners were selected from the chart (shown in Fig. 3.6).

Table 3.1 lists the roundness and the circle-ratio sphericity obtained from the two image analysis methods. In general, a good agreement is evident between the circle-ratio sphericity values obtained from ImageJ and MATLAB although the sphericity from the MATLAB approach shows slightly larger values. For practical purposes, these differences may be neglected. However, significant differences are noticed for roundness, where for grains A, C and D, the roundness obtained from ImageJ is significantly larger than that obtained from MATLAB. This is because the roundness obtained from ImageJ is defined
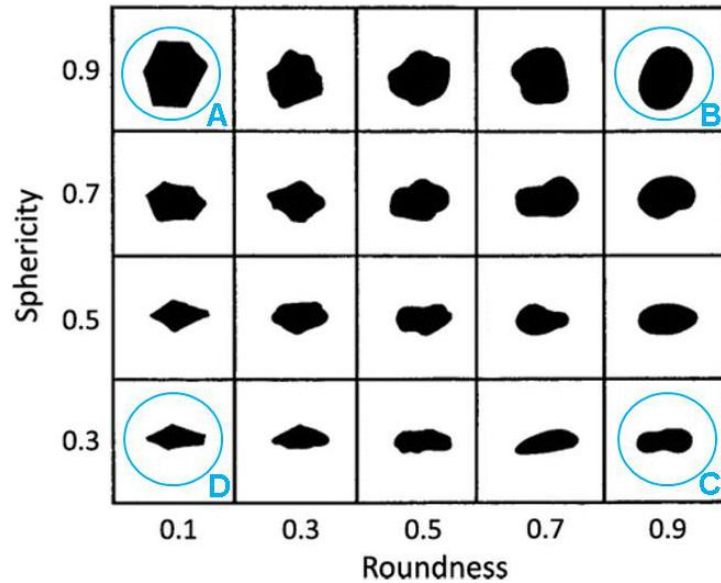
Figure 3.6: Extreme four shapes selected from the classical Krumbein & Sloss (1963) chart for the purpose of validation of the grain shapes using MATLAB and ImageJ approaches

as the ratio of the area of the grain to the area of the circle having the major Feret dimension L as the diameter, which is not similar to the classical definition listed previously and calculated in MATLAB (Rodriguez et al. 2012). Therefore, for determination of the roundness, the results from ImageJ were not further used.

Table 3.1: Comparison between the roundness and sphericity values obtained by ImageJ plugin *Particles*8 and the MATLAB script modified after Zheng & Hryciw (2015)

Grain	ImageJ *Particles*8		MATLAB (Zheng & Hryciw 2015)	
	Roundness	Sphericity	Roundness	Sphericity
A	0.78	0.72	0.17	0.80
B	0.77	0.74	0.90	0.78
C	0.46	0.32	0.87	0.42
D	0.36	0.32	0.16	0.41

3.4.4 Pros and cons of the two approaches for grain morphology characterization

The main advantages of Particles8 over MATLAB approach is that from a single binary figure, a larger number of grain shape descriptors can be obtained simultaneously in addition to other features such as the individual grain area, perimeter (in terms of the

number of pixels) as well as coordinates denoting the location of the particular grain. Since it is a built-in plugin available for free usage in ImageJ, no third party software is needed. However, there are a couple of disadvantages: the calculation of roundness in Particles8 is different since it is defined as the ratio of the area of the grain to the area of the circle having the major Feret dimension L as the diameter, which is not similar to the classical definition described previously in Eq. 2.12 which denotes grain shape in the meso-scale. In addition, some shape parameters such as particle regularity are missing, and cannot be calculated.

For the approach using MATLAB, more reliable results relating to grain roundness and the different forms of sphericity are evident in the previous subsection. However, a drawback is that a longer time is needed to obtain the 6 shape descriptors that are evaluated by the MATLAB script. Furthermore, since in the calculation of roundness, circles are fitted into the various grain corners, images of sufficient quality are needed to avoid pixellation effects which would result in inconsistent and erroneous values of roundness. The same is true for other shape descriptors as well.

3.5 Effect of particle characteristics on the index void ratios

The void ratio is an important state parameter with respect to the mechanical and hydromechanical properties of soils. The difference between the actual void ratio and the stress-dependent critical void ratio has a strong influence on the deformation and strength characteristics of granular soils. The void ratio is typically bounded by two extremities, denoted as e_{max} and e_{min}. Producing samples with specific densities helps in making intelligent approximations of many material and state-dependent parameters (Shen et al. 2019). This section describes the basic laboratory experiments that are needed to determine various intrinsic soil parameters such as the index void ratios, the specific gravity and the grain size distribution.

3.5.1 Test materials

For the experiments, two classes of materials were chosen - glass beads and natural sands. Round glass beads of various sizes were obtained from the company *Mühlmeier GmbH*, Germany. Six different glass beads having a wide range of grain sizes from 0.125 mm till

6.5 mm were considered. An attempt was made to also incorporate a large range of the uniformity coefficient (C_u) in the study through mixing of glass beads of various sizes. However, it was observed that during funnel deposition for determination of e_{max} following DIN-18126 (1996) procedure segregation took place, i.e. the smaller glass particles settled faster leaving behind the larger ones thus giving rise to separate layers of glass beads having different sizes. This would cause erroneous results during the determination of the maximum void ratio. Therefore, a relatively small range of C_u representing poorly graded mixtures has been finally used for the study. A study on the void ratios for glass beads incorporating a wide range of C_u values is extremely difficult and remains an open task to be investigated in future. The glass beads are spherical in nature having roundness and sphericity values of about 0.9 respectively, consequently issuing a regularity of 0.9. The value of the specific gravity following standard DIN-18124 (2011) was determined to be 2.54. The various properties of the beads are summed up in Table 3.2.

The natural sands originated from various parts of the world; however, they were readily available in the Laboratory of Soil Mechanics, Foundation Engineering and Environmental Geotechnics (BGU) at the Ruhr-Universität Bochum. The various index quantities of these sands are summarized in Table 3.3. The grain size distribution curves of the various glass beads and sands as determined using DIN-18123 (2011) are shown in Figs. 3.7 and 3.8.

Table 3.2: Physical properties of the various glass beads considered for the experimental program

Material	Size range	C_u	$d_{50}[mm]$	R	S	ρ	e_{max}	e_{min}	G_s
Glass beads-1	0.125-0.2	1.21	0.17	0.9	0.9	0.9	0.69	0.52	
Glass beads-2	0.25-0.5	1.43	0.38	0.9	0.9	0.9	0.73	0.56	
Glass beads-3	0.4-0.6	1.24	0.50	0.9	0.9	0.9	0.72	0.56	2.54
Glass beads-4	0.5-0.71	1.19	0.61	0.9	0.9	0.9	0.70	0.55	
Glass beads-5	1.25-1.55	1.10	1.40	0.9	0.9	0.9	0.64	0.60	
Glass beads-6	4.5-6.5	1.21	5.50	0.9	0.9	0.9	0.64	0.60	

3.5.2 Analysis of results

i) Effect of particle characteristics on index void ratios for glass beads

As all the shape parameters were similar for round glass beads, the relation between the void ratios and mean grain size d_{50} was examined based on the data for the glass beads. A wide range of mean grain sizes was included in the study including those from literature

Table 3.3: Physical properties of the natural sands considered for the experimental program

Name of sand	C_u	$d_{50}[mm]$	R	S	ρ	e_{max}	e_{min}	G_s
Rhein sand small	2	0.25	0.44	0.77	0.61	0.924	0.539	2.65
Hostun sand	2	0.25	0.40	0.75	0.58	1.012	0.621	2.65
Siligram sand	2	0.25	0.49	0.78	0.64	0.827	0.509	2.64
Silber+Black sand	2	0.25	0.45	0.77	0.61	0.940	0.549	2.67
Greywacke	2	0.25	0.31	0.77	0.54	1.167	0.592	2.82
Sackware 1-2 mm	1.33	1.5	0.48	0.78	0.63	0.870	0.616	2.64
Sackware 0.2-1 mm	2.03	0.53	0.54	0.78	0.66	0.872	0.526	2.64
Sackware 0.1-0.5 mm	1.68	0.3	0.58	0.8	0.69	0.935	0.557	2.64
Sackware (Sand 0.5-1 mm)	1.54	0.74	0.55	0.75	0.65	0.874	0.575	2.64
Cardiff sand	1.38	0.17	0.56	0.75	0.66	0.832	0.483	2.64
Silbersand 4442	1.78	0.22	0.45	0.77	0.61	0.892	0.548	2.64
Black sand	6.1	0.85	0.45	0.76	0.61	0.679	0.401	2.71
Norm sand	1.62	0.19	0.51	0.79	0.65	0.877	0.517	2.63
Sackware fS S90	1.5	0.17	0.52	0.77	0.65	1.035	0.620	2.65
Mix sand (sand 1)	3.3	0.4	0.45	0.79	0.62	0.830	0.470	2.64
Mix sand (sand 2)	4.5	0.75	0.52	0.8	0.66	0.780	0.430	2.64
Mix sand (sand 3)	3.7	0.5	0.54	0.74	0.64	0.810	0.470	2.64
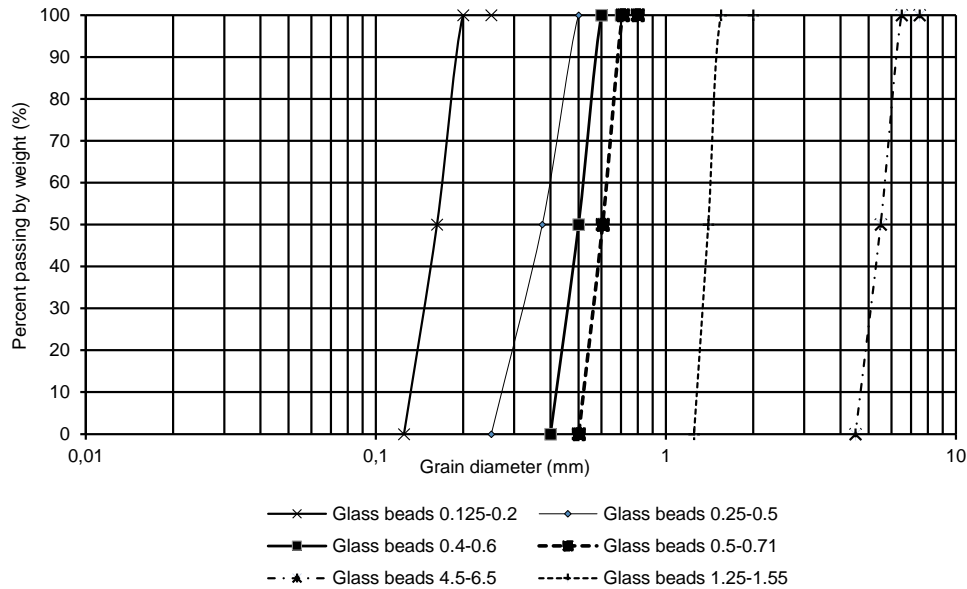
Figure 3.7: Grain size distribution of the various glass beads considered for analysis

for a better validation and interpretation of the results. Fig. 3.9(a) shows e_{max} and e_{min} against d_{50}. Good correlation exists between the limit maximum void ratio and d_{50}, which
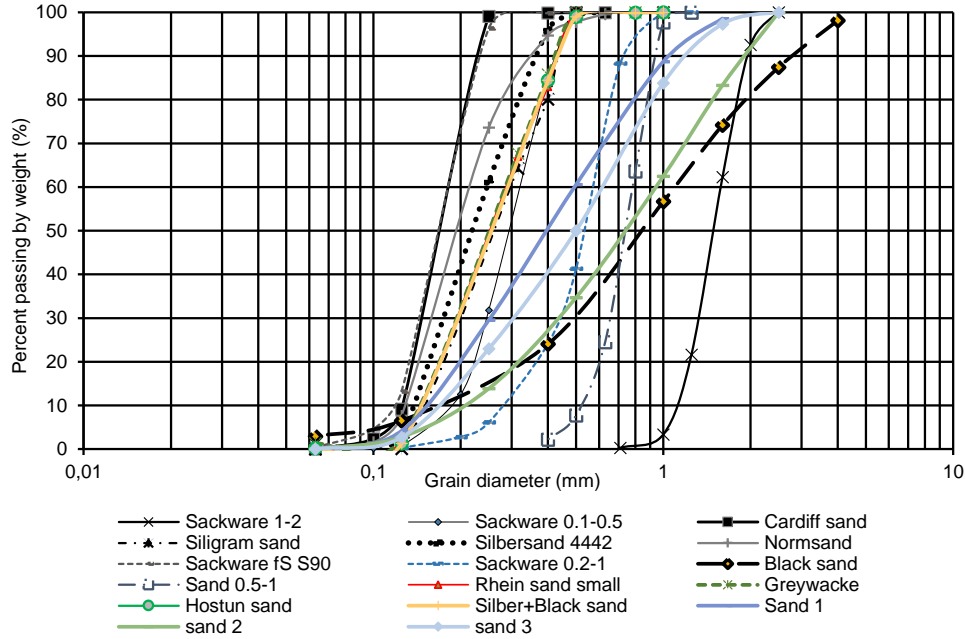
Figure 3.8: Grain size distribution of the seventeen sands considered for analysis

is in agreement with the decreasing e_{max} with increasing d_{50} trend observed in Cubrinovski and Ishihara (2002). In contrast, e_{min} increases with d_{50}. These two relationships and may be described by the following equations:

$$e_{max} = f(d_{50}) = 0.69\,d_{50}^{-0.029} \tag{3.1}$$

$$e_{min} = f(d_{50}) = 0.5675\,d_{50}^{0.038} \tag{3.2}$$

A standard deviation (SD) of 0.02 and 0.008 for e_{max} and e_{min} were observed. Following a similar procedure, the relation between uniformity coefficient C_u and the extreme void ratios is plotted in Fig. 3.9(b); however, no definite relation was found between these two parameters owing to the small range of studied C_u values and some scatter in the results.

Contrary to expectations, e_{max} and e_{min} converged for larger grain sizes. The surface of the glass particles is smooth, which facilitates rolling of particles. With a constant mold volume, the total number of particles that fits into the mold decreases with increasing d_{50}. Apparently, there seems to be less compaction in the e_{min} test in case of the larger glass beads, probably due to lower degrees of freedom for the glass beads to reorient themselves and form denser packings, thus explaining the convergence of the values of e_{max} and e_{min} for larger grain sizes.
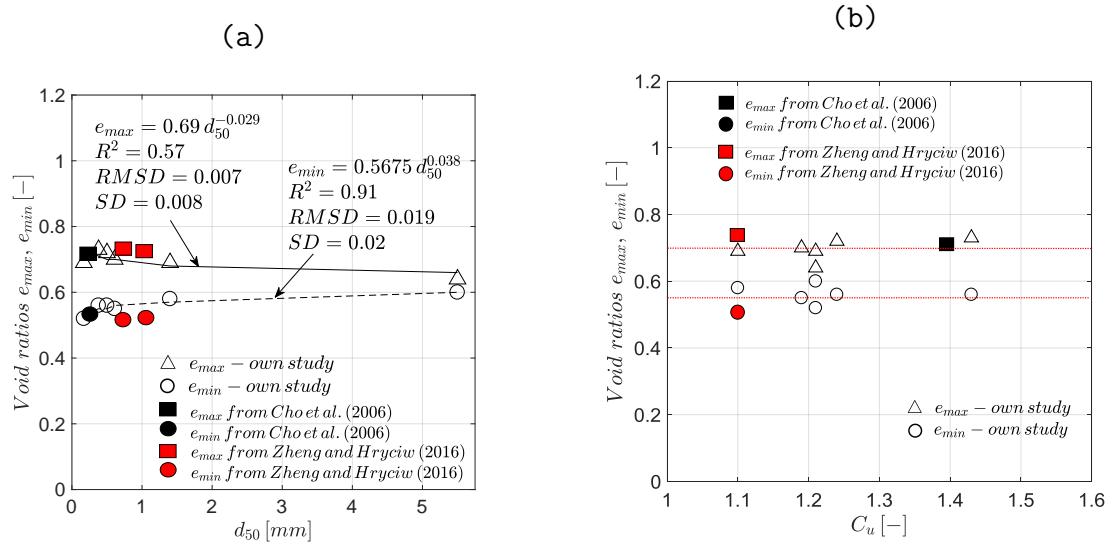
Figure 3.9: Plots showing the variation of the maximum and minimum void ratios for glass with (a) the mean grain size d_{50} and (b) the uniformity coefficient C_u

Table 3.4: Index properties for various glass materials (both angular and round) as obtained from literature

Source	Soil	G_s	$d_{50}[mm]$	ρ	e_{max}	e_{min}
Cho et al. (2006)	Glass beads	–	0.32	1	0.72	0.54
Bui (2009)	Glass round	2.5	0.89	0.95	0.69	0.53
	Glass nugget	2.5	1.3	0.45	1.24	0.74
	Glass glitter	2.5	1.59	0.42	1.36	0.73
Zheng & Hryciw (2016)	Glass beads	2.55	0.32	1	0.72	0.54
	Small glass beads	2.55	0.70	1	0.75	0.50
	Large glass beads	2.55	0.97	1	0.74	0.50
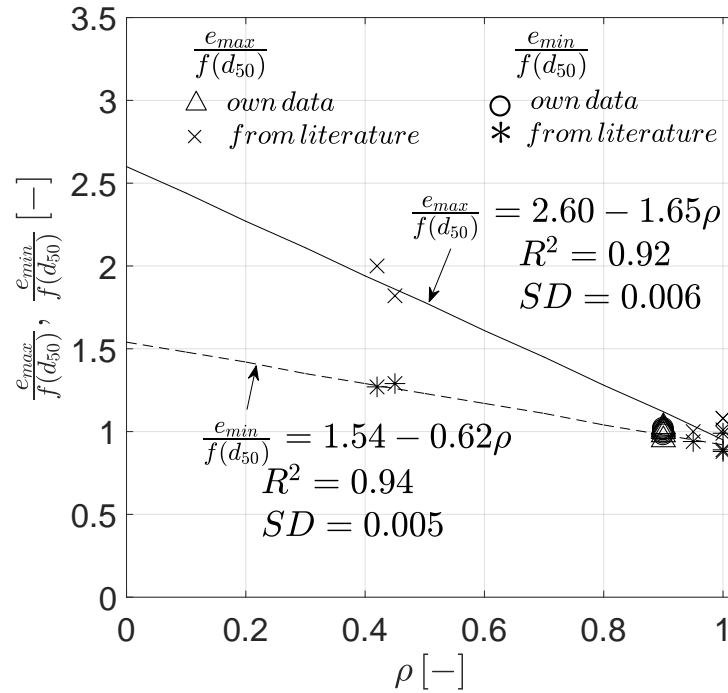
Figure 3.10: Plots showing the variation of the extreme void ratios normalized with respect to the mean grain size with regularity (ρ)

Next, the influence of grain shape is analyzed. The own data set analyzed so far contains only round glass beads. The data for very angular particles, like crushed glass, are rare in the literature. However, existing experimental data from a couple of past studies was used in the present analysis, details of which can be found in Table 3.4. The void ratios were initially normalized with respect to the mean grain size using Eqs. 3.1 and 3.2 and then analyzed with respect to the regularity, which was obtained directly from the respective literatures or determined following the approach of Zheng & Hryciw (2015) similar to the case of sands. A reduction of the normalized limit void ratios with increasing ρ was encountered as evident from Fig. 3.10, with a faster decrement for e_{max}, although at $\rho = 1$, they seem to almost converge. The following linear equations are able to capture the above-said variation while a strong correlation ($R^2 = 0.92$ and 0.94 / SD = 0.006 and 0.005 for e_{max} and e_{min} respectively) between the normalized void ratios and the regularity is obtained.

$$\frac{e_{max}}{f(d_{50})} = f(\rho) = 2.6 - 1.65\,\rho \tag{3.3}$$

$$\frac{e_{min}}{f(d_{50})} = f(\rho) = 1.54 - 0.62\,\rho \tag{3.4}$$
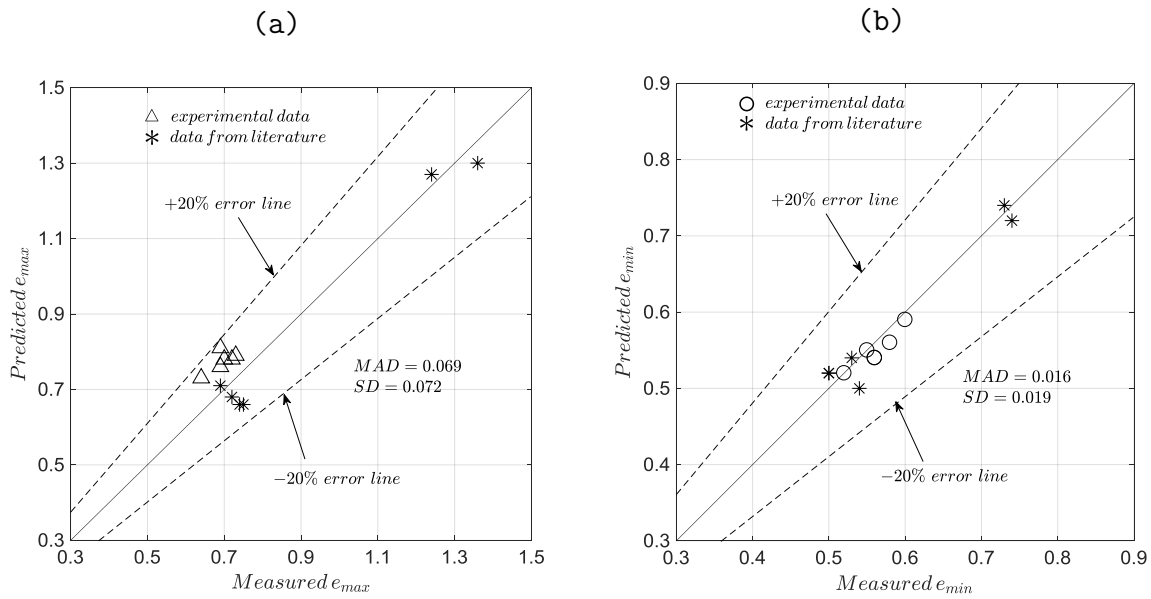
Figure 3.11: Comparison between the measured and predicted (a) maximum void ratio, and (b) minimum void ratio for all the data for glass materials obtained from the current study and literature using the suggested mathematical model in Eqs. 3.5 and 3.6

Therefore, combining both the effects of d_{50} and ρ, the overall mathematical expression may be summed up as follows:

$$e_{max} = f(d_{50})f(\rho) = (1.794 - 1.139\,\rho) \times d_{50}^{-0.029} \tag{3.5}$$

$$e_{min} = f(d_{50})f(\rho) = (0.874 - 0.352\,\rho) \times d_{50}^{0.038} \tag{3.6}$$

Furthermore, a comparison between the measured and predicted maximum and minimum void ratios for all the data obtained from own experiments and literature using the suggested mathematical model for glass materials was carried out as shown in Figure 3.11. As evident, a good estimation of the experimental void ratios is obtained with the model performing relatively better for predicting the minimum void ratio compared to the maximum void ratio, yielding a mean absolute deviation (MAD) of 0.016 for e_{min} as against 0.069 for e_{max}.

ii) Effect of particle characteristics on index void ratios for sands

Initially five sands with the same d_{50} and C_u were taken to formulate a relationship between the regularity and the limit void ratios. Fig. 3.12 shows the data, where e_{min} and e_{max} decrease with increasing regularity. The relations have been expressed by two exponential equations:

$$e_{max} = f(\rho) = 1.05 \ \exp^{(0.45-0.9\rho)} \tag{3.7}$$

$$e_{min} = f(\rho) = \exp^{(0.009-\rho)} \tag{3.8}$$
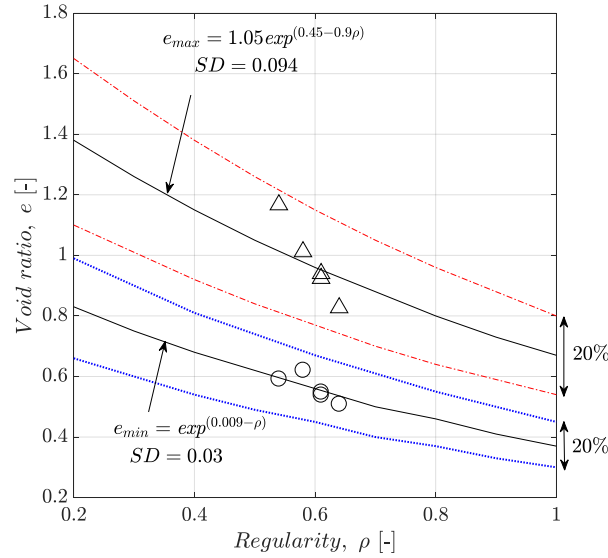
Figure 3.12: Relation between the extreme void ratios and the regularity for sands having similar C_u and d_{50} (red dashed and blue dotted lines represent an error boundary of 20%)

A decent correlation between the regularity and the limit void ratios was achieved using an exponential function, having SDs of 0.094 and 0.03 respectively. It is worthy to mention that the red dashed and blue dotted lines in Fig. 3.12 denote error limits of 20%.

With Eqs. 3.7 and 3.8, the limit void ratios were normalized to remove the effects of ρ and a possible correlation between the normalized void ratios and C_u and d_{50} was analyzed based on the own experimental data as shown in Figs. 3.13 and 3.15 (in 3D), and Figs. 3.14 and 3.16 (in 2D with dashed line in Figs. 3.14b and 3.16b signifying the trend obtained keeping $C_u = 2$). It was found that the normalized void ratio reduces with increasing C_u (see Fig 3.14a for e_{max}, Fig. 3.16a for e_{min}) but no definite conclusion can be drawn with respect to the influence of mean grain size as the scatter is considerable (see Fig. 3.14b for e_{max}, Fig. 3.16b for e_{min}). This is contrary to the observations for glass beads where d_{50} was found to play a more dominant role with respect to e_{max} and e_{min}. This observation for sands is supported in previous works as well (Youd 1973; Zheng & Hryciw 2016). The observations can be described in the form of mathematical equations as given below:

$$\frac{e_{max}}{f(\rho)} = f(C_u) = 1.08 \, C_u^{-0.172} \tag{3.9}$$

$$\frac{e_{min}}{f(\rho)} = f(C_u) = 1.17\, C_u^{-0.241} \tag{3.10}$$

Note that in this analysis, a wide range of C_u ranging from 1.33 till 6.1 was considered. A decent correlation was obtained for both void ratio limits ($R^2 = 0.6$ for e_{max}, $R^2 = 0.78$ for e_{min}). Therefore, the complete relation capturing the dependence of the void ratio limits on ρ and C_u for sand can be expressed through the following equations:

$$e_{max} = f(\rho)f(C_u) = 1.13\, \exp^{(0.45-0.9\rho)}\, C_u^{-0.172} \tag{3.11}$$

$$e_{min} = f(\rho)f(C_u) = 1.17\, \exp^{(0.009-\rho)}\, C_u^{-0.241} \tag{3.12}$$
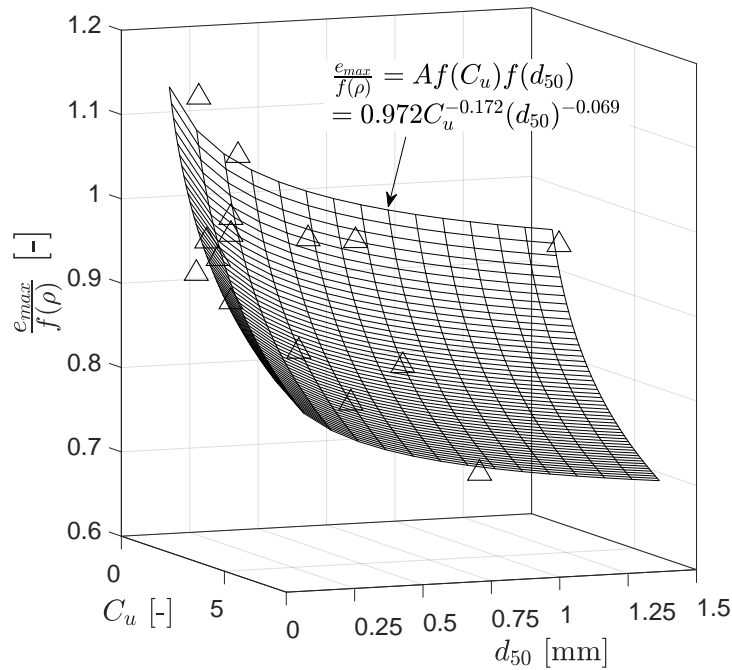
Figure 3.13: 3D plot showing the variation of the normalized maximum void ratio with uniformity coefficient and the mean grain size for the various sands tested presently

The correlations between the void ratio limits, ρ and C_u developed based on the own experimental data were validated with an extensive dataset of available results for various sands from the literature, which are summarized in Table 3.5. While the method of determination of the limit void ratios are not explicitly documented in Sladen et al. (1985), the studies of Cho et al. (2006), Zheng & Hryciw (2016), Sukumaran & Ashmawy (2001), Cabalar et al. (2013), Thomann (1990) and Zelasko et al. (1975) followed the procedure outlined in ASTM-D4253 (2002) and ASTM-D4254 (2002). Bui (2009) used the procedure employed by Cresswell et al. (1999) and Kolbuszewski (1948) for determining
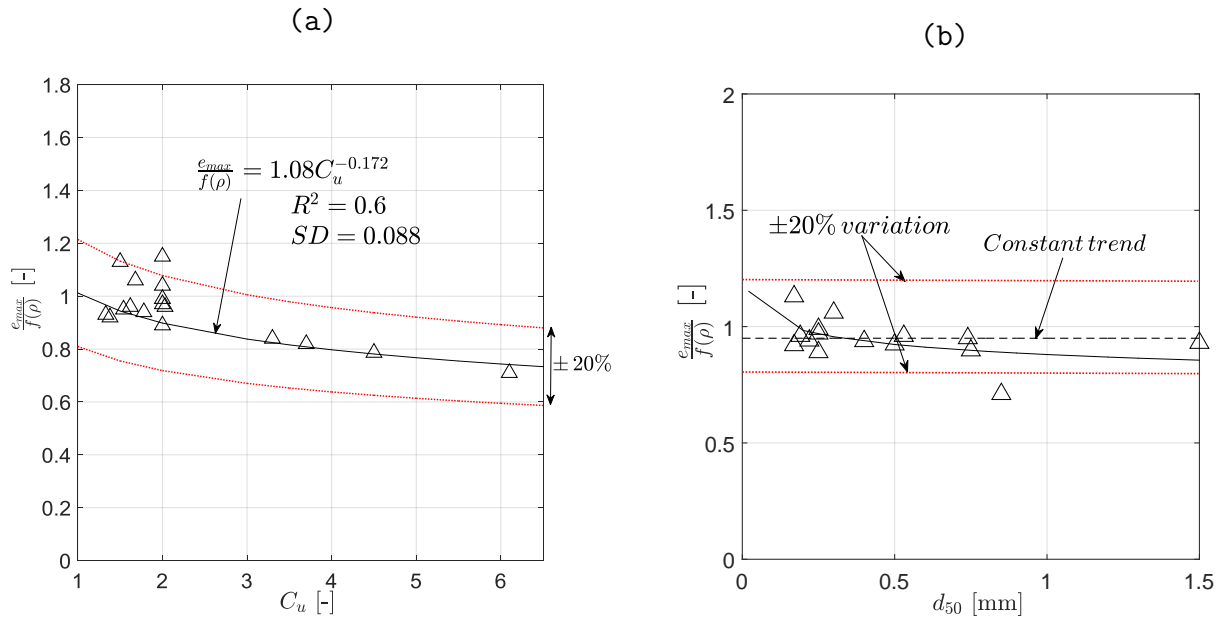
Figure 3.14: 2D plot showing the variation of the normalized maximum void ratio with respect to (a) uniformity coefficient, and (b) mean grain size; solid or dashed black line denote the trend, dotted red lines represent a 20% variation
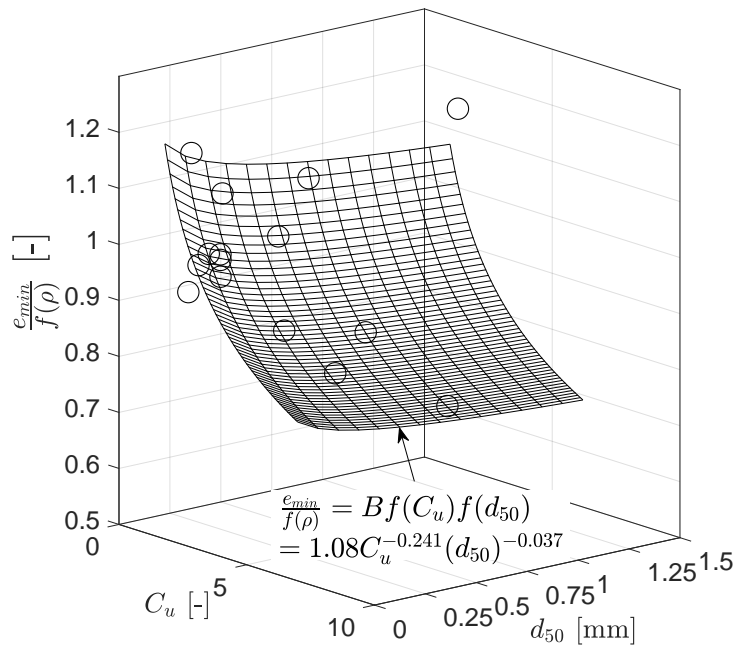
Figure 3.15: 3D plot showing the variation of the normalized minimum void ratio with uniformity coefficient and the mean grain size for the various sands tested presently

the maximum and minimum densities respectively. The British Standard BS-1377 (1) was employed by Rees (2010), while Yasin & Safiullah (2003) used the procedure applied in Bowels (1986). Finally, Tsomokos & Georgiannou (2010) employed the methods of Kol-
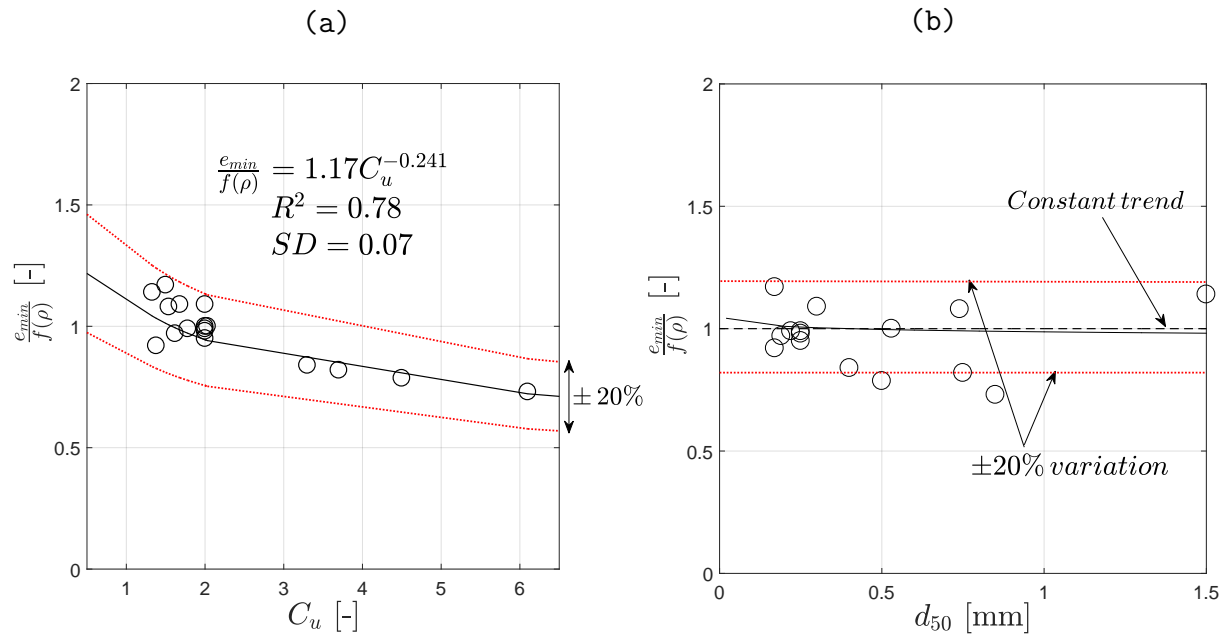
Figure 3.16: 2D plot showing the variation of the normalized minimum void ratio with respect to (a) uniformity coefficient, and (b) mean grain size; solid or dashed black line denote the trend, dotted red lines represent a 20% variation)

buszewski (1948), while the Japanese standard JGS-0161 (2015) was used by Moroto & Ishii (1990).

Figs. 3.17 and 3.19 show the 3D representations of the maximum and minimum void ratios plotted versus the regularity and the uniformity coefficient for the various sands. 2D representations of the same data are shown in Figs. 3.18 and 3.20 respectively. The equation suggested by Cho et al. (2006) between the void ratios and regularity has also been plotted simultaneously in Figures 3.18(a) and 3.20(a) along with dashed red lines for an error of 20%. From Figs. 3.18(b) and 3.20(b), a considerable scatter can be noted in the datasets for the samples having a relatively small value of C_u. There may be two reasons for this observation: firstly, different testing methods as suggested by various standards create different values of the extreme void ratios. Another factor may be the roughness of the grain surface, which besides roundness and sphericity, is another particle characteristic which may influence the packing density and the mechanical behavior, and which has not been taken into consideration for the above analysis.

Table 3.5: Data of various sands as obtained from literature: 1- Sladen et al. (1985), 2- Cho et al. (2006), 3- Bui (2009), 4- Rees (2010), 5- Zheng & Hryciw (2016), 6- Sukumaran & Ashmawy (2001), 7- Cabalar et al. (2013), 8- Zelasko et al. (1975), 9- Thomann (1990), 10- Moroto & Ishii (1990), 11- Yasin & Safiullah (2003), 12- Tsomokos & Georgiannou (2010)

Source	Soil	$d_{50}[mm]$	C_u	G_s	ρ	e_{max}	e_{min}
1	Nerlerk	0.28	2	2.65	0.59	0.94	0.62
	Leighton Buzzard	0.86	1.2	2.68	0.66	0.82	0.54
2	Fraser river sand	0.3	1.9	2.69	0.38	1.13	0.78
	Ottawa #60#80 sand	0.21	2.4	2.65	0.72	0.85	0.55
	Ottawa #90 sand	0.27	2.2	-	0.5	1.1	0.73
	ASTM graded sand	0.35	1.7	2.65	0.85	0.82	0.5
	Ponte Vedra sand	0.18	1.8	2.80	0.58	1.07	-
	Nevada sand	0.15	1.8	2.67	0.73	0.85	0.57
	Margaret river sand	0.49	1.9	-	0.7	0.87	-
	Jekyll Island sand	0.17	1.7	-	0.58	1.04	-
	Sandboil sand	0.36	2.4	2.62	0.63	0.79	0.51
	5Z9 crushed sand	0.40	3.6	-	0.6	0.89	-
	6H1 crushed sand	0.33	3.8	-	0.5	0.97	-
	Granite powder	0.09	6.2	2.58	0.32	1.296	-
	ASTM #20#30 sand	0.60	1.4	2.65	0.85	0.69	-
	Ottawa F-110 sand	0.12	1.7	-	0.7	0.848	0.535
	Syncrude tailings	0.18	2.5	2.58	0.55	1.14	0.59
	Ticino sand	0.58	1.5	2.68	0.6	0.99	0.574
	Blasting sand	0.71	1.9	2.65	0.43	1.025	0.698
	Ottawa #20#30 sand	0.72	1.2	2.65	0.9	0.742	0.502
	Daytona beach sand	0.23	1.4	2.64	0.66	1	0.64
	Michigan dune sand	0.33	1.5	2.63	0.82	0.8	0.56
	Ottawa #20#70 sand	0.21	2.4	2.65	0.79	0.78	0.47
	Ottawa #45 sand	0.57	2.1	2.57	0.57	1.11	0.75
3	Leighton Buzzard B	-	1.57	-	0.73	0.83	0.48
	Leighton Buzzard E	-	1.38	-	0.69	1.01	0.63
4	PSM1	0.208	2.2	2.66	0.7	0.927	0.642
	PSM2	0.175	2.2	2.66	0.73	0.941	0.637
	FBM1	0.168	2	2.65	0.67	0.907	0.628
5	Chesterton, Indiana dunes	0.26	1.3	2.68	0.7	0.87	0.57
	Ottawa 20-30	0.71	1.4	2.65	0.79	0.74	0.49
	Michigan 2NS	0.50	2.3	-	0.6	0.82	0.54
	New Madrid, Missouri	0.32	2.2	-	0.65	0.81	0.52

Table 3.5 continued from previous page

Source	Soil	d_{50}	C_u	G_s	ρ	e_{max}	e_{min}
	Michigan dunes	0.30	1.5	2.68	0.67	0.85	0.56
	Oakland County, Michigan	0.31	1.6	2.63	0.69	0.86	0.53
	Michigan 30A	0.58	7	2.84	0.42	0.92	0.55
	Fused aluminum oxide	1.80	1.6	-	0.50	0.92	0.63
	Scotts Valley, California	0.33	1.5	2.85	0.57	0.94	0.6
	Upper Peninsula, Michigan	0.60	2.8	-	0.6	0.85	0.54
	Rincon, New Mexico	0.36	3	2.61	0.69	0.8	0.51
	Crushed gabbro	0.80	5.5	-	0.4	0.96	0.6
	Capitola, California	0.35	1.6	2.60	0.6	0.89	0.57
	Brady, Texas	0.61	1.4	2.63	0.72	0.84	0.57
	Class IIA, Michigan	0.21	1.9	2.65	0.66	0.86	0.56
	Griffin, Indiana	0.74	4.3	-	0.65	0.79	0.51
	Chesterton, Indiana beach	0.64	2.9	2.65	0.65	0.85	0.54
	Muskegon, Michigan	0.40	1.6	2.66	0.65	0.84	0.56
	Nevada sand	0.16	1.3	2.65	0.67	0.88	0.58
	Treasure Island, California	0.25	1.8	-	0.64	0.85	0.57
6	Daytona Beach sand	0.23	1.4	2.64	0.5	1	0.64
	Fraser River sand	0.30	1.9	2.79	0.47	1.13	0.78
	Ottawa #20/70 sand	0.53	2.4	-	0.57	0.78	0.47
	Ottawa #45 sand	0.57	2.1	2.57	0.46	1.11	0.75
	Ottawa #60/80 sand	0.21	2.4	2.65	0.72	0.85	0.55
	Ottawa #90 sand	0.27	2.2	-	0.38	1.1	0.73
	Syncrude Tailings	0.18	2.5	2.65	0.41	1.14	0.59
7	Narli	1	3.7	2.66	0.7	0.83	0.52
	Crushed stone sand	1.40	2.5	2.68	0.53	0.93	0.62
	Birecik	0.86	3.3	-	0.69	0.8	0.55
	Trakya	0.72	6.3	-	0.5	0.7	0.49
8	Ottawa 20-30	0.72	1.2	2.65	0.76	0.78	0.46
	Ottawa 35-45	0.42	1.2	-	0.75	0.82	0.58
	Ottawa 50-70	0.25	1.2	-	0.71	0.89	0.53
	Ottawa 70-100	0.18	1.2	-	0.7	0.92	0.54
	Ottawa 100-140	0.12	1.2	-	0.7	0.92	0.54
	Evanston Beach 20-30	0.72	1.2	-	0.58	0.92	0.55
	Evanston Beach 35-45	0.42	1.2	-	0.58	0.9	0.52
	Evanston Beach 50-70	0.25	1.2	-	0.57	0.92	0.54
	Evanston Beach 70-100	0.18	1.2	-	0.57	0.93	0.52

	Table 3.5 continued from previous page						
Source	**Soil**	d_{50}	C_u	G_s	ρ	e_{max}	e_{min}
	Franklin Falls 20-30	0.72	1.2	-	0.44	1.08	0.62
	Franklin Falls 35-45	0.42	1.2	-	0.44	1.04	0.63
	Franklin Falls 50-70	0.25	1.2	-	0.43	1.1	0.64
9	Ottawa 20-30	0.75	1.2	2.65	0.83	0.72	0.51
	Ottawa 50-70	0.22	1.1	2.65	0.75	0.84	0.57
	Ottawa 100-200	0.13	1.9	-	0.63	0.9	0.59
	Douglas Lake sand	0.23	2.4	-	0.6	0.83	0.54
	Ackerman Lake sand	0.34	2.5	-	0.7	0.72	0.48
	Agsco 50-80	0.25	1.3	2.67	0.35	1.24	0.79
	Daedalus sand	0.60	4.7	-	0.83	0.61	0.36
10	Gabbro	-	1.6	-	0.51	0.9	0.65
	Greywacke	-	1.6	-	0.48	0.97	0.72
	Onahama	-	1.6	-	0.52	0.99	0.71
	Dolelite	-	1.6	-	0.58	0.96	0.69
	River gravel	-	1.6	-	0.57	0.84	0.55
	Beach gravel	-	1.6	-	0.66	0.74	0.53
11	Teesta sand	0.50	2.5	-	0.53	0.92	0.57
	Meghna sand	0.23	1.9	-	0.47	0.97	0.66
	Yamuna sand	0.13	1.9	2.69	0.39	1.14	0.72
12	Ham River sand	0.30	1.3	2.66	0.65	0.87	0.53
	Fontainebleau sand	0.21	1.2	2.64	0.68	0.87	0.54
	M31 sand	0.30	1.3	2.65	0.73	0.87	0.53
	Longstone sand	0.15	1.3	2.64	0.48	1	0.61

Fig. 3.21 shows the void ratios predicted by Eqs. 3.11 and 3.12 versus the measured void ratios for the sands tested in the own experimental study as well as the data collected from literature. Statistical analysis including regression (R^2), standard deviation (SD), and mean average deviation (MAD) was performed on the data set to evaluate the model performance. The MAD was determined as 0.067 for e_{max} and 0.051 for e_{min}. The current work is compared with the results obtained by Koerner (1969) and Hryciw et al. (2016) and documented in Hryciw et al. (2016). Koerner's model delivers a MAD of 0.15 and 0.06 for e_{max} and e_{min} respectively. While the mathematical description by Eqs. 3.11 and 3.12 is definitely an improvement over this existing work, the same cannot be said for the comparison with Hryciw et al. (2016) (ref. Eqs. 2.19 and 2.20) which uses roundness and sphericity parameters, and which has a MAD of 0.034 for both e_{max} and e_{min}. The reason
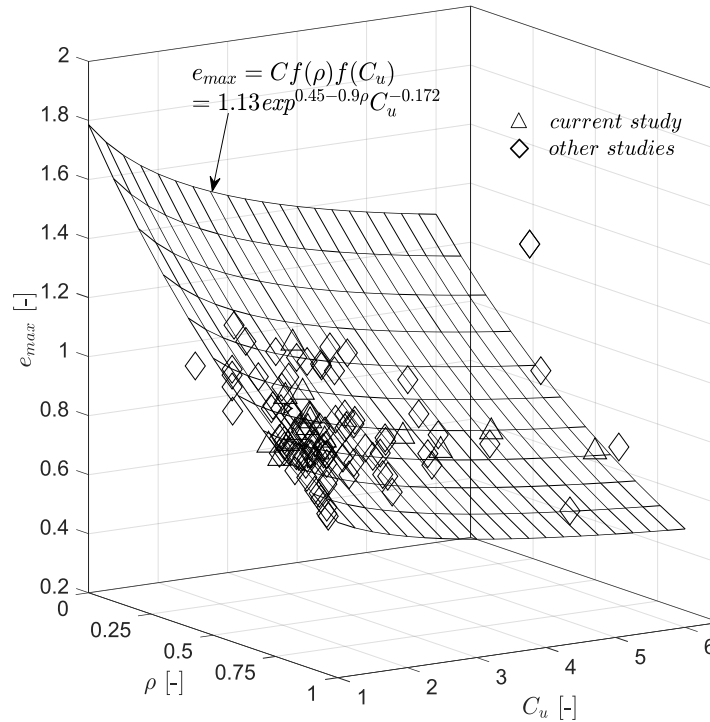
Figure 3.17: 3D plot showing the variation of the maximum void ratios with the regularity and the uniformity coefficient for sands including data from literature

could be attributed to the unequal contribution of both the two shape parameters roundness and sphericity as was suggested in their model, while the current model considers regularity as a single shape parameter, being the mean value of roundness and sphericity. However, the primary advantage of the current model is that two shape parameters are replaced by only one parameter without a significant loss of prediction quality.

In addition, another comparison was performed between the model of Nguyen et al. (2020b) and the proposed model using only the own experimental results. Nguyen et al. (2020b) proposed a model based on the grain roundness R and the sphericity S as below:

$$e_{max} = 1.330 - 0.12 \times S - 0.545 \times R \tag{3.13}$$

$$e_{min} = 0.877 - 0.149 \times S - 0.308 \times R \tag{3.14}$$

Their formulation yields a MAD of 0.105 and 0.084 for e_{max} and e_{min} respectively, while 0.057 and 0.025 are obtained from the proposed model. This larger discrepancy between predicted and measured values can be majorly attributed to the fact that the model of Nguyen et al. (2020b) considers only the grain shape but does not consider the grain size

parameters (C_u or d_{50}), which leads to a relatively larger scatter of data.
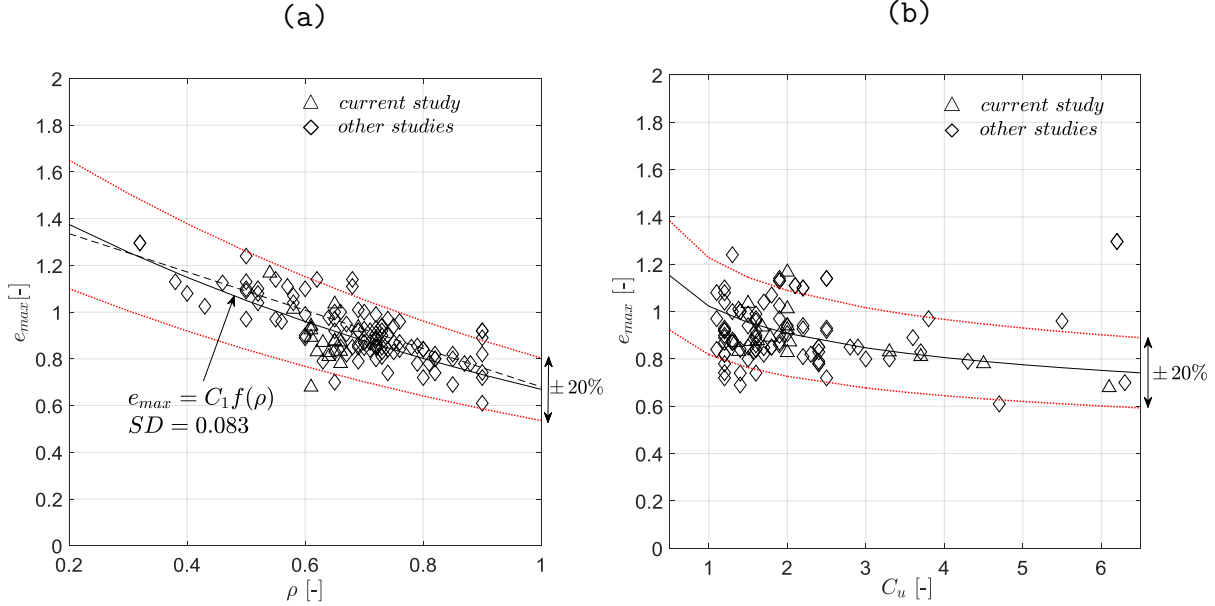
Figure 3.18: 2D plots showing the variation of the maximum void ratios with the (a) regularity and (b) uniformity coefficient (black solid lines correspond to Eqs. 3.11 and 3.12, black dashed line in (a) shows the equation suggested by Cho et al. 2006, dotted red lines represent a 20% variation)

iii) Comparison between round glass beads and rounded sands

Round glass beads and naturally rounded sands were further considered to investigate the effect of specific gravity on the extreme values of the void ratios. Data of a few naturally rounded sands having a regularity of more than 0.80 were used for the analysis considering the model developed based on the data for glass beads (see Table 3.6). To consider the effect of specific gravity, a term called the specific gravity ratio, which is the ratio of the specific gravity of the material (G_m) to that of the reference material which is glass (G_g) (considered as 2.54 in the current study), was taken. After incorporating the above mentioned term, the equations take the following form:

$$e_{max} = f(D_{50})f(\rho)f(G_m) = (1.794 - 1.139\,\rho) \times d_{50}^{-0.029} \times \left\{\frac{G_m}{G_g}\right\}^{-\alpha} \tag{3.15}$$

$$e_{min} = f(D_{50})f(\rho)f(G_m) = (0.874 - 0.352\,\rho) \times d_{50}^{0.038} \times \left\{\frac{G_m}{G_g}\right\}^{-\alpha} \tag{3.16}$$
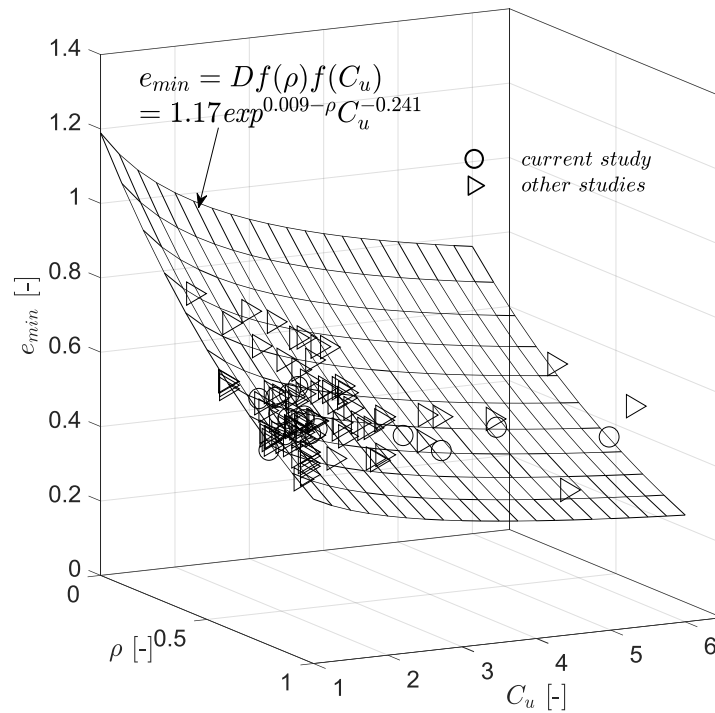
Figure 3.19: 3D plot showing the variation of the minimum void ratios with the regularity and the uniformity coefficient for sands including data from literature
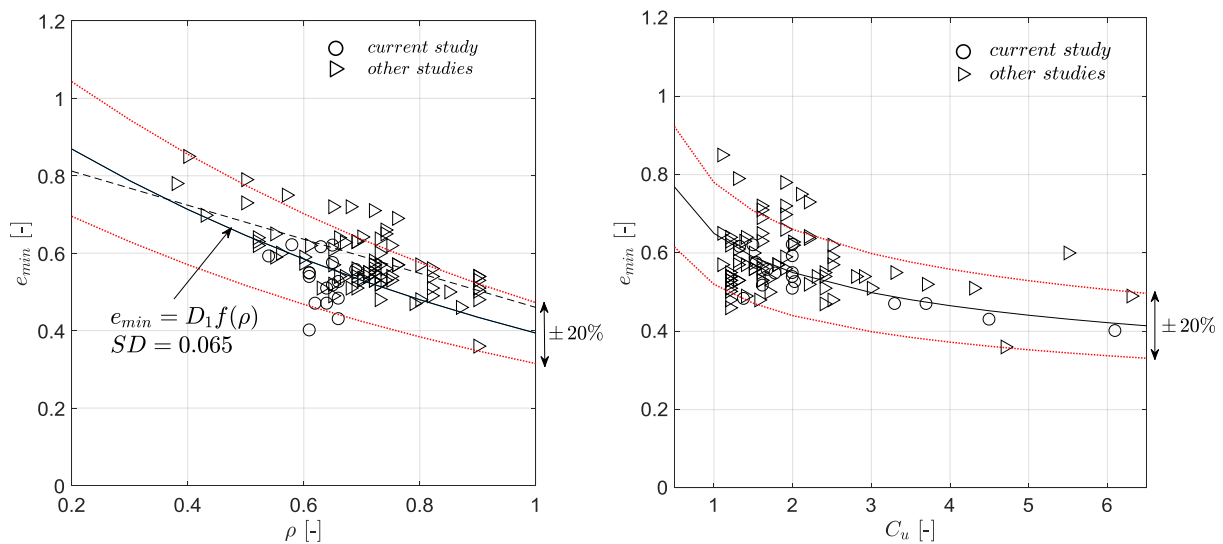
Figure 3.20: 2D plots showing the variation of the minimum void ratios with the (a) regularity and (b) uniformity coefficient (black solid lines correspond to Eqs. 3.11 and 3.12, black dashed line in (a) shows the equation suggested by Cho et al. 2006, dotted red lines represent a 20% variation)
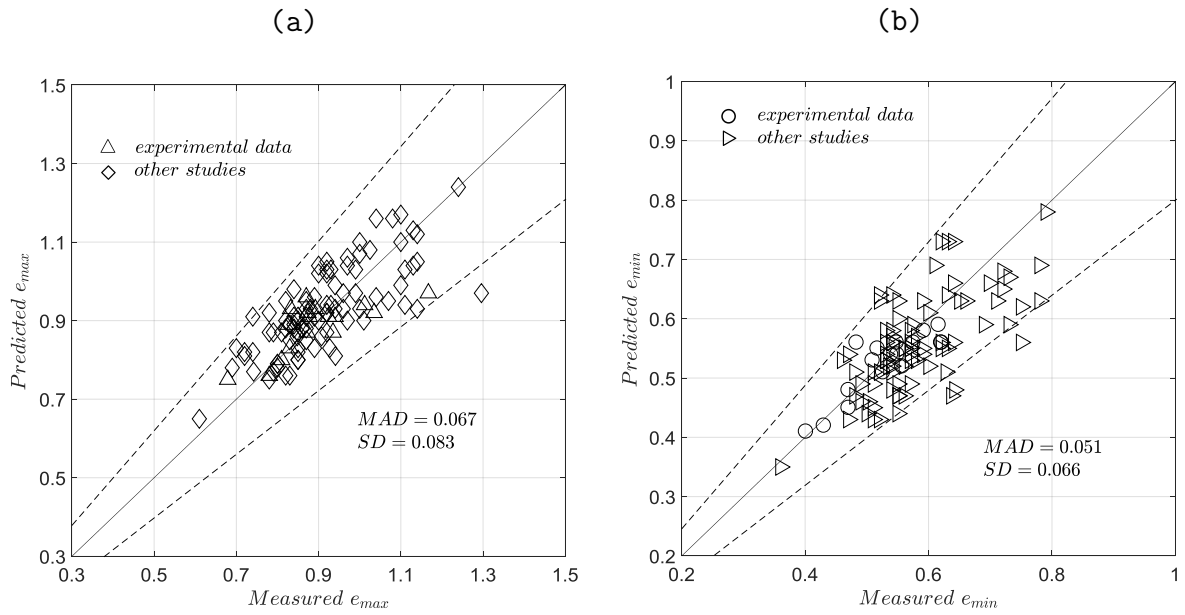
Figure 3.21: Comparison between the measured and predicted (a) maximum and (b) minimum void ratios for sands using all the data obtained from the current study and literature and applying the suggested mathematical model (dashed lines represent error of 20%)
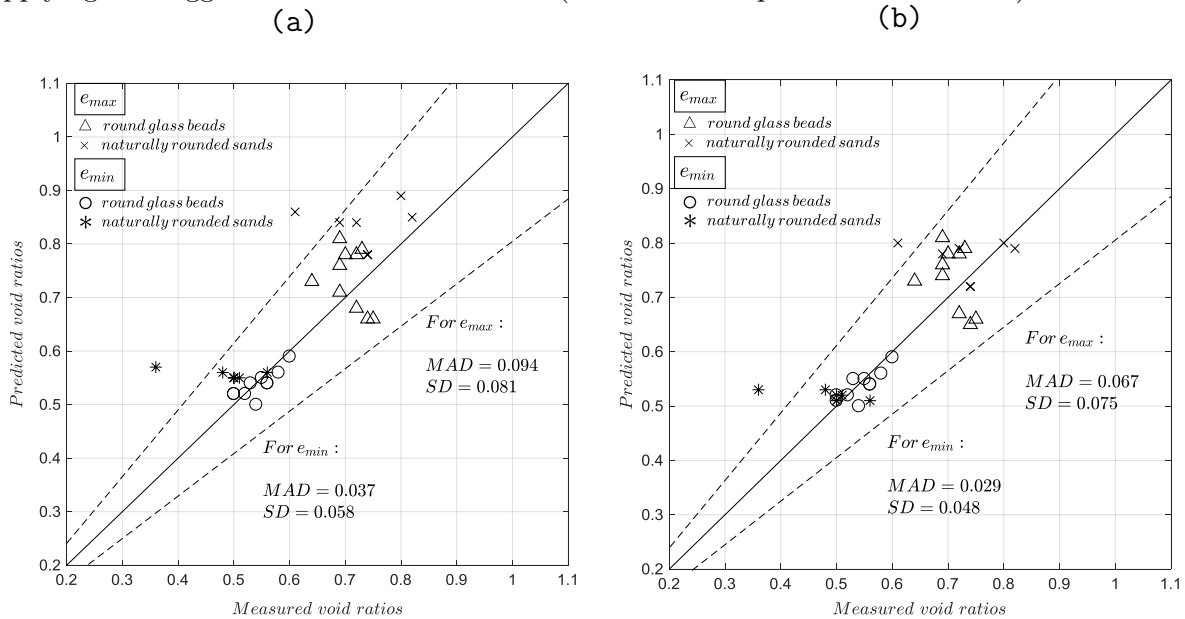
Figure 3.22: Comparison between the measured and predicted limit void ratios for both rounded glass beads and naturally rounded sand (a) without, and (b) with considering the effect of specific gravity (data taken from literature; dashed lines represent an error of 20%)

A value of $\alpha = 1.8$ was found to be the best fit for the above operation. Figs. 3.22 (a and b) show the measured versus the predicted void ratios for the above materials using only the equations suggested for glass without (Fig. 3.22a) and with (Fig. 3.22b) considering the specific gravity ratio respectively. The first model leads to a MAD of 0.094 and 0.037 for

Table 3.6: Data for naturally rounded sand (data taken from literature) for comparison with the model suggested for glass

Source	Soil	G_s	$d_{50}[mm]$	ρ	e_{max}	e_{min}
Cho et al. (2006)	ASTM graded sand	2.65	0.35	0.85	0.82	0.5
	Ottawa #20#30 sand	2.65	0.72	0.9	0.74	0.502
	ASTM 20-30	2.65	0.6	0.85	0.69	-
	Michigan dune sand	2.68	0.33	0.82	0.8	0.56
Thomann (1990)	Daedalus sand	-	0.6	0.83	0.61	0.36
DeJong & Christoph (2009)	ASTM 20-30 sand	2.65	0.74	0.9	0.74	0.51
Georgiannou & Konstadinou (2013)	Ottawa sand	2.65	0.72	0.9	0.74	0.5
Baxter & Mitchell (2004)	Density sand	2.64	0.5	0.85	0.72	0.48

e_{max} and e_{min} respectively, while after incorporating the specific gravity ratio, the value of the same is reduced to 0.067 and 0.029 respectively, concluding that specific gravity slightly interferes in the determination of void ratio although for practical purposes, this may be considered minimal.

Using the specific gravity ratio factor introduced in the previous step, the analysis was further extended to Eqs. 3.11 and 3.12 which were developed for sand. The optimum value of α obtained through regression was 0.4 for sands. Therefore, incorporating the specific gravity ratio, Eqs. 3.11 and 3.12 can be rewritten as:

$$\frac{e_{max}}{f(\rho)} = f(C_u) = 1.08\, C_u^{-0.172}\, \exp^{(0.45-0.9\rho)} \times \left\{\frac{G_m}{G_g}\right\}^{-0.4} \tag{3.17}$$

$$\frac{e_{min}}{f(\rho)} = f(C_u) = 1.17\, C_u^{-0.241}\, \exp^{(0.009-\rho)} \times \left\{\frac{G_m}{G_g}\right\}^{-0.4} \tag{3.18}$$

Figure 3.23 shows the measured versus the predicted void ratios considering the effect of specific gravity for the complete dataset for sand (both documented in literature in Table 3.5 and current experiments). Without the effect of specific gravity, the MAD for e_{max} and e_{min} was found to be 0.067 and 0.047 respectively. Using the specific gravity ratio, the MAD values for e_{max} and e_{min} decrease to 0.065 and 0.044 respectively, thus slightly increasing the accuracy of prediction. However, considering the minor influence, one may ignore this additional term for the sake of simplicity. For further increase in accuracy, additional studies should be conducted to assess the effect of surface friction on the e_{max} and e_{min} values.
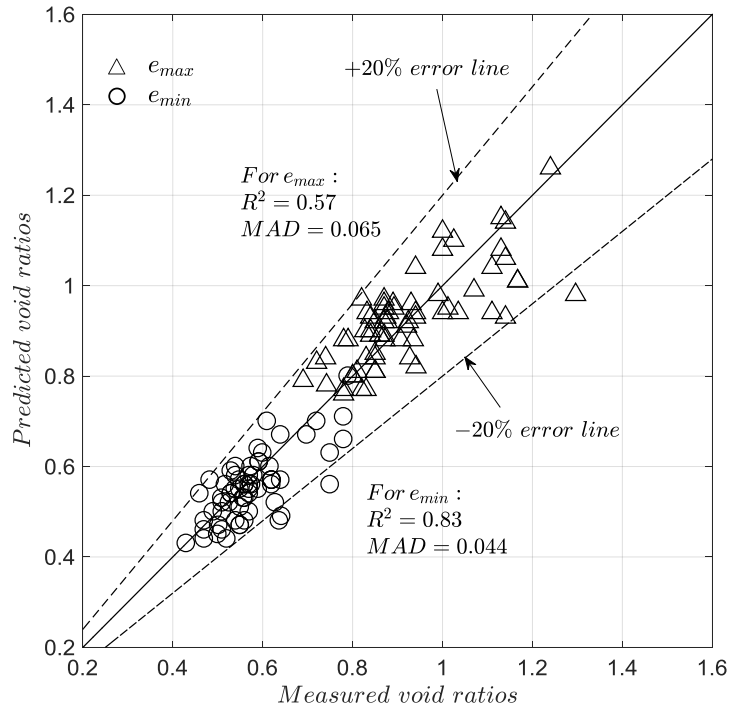
Figure 3.23: Comparison between the measured and predicted void ratios for all the available data for sands considering the effect of the specific gravity of the materials

3.6 Summary

In this chapter, an attempt was made to correlate the particle characteristics with the maximum and minimum void ratios of granular materials. The concept of regularity was employed to capture roundness and sphericity of a particle, while excluding the effect of particle surface roughness. The current study considers own experimental results for glass beads and sands as well as an extensive dataset obtained from literature. DIN standards were followed for the determination of the index properties of granular matter. For poorly graded glass beads, the e_{max} and e_{min} values were found to correlate stronger with d_{50} than with C_u. A good fit between the experimental results and the data obtained from literature is found for glass particles. There is a tendency of e_{max} to decrease with d_{50}, while e_{min} increases, thus both limit void ratios approach each other with increasing grain size. Furthermore, these relationships have been fitted by empirical equations, considering also data for glass materials from the literature.

For sand, the suggested model has been demonstrated to be an improvement over an existing model. The considerable scatter obtained in the plots of void ratios versus C_u can probably be attributed to the effect of roughness of the grain particles. The e_{min} and

e_{max} values for sands were found to significantly drop with increasing C_u and increasing regularity, while no clear tendency with d_{50} could be found. In a similar way, empirical equations were validated based on extensive collected data from the literature.

Besides, the data of glass beads and naturally rounded sands was analyzed to investigate the effect of specific gravity on the void ratio limits, which was captured through the introduction of a parameter called the specific gravity ratio. A better prediction of the extreme values of void ratio was achieved using this ratio with glass as the reference material. In addition, incorporating the specific gravity ratio into the model developed for sands, a better degree of accuracy is achieved in estimating e_{max} and e_{min}, although it is acknowledged that the influence of the specific gravity is very small and can be neglected for practical purposes.

4 Experimental methods

4.1 Introduction

The investigation of the combined effect of particle size and shape on the mechanical characteristics (static, cyclic and dynamic characteristics) of granular soils is the main goal of this research. For this, a rigorous and systematic experimental program incorporating various types of experiments was followed, which forms the backbone of this study. The purpose of the present chapter is to introduce and briefly describe the various experimental devices used along with their mode of operation. Furthermore, the test materials are characterized.

4.2 Materials used

In the majority of the experimental program discussed in subsequent chapters, three materials - round glass beads, crushed angular glass and sub-angular Rhein (Rhine) sand were considered. All the three materials have quartz as the dominant mineralogical content. The round glass beads were purchased from a well-known local company specialized in glass products, *Mühlmeier GmbH*. The Rhein sand was procured from the banks of the river Rhine, which flows across the state of North Rhine-Westphalia (NRW) in Germany. The crushed glass, however, was not readily available; therefore, it had to be artificially produced from the round glass beads using a Los Angeles abrasion machine, which was readily available at the laboratory of the *Lehrstuhl für Verkehrswegebau* (Chair of Highway and Road Engineering), Ruhr-Universität Bochum (Fig. 4.3). The principle of the Los Angeles abrasion machine is described later. The obtained crushed glass was washed to remove the fines and then dried in the oven for 24 hours at a temperature of 105°C.

To obtain a similar particle size distribution, round glass beads of various sizes were mixed in certain proportions to match the grain size distribution of the crushed angular glass, which has a mean grain size of $d_{50} = 0.45$ mm and a uniformity coefficient of

$C_u = 5$. Finally, the Rhein sand was sieved to correspond to a similar gradation as the crushed glass. The particle size distribution curves for the three materials before commencement of the monotonic tests is displayed in Fig. 4.1. In this thesis the crushed glass, round glass beads and Rhein sand are generally abbreviated as *CG*, *RG* and *Rhein*. The index properties of the three materials summarized in Table 4.1 were determined through standardized tests (DIN-18124 2011 and DIN-18126 1996 for specific gravity and the limiting void ratios). Evidently, it is expected that the particle shape of crushed glass would be the most angular, followed by the shape of Rhein sand while the round glass beads are expected to be the most rounded. Image analysis procedures (details of which have been described in the preceding chapter) were used to quantify particle shape. The microscopic images of the three materials are shown in Fig. 4.2 whereas Table 4.1 provides the determined shape parameters.
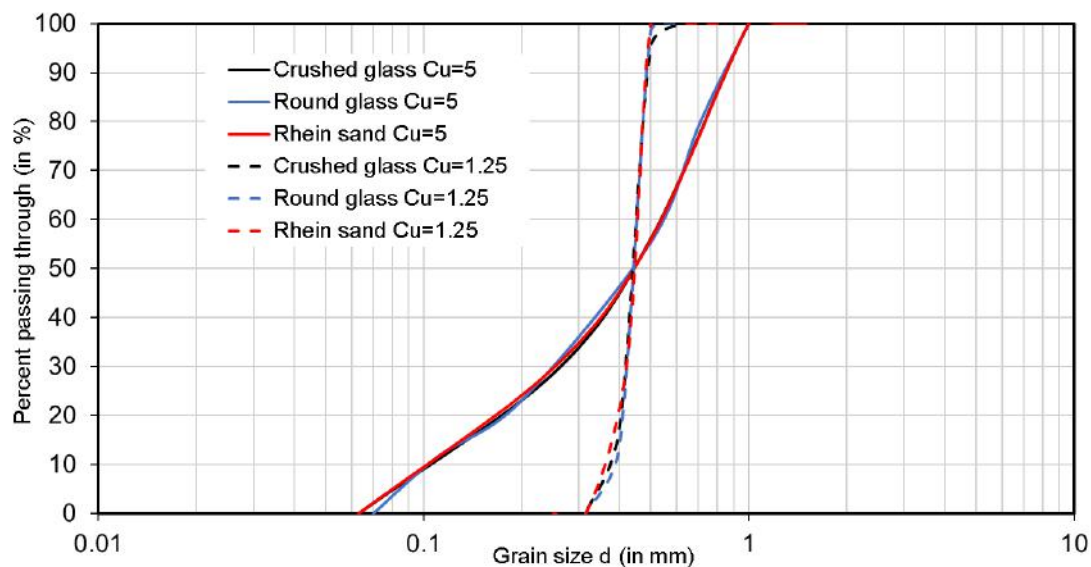
Figure 4.1: Grain size distribution curves of the crushed glass, round glass beads and Rhein sand with two different C_u values.

To assess the influence of the particle gradation on the mechanical behavior of granular soils with different particle shapes, three more mixtures of glass beads, natural sand and crushed glass with a similar $d_{50} = 0.45$ mm but a lower $C_u = 1.25$ were generated. The physical properties of these three additional materials are listed in Table 4.1 while Fig. 4.1 shows their grain size distribution curves.

To obtain crushed glass conforming to a specified particle size, large glass beads with a size in the range 4.5-6.5 mm were used considering the fact that it is easier to crush larger
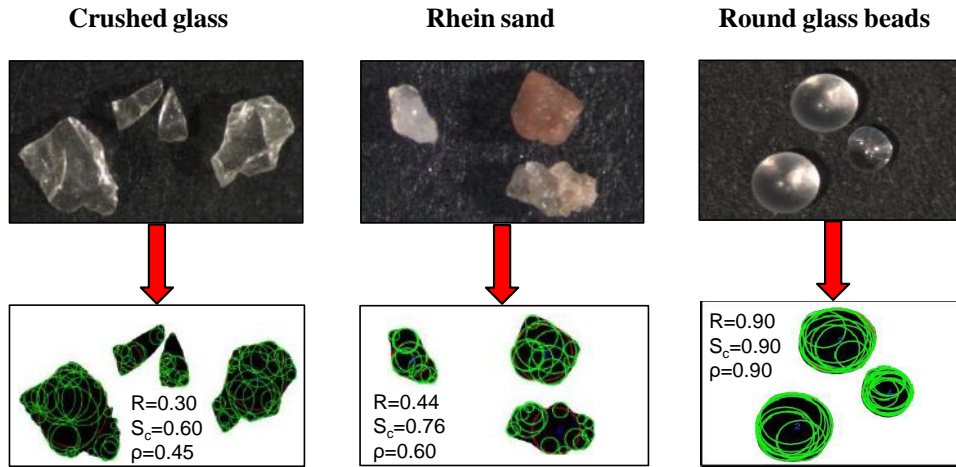
Figure 4.2: Microscopy images of the three materials with $C_u = 5$: (left to right) crushed glass, Rhein sand and round glass beads, both raw and analyzed images

Table 4.1: Physical properties of the materials considered in the analysis

Material	C_u	d_{50} (mm)	R	S_c	ρ	e_{max}	e_{min}	G_s
Crushed glass	5	0.45	0.3	0.6	0.45	1.03	0.50	2.54
Rhein sand	5	0.45	0.44	0.76	0.6	0.83	0.47	2.65
Round glass beads	5	0.45	0.9	0.9	0.9	0.53	0.38	2.54
Crushed glass	1.25	0.45	0.3	0.6	0.45	1.15	0.68	2.54
Rhein sand	1.25	0.45	0.44	0.76	0.6	0.90	0.57	2.65
Round glass beads	1.25	0.45	0.9	0.9	0.9	0.74	0.58	2.54

glass beads than smaller ones in the Los Angeles machine (Fig. 4.3). For crushing round glass beads, the following steps were followed:

- Around 5 kg of glass beads were poured inside the chamber of the Los Angeles abrasion machine along with 12 steel charges.

- The cover is put on and tightly fastened using four screws placed diagonally to each other.

- The machine is mechanically rotated at a speed of 33-34 revolutions per second and for a total of 500 revolutions.

- Since the round beads were to be crushed to a desired gradation, the process was repeated for another 2 times on the same material to achieve a higher degree of crushing.

Figure 4.3: (a) The Los Angeles abrasion device adopted for crushing glass beads, (b) steel charges for crushing

- After completion, the material inside was poured into a steel tray and sieved.

- The portion which corresponded to the desired particle size was separated while the remaining larger fraction was again re-used for further crushing along with additional glass beads.

4.3 Adopted devices

4.3.1 Direct shear device

A direct shear apparatus (Wykeham Farrance Eng. Ltd., England) was used to verify a set of data obtained from the triaxial tests. In this device (Fig. 4.4), the specimen size was 6 cm by 6 cm in horizontal directions, and 2 cm in the vertical direction. The device allows free rotation of both upper frame and loading plate, and the horizontal shearing plane is located at a distance of 1 cm from the bottom surface of the specimen. The vertical stress was applied by placing weights on a loading beam and was transmitted to the specimen through a steel ball to ensure uniform stress distribution. The strain rate was adjusted using a combination of gears for the desired speed. Both the horizontal and the vertical displacement and the horizontal (shear) load were continuously measured during the entire duration of the test.
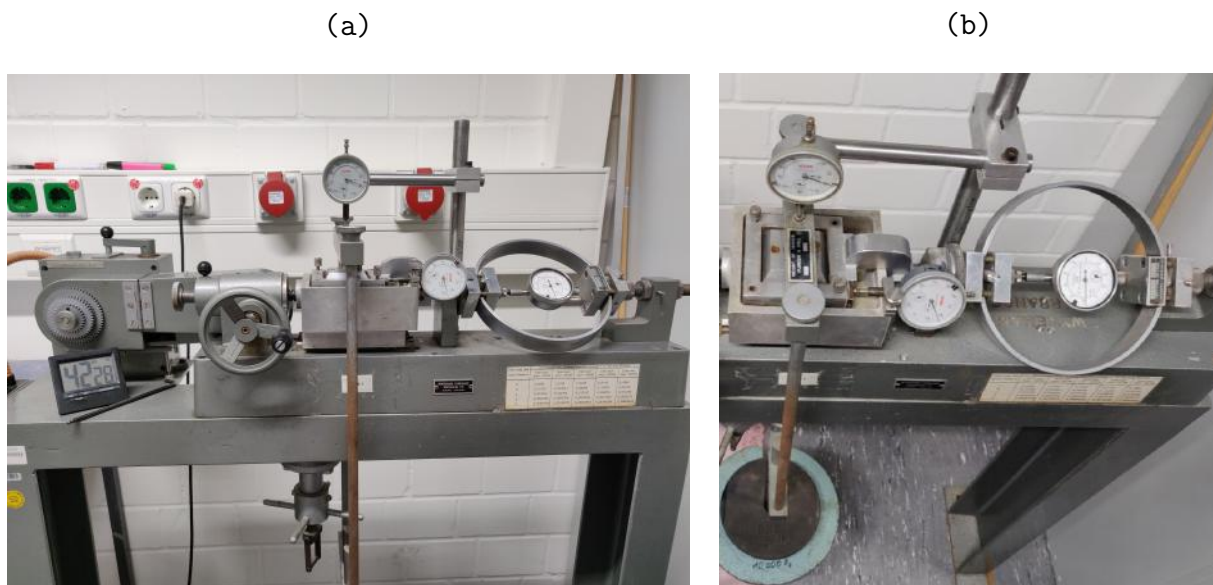
Figure 4.4: (a) Front and (b) top views of the direct shear device used for the experiments

Testing procedure

To conduct the direct shear tests, the dry mass of the material for a target relative density to be tested was first calculated based on the volume of the direct shear box. Both the top and bottom parts of the box were kept together in place with the help of two screws diagonally opposite to each other. After that, the dry material was slowly poured inside the box in three layers. For dense specimens, the specimen was gently tamped occasionally to obtain the required density. It was ensured that after pouring each layer, the top surface of the material was scratched to ensure a better interlocking between successive layers. Afterwards, the direct shear box was transported and mounted into the direct shear device and kept in position for further testing.

Once in position, the top cap (with a groove at the top of it for placing a steel ball) was placed on top of the sample and the screws were detached. Then the loading frame was slowly lowered onto the top cap so that it rested on top of the steel ball. The desired load was applied by placing weights onto the beam loading device. The shearing was performed at a constant rate of deformation, presently 0.24 mm/min. Three proving rings simultaneously measured the horizontal and vertical displacement, as well as the shear force while the test was in progress. Readings were made at intervals of 30 seconds. All direct shear tests were peformed on dry samples.

4.3.2 Triaxial devices

i) Triaxial device used for tests with monotonic loading

The triaxial device is a common geotechnical laboratory device to measure the intermediate and large-strain properties of geo-materials. The monotonic triaxial tests were carried out on a Wykeham Farrance Eng. Ltd. (England) strain controlled loading machine as adopted in previous studies by Wichtmann (2005). The applied device is shown in Fig. 4.5. For the triaxial testing program, the specimens were formed into a cylindrical shape with 10 cm in diameter and 20 cm in height. The load piston is positioned at the top, counteracted by a horizontal beam, and the loading is applied from the bottom at a specified displacement rate which can be adjusted by changing positions of the loading gears. The adopted displacement rate in this study was 0.1 mm/min. Axial deformation of the specimen was measured with a displacement transducer (LVDT) mounted to the load piston at the top of the triaxial device. The volume change of the specimen was measured through a burette system. The specimen was fully saturated and the drainage lines were connected to a burette. Changes in water level correspond to volume changes of the sample. The changes in water level are measured by a differential pressure transducer, which compares the water pressure in the measuring burette with that in a reference burette having a constant water level. Cell pressure and back pressure sensors are mounted at two exits of the pressure cell or the drainage system, respectively. The axial loading was measured through an external load cell installed at the top of the triaxial frame. The data of all sensors is recorded at a PC using HP-VEE software.

The chosen rate of axial deformation ensured that the pore water pressure response inside the sample developed uniformly during undrained shearing. For drained shearing, this ensured drained conditions during the whole test. This rate was generally found to be suitable (Verdugo & Ishihara 1996; Rahman 2009; Rahemi 2017).

ii) Triaxial device used for tests with cyclic loading

The cyclic undrained triaxial tests were carried out in an electro-mechanically driven load press manufactured by *Wille Geotechnik, GmbH*, Germany (Fig. 4.6). A similar triaxial cell as used in the monotonic tests was applied. However, there were a few changes compared to the monotonic tests. The axial load was measured with a load cell located inside the pressure cell, below the sample base. The cyclic loading was triangular in shape and applied stress-controlled, implying that the direction of loading was reversed after

Figure 4.5: Triaxial device used for the various monotonic triaxial experiments

the maximum or minimum values of deviatoric stress corresponding to a certain stress amplitude were reached (refer Fig. 4.7). The vertical displacements were measured from the movement of the loading piston. For data logging and general control of the triaxial device (e.g. movement of the load piston, application of the back pressure, measurement of vertical deformation), Geosys software was used. For the application of back pressure and the measurement of the volume changes during consolidation and testing, the burette system was replaced by a volume pressure controller (VPC) for achieving a higher degree of accuracy. The VPC has a capacity of approximately 1 liter. A pressure sensor was further mounted on it which is used to control the back pressure as well as double check the measurement of the back pressure sensor connected to the drainage system at the bottom of the cell (marked with yellow circle in Fig. 4.8). The positioning of the other sensors can also be seen in the same figure.
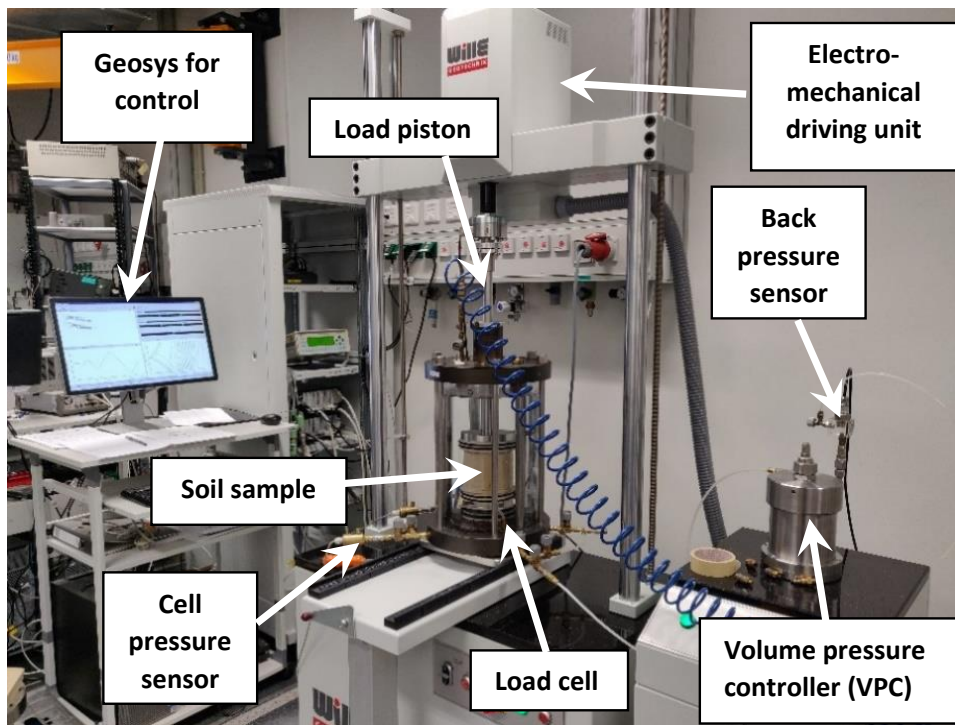
Figure 4.6: Electro-mechanical triaxial device manufactured by *Wille Geotechnik GmbH* used for the various cyclic undrained triaxial tests
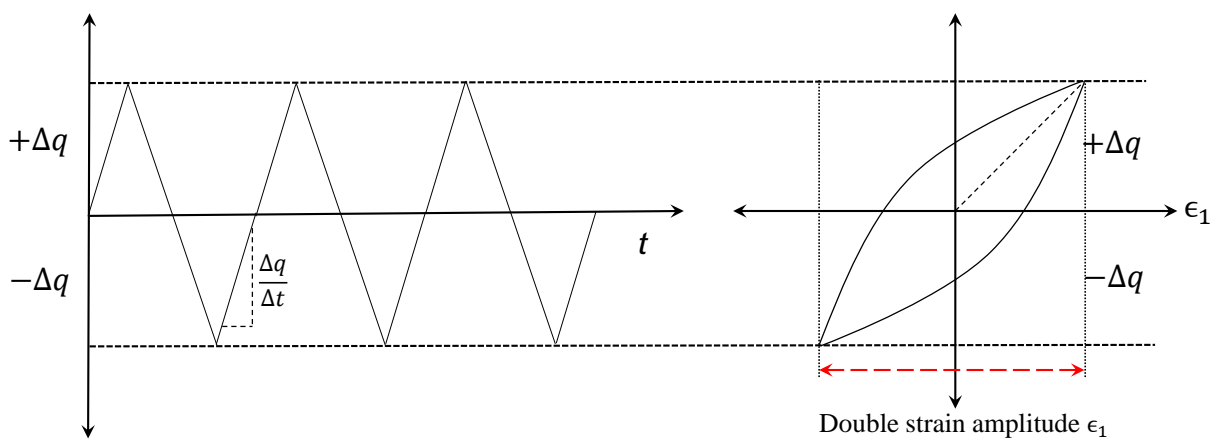
Figure 4.7: Triangular deviatoric loading against time t used for the cyclic tests and typical deviatoric stress - axial strain relationship
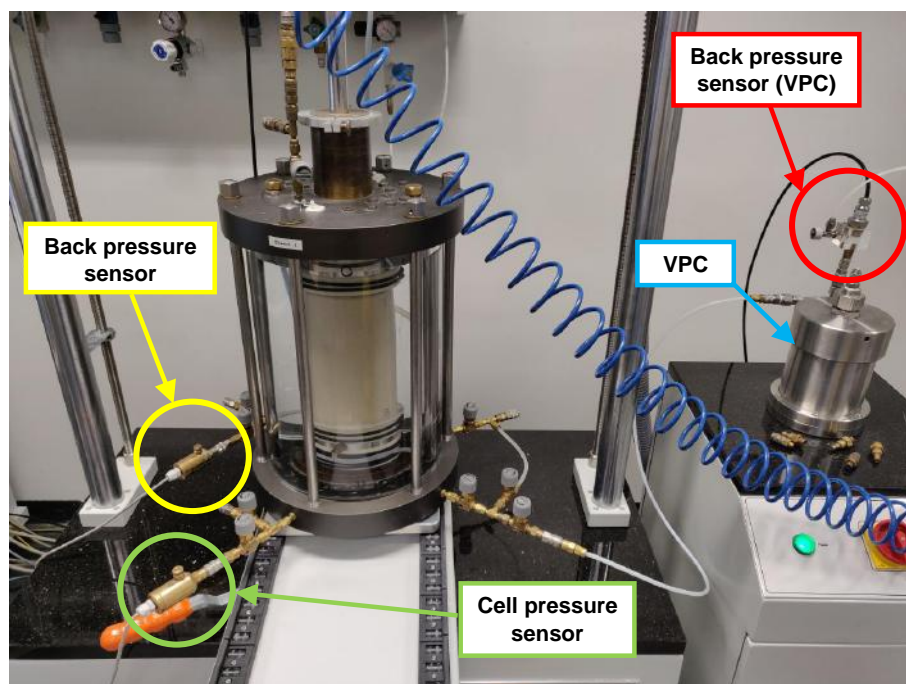
Figure 4.8: Cell and back pressure sensors in the triaxial device used for the various cyclic undrained triaxial tests

iii) Testing procedure in the triaxial tests

Before performing regular tests, calibration was rigorously done on the various sensors/transducers to ensure accuracy of results. The system deformation was quantified in preliminary tests using a steel dummy of 10 cm in diameter and 20 cm in height.

A membrane with thickness of 0.7 mm was used for all the monotonic tests performed in this research. Besides, the usage of a large specimen in combination with granular materials with small mean grain size (d_{50}) minimized the effects of membrane penetration (Baldi & Nova 1984). This was further supplemented by an independent analysis of the effect of membrane penetration and membrane resistance, the values of which were too small to affect the outcome of the test results significantly, so that they were hence not taken into consideration further (further details in Chapter 5). It is noteworthy to mention that end bearing friction was significantly minimized using rigid stainless steel platens with a small (diameter 20 mm) central porous stone, and was therefore deemed negligible to affect the experimental results (Tatsuoka et al. 1986; Omar & Sadrekarimi 2014).

a) Sample preparation

Initially, the split mold was placed on the bottom platen of the triaxial device containing the rubber membrane and fastened with six screws. A vacuum was applied to the mold from the outside to suck the membrane to the inner sides of the mold. Considering that different sample preparation methods (refer to Chapter 2) lead to different soil fabric which subsequently influences soil behavior, air pluviation method was adopted as it best simulates natural deposition of sands. Furthermore, the samples in all subsequent tests in the scope of the present study were prepared using air pluviation to ensure a similar soil fabric in all tests.

After the mold was filled with the material, the excess material in the form of a cone at the top was carefully brushed off using a straight steel scale and carefully collected into a container. Then the top cap of the triaxial cell with the top platen was placed and fastened with the help of two brass screws. A vacuum of 50 kPa was applied inside the specimen through both the top and bottom drainage pipes, the magnitude of which was measured by the back pressure sensor. The vacuum stabilizes the specimen and thereby, enables the removal of the mold. Once the mold is removed, the membrane is checked for any possible leakages which might have arisen from the specimen preparation and mold removal process. This is achieved through closing the bottom and the top drainage paths one by one and checking if the magnitude of vacuum inside the sample stays constant. A steady decrease in the amount of negative pore pressure would imply either a leakage in the membrane or compromised connections at the drainage paths.

If the measured vacuum value stays constant, confirming an intact membrane, one can then proceed with measuring the dimensions of the sample. For determining the diameter, five measurements were made across the height of the specimen, and this process was repeated for another two angles. Therefore, one obtains a total of 15 values for the diameter along the height of the sample considering three different angles. In a similar manner, the height of the sample was determined by measuring the distance between the top of the load piston and the top surface of the triaxial cell. This measurement was previously calibrated using a steel dummy of known height.

Afterwards, the plexiglass cell was mounted and was fixed through the outer ring of the triaxial cell and 6 rods connecting the top and base plates of the triaxial cell. The cell was then filled with water from the bottom slowly, until the specimen was completely submerged. Meanwhile, the linear vertical deformation transducer (LVDT) was mounted to the axial load piston to measure vertical deformations during consolidation and shearing.

The cell pressure sensor was then mounted and the cell pressure was increased in steps to 50 kPa along with decreasing the vacuum inside the sample to zero. This ensured that the specimen was always subjected to a constant effective confining stress of 50 kPa.

b) Saturation

One of the major aims of triaxial testing is to ensure a high degree of saturation of the sample. This was done in three steps: the first step involved and replacing the air phase with carbon dioxide (CO_2) which has a higher solubility in water; the second step involved saturation through de-aired and de-ionized water for a longer time (usually 3-4 hours), whereas the third step was back pressure saturation which took place for the longest duration (around 12-14 hours, usually overnight).

CO_2 was supplied through a large saturation tank available in the geotechnical laboratory. The de-ionized water inside the tank was de-aired for 1 hour using CO_2 and later, through vacuum. The flow rate of CO_2 through the dry sample was kept at 1-2 bubbles per second, which was easily verified by placing the outlet into a jar containing water. CO_2 was slowly percolated from the bottom platen of the device under a constant cell pressure of 50 kPa. This process was carried out for a couple of minutes to ensure that CO_2 had replaced all the air at the bottom drainage. Later, the bottom drainage was closed and the top drainage was simultaneously opened for the gas to percolate through the sample. This process took around 1 hour, and after completion, it was assumed that all the air inside the sample was replaced with CO_2.

The second step involved saturation using de-aired and de-ionized water, initially flown steadily from the tank through a connected tube to the bottom platen of the specimen. The bottom drainage was kept open to facilitate passage of the air bubbles from the bottom part out of the sample. The de-aired water occupies the voids replacing the CO_2. This process was continued for around 15-20 minutes till there were no visible air bubbles in the bottom drainage pipe. Then, the top drainage was opened and the bottom drainage closed. The flow of de-aired water through the sample was kept very low (around 1-2 drops per second at the outlet) to ensure a homogenous degree of saturation throughout and in order not to disturb the fabric of the granular material. This process took around 3 hours. Once the desired volume of de-aired water had flown through the sample (approximately around 2 liters), the second step of saturation was considered to be completed.

For the final step of saturation, the exit of the drainage pipes was connected to the burettes of the volume measuring device. After the burettes were filled to the same height of water

as in the saturation tank, the water inflow was closed. The back pressure was then steadily increased along with the cell pressure to 200 kPa and 240 kPa respectively. After a period of 12-14 hours, the saturation of the specimen was checked using Skempton's B-value test, where $B \geq 0.95$ implies a sufficient degree of saturation, which enables to proceed to the consolidation phase.

c) Consolidation

After obtaining an acceptable B-value, the specimens were isotropically consolidated under a target mean effective stress. To guarantee an isotropic stress condition during the increase of cell pressure, an additional vertical load has to be applied via the load piston, because the load piston is rigidly connected to the sample top cap and thus cell pressure is not acting on the cross-sectional area of the load piston. For cyclic triaxial tests, for that purpose the axial piston was fastened to the piston of the load press and the additional load was controlled by the Wille load press, whereas for the monotonic loading tests the additional load had to be applied manually using the wheel of the Wykeham Farrence load press. During this process, the drainage from both ends was opened to allow flow of pore water into the burette of the volume measuring unit. Specimens were allowed to consolidate for 1 hour, while the vertical deformation and volume change were continuously monitored throughout this process. The process of consolidation was deemed complete once the specimen volume remained almost unchanged over a longer period of time. The changes of volume and height during consolidation were recorded and the actual sample dimensions, void ratio and relative density corresponding to the end of consolidation and the start of the shearing phase were determined.

d) After testing

Before commencing a test, the membrane (either new or re-used) must be checked for any possible leakages. For this, a membrane controller consisting of two cylinder platens, an air pressure tube, and two O-ring seals, was used. The procedure was simple: (a) a rubber membrane was installed on two cylinder platens and sealed with the O-rings, (b) a low air pressure was applied inside the membrane, and (c) the entire membrane was immersed in water. If there were any possible leakages, then the air inside the membrane would escape and continuous air bubbles would appear on the surface of the water. If the integrity of the membrane was intact, it could be reused for future tests.

Once the testing was completed (either monotonic or cyclic), the HP-VEE/Geosys program was stopped and the axial loading piston was disconnected from the loading frame. The pressure was reduced and the water inside the plexiglass cylinder was drained off. This was followed by taking off the plexiglass cylinder, disconnecting the top drainage pipe and taking off the top cap along with the platen. The sample was carefully removed and collected in a container, and was oven-dried for 24 hours at a temperature of 105°C for future tests.

4.3.3 Resonant column device

The resonant column device (abbreviated as RC) or measurements with piezoelectric elements are widely used methods in geotechnical laboratories to measure the small and intermediate strain properties of geo-materials. Early studies (Jovicic & Coop 1988; Kuwano & Jardine 2004; Wang & Mok 2008) have extensively used piezoelectric elements mounted in various laboratory devices to measure the shear wave velocity and thus maximum shear modulus at low amplitudes of vibration. In addition, these elements may also be implemented indirectly to determine modulus reduction curves and damping ratio of soils (e.g. Choo et al. 2013).

One of the more popular and standard devices to measure small and intermediate strain properties as defined by ASTM-D4015 (2000) is the resonant column (RC) device. This device is based on the oscillation of a cylindrical sample on one of its three possible vibration modes: the flexural mode (Cascante et al. 1998), normal mode (Saxena & Reddy 1989) and torsional mode, whichever is applied to determine the resonant frequency of the sample.

Out of all the three modes of vibration, the torsional resonant column device is the most common one. The first mention of this type of device may be encountered in Iida (1937) to evaluate the influence of water content on wave velocity. Since then, the device has gone through significant modifications and improvements in the last few decades (e.g. Hardin & Black 1966; Hardin & Drnevich 1972a; Hardin & Drnevich 1972b; Stokoe et al. 1999) to study small strain properties of soils.

There are two types of torsional RC device: free-free and fixed-free. In the free-free RC device, the actuator is mounted on the top or bottom of the sample whereas the other end is free in rotation. Usage of this type of RC device may be found in the works of Drnevich and Stokoe. The free-free RC device at Ruhr-Universität Bochum was designed so that the polar mass moment of inertia of the bottom part (J_0) measures about 17.2

Figure 4.9: The Resonant Column device at Ruhr-Universität Bochum

times the polar mass moment of inertia of the top part (J_L). This device (refer Fig. 4.9) has previously been used in the works of Wichtmann (2005) and Goudarzy (2015) by employing the relationships developed based on the free-free boundary conditions. COnsidering these boundary conditions the shear modulus G is obtained through the expressions given below (Eqs. 4.1 and 4.2):

$$a \tan(a) - \frac{J^2}{J_0 \cdot J_L} \frac{\tan(a)}{a} = \frac{J}{J_0} + \frac{J}{J_L} \tag{4.1}$$

$$G = \left(\frac{2\pi L f_r}{a} \right)^2 \cdot \rho \tag{4.2}$$

where a is defined as $\omega L / v_s$ with ω being the rotational frequency and v_s the shear wave velocity. J_0 and J_L are the polar mass moments of inertia of the bottom and top parts respectively, J is the polar mass moment of inertia of the sample, ρ is the sample density, f_r is the resonant frequency and L is the height of the sample. The equations for the fixed-free condition are obtained by setting J_0 to infinity in Eq. (4.1). Then Eq. (4.1) reduces to Eq. (4.3):

$$a\tan(a) = \frac{J}{J_L} \tag{4.3}$$

The top part of the Bochum RC device includes two mini-shakers for applying a rotational excitation at the top of the sample. Two transducers (accelerometers) were mounted on the weight accelerated by the mini-shakers, while two more accelerometers are mounted on the top part itself. The signals of one accelerometer on the mini-shaker and one on the top part are monitored at an oscilloscope. The excitation frequency is varied until the resonant frequency of the system composed of the sample and the two end masses is found. At the resonant frequency, the phase difference between the signals received from the acceleration transducers mounted on the mini-shakers (corresponding to applied force) and the top part (after double integration corresponding to displacement) must be $\pi/2$.

To guarantee accuracy of the results, the values of J_L, J_0 and J must be determined accurately. The bottom part of the device and the sample have a cylindrical shape with a given density and dimensions, which enables to calculate J_0 and J using geometric relations. However, the top part has a complex shape compounded by electrical equipment, cables and holes, which makes the determination of J_L more challenging. Experimental methods are therefore used to determine J_L. The procedure using an aluminium sample is explained in detail in Goudarzy (2015), and therefore, not repeated herein. The final value of J_L was determined to be 0.0647 kg·m^2.

Newly-designed RC device to include axial mode of vibration

As described in the previous section, the most common resonant column technique is based on torsional oscillations of a cylindrical specimen to measure its resonant frequency. Two other modes of vibration are possible: the flexural and axial or longitudinal modes (see Fig. 4.10b and c). The newly developed device introduced herein has been additionally designed for the axial or longitudinal mode of vibration. In this device the bottom of the specimen is fixed, whereas the top part is free in vibration. The axial vibration is applied on the top of the specimen, thereby representing fixed-free boundary conditions (Fig. 4.10a). This device includes three main parts, which are surrounded by a plexiglass cell. These parts are: (i) driving system, (ii) specimen, and (iii) volume change measurement elements.
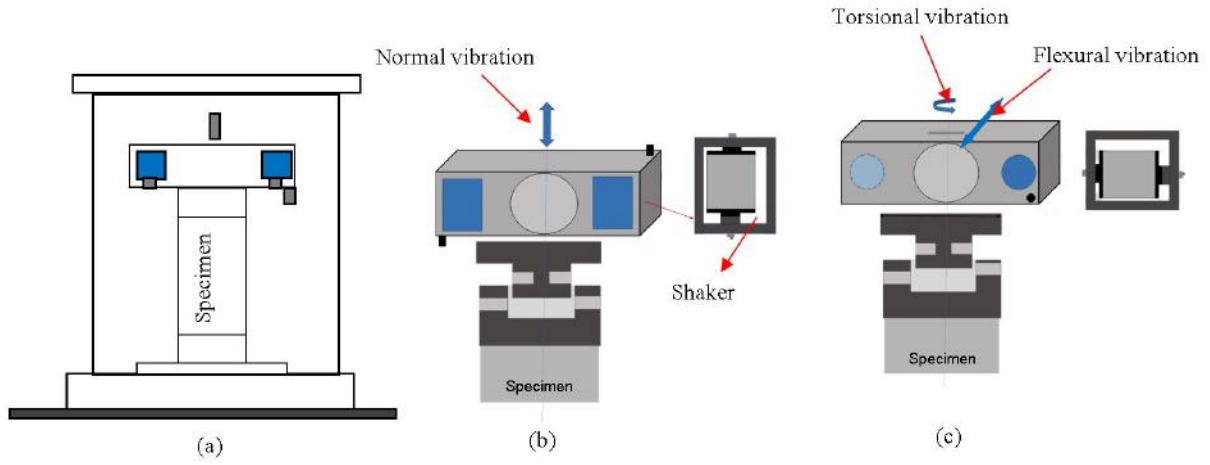
Figure 4.10: (a) Newly designed resonant column device for different modes of vibration under isotropic and anisotropic loading, (b) normal mode, and (c) flexural and torsional mode of vibrations
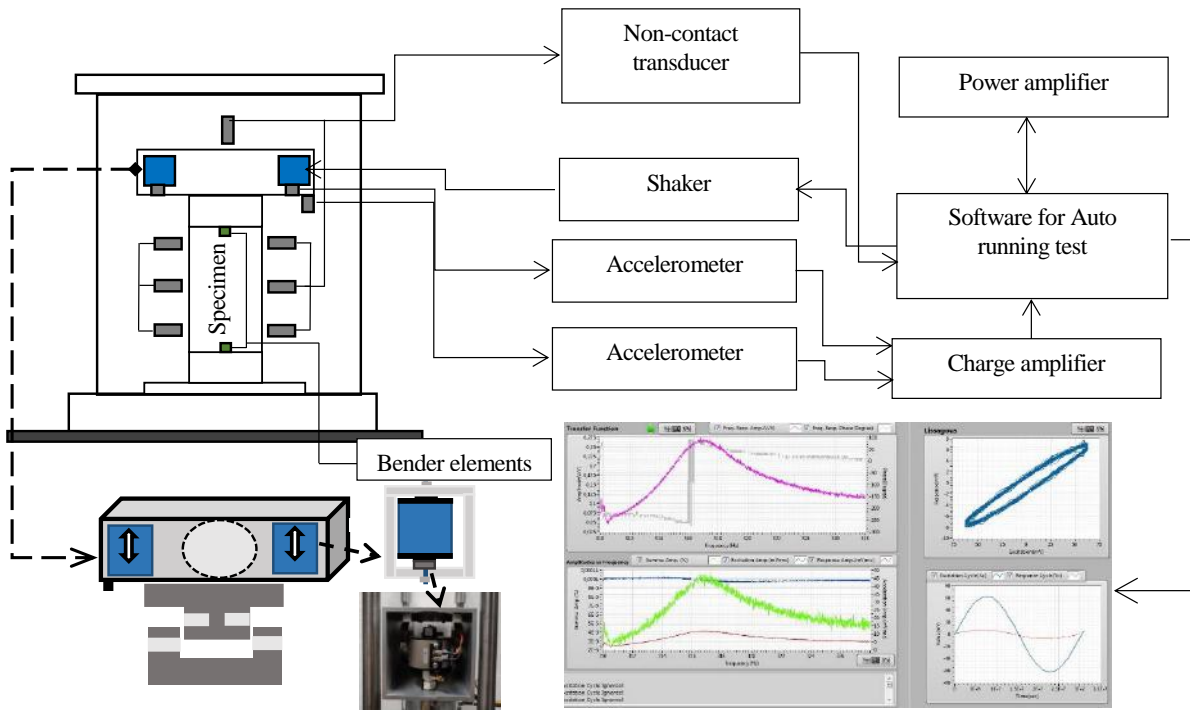
Figure 4.11: Schematic diagram of the newly designed device for axial/compression/normal mode of vibration

i) Driving system

In this device, the top and bottom caps of the specimen are designed so that piezoelectric elements can be easily placed in them, thus providing additionally the possibility of performing RC tests and shear or compression wave velocity measurements simultaneously (Fig. 4.12).

Figure 4.12: The top and bottom caps of the specimen with a piezoelectric compression element installed

The vibration source (driving system), is an electromagnetic device capable of applying a sinusoidal axial vibration and/or torsional vibration to the active end platen to which it is rigidly coupled (Figs. 4.10b and 4.10c). The driving system is composed of a cubic aluminum mass, which includes two mini-shakers for applying vibration and also two accelerometers to record displacement signals (the driving system is called actuator hereafter). The adopted mini-shakers are of the electrodynamic type with a permanent field magnet. A coil is flexibly suspended in the field of the permanent magnet. An alternating current signal is passed through the coil to produce a vibration. Two accelerometers were also mounted on the shaker (Excitation signal) and at the corner of the actuator (Received signal) for visualization of signals (see Fig. 4.11). In the following the signals are abbreviated as Exc. and Rec. respectively. These accelerometers are used to detect the applied force through the shaker using Exc., and displacement of the actuator during vibration using Rec. The frequency of excitation is adjustable and controlled using the prepared software in $LabVIEW$. A sinusoidal current is applied with a means of adjusting the frequency over the entire range of operating frequencies. This instrument provides

sufficient power to produce the required vibration amplitude. In addition, the output signals from the transducers may be electronically amplified to assist in the visualization of the signals. The strain amplitude measurements shall only be made at the resonant frequencies. Thus, for a given current applied to the excitation device, the Rec. outputs recorded at the resonant frequency give sufficient information to calculate strain amplitude, stiffness, and damping ratio. To increase or decrease strain amplitude, the current to the vibration excitation device must be increased or decreased. After making a change in current applied to the vibration excitation device, the procedure is followed to find the corresponding resonant frequency and record signals at the resonant frequency.

ii) Specimen

The size of the specimens that can be tested in the axial mode of vibration ranges between 70/150 mm and 150/300 mm (diameter/height). The specimen is prepared outside the device and after preparation, transferred into the cell. According to Drnevich (1978), the largest particle contained within the specimen shall be smaller than 1/10 of the specimen diameter for specimens having a diameter smaller than 70 mm, and smaller than 1/6 of the specimen diameter for larger specimen diameters (Drnevich 1978).

iii) Measurements of volume change

To make the system completely free in vibration, the volume change of the specimen is monitored using 7 non-contact displacement transducers, which are mounted around the specimen. Six non-contact displacement transducers along the sides detect changes in the diameter while the one at the top detects the vertical settlement of the specimen due to the increase of cell pressure or during the increase of vibration amplitude (see Fig. 4.11).

iv) Calculation of the elastic modulus E, axial strain ϵ_1 and damping ratio D

a) Elastic modulus, E

In the axial resonant column technique, a column of material is excited longitudinally in one of its normal modes, and the wave velocity is determined from the frequency at resonance and from the dimensions of the specimen. For axial vibration, displacement is zero at the fixed end, but at the free end a force is exerted on the rod which is equal to

the inertia force of the concentrated mass (see Richart et al. 1970 for details). This force can be expressed as:

$$F = \frac{\delta u}{\delta x} AE = -m \frac{\delta^2 u}{\delta t^2} \tag{4.4}$$

where, m is the mass of the specimen, A is cross-sectional area, E is Young's modulus, F is the applied force and u is the vertical displacement in the vertical direction x. To calculate E, Eq. 4.5 is generally employed (after Richart et al. 1970):

$$\alpha \tan(\alpha) = \frac{m}{M_L} \tag{4.5a}$$

$$E = \rho v_L^2 = \rho \left(\frac{L \omega_n}{\alpha} \right)^2 = \rho \left(\frac{2\pi f_r}{\alpha} \right)^2 \tag{4.5b}$$

where ρ denotes the density of the sample, L the sample height, m and M_L the mass of the specimen and the bottom part of the device, v_L the longitudinal wave velocity, $\alpha = \frac{\omega_n L}{v_L}$ (with $\omega_n = 2\pi f_r$ being the rotational frequency), and f_r denotes the resonant frequency.

b) Vertical strain, ε_1

As has been described by Drnevich (1978), the average strain amplitude, ε_1, for longitudinal motion can be calculated by:

$$\varepsilon_1 = SF \cdot \frac{\lambda \cdot RMS}{L} \tag{4.6}$$

where λ is the longitudinal motion transducer calibration factor for the transducer used in establishing resonance, $RMS=$ longitudinal transducer output, $SF =$ strain factor and $L =$ specimen length.

c) Damping ratio, D

By recording two signals from shakers, acceleration corresponding to force (excitation signal, abbreviated as Exc. Signal) and displacement (received signal, abbreviated as Rec. Signal) as functions of time and visualizing them at the oscilloscope, damping ratio can be estimated using three different methods: a. Bandwidth method, b. Free vibration decay curve and c. Lissajous figure or energy method.

i) Bandwidth method (BW)

This method is accurate for materials with low damping ratio or to measure damping ratio at small strain levels since for higher strain levels the accuracy of this method decreases significantly (Stokoe et al. 1999). In this method, longitudinal transducer output RMS of Rec. Signal is drawn against the frequency. The peak point in the RMS-frequency curve corresponds to the resonant frequency, f_r. f_1 and f_2 are the frequencies, where the RMS is equal to $1/\sqrt{2}$ of maximum RMS, where $f=f_r$. Damping ratio can be estimated using the following relationship:

$$D = \frac{f_2 - f_1}{2f_r} \qquad (4.7)$$

ii) Free vibration decay method (FVD)

The process by which the amplitude of vibration steadily diminishes with time is called damping; hence, this can also be utilized to estimate damping ratio. In the free vibration decay curve, after hitting resonant frequency during the sweep time (the time in which the excitation frequency is varied to find the resonant frequency and determine damping), the input power of the exciters is suddenly disconnected and the received signal Rec. is recorded. The recorded signal is used to determine the damping ratio using Eq. 4.8 (Richart et al. 1970):

$$Z = \frac{1}{N} \ln \left(\frac{x_0}{x_{N+0}} \right) \qquad (4.8)$$

where x_0 and x_{N+0} are the amplitudes of two cycles, with N being the number of cycles between the two analyzed ones. The material damping ratio D can be obtained using Eq. 4.9:

$$D = \left[\frac{Z^2}{4\pi^2 + Z^2} \right]^{1/2} \qquad (4.9)$$

iii) Energy method

Here, the damping ratio is determined using the hysteresis loops after application of a cycle of vibration. Damping ratio is defined as the ratio of the dissipated energy in one cycle of loading (ΔW) over 4π times of the total energy (W). If the Rec. Signal is drawn

with respect to the Exc. Signal, this generates the a Lissajous figure (refer Fig. 4.11). This loop will be vertical at resonant frequency, because the phase difference between Exc. signal and Rec. signal is $\pi/2$ at resonant frequency. Signals from Exc. and Rec. during RC experiments are converted to force and displacement, using the corresponding calibration or convert factors. Doing so, the Lissajous Figure will be displayed in the space of displacement (U) versus force (F). The area of the loop in $F - U$ space is equal to the dissipated energy ΔW. The total energy W is calculated as the area of the triangle below the central axis of the hysteresis loop in the stress-strain space (Wichtmann et al. 2001). This method is affected by noises at low strain levels, because the values of peak amplitude from accelerometers are used directly in the equations. These outputs are susceptible to be affected by noises when the amplitude of vibration is lower than the amplitude of noises. Therefore, this method may not be accurate for low amplitudes of vibration (strain less than 10^{-6}), but the accuracy of this method increases significantly with increasing vibration amplitudes.

As also reported by Stokoe et al. (1999), for measurements at small strains ($<10^{-5}$), background noise can have a more adverse effect on the free vibration decay curve than on the frequency response or bandwidth method. However, at large strains, the assumptions in the derivation of equations in the bandwidth method will not be valid, and a serious error in the measurement of damping ratio can be encountered. As long as the amplitude of noises is larger than the amplitude of vibration, the D obtained from free vibration decay and energy methods might be affected by noises.

4.4 Calibration and validation of the adopted devices

4.4.1 Calibration and validation of triaxial device

4.4.1.1 Monotonic triaxial device

Before starting extensive testing, the results obtained by the triaxial device used for monotonic testing were checked by repeating an experiment already documented in Rahemi (2017). The test was carried out on clean Hostun sand (material properties are listed in Chapter 3) with the same boundary conditions as outlined in Rahemi (2017). The sample of height 20 cm and diameter 10 cm was prepared and was saturated using a back pressure of 200 kPa, leading to a B-value higher than 0.95. The test was carried out on a relatively dense sample (relative density $I_D = 76\%$ in Rahemi 2017 and $I_D = 78.1\%$ in the current

experiment) under an effective confining stress of 300 kPa. The shearing was continued till an axial strain of about 16% as in Rahemi (2017). The only major point of difference was in the sample preparation method where Rahemi (2017) used moist tamping method, whereas air pluviation was applied for the control experiment. Further details about the testing procedure were already discussed in the previous chapter.

(a)   (b)
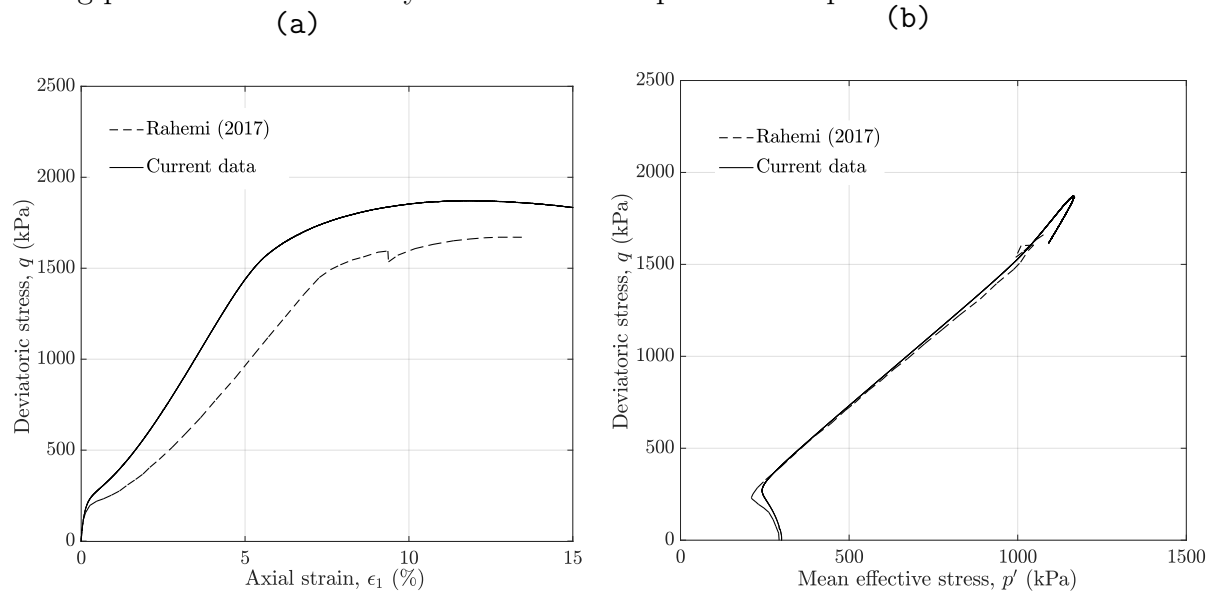
Figure 4.13: Comparison of the (a) $q - \epsilon_1$, and (b) $q - p'$ data for clean Hostun sand measured in a test of the current research with a previous test of Rahemi (2017); the slight differences may be attributed to the different sample preparation methods employed, while the slope of the steady state line remains the same

The $q - p'$ and $q - \epsilon_1$ curves for both the tests are shown in Fig. 4.13. Clearly, there is a relatively good match between the two results, in particular with respect to the effective stress paths. The difference in the $q - \epsilon_1$ relationships noticed after an axial strain of 0.31% can probably be mainly attributed to the different sample preparation methods, which is well known to affect the stress-strain and volume change response of soils. Vaid et al. (1999) showed that at identical initial void ratio and effective stress state, samples prepared through moist tamping may be potentially liquefiable, while the response of but the water deposited samples may even be dilative. The samples prepared by air pluviation lay in between these two extremities. Also, the compressibility of the samples prepared by moist tamping were higher than in case of the other two methods. The results in Fig. 4.13a show a similar trend to the results of Vaid et al. (1999). In addition, Sadrekarimi & Olson (2011) stated that various sample preparation techniques do not influence the steady state of soils, further elaborating that "at critical state the initial sand structure has been largely destroyed". This implies that at the steady state, all the samples are

expected to reach a similar fabric irrespective of the initial fabric generated by the chosen sample preparation method. Therefore, the slope of the steady state line (SSL) prepared by both method remains the same, which is evident from Fig. 4.13b.

4.4.1.2 Cyclic triaxial device

To assess the quality and reliability of the own cyclic triaxial tests, the results were compared with published data. For this purpose, the cyclic tests with isotropic consolidation and stress cycles performed on Karlsruhe fine sand (Wichtmann 2016) were selected. The Karlsruhe fine sand, also referred to as KFS sand, is a fine-grained semi-angular sand with a very small percentage of fines. The grain size distribution of the sand is shown in Fig. 4.14. The fines (grains with size smaller than 0.063 mm) were initially washed out prior to testing, thus any possible migration of fines into the porous discs was avoided. The uniformity coefficient C_u and the mean grain size d_{50} were found to be 1.48 and 0.16 mm respectively. It should be noted that the d_{50} of the KFS sand tested in the present thesis was slightly higher than that reported by Wichtmann (2016), possibly resulting from using a different batch of the sand. The specific gravity of the sand following DIN-18124 (2011) was 2.65, whereas the e_{max} and e_{min} (DIN-18126 1996) values were 1.054 and 0.677 respectively.

Following preparation by air pluviation and flushing of the sample with CO_2, three stages of saturation using de-aired and de-ionized water were employed: under the influence of gravity, under a back and cell pressure of 200 and 240 kPa respectively, and under a back and cell pressure of 400 and 440 kPa respectively to achieve a very high degree of saturation. Once in the final phase of saturation, the sample was allowed to rest for a certain time to allow any remaining air bubbles to dissolve completely. Therefore, the B values measured were above 0.99 in all the tests on KFS. The tests were carried out under cell and back pressures of 700 and 500 kPa respectively ($p_0' = 200$ kPa) with different amplitudes, similar to the studies of Wichtmann (2016).

Influence of various end restraints on the cyclic undrained behavior of KFS

There are two possible configurations of the end plates in triaxial testing: The first one uses porous discs covering the whole cross-sectional area of the top and bottom end plate. Using this configuration effects of friction between the soil sample and the porous plates are accepted. This configuration is adventageous for saturation of fine-grained soils or granular soils with fines. In the second configuration a small central porous stone is used

Figure 4.14: Comparison of the grain size distribution curves of the Karlsruhe fine sand (KFS) used for the purpose of validation along with that used in Wichtmann (2016)

in combination with smeared end plates. In this case lubrication and a membrane at the end platens are used to reduce end friction. The reduction of end friction is of particular importance when testing samples with a height-to-diameter ratio of 1.

ASTM-D4767 (11) and ASTM-D7181 (20) do not specify the size of the porous disc for consolidated undrained or drained monotonic testing of soils respectively. For cyclic tests, ASTM-D5311/D5311M-13 (2013) demands the porous disks to be equal in diameter to the specimen. German standards for consolidated triaxial compression tests on soils (DIN-EN17892-9 2018) and cyclic tests on unbounded mixtures (DIN-EN13286-7 2004) also recommend to chose the diameter of the porous discs to be similar to sample diameter. However, no reason for such specific choice of diameter is provided. Naturally, the question arises to what degree the size of the porous discs might play a role in the cyclic undrained behavior of sands under otherwise similar conditions. Till now, there has been no investigation of this issue, leading to an uncertainty in the choice of the porous disc to be used for cyclic testing programs.

In the present study, two different densities (Scenario 1: $I_D\%$ ranging between $63.6-67.9\%$ and Scenario 2: I_D around 27%) with a cyclic stress ratio (CSR=$q^{ampl}/2p'_0$) of 0.15 were

tested, and the number of cycles to initial liquefaction (defined as the numbers of cycles N_c required to reach $p' = 0$ kPa) were compared. It should be mentioned that the studies of Wichtmann (2016) were performed on 1:1 samples ($D = 100$ mm, $H = 100$ mm, $H/D = 1$) with a loading rate of 0.05 mm/min. Unless otherwise specified, the tests of the present study were performed on 2:1 specimens ($D = 100$ mm, $H = 200$ mm, $H/D = 2$). To obtain a similar strain rate, the new tests were performed with a displacement rate of 0.1 mm/min. Two different sizes of porous stones were used for Scenario 1: a small porous stone with a diameter of 2 cm and a large one with a diameter of 10 cm equal to the specimen diameter. The end plates with the two different porous stones can be seen in Fig. 4.15. For the tests with Scenario 2, only the small porous stone was used. In case of the small porous stone end platens were smeared with a medium viscous lubricant, followed by application of a membrane of 0.4 mm thickness on both ends. Air bubbles were carefully squeezed out to ensure a good degree of saturation. In some additional tests filter papers were laid on the large porous disks to prevent any fines to penetrate. Furthermore, the influence of the thickness of membrane was varied to study its influence.
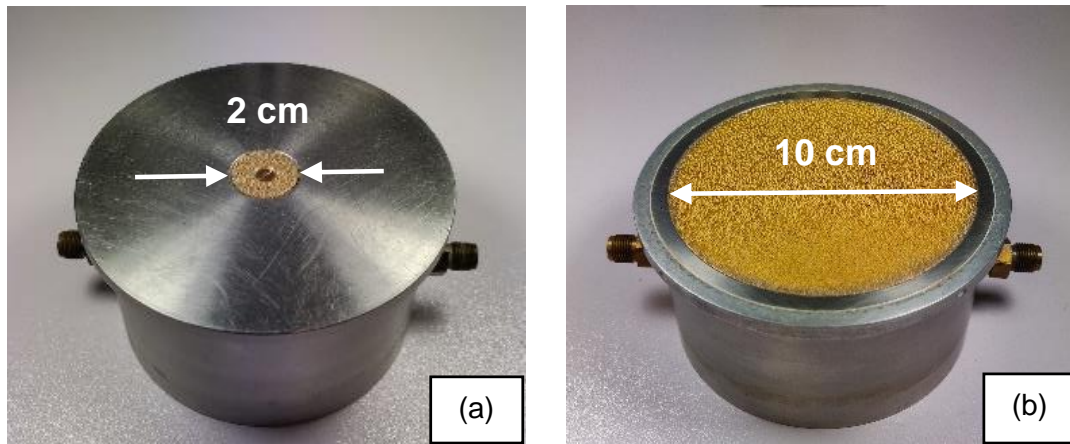
Figure 4.15: The two porous stones of different diameters tested in the present case: (a) small porous stone with a diameter of 2 cm, and (b) large porous stone with a diameter of 10 cm

(i) Observations - Scenario 1: $p'_0 = 200$ kPa, CSR $= 0.15$

The influences of the size of the porous disc, usage of filter papers or smeared end platens, sample size and thickness of the membrane were tested only on specimens with I_D ranging between 63.6% and 67.9%, corresponding to the first scenario in the present study. The details of the tests are listed in Table 4.2.

Table 4.2: Tests performed to assess the influence of various boundary conditions on the cyclic undrained response of KFS sand

Case	Size of porous disc	Restraint	I_D (%)	Membrane thickness	H/D
I	Small	Smeared end platens	63.6	0.7 mm	2
I-S	Small	Smeared end platens	64.2	0.7 mm	1
I-M	Small	Smeared end platens	66.7	0.4 mm	2
II	Small	Filter paper	66.0	0.7 mm	2
III	Large	-	66.1	0.7 mm	2
IV	Large	Filter paper	67.9	0.7 mm	2

a) Influence of sample size ratio

A 1:1 sample (Case I-S) with the same dimensions as in Wichtmann (2016) was reproduced for the purpose of comparison. The small porous disc along with smeared end platens, a membrane of thickness 0.7 mm and a small filter paper above the porous disc was used. The rate of loading was 0.05 mm/min similar to Wichtmann (2016) on their 1:1 sample. As evident in Fig. 4.16 from the $q - p'$ and $q - \epsilon_1$ curves, a good agreement between the new test data and the results reported by Wichtmann (2016) (marked as TCUI7, Fig. 4.16a, b) can be concluded. Both experiments show a cyclic mobility after initial liquefaction, characterized by butterfly-shaped effective stress paths and the increase of the strain amplitude with each further cycle. While the sample of Wichtmann (2016) was found to liquefy at the end of the 11th cycle (Fig. 4.16a and b), the present sample liquefied at the end of the 16th cycle (Fig. 4.16c and d). The slightly higher number of cycles may be attributed to the small variations in the grain size distribution between the two sets of KFS, where the present KFS is slightly coarser as previously noted in Fig. 4.14. A slower build-up of pore water pressure resulting in larger number of cycles to initial liquefaction under otherwise similar conditions with increasing mean grain size has been also reported by other researchers (Wong et al. 1975; Lade & Hernandez 1977; Martin et al. 1978; Choobbasti et al. 2014).

To compare the influence of two different sample size ratios keeping same diameter, a 2:1 specimen (referred to as Case I) was tested and compared with the reference test on the 1:1 sample, i.e. case I-S. Fig. 4.17 shows a comparison between the two cases. To reach initial liquefaction, the 1:1 sample took 16 cycles, whereas 18 cycles were needed in case of the 2:1 sample. The difference is negligible as far as the number of cycles is concerned.
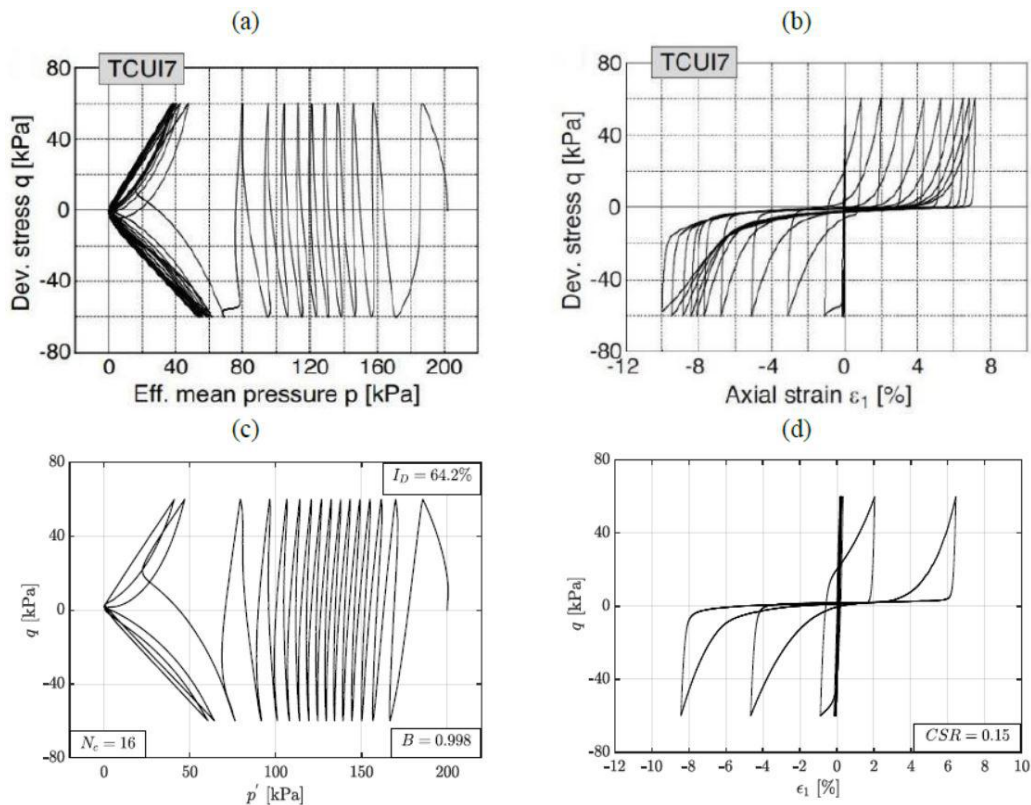
Figure 4.16: (a) $q-p^{'}$ and (b) $q-\epsilon_1$ response of a medium dense ($I_D = 67\%$) sample as reported in Wichtmann (2016), (c) $q - p^{'}$ and (b) $q - \epsilon_1$ response of the 1:1 sample tested under similar conditions (Case I-S)

In fact, the $q-p^{'}$ path is largely similar at the beginning of the test, where the decrease in $p^{'}$ for the 1:1 sample is slightly faster than in case of the 2:1 sample. Also, after reaching initial liquefaction, the axial strains for the 1:1 sample develop comparatively faster than for the 2:1 sample (see Fig. 4.17b).

b) Influence of membrane thickness

To assess the influence of membrane thickness, a test was performed on a specimen with membrane of 0.4 mm thickness (case I-M). The smaller porous disc was used in combination with smeared end platens similar to the reference case. Fig. 4.18 shows the $q - p^{'}$ and $q - \epsilon_1$ curves of the test I-M, while Fig. 4.19 compares the two cases, where it can be observed that the sample with the thinner membrane undergoes initial liquefaction at 20 cycles, 2 more than in the reference case.
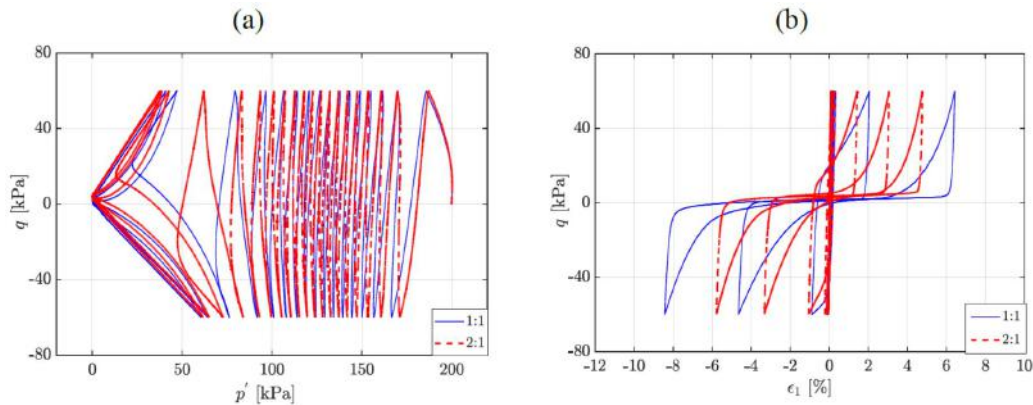
Figure 4.17: Comparison of (a) $q - p'$ and (b) $q - \epsilon_1$ response of 1:1 and 2:1 samples tested under similar conditions (case I-S)
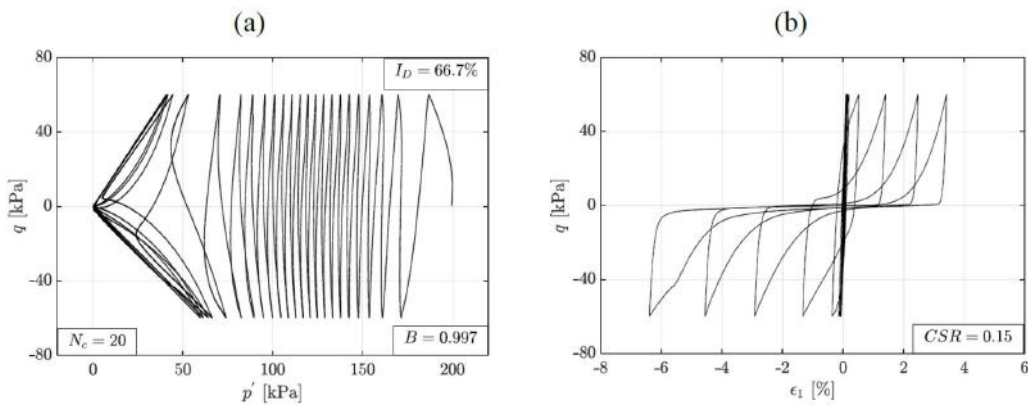
Figure 4.18: (a) $q - p'$ and (b) $q - \epsilon_1$ responses of KFS with smeared end platens and with a membrane thickness of 0.4 mm (case I-M)

It is known that the effects of membrane penetration are relatively larger when using thinner membranes since they press more easily into the voids between individual grains at the sample boundary during an increase in the effective lateral stress, σ_3' (Baldi & Nova 1984; Omar & Sadrekarimi 2014; Wichtmann 2005). Thus, during application of cyclic loading, the liquefaction resistance of samples with thinner membranes is expected to increase due to the delay of pore water pressure build-up caused by membrane penetration. This results in a slower decrease in p' till initial liquefaction is achieved. The present set of results shows a similar trend (refer Fig. 4.19). However, for fine-grained sands as the tested KFS the membrane penetration effects can be regarded as almost negligible for practical purposes.
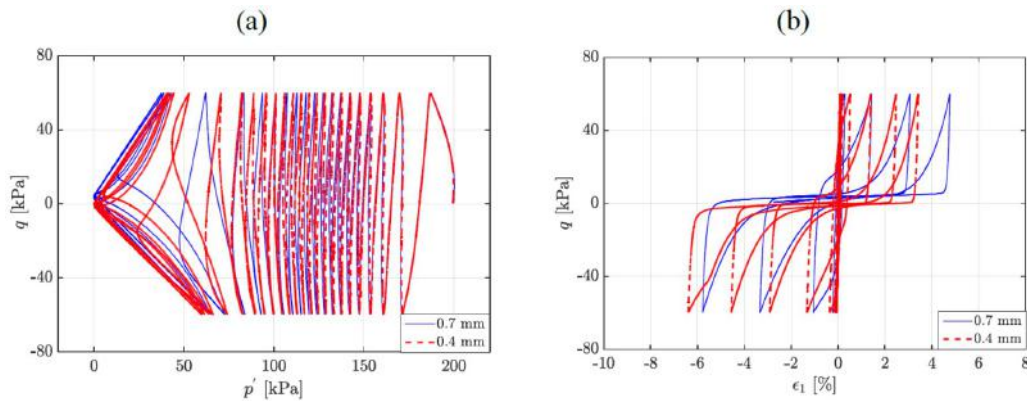
Figure 4.19: Comparison between the test results with small porous discs using two different membranes (cases I and I-M): (a) $q - p'$ and (b) $q - \epsilon_1$ responses

c) Influence of roughness of the end platens

To compare the influence of differing roughness of the end platens, the two different diameters of porous discs shown in Fig. 4.15 were used - one with a diameter of 2 cm and the other with a diameter of 10 cm. For the purpose of comparison, the standard 2:1 samples were used. Furthermore, three subcases were studied as discussed below.

1) Using the smaller porous discs without smearing of the end plates, but with a filter paper covering the end platens (case II)

In this case, the small porous stone was used without smearing the end plates. Instead, a standard filter paper was introduced between the sand and the end platens. Therefore, the sand was not in direct contact with the end platens, but with the filter paper sandwiched between them. The $q - p'$ and $q - \epsilon_1$ curves from this test are shown in Fig. 4.20. The total number of cycles to reach initial liquefaction is 16, which is 2 cycles less than in case of the reference sample (case I with 2:1 sample, small porous disc and smeared end plates).

Fig. 4.21 facilitates a direct comparison between the reference sample and case II. As can be seen from Fig. 4.21a, the evolution in the $q - p'$ path for the first cycle under both boundary conditions mirrors each other. For the intermediate cycles, the sample in case I showed slightly more resistance, which resulted in a relatively slower decrease of p'. In the post-initial liquefaction regime, the increase of axial strain with increasing number of cycles is similar for both cases. Evidently, there seems to be a minimal difference between the application of smeared end platens and a filter paper covering the entire end platens.
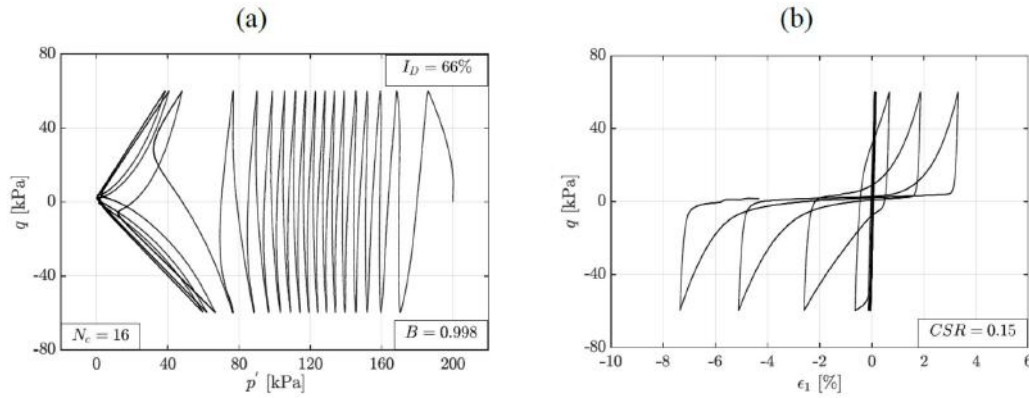
Figure 4.20: (a) $q - p^{'}$ and (b) $q - \epsilon_1$ responses of a 2:1 KFS sample using a small porous disc with filter paper over the end platens (case II)
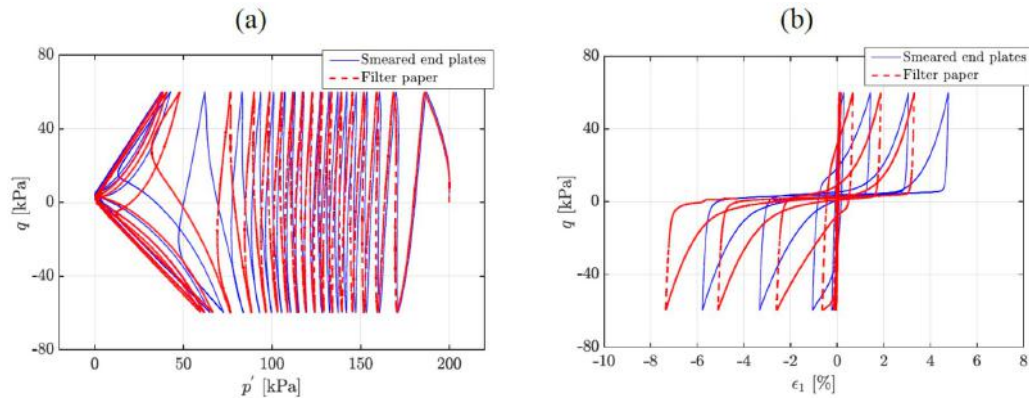
Figure 4.21: Comparison between the test results with a filter paper and smeared end platens (cases I and II): (a) $q - p^{'}$ and (b) $q - \epsilon_1$ responses

2) Using the larger porous discs without filter paper (case III)

Here, the porous disc was changed to a larger size (diameter of 10 cm, shown previously in Fig. 4.15b). Owing to the large size of the disc, using smeared end platens was not feasible, which is why the sand was pluviated directly into the mold thereby ensuring direct contact between the sand and the underlying disc. As the fines were washed out previously, migration of the smaller grains into the porous discs and subsequently into the drainage pipes was not encountered in the tests. The rest of the procedure was similar as in the case of the smaller porous disc. However, from the test results as seen in Fig. 4.22, the number of cycles till initial liquefaction in the case of a large porous disc was significantly higher than in the previous cases, with the sample needing 39 cycles to reach $p^{'} = 0$ kPa.
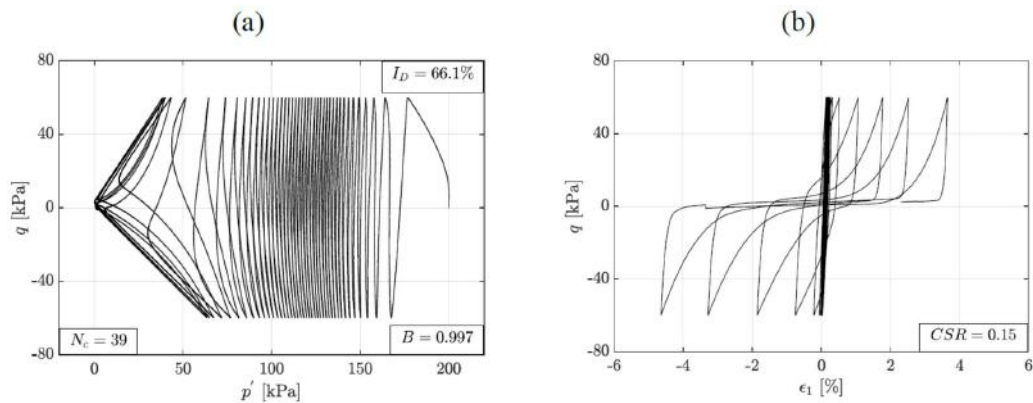
Figure 4.22: (a) $q - p'$ and (b) $q - \epsilon_1$ responses of 2:1 KFS sample using the large porous disc (case III)

The reason is clear - a direct contact between the sample and the porous disc is responsible for increasing friction at the interface, therefore, causing significantly increased resistance to liquefaction by obstructing the build-up of pore water pressure. This is significantly more prominent after the first cycle has been applied. The subsequent cycles show a slower build-up of pore water pressure, leading to a comparatively larger number of cycles to initial liquefaction.
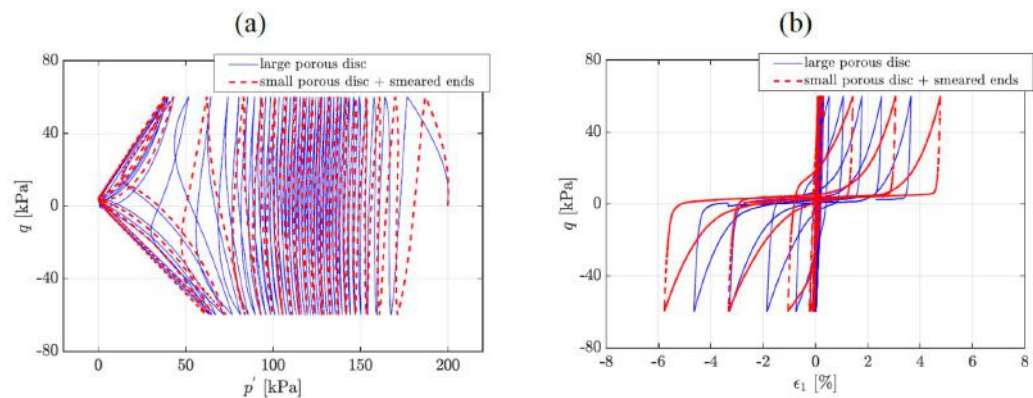
Figure 4.23: Comparison between the test results for the two different porous discs (cases I and III): (a) $q - p'$ and (b) $q - \epsilon_1$ responses

To enable a comparison between the results for the two different sizes of porous disc, Fig. 4.23 shows the overlapped $q - p'$ and $q - \epsilon_1$ curves obtained for the two cases I and III. At first glance, the large magnitude of reduction in p' for case III during the first half-cycle is evident, where it goes down to 170 kPa against 179 kPa in case I. However, subsequently, owing to mobilization of the frictional forces in subsequent cycles, the decrease in p' is

hindered which is strongly characterized by the ever-decreasing rates of p' reduction for subsequent cycles before initial liquefaction, while in case I the decrease in p' for subsequent cycles is more or less equal. From the $q - \epsilon_1$ curve in Fig. 4.23b one can conclude that after initial liquefaction, the axial strains induced by subsequent cycles are relatively smaller for case III compared to case I.

3) Using the larger porous discs with filter paper (case IV)

Two filter papers were used in between to prevent direct contact between the sand and the porous disc. The results are displayed in Fig. 4.24. The number of cycles to initiate initial liquefaction was 30, which is still significantly higher than in case of the tests with the smaller porous disc, but lower than for the larger porous discs without filter papers. It seems that preventing direct contact between the rough porous discs and the sand actually results in a reduced end friction, which in turn causes a slight reduction of the liquefaction resistance.
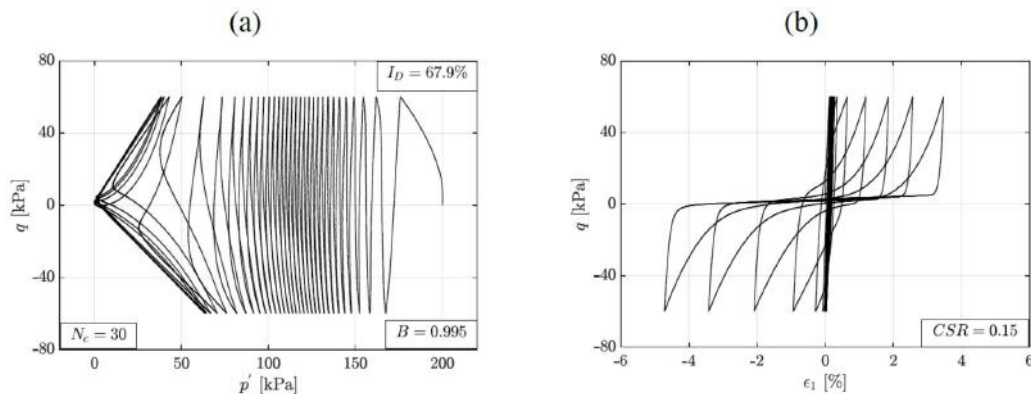
Figure 4.24: (a) $q - p'$ and (b) $q - \epsilon_1$ responses of 2:1 KFS sample using the large porous disc with a filter paper separating the sand from the disc (case IV)

To further illustrate this, a direct comparison between the reference case and the case with a large porous disc with filter papers (cases I and IV) is performed in the $q - p'$ and $q - \epsilon_1$ space in Fig. 4.25. Clearly, a similar observation as noted in the previous sub-section is evident. The first half-cycle in case IV is similar to case III, where the sample shows a strong tendency to contract resulting in a faster increase of the pore water pressure, thereby causing a significant reduction in the p', whereas the decrease in p' in the first half-cycle was much smaller in the reference case I. In contrast, in all subsequent cycles the rates of pore water pressure build-up were much smaller in case IV compared to case

I. In a similar fashion, the deformations post initial liquefaction developed at a lower rate for case IV. Using a filter paper preventing direct contact between the sand and the disc helps in reducing the friction, however, friction is still larger than in the case of smeared end plates, leading to a reduction in p' with increasing number of cycles which is comparatively slower than in the reference case.
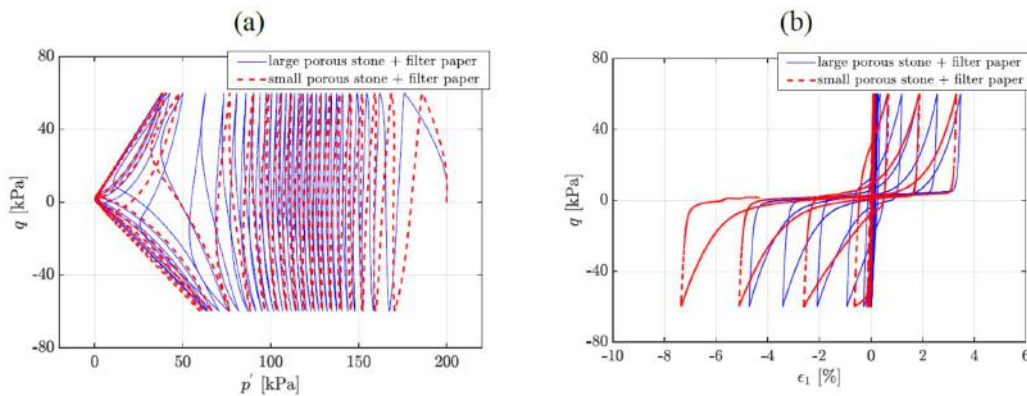
Figure 4.25: Comparison between the test results for the two different porous discs (cases I and IV): (a) $q - p'$ and (b) $q - \epsilon_1$ responses

To summarize, the total numbers of cycles required to initiate initial liquefaction for the various cases discussed are listed in Table 4.3. As mentioned previously, various standards (ASTM or DIN) have only suggested using a filter disc equal in diameter to the sample, but the reasoning behind that is unclear. As clearly pointed out in this study, such large porous discs may result in an underestimation of the actual liquefaction susceptibility of clean sands, which may lead to erroneous geotechnical designs of sub/superstructures under earthquake conditions. Therefore, it is suggested to resort to cyclic liquefaction testing of clean sands with a smaller porous disc so as not to over-estimate the liquefaction resistance of soils in future. In addition, reporting the size of the disc is recommended for future calibration and replicability of test results.

Therefore, owing to the larger frictional component yielded through the end platens with a larger porous stone, all tests in this research were performed using the smaller porous stone and smeared end plates. For the purpose of validation of the device, a second test on a loose specimen with a relative density I_D=27% was performed and the results were compared with Wichtmann (2016).

Table 4.3: Comparison of the number of cycles (N_c) to initial liquefaction (defined at $p'{=}0$ kPa) for the various cases tested presently

Case	N_c
I	18
I-S	16
I-M	20
II	16
III	39
IV	30

(ii) Observations - Scenario 2: $p'_0 = 200$ kPa, CSR = 0.075

Fig. 4.26 shows the $q - p'$ and $q - \epsilon_1$ curves from the present experiment along with the curves from Wichtmann (2016) (marked as TCUI1). Quite similar effective stress paths and stress-strain relationships for both experiments can be concluded. The loose sample did not show the formation of butterfly-shaped loops in the effective stress paths, since the axial strain ϵ_1 exceeded the chosen failure criterion of 10% in a single cycle after initial liquefaction. For reaching initial liquefaction, the specimen in Wichtmann (2016) ($I_D = 30\%$) required 72 cycles. The present specimen, with a post-consolidation relative density of 27.1% took 71 cycles to liquefy showing that the results yielded by the adopted device are in good agreement with those reported by Wichtmann (2016).

4.4.2 Calibration and validation of RC device

4.4.2.1 Torsional mode of vibration

The calibration and validation of the RC device for the torsional mode of vibration was performed using different aluminum specimens (AL) of varying diameters (2, 4 and 6 cm) and a height of 30 cm. Three methods were followed to determine the resonant frequency of samples. In the first method, the AL samples were mounted in the RC device, and the resonant frequency was determined. In the second method (so called theoretical method), an approximation was made for the stiffness of AL samples (considered as 25 GPa) and the actual stiffness was determined using Eqs. 4.1 and 4.2. In the third approach, finite element simulations were used to determine the resonant frequency of the samples. Further details of these three approaches may be found in Goudarzy (2015), and are not subsequently discussed.
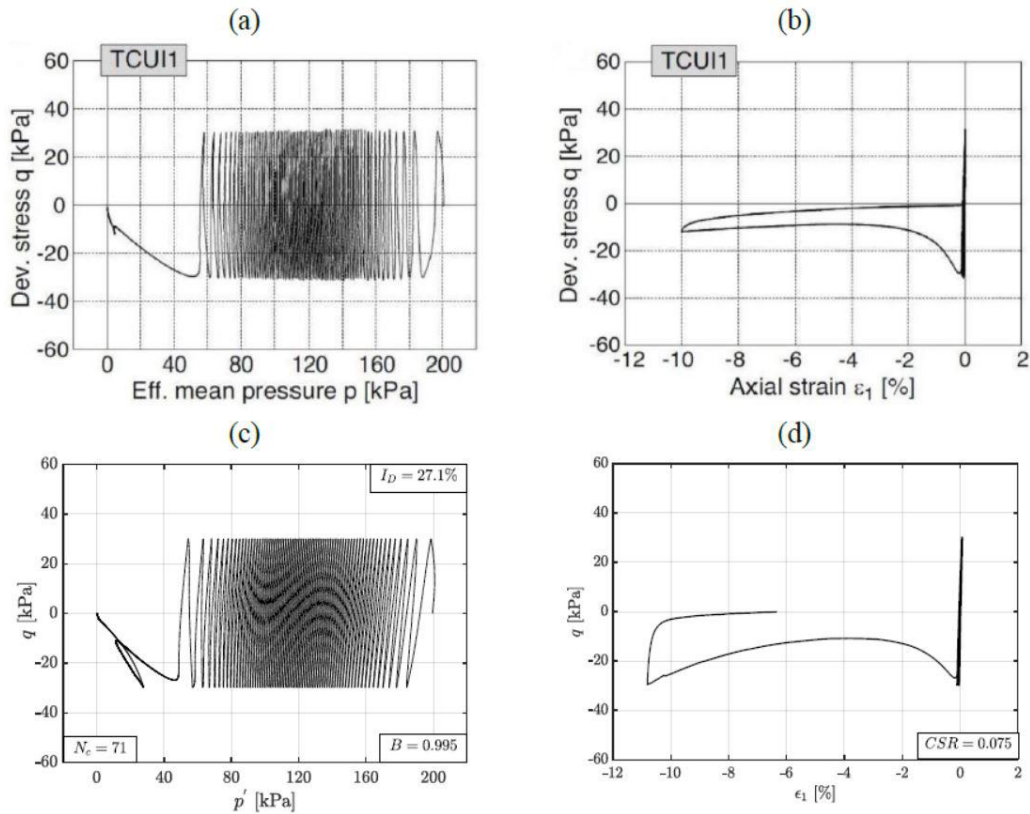
Figure 4.26: Comparison of the $q - p'$ and $q - \epsilon_1$ curves of the tests of (a, b) Wichtmann (2016) with (c, d) the present study

4.4.2.2 Axial mode of vibration

i) Validation with an aluminum sample

An aluminum specimen with 2 cm in diameter and 30 cm in height was used to control the performance of the resonant column device for the axial mode of vibration. The aluminum specimen was mounted in the RC device and the resonant frequency and consequently the stiffness were determined under cell pressures of 0, 50, 100, 200, 300 and 400 kPa (Fig. 4.27). As can be seen in Figs. 4.28a and 4.28b, the resonant frequency for a cell pressure of 0 kPa was about 608 Hz and then it slightly decreased with increasing cell pressure till 100 kPa, which could be due to the compliance of contacts between the aluminum specimen and top and bottom platens. Furthermore, considering the slenderness of the sample, the results might be affected by the flexural mode of vibration, i.e. bending of the specimen during axial vibration, due to the shape of the actuator and the size of the specimen. However, the resonant frequency remains almost constant with further increase

of cell pressure. The total mass of the actuator and top cap, M_L, for the tests on the aluminum sample is about 4.35 kg, which can be used to estimate stiffness from Eqs. 4.5. Figure 4.28b shows the resulting stiffness of the aluminum specimen, E, as a function of cell pressure. As Fig. 4.28b shows, the estimated E for the tested aluminum specimen is about 63.80 GPa which matches well with previous experimental results (Lambe & Whitman 1979; Cascante et al. 1998; Kumar & Madhusudhan 2011).
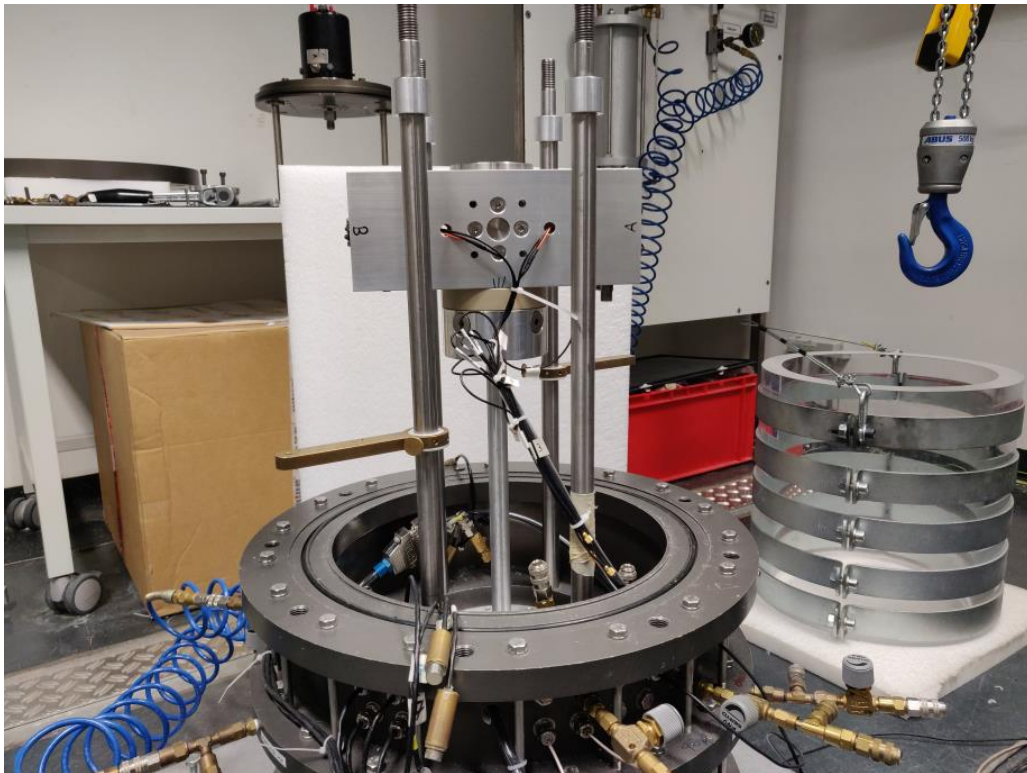
Figure 4.27: RC device with aluminium specimen and top part including the shakers

Damping of aluminum is very small, approximately zero, thus measured damping for the aluminum specimen is related to the dissipation of energy in the device (damping of the device). The same aluminum specimen was used to determine the damping of the device. The bandwidth method was adopted to estimate the damping ratio for the vertical mode of vibration. The current of 30 mV was applied as an amplitude to the shakers and consequently to the actuator, while varying the excitation frequency. Fig. 4.29a shows the amplitude ratio (receiver / excitation signal) versus frequency curve from this experiment. The peak amplitude is observed at the resonant frequency, $f_r = 608$ Hz. The normalized amplitude at this point is 0.62. The frequencies of f_1 and f_2 in Eq. 4.7 (Richart et al. 1970) are frequencies at an amplitude amounting 70.7% of the peak, which is 0.44 in
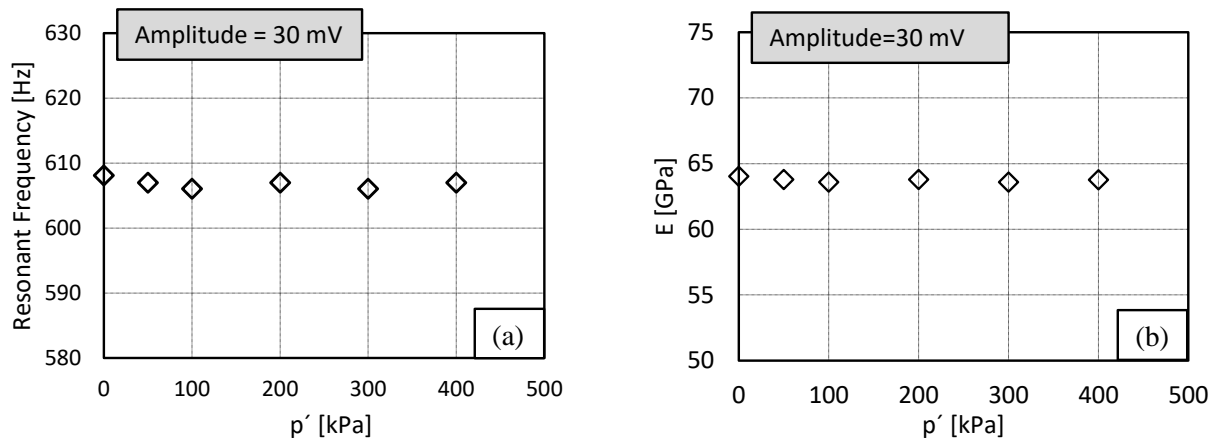
Figure 4.28: Effect of cell pressure on a) the resonant frequency and b) the stiffness, E of the adopted aluminum specimen

this experiment. Therefore, by getting f_r, f_1, and f_2 from this figure damping D can be calculated, which is equal to 0.0098. Fig. 4.29b shows the effect of cell pressure on the amplitude ratio-frequency curves for the adopted aluminum specimen. As can be seen, the effect of cell pressure on the resonant frequency, f_1, f_2 and consequently damping ratio (D) can be neglected.
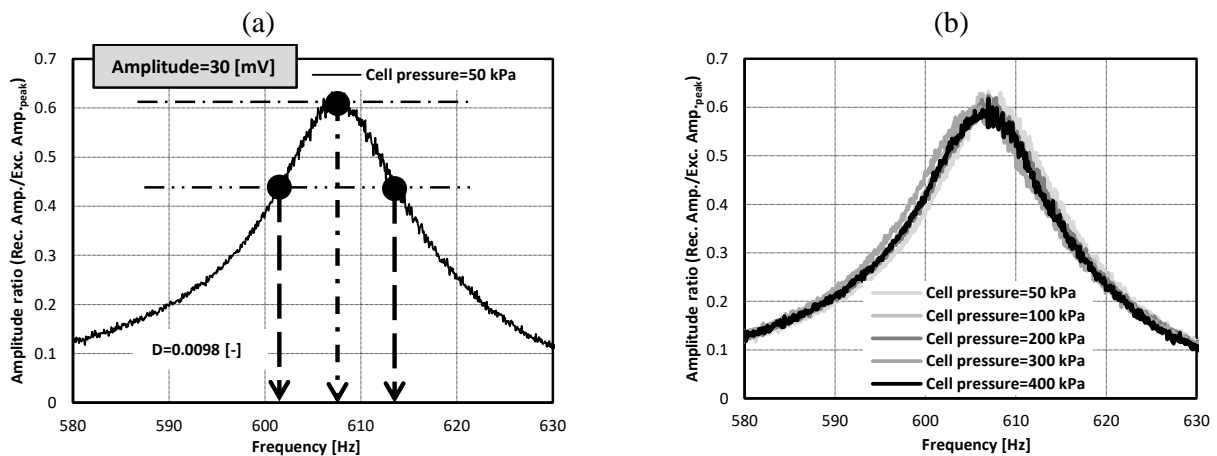
Figure 4.29: a) Bandwidth method to estimate damping ratio and resonant frequency from a test on the aluminum sample; b) the effect of cell pressure on the amplitude-frequency curves

Figure 4.30 shows the effect of the vibration amplitude on the measured damping ratio for the AL specimen. At very small strain ranges corresponding to a low vibration amplitude, the damping ratio is higher than at intermediate strain levels. This could be due to the effect of noises and near field conditions. However, this effect decreases with increasing the vibration amplitude to 300 mV and will not change with further increase in the vibration
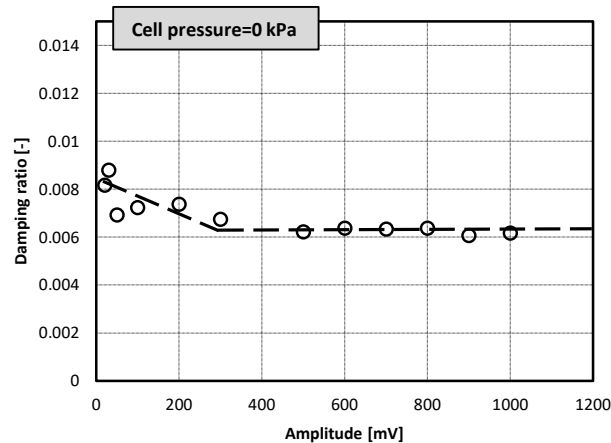
Figure 4.30: The effect of the amplitude of vibration on the estimated damping ratio for aluminum specimen

amplitude. According to the observed results, two calibration lines can be defined for the measured damping ratio using the adopted device (Figure 4.30).

ii) Validation with experiments on crushed and round glass beads

The crushed and round glass beads having a $C_u = 5$ were used in the experiments to validate the device for the axial mode of vibration.

a) Experimental procedure

Specimens with diameter and height of 10 and 20 cm respectively were prepared using air pluviation method. A vacuum of 50 kPa was applied to the sample through the bottom platen to stabilize it during the assembling of the RC device (Figure 4.12b). The prepared specimen was subsequently installed inside of the RC cell. Afterwards the actuator was attached firmly to the top platen and all non-contact transducers were mounted to measure the volume change of the specimen during experiments. After that, the plexiglass cylinder was placed, the top cap of the RC device was mounted and fixed to its base by eight rods, and cell pressure was increased to 50 kPa while vacuum was reduced to 0 kPa step by step keeping a constant effective pressure of 50 kPa on the specimen. RC experiments were conducted after consolidation of specimen for the target cell pressure.

The frequency was altered between a minimum and maximum value in a predefined domain in the prepared software $LabVIEW$. The amplitude of vibration was changed by changing the frequency. It is to be noted that the mass of top cap and actuator, M_L, for

experiments on soil specimens is 5.229 kg. The recorded data (amplitude ratio - frequency) are used to determine f_r, axial strain corresponding to f_r, and D. Fig. 4.11 shows an example of the recorded data for a specimen of crushed glass with a relative density of 56% under isotropic stresses of 100 and 400 kPa respectively. The frequency corresponding to the peak amplitude is the f_r and the D can be calculated using the bandwidth method or other aforementioned methods.

b) Validation with piezoelectric compression elements

The first validation was done using piezoelectric compression elements that were installed in the resonant column device. Compression wave velocity measurements were conducted on the same sample before performing axial RC tests. A sinusoidal wave with a frequency of 10 kHz was sent from the compression element in the bottom cap (sender), and the signal was received by the compression element in the top cap (receiver) being aligned in the same orientation. The first arrival or deflection method was adopted to detect the travel time, t_p (e.g. Yamashita et al. 2009). The height h of the sample and t_p are used to calculate the compression wave velocity of the sample as $v_p = h/t_p$. To ensure reliability of results, regular calibration and validation of the adopted compression elements were done with aluminum samples before performing the tests, which is documented in detail in Goudarzy et al. (2016).

Compression modulus (M) was measured using compression elements, whereas the shear modulus (G) was obtained using the torsional mode of excitation in the RC device (Goudarzy & Wichtmann 2019). The Young's modulus (E) was calculated from both quantities using:

$$E = \frac{G\,(3M - 4G)}{M - G} \tag{4.10}$$

c) Validation with drained cyclic triaxial tests

Drained triaxial tests with high-cyclic loading were carried out on dense and medium dense samples additionally to determine the small-strain Young's modulus E_{max} for the two materials under isotropic effective stresses of 100 and 200 kPa. The specimens were prepared through air pluviation with the same dimensions as in the resonant column device. After saturation following the procedure described in Section 4.3.2, consolidation under the target effective stress values followed. Load cycles with a rather small deviatoric
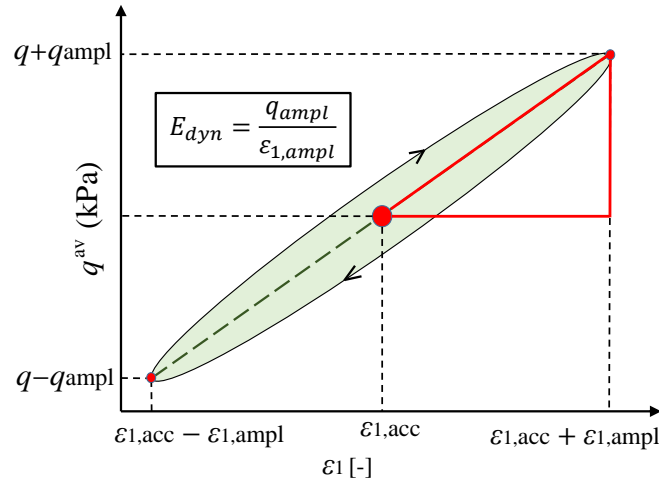
Figure 4.31: Stress-strain loop under drained cyclic loading. q_{ampl} and $\varepsilon_{1,ampl}$ denote the deviatoric stress and axial strain amplitudes during a cycle of loading. E_{dyn} represents the dynamic elastic modulus, q^{av} and $\varepsilon_{1,acc}$ denote the average value of deviator stress (zero under initial isotropic conditions before commencing cyclic loading) and accumulated axial strain respectively.

stress amplitude of 10 kPa under a frequency of 1 Hz were then applied till 100000 cycles were reached. The vertical deformation and volume changes were measured continuously throughout the application of cyclic loading. From the data recorded using HP-VEE software, the stress-strain loops were obtained at the end of 1, 100, 1000, 10000 and 100000 cycles (100 points for each cycle), and the E_{max} was subsequently calculated from the slope of the stress-strain curves (refer to Fig. 4.31, denoted as E_{dyn} there). For the crushed glass, the vertical strain amplitudes ($>10^{-5}$) were considerably larger than for the glass beads, therefore, it was not possible to compare the results with the RC data, where the measured strains were lower than 10^{-5}.

Fig. 4.32 shows the results from the different devices in terms of E_{max} versus void ratio, where a good agreement between the measured E_{max} values using the adopted devices is evident, for both tested materials and both levels of effective stress.

The variation of the maximum Young's modulus with increasing confining pressure and void ratio derived from the RC tests in the axial mode of vibration is shown for both materials in Fig. 4.33. The diagrams reveal the well-known decrease of modulus with increasing void ratio and the increase with increasing mean effective stress. Two curves of type $kf(e)$, where the void ratio function $f(e)$ is either from Eq. 2.22 (Hardin) or Eq. 2.24 (Jamiolkowski) and k is a fitting parameter, have been fitted to the experimental
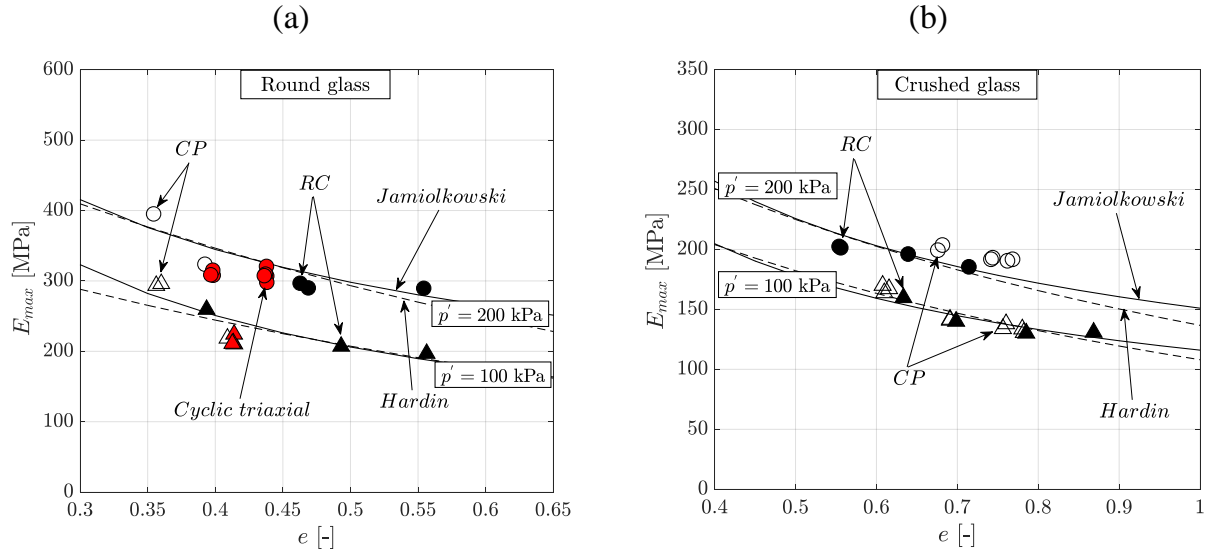
Figure 4.32: Small-strain Young's modulus E_{max} for specimens containing a) round glass particles or b) crushed glass particles using either the RC device in the axial mode of vibration, or compression elements (CP) or drained cyclic triaxial tests. The dashed and solid lines represent the void ratio functions of Hardin & Black (1966) and Jamiolkowski et al. (1991) respectively.

data to get the maximum R^2. Table 4.4 shows the values of c and d in Eqs. 2.22 or 2.24 respectively.

Table 4.4: Summary of the fitting parameters of Eqs. 2.22 and 2.24 to characterize E_{max}

Crushed glass					Round glass				
p' [kPa]	k_i	d_i			p' [kPa]	k_i	d_i		
50	82	0.63			50	62	1.05		
100	116	0.62			100	112	0.88		
200	151	0.58			200	190	0.65		
400	220	0.50			400	225	0.80		
		d	n	A			d	n	A
Average		**0.58**	**0.43**	**113.67**	**Average**		**0.85**	**0.46**	**155.10**

E_{max} was normalized with respect to $f(e)$, where $f(e)$ was taken from Eq. 2.24 and the averaged value from Table 4.4 was considered for d. The normalized E_{max} is drawn with respect to the normalized mean effective stress p'/p_a, with atmospheric pressure p_a=100 kPa, in Figs. 4.34a and 4.34b. The parameters A and n in Eq. 2.21 were determined using power regression of the data shown in Fig. 4.34. Table 4.4 summarizes the fitting parameters of Eq. 2.21 for specimens of round and crushed glass particles. As evident, parameters d, A, and n for round glass particles are higher than those for the crushed
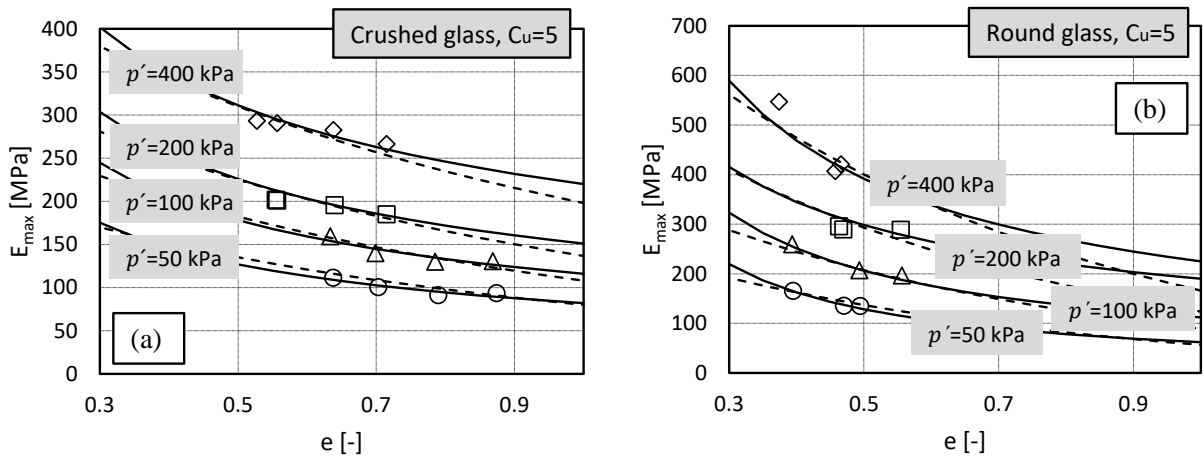
Figure 4.33: The effect of void ratio and mean effective stress on maximum Young's modulus, E_{max} of: a) specimens containing crushed glass and b) specimens containing round glass particles. Solid lines denote $kf(e)$ curves, where $f(e)$ is from Eq. 2.24, and dashed lines are $kf(e)$ curves, where $f(e)$ is from Eq. 2.22

particles. Considering the same grain size distribution, this difference can be attributed to the particle shape.
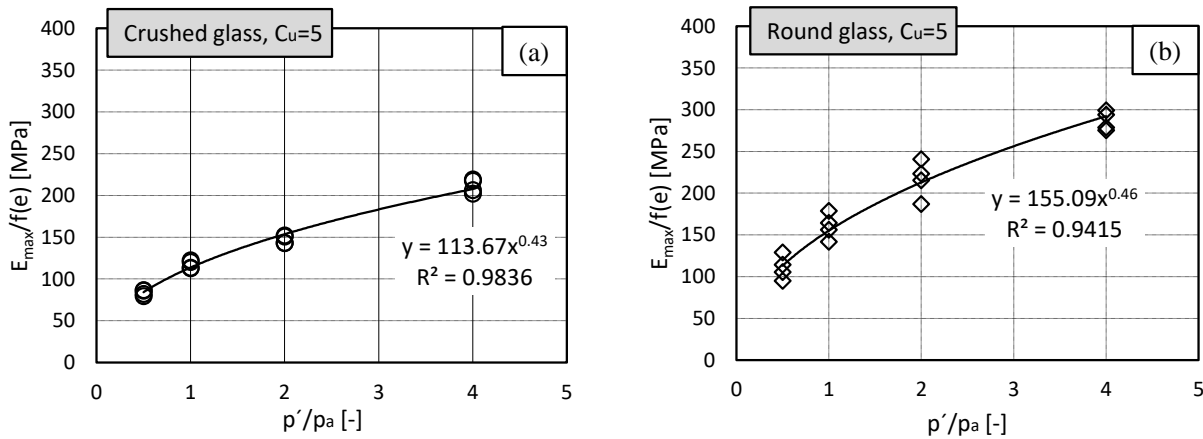
Figure 4.34: Normalized E_{max} with respect to the normalized p': a) specimens containing crushed glass and b) specimens containing round glass particles

d) Intermediate strain properties $E(\epsilon)$ and $D(\epsilon)$

RC experiments were conducted to assess the axial dynamic characteristics of the adopted round and crushed glass particles at small to intermediate strain levels. The experiments were performed on samples of dry materials having different relative densities and the

sweep time was 5 sec, which will apply around 200-300 cycles on the specimen. The excitation amplitude was successively increased. The modulus for each strain amplitude was calculated using Eq. 4.5 and the strain level was estimated using Eq. 4.6.

i) Effect of grain shape

The effect of the shape of the particles on $E/E_{max} - \epsilon_1$ and $D - \epsilon_1$ curves is analyzed based on Figs. 4.35 and 4.36. Fig. 4.35a shows that the $E/E_{max} - \epsilon$ curves of specimens containing crushed glass particles are located slightly above those of the specimens containing round glass particles. Furthermore, the strain level at which the modulus starts to decrease in round glass specimens is less than the corresponding value for crushed glass. Fig. 4.35b presents the E/E_{max} values at three different strain levels, 5×10^{-6}, 5×10^{-5}, and 1×10^{-4} versus the shape factor ρ, which is 0.45 for the crushed glass and 0.90 for the round glass beads. For each strain level, E/E_{max} for round glass is less than for crushed glass.

Fig. 4.36a shows that the damping ratio for the axial mode of vibration is lower for the specimens containing crushed glass particles than for the specimens composed of round glass particles. Fig. 4.36b plots the damping ratio for three different strain levels, 5×10^{-6}, 5×10^{-5}, and 1×10^{-4} versus the shape factor. For each strain level, damping ratio in the specimen containing round glass is found higher than in the specimen of crushed glass.
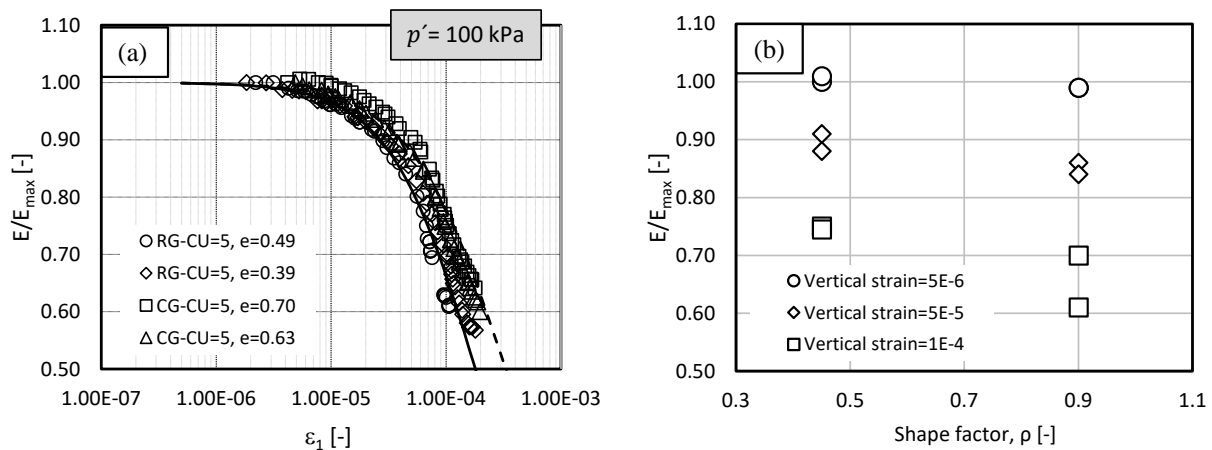
Figure 4.35: a) Effect of shape of particles on $E/E_{max} - \epsilon_1$ curves and b) E/E_{max} versus regularity factor ρ - the average of roundness and circle-ratio sphericity, for three different strain levels
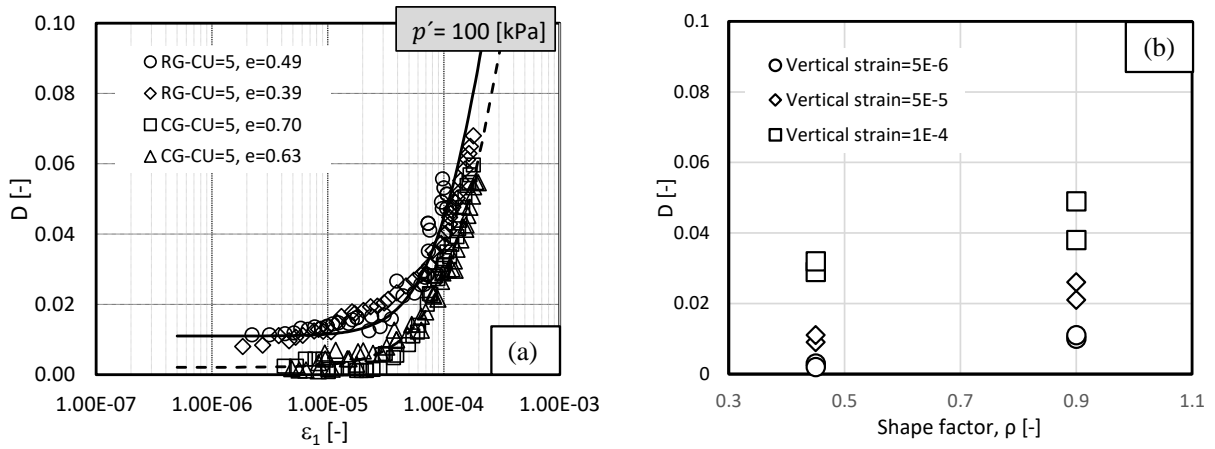
Figure 4.36: a) Effect of shape of particles on $D - \epsilon_1$ curves, and b) D versus regularity factor ρ for three different strain levels

ii) Effect of density and mean effective stress

The experiments were designed to assess the effect of vertical strain level, density, and mean effective stress on the axial dynamic characteristics of the adopted materials. Fig. 4.37 shows the effect of the density on the $E - \epsilon_1$ curves of the crushed glass specimens subjected to 100 kPa (Fig. 4.37a) and 400 kPa (Fig. 4.37b) mean effective stress. As expected, modulus decreases with increasing void ratio and increases with increasing pressure. The data also show the significant decrease of E with increasing vertical strain amplitude at strains $\epsilon > 10^{-5}$. Fig. 4.38a presents the normalized modulus E/E_{max} with respect to the vertical strain, ϵ, in the specimens containing crushed glass particles subjected to 100 and 400 kPa cell pressure. These data demonstrate that the $E/E_{max} - \epsilon_1$ curves are independent of the density of the specimen, while showing a significant effect of the isotropic stress on $E/E_{max} - \epsilon$ curves. Evidently, the modulus degradation is faster for lower pressures. The effect of density and mean effective stress on damping ratio is also shown in Fig. 4.38b. As can be seen, the damping ratio is also independent of the density of the specimen while it decreases significantly with increasing mean effective stress. Interestingly the minimum damping ratio is almost independent of the mean effective stress. The same tendencies were also observed for the specimens containing round glass particles. As can be seen in Fig. 4.39a and 4.39b, the experimental data confirm the significant effect of the vertical strain and the negligible effect of the density.

Similar to Eq. 2.30 describing the variation of G/G_{max} against γ, Eq. 4.11 is employed to capture the variation of E/E_{max} against axial strain ϵ_1:
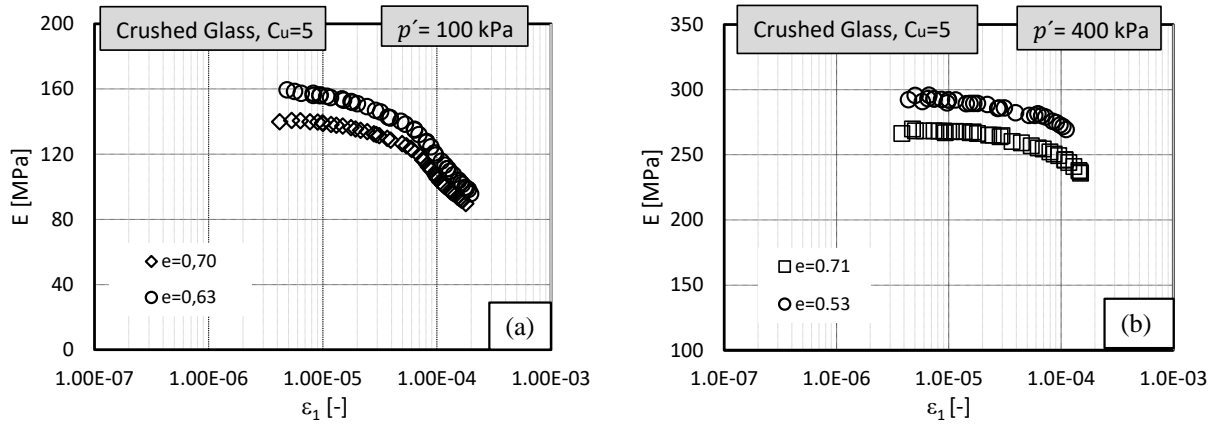
Figure 4.37: Young's modulus E versus axial strain ϵ_1 for the specimens containing crushed glass particles of different densities and subjected to the mean effective stress of: a) 100 kPa and b) 400 kPa

$$\frac{E}{E_{max}} = \frac{1}{1 + \left(\frac{\epsilon_1}{\epsilon_r}\right)^\alpha} \tag{4.11}$$

ϵ_r denotes the reference axial strain which corresponds to the value of the axial strain at $E/E_{max} = 0.50$, where as α is a fitting parameter. The solid and dashed lines in Figure 4.35a show the fitted curves in form of Eq. 4.11. The fitting parameters of the equation are shown in Table 4.4. The results show the significant effect of the mean effective stress on the reference vertical strain.

Eq. 2.34 to describe the damping ratio in specimens subjected to torsional shear strain was also adopted to characterize the damping in specimens subjected to the axial mode of vibration, yielding the $D - \epsilon_1$ curve using:

$$\frac{D(\epsilon_1)}{D_{min}} = \Gamma\left(\frac{\frac{\epsilon_1}{\epsilon_r}}{1 + \frac{\epsilon_1}{\epsilon_r}}\right)^\Omega + 1 \tag{4.12}$$

where, Γ and Ω are the fitting parameters. The solid and dashed lines in Fig. 4.36a show the fitted curves in form of Eq. 4.12 to the experimental data. The fitting parameters used are shown in Table 4.4. As evident, the reference axial strain and minimum damping ratio in specimens containing crushed glass particles are higher than for specimens containing round glass particles.
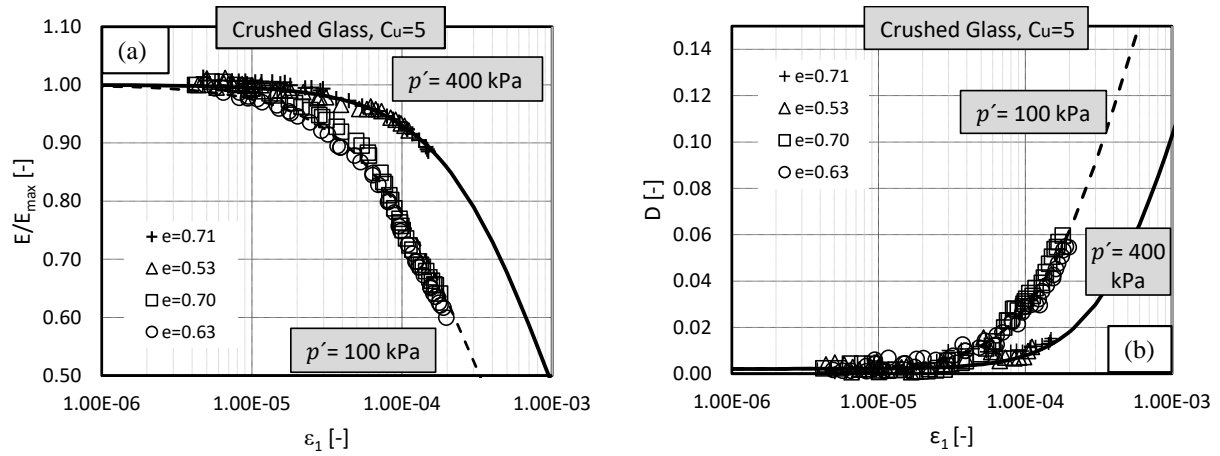
Figure 4.38: Effect of strain level and density on: a) $E/E_{max} - \epsilon_1$ curves and b) $D - \epsilon_1$ curves for the specimens containing crushed glass beads
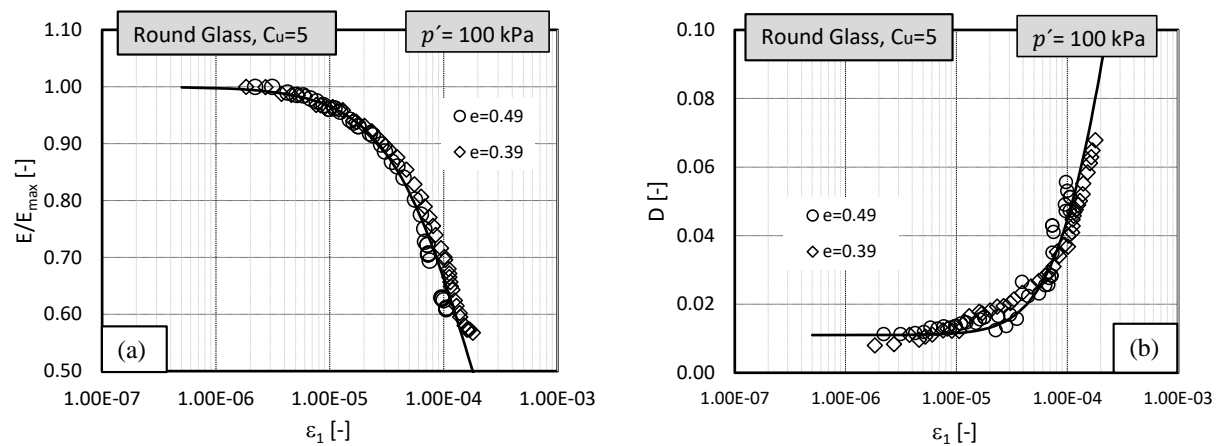
Figure 4.39: Effect of strain level and density on: a) $E/E_{max} - \epsilon_1$ curves and b) $D - \epsilon_1$ curves in the specimen containing round glass beads

iii) Comparing present test results with Saxena & Reddy (1989)

Saxena & Reddy (1989) conducted a series of tests using the Drnevich longitudinal and torsional resonant column device on Monterey No. 0 sand. They tested samples with relative densities of 25, 40, 60, and 80% under isotropic pressures between 50 and 588 kPa. The open points in Figs. 4.40 show the $E/E_{max} - \epsilon_1$ (calculated from $E - \epsilon_1$ curves in Saxena & Reddy 1989) and $D - \epsilon_1$ curves respectively. The solid lines in Figs. 4.40 show the upper and lower bounds that can be defined for their experimental data using Eqs. 4.11 and 4.12. The experimental data from the current study on crushed glass particles under cell pressures of 100 and 400 kPa (solid gray points) have been compared with their data. The visible differences might be due to the effect of the shape of particles as the
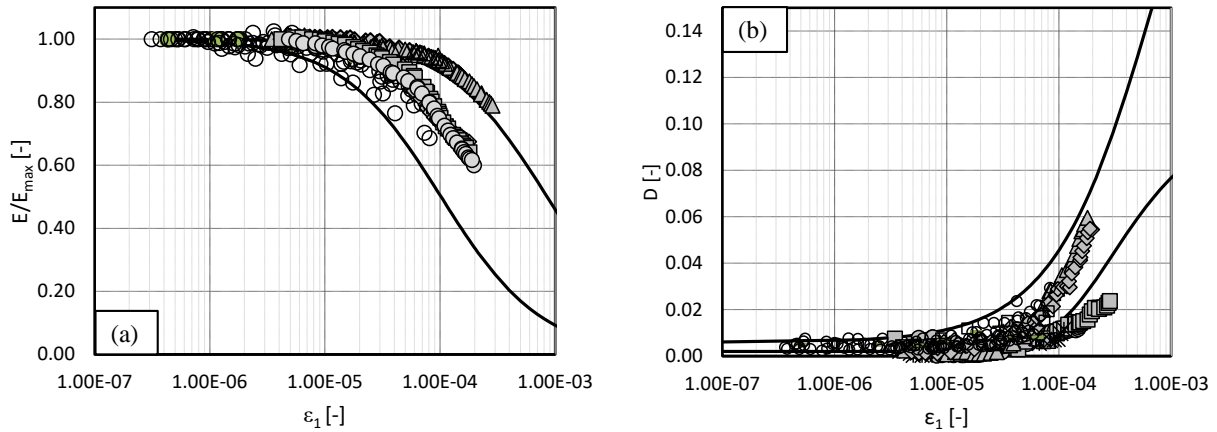
Figure 4.40: a) $E/E_{max} - \epsilon_1$ curves and b) $D - \epsilon_1$ curves from Saxena & Reddy (1989) (open points) in comparison with the data for crushed glass from current study (solid gray points)

crushed particles are more angular compared to the natural Monetery No. 0 sand, or due to differences in the uniformity coefficient of the adopted soils, where Monterey No. 0 sand has C_u=1.25 while the crushed glass material has C_u=5.

4.5 Summary

In this chapter, an introduction into the various devices used in the scope of the present research is given. In addition, various calibration tests were performed to check the performance of the devices and ensure the accuracy of the test results. In addition, the usage of porous discs of larger diameter was found to increase the frictional resistance during cyclic undrained triaxial tests on Karlsruhe fine sand leading to a higher number of cycles to initial liquefaction. Therefore, in all further test series performed in the framework of this research, a smaller porous disc and smeared end plates were employed. For the RC tests, a new device to assess the dynamic properties of soils under axial mode of vibration was introduced and the results were validated with several independent test results using aluminum specimens, measurements of compression wave velocity by means of piezoelectric elements, and high-cyclic drained triaxial tests as well as results from existing literature.

5 Static and cyclic behavior of granular soils: effect of particle characteristics

5.1 Introduction

This chapter introduces the experimental program of static/monotonic and cyclic triaxial tests that were carried out to investigate the influence of the particle characteristics on various engineering properties of granular materials under monotonic and cyclic loading conditions. The results of the experiments are shown and thoroughly analyzed. The chapter is divided into two parts: the first part deals with the monotonic tests, while the second part is dedicated to the cyclic undrained tests. Furthermore, based on the results, a comprehensive discussion based on micro-mechanics of granular materials (further details of micro-mechanical behavior is also facilitated in a later chapter) and critical/steady state soil mechanics is also provided.

5.2 Direct shear tests

5.2.1 Schedule of the direct shear tests

Table 5.1 lists the details of the experiments conducted through the direct shear device. The tests were restricted to the well-graded materials (i.e. $C_u = 5$) of angular glass, sub-angular sand and round glass beads. Each material was tested in a loose (relative density $I_D = 0.234$ - 0.338) and a dense state ($I_D = 0.785$ - 0.811). All tests were performed with a vertical stress of 50 kPa and a horizontal displacement rate of 0.244 mm/min.

Table 5.1: Details of the direct shear tests performed on two densities of the well-graded materials having a $C_u = 5$

Material	I_D (-)	Vertical stress, σ (kPa)	Shear strength τ (kPa)	ϕ_p (°)
Crushed glass	0.338	50	41.1	39.36
	0.795	50	49.36	44.57
Rhein sand	0.234	50	33.55	33.80
	0.785	50	34.49	34.54
Round glass	0.317	50	20.08	21.84
	0.811	50	20.20	21.96

5.2.2 Results of direct shear tests

Fig. 5.1 shows the development of shear stress with horizontal displacement for the loose and the dense samples. Evidently, the crushed glass shows a higher strength than the natural sand, while the by far lowest strength is observed for the glass beads. Therefore, shear strength increases with increasing angularity of the particles, due to a better interlocking and prevented rolling of adjacent particles. Besides, the unevenness of the curves for crushed glass may be caused by rearrangements of particles during shearing.

The peak shear stresses and the peak friction angles obtained from all direct shear tests are listed in Table 5.1. The angular material shows the maximum shear strength for both tested densities while the glass beads show the least. In terms of the peak friction angle, a similar trend is seen, where with higher angularity, larger friction angles are evident. Additionally, the friction angle increases with an increase in the relative density. It is interesting that for crushed glass, the peak friction angle increases by over 5° for a change in density from 0.338 to 0.795, while this increase is least for the glass beads, where practically similar peak friction angles can be noted.

5.3 Monotonic triaxial tests

5.3.1 Schedule of the monotonic triaxial tests

To capture the influence of grain shape on the monotonic triaxial test results, the three materials - crushed glass, Rhein sand and round glass beads with C_u=5 were tested. Table 5.2 states the type of test (consolidated drained - CD or consolidated undrained - CU), intial relative density, peak and steady state friction angles along with the dilation angles.
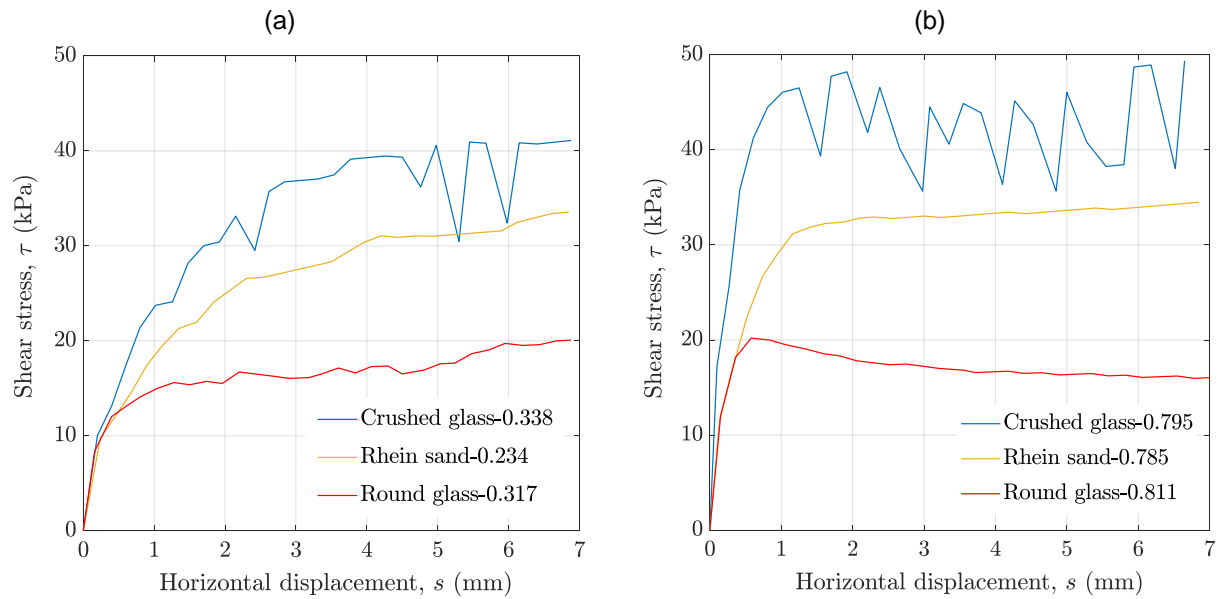
Figure 5.1: Results of the direct shear tests on the three materials with different densities: (a) loose, and (b) dense specimens

Four different effective confining stresses ($p_0' = 50$, 80, 150 and 300 kPa) were tested in both drained and undrained conditions. Overall, 16 consolidated undrained (CU) and 5 consolidated drained (CD) triaxial tests were conducted on the adopted granular materials with initial relative densities ranging between 0.234 and 1.27. Table 5.3 lists the details of all the tests that were carried out in this experimental program, including the initial void ratio e_i, void ratio after consolidation e_0 and the steady state void ratio e_{cs} as well as the confining stress at steady state p_{ss}'. The tests were carried forward till an axial strain of 25%. As was pointed out before, axial strains beyond this value were not possible due to the limitation of the device.

5.3.2 Consolidated drained triaxial tests

For the sake of simplicity, loose specimens were considered as samples having $I_D \leq 0.451$, 0.280 and 0.341 for crushed glass, Rhein sand and round glass respectively. The other samples with $I_D \geq 0.752$, 0.781 and 1.170 for the crushed glass, Rhein sand and round glass are considered dense. The adopted legend throughout the current study shows the name of material, applied effective stress and relative density of the specimen. In addition, for drained cases, the abbreviation 'Dr' has been added whereas the same is omitted for undrained cases. For example, "CG-50-0.338-Dr" denotes a test on crushed glass under an

Table 5.2: Test type, initial mean effective stress p'_0 and relative densities (I_D) of the monotonic triaxial tests, along with the peak and critical friction angles and the dilation angle derived from the test data

Material	Test type	p'_0	I_D (-)	ϕ_p (°)	ϕ_{cs} (°)	ψ (°)
	CD	50	0.338	37.6	33.68	7.84
	CU	80	0.386	39.2	34.93	8.54
	CU	80	0.824	45	34.71	20.57
Crushed glass	CU	150	0.451	40.2	35.68	9.05
	CU	300	0.347	37.9	35.94	3.91
	CU	300	0.438	38.2	34.86	6.68
	CU	300	0.752	44	36.77	14.46
	CD	50	0.234	29.8	3.42	28.09
	CD	80	0.252	33.3	31.63	3.35
	CU	80	0.280	32.9	30.64	4.52
Rhein sand	CU	80	0.818	37.1	26.88	20.44
	CU	150	0.250	32.6	31.58	2.04
	CU	150	0.781	35.7	26.92	17.57
	CU	300	0.900	38.4	29.68	17.44
	CD	50	0.317	24.7	21.20	7.00
	CD	80	0.256	24.4	22.64	3.52
	CU	80	0.323	24.5	21.39	6.22
Round glass	CU	80	1.270	36.2	21.92	28.55
	CU	150	0.341	23.5	20.78	5.44
	CU	150	1.215	35.8	23.05	25.49
	CU	300	1.170	32.1	21.08	22.05

effective initial stress (p'_0) of 50 kPa, having a relative density of 0.338 and under drained conditions.

Figs. 5.2 and 5.3 compare the drained responses, i.e. deviatoric stress versus axial strain, $q - \epsilon_1$ and volumetric strain versus axial strain, $\epsilon_v - \epsilon_1$ of the three materials with different grain shape and $C_u = 5$ under an effective confining stress of 50 kPa. All samples had a loose initial state. As can be seen from Fig. 5.2(a), the maximum deviatoric stress reached in the tests increases significantly with increasing angularity of the material. For crushed glass, q_{peak} is noted at 197 kPa, whereas the same is found to be 125 kPa and 71 kPa for Rhein sand and round glass beads respectively. After the peak all samples show a slight softening, which is somewhat more pronounced for the more angular materials. Fig. 5.2(b)

Table 5.3: Details of the tests conducted through the monotonic triaxial device

Material	Nomenclature	e_i	e_0	p'_0(kPa)	e_{cs}	p'_{ss}(kPa)	Test type
	CG-50-0.338-Dr	0.852	0.850	50.7	0.839	116.1	CD
	CG-80-0.386	0.827	0.822	78.7	0.821	149.2	CU
	CG-80-0.824	0.595	0.593	77.8	0.592	725.0	CU
Crushed glass	CG-150-0.451	0.792	0.781	147.2	0.779	270.4	CU
	CG-300-0.347	0.847	0.815	295.9	0.813	297.9	CU
	CG-300-0.438	0.799	0.773	298.3	0.772	299.7	CU
	CG-300-0.752	0.633	0.619	297.9	0.616	853.0	CU
	Rhein-50-0.234-Dr	0.747	0.746	49.2	0.751	89.6	CD
	Rhein-80-0.252-Dr	0.741	0.737	79.4	0.748	141.9	CD
	Rhein-80-0.28	0.731	0.727	78.9	0.725	120.5	CU
Rhein sand	Rhein-80-0.818	0.538	0.536	79.0	0.535	644.0	CU
	Rhein-150-0.25	0.742	0.728	149.0	0.726	151.5	CU
	Rhein-150-0.781	0.551	0.546	149.5	0.545	773.8	CU
	Rhein-300-0.90	0.508	0.500	298.7	0.499	1139.0	CU
	RG-50-0.317-Dr	0.485	0.485	49.1	0.466	74.4	CD
	RG-80-0.256-Dr	0.495	0.492	82.2	0.470	118.7	CD
	RG-80-0.323	0.484	0.482	77.9	0.481	345.3	CU
Round glass	RG-80-1.27	0.340	0.339	78.9	0.339	663.7	CU
	RG-150-0.341	0.482	0.476	148.6	0.476	303.6	CU
	RG-150-1.215	0.348	0.336	145.0	0.336	804.0	CU
	RG-300-1.17	0.354	0.349	293.8	0.349	929.0	CU

shows the difference in the initial stress-strain behavior of the three materials till a strain level of 1% along with the respective secant moduli E_{50}, which are calculated as the 50% of the maximum deviator stress divided by the corresponding axial strain. The crushed glass and the round glass show the same slope of the stress-strain curve at very low strain levels, which is steeper than that measured for the Rhein sand. Since the sample of glass beads reaches its maximum deviatoric stress at much lower axial strains, this results in a much larger value of E_{50}, followed by the E_{50} values of crushed glass and Rhein sand. The observed stress-strain behaviour may be explained from a micro-mechanical perspective, where due to the lack of surface texture in round glass beads, rolling motion dominates soon after the application of a deviator stress. At higher strain levels, this culminates in the form of a stick-slip behavior as evident in the $q - \epsilon_1$ curve in Fig 5.2a. For the crushed glass, due to high interlocking between individual particles, the rolling motion is

hindered and sliding motion predominates which results in a higher deviatoric stress with increasing axial strain. The sub-angular material Rhein sand lies somewhere in between.
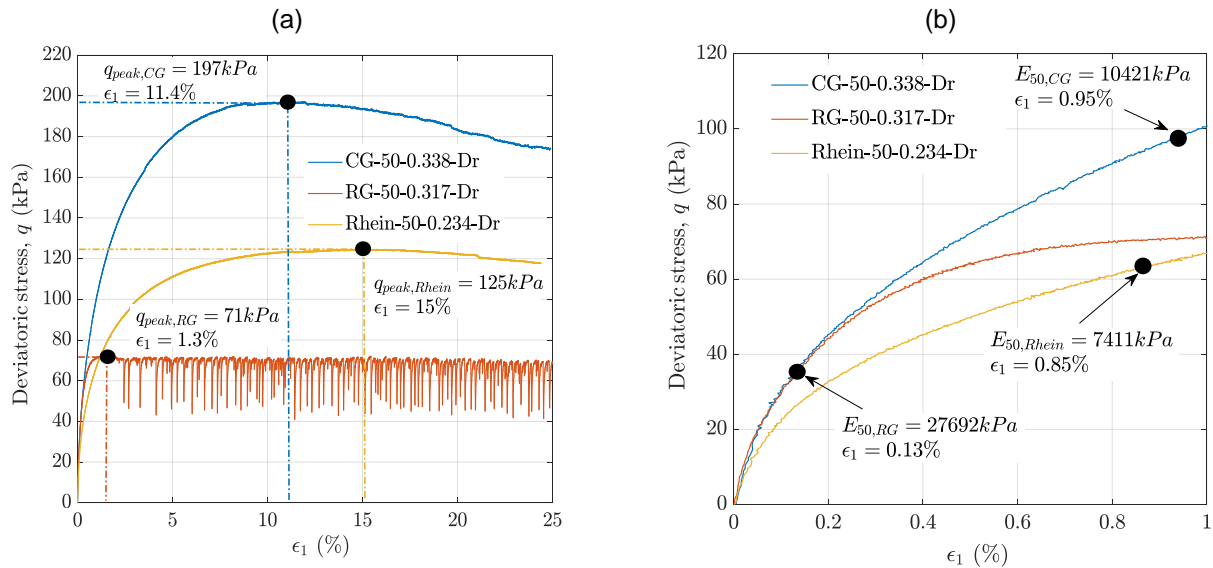
Figure 5.2: Comparison between the drained responses of the three materials under an effective confining stress of 50 kPa: (a) $q - \epsilon_1$, (b) $q - \epsilon_1$ magnified for a low strain level till 1%
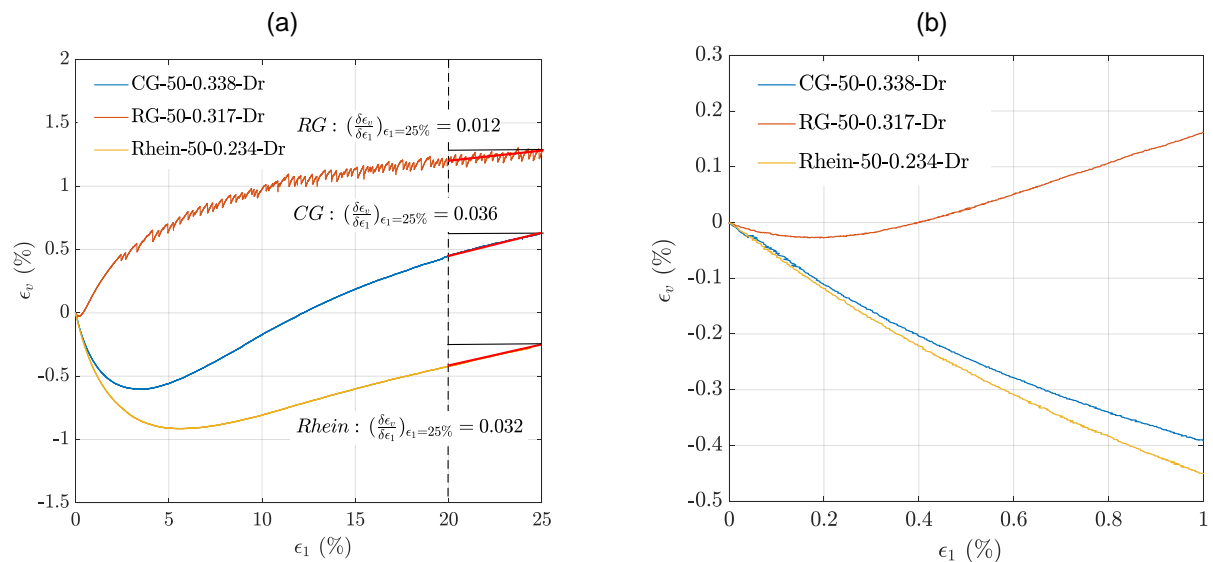
Figure 5.3: Comparison between the drained responses of the three materials under an effective confining stress of 50 kPa: (a) $\epsilon_v - \epsilon_1$, (b) $\epsilon_v - \epsilon_1$ magnified for a low strain level till 1%

The development of volumetric strain versus axial strain is shown in Fig. 5.3(a), with a zoomed image till an axial strain of 1% in Fig. 5.3(b). All the materials initially undergo

densification, which is denoted by a negative volumetric strain. However, for round beads, the initial densification is much smaller than for crushed glass or Rhein sand. Furthermore, for round glass dilation already starts at very small axial strain levels of about 0.2%, while the volume change tendency reverses at about 3.5% and 6% for crushed glass and natural sand, respectively. The lower volume change of the glass beads can be inferred from the low difference between the maximum and minimum void ratios ($e_{max} - e_{min} = 0.15$) as compared to the crushed glass ($e_{max} - e_{min} = 0.53$) and Rhein sand ($e_{max} - e_{min} = 0.36$). Due to easy rolling motion in glass beads, the process of densification reverses to dilatancy much faster than in case of the other materials. For all three materials after completion of initial densification, a dilative behavior is encountered which continues throughout the remaining of the test thus yielding less negative (Rhein sand) or even positive volumetric strain values (round and crushed glass) at the end of the test. The absolute values of volume change are also partially influenced by the slightly different relative densities, which were 0.317 for round glass beads, 0.234 for natural sand and 0.338 for crushed glass.

Considering the characteristic state of the materials (a feature of drained triaxial testing where the rate of volume change is zero), Lade & Ibsen (1997) and Nguyen et al. (2018) stated that for a loose sand, the characteristic state may be considered to be attained at the steady state. In the tests, it was assumed that the steady state has been reached at an axial strain of 25% purely based on the limitation of the displacement transducer used, however, a more valid assumption would be to observe when the volumetric strain also remains constant at larger strains (for both loose and dense specimens). From Figs. 5.3(a and b), the rate of volumetric stain attains zero value for the first time at 3.5%, 6% and 0.2% axial strain, corresponding to deviator stresses in Fig. 5.2(a) of 168 kPa, 115 kPa and 43 kPa for crushed glass, Rhein sand and round glass beads respectively. It was seen that in the range $20\% \leq \epsilon_1 \leq 25\%$, the crushed glass shows the maximum rate of change of volumetric strain with the glass beads showing the minimum (see Fig. 5.3a) although the volumetric strain never became constant even at an axial strain of 25% (pointing out that the steady state was not fully reached at $\epsilon_1 = 25\%$). This observation clearly shows the significant effect of particle angularity on the characteristic state of drained triaxial tests. The positive volumetric strain at the end of the test may be explained by the crushed glass having a slightly higher density compared to Rhein sand. For the Rhein sand, the material being in a comparatively looser configuration (I_D=0.234) than the crushed glass, the dilative behavior is observed later on during the test.

As previously mentioned, the stick-slip behavior is encountered for all samples of the round glass beads under triaxial compression. For crushed glass and Rhein sand such a phenomenon is not observed due to high interlocking between individual particles caused by surface roughness and angularity eventually resulting in a resistance against slippage.

5.3.3 Consolidated undrained triaxial tests

Fig. 5.4 shows the results from all undrained tests in terms of the effective stress path $(q - p')$ and the development of pore water pressure with axial strain $(u - \epsilon_1)$ which are further discussed in the following subsections, concentrating on two extreme cases of regularity, i.e. crushed and round glass.

5.3.3.1 Effect of relative density

Fig. 5.5 shows the $q - \epsilon_1$ and $q - p'$ curves for the two materials under various relative densities but subject to an initial effective stress of 80 kPa. The loose specimen of crushed glass in Fig. 5.5(a) and (b) initially shows a slight decrease in p' followed by a re-increase with further increase in axial strain. There is no distinct quasi-steady state, instead a PT point is passed. Such PT is hardly encountered for the round glass beads, where the sample shows a dilatant tendency from the beginning (Fig. 5.5b and d). For both materials, at a certain axial strain higher values of q are achieved in dense specimens compared to loose ones as evident from Figs. 5.5(a) and (c). Interestingly, a strain-softening behavior is very prominent for dense round glass beads soon after reaching peak deviator stress, which occurs at a much larger strain for crushed glass.

One possible reason for the strong softening observed for dense round glass beads, becoming visible also as large kinks in the effective stress paths (Fig. 5.5d), is that the pore pressure dros and reaches negative values pretty fast. One recommendation could be to perform future tests with a larger back pressure to avoid this issue. Due to the continuous deformation of the specimen coupled with a high degree of surface smoothness present in round glass beads, the particles slide over each other, continuously dilating and contracting, thus creating a pronounced 'stick-slip' behavior throughout the entire duration of the test (Hayman et al. 2011; Doanh et al. 2013; Tordesillas et al. 2010; Tordesillas et al. 2014). In other words, the glass beads are close to attaining the steady state after which there is a sudden contraction causing the large drop. This is again followed by a dilation phase after which the above process is repeated throughout the duration of the test. In
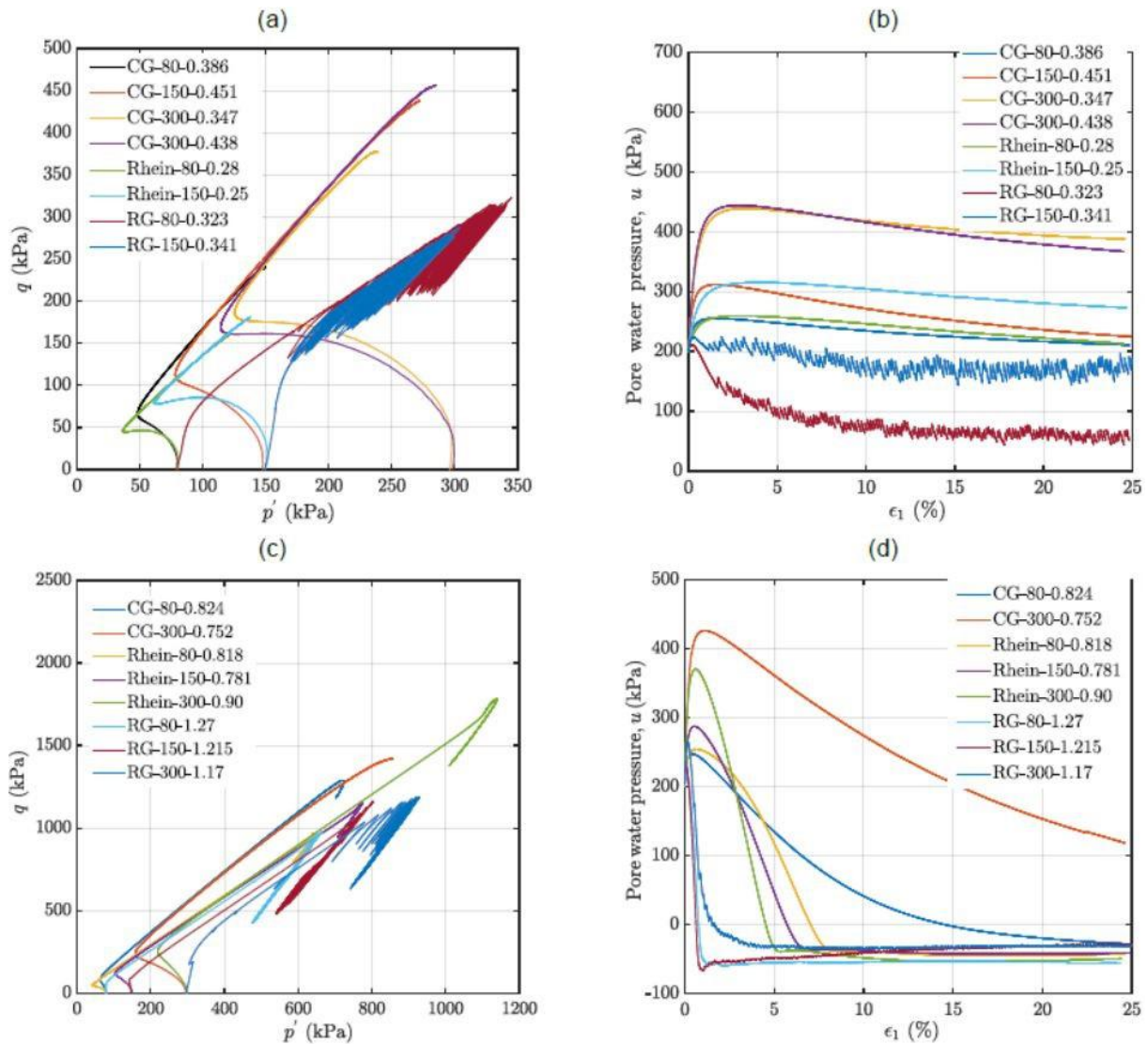
Figure 5.4: Comparison between the undrained monotonic responses for the materials under investigation for all specimens with various relative densities (loose and dense configurations respectively): (a) and (c) effective stress path $q - p'$, and (b) and (d) pore water pressure versus axial strain $u - \epsilon_1$

the current set of triaxial experiments, most of the results from round glass beads show this characteristic behavior. Owing to the limitation of the device, it was not possible to go beyond axial strains of 25%. Therefore, the steady state has been assumed to be reached at the maximum value of strain recorded in the test. It is interesting to note that the inclination of the effective stress path up to the maximum deviatoric stress depends strongly on the density in case of the glass beads, while this dependence is much less pronounced in case of the crushed glass.
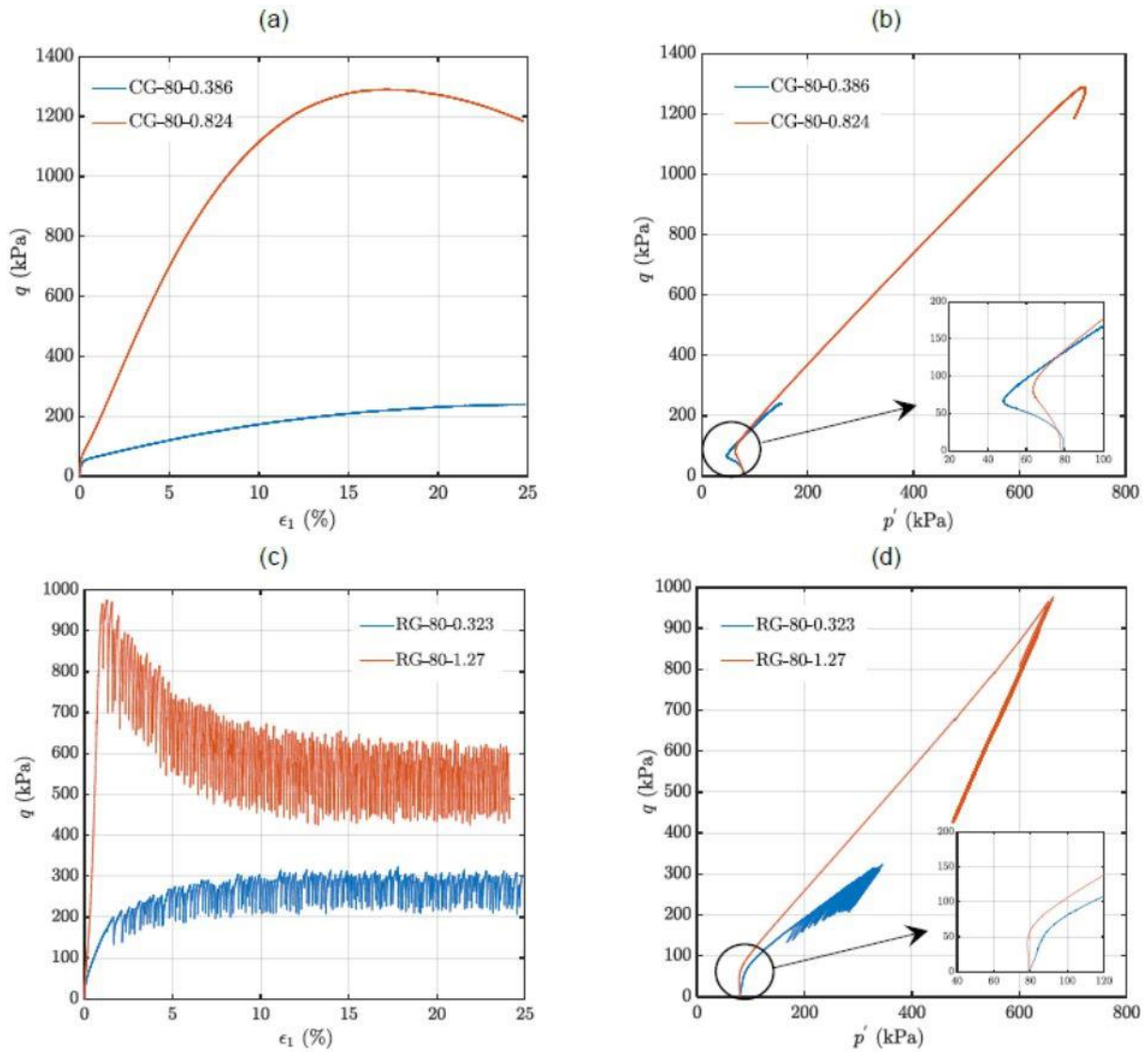
Figure 5.5: Comparison between the responses obtained from loose or dense samples of crushed and round glass beads under constant initial effective stresses: (a) $q - \epsilon_1$, (b) $q - p'$ for crushed glass, and (c) $q - \epsilon_1$, and (d) $q - p'$ for round glass beads respectively

5.3.3.2 Effect of effective stress

Tests on the two extreme materials with a loose relative density but under different confining stresses are compared in Fig. 5.6. It is interesting to note that prominent PT points are observed for crushed glass (see Figs. 5.6a and b), which are completely absent for the round glass beads (Figs. 5.6c and d). The round glass beads show a dilating tendency, leading to an increase of mean effective stress, from the beginning of the shearing. The steady state line in the $q - p'$ plane has a similar slope under various confining stresses as

can be concluded from Figs. 5.6(b) and (d). From the tests on round glass beads, despite the significant fluctuation of the deviatoric stress, it can be concluded that the steady state is achieved at about 10% axial strain. However, for crushed glass, the deviatoric stress increases with further increase in the axial strain and the steady state is assumed to be reached at the strain level of 25%.
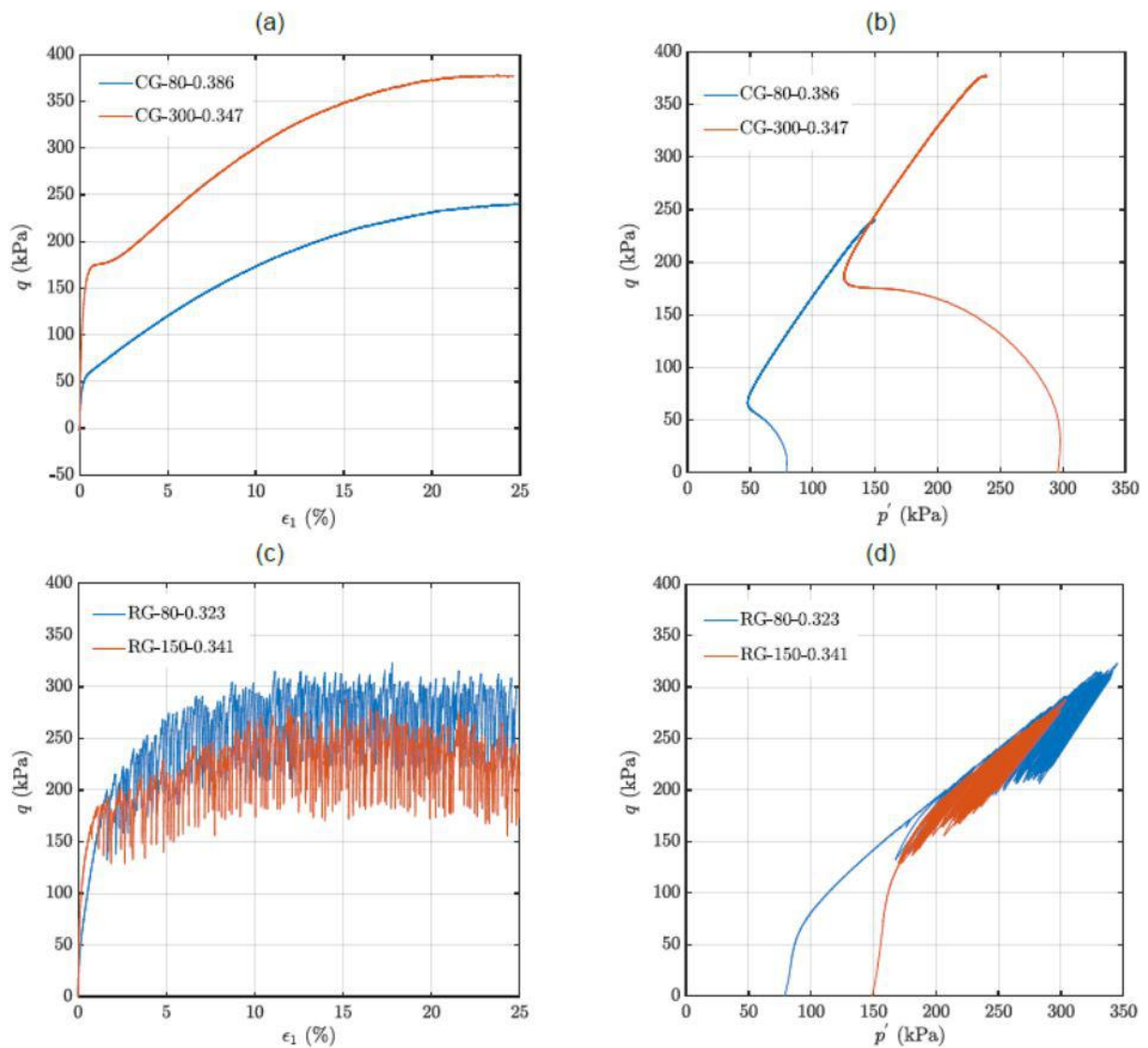
Figure 5.6: Comparison between the responses obtained from experiments on crushed and round glass beads under similar densities: (a) $q - \epsilon_1$, (b) $q - p'$ for crushed glass, and (c) $q - \epsilon_1$, and (d) $q - p'$ for round glass beads respectively

5.3.3.3 Effect of particle shape

Fig. 5.7 facilitates a comparison between three specimens with similar boundary conditions but different particle shape. All samples were dense and sheared from an initial effective stress of 80 kPa. From Fig. 5.7(a), it can be clearly seen that in the initial stage of the test the deviatoric stress increases much faster with increasing axial strain for the round glass beads than for the two more angular materials, i.e. the stiffness increases with increasing roundness or regularity, respectively. In contrast, the maximum deviatoric stress reached during shearing and the inclination of the steady or critical state line in the $q - p'$ plane increase with increasing angularity of the granular material (Fig. 5.7b).
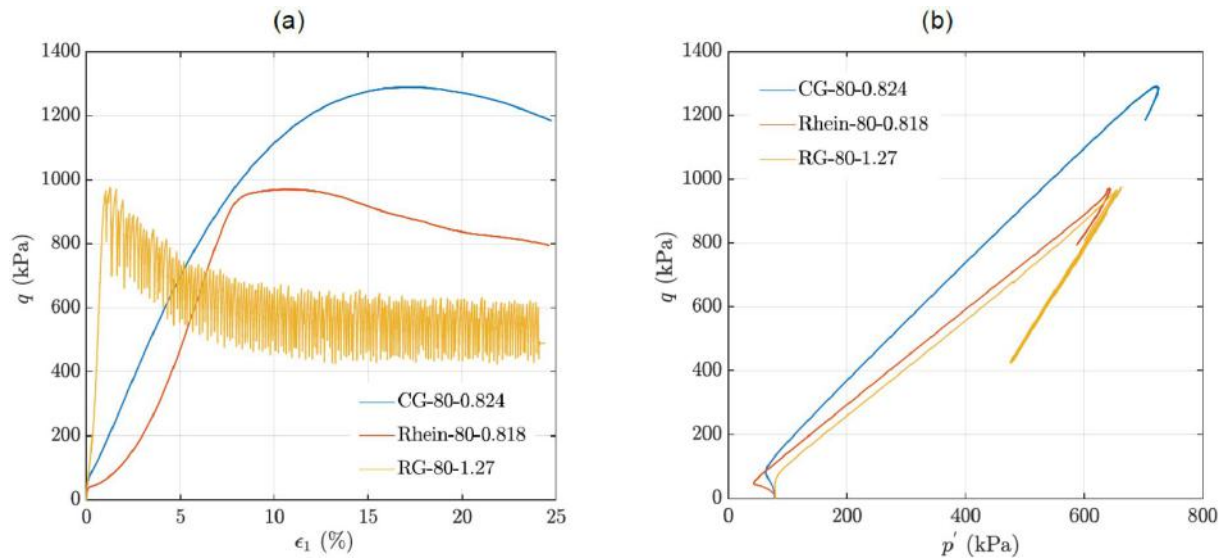
Figure 5.7: Comparison between the responses of the three materials under same initial effective stress and similar densities: (a) $q - \epsilon_1$, and (b) $q - p'$

Before and after the completion of the whole testing program, the particle size distribution was determined for the crushed glass and the natural sand. As shown in Fig. 5.8, no significant particle breakage was observed. It is to be noted that particle crushing in round glass beads was not expected and not examined as the range of stresses under which the specimens was tested were much lower than the crushing strength of glass, which was reported to be 10 MPa by Wu et al. (2016). It can be concluded that the mechanical behaviour of the different materials studied in this thesis is not significantly influenced by particle breakage effects.
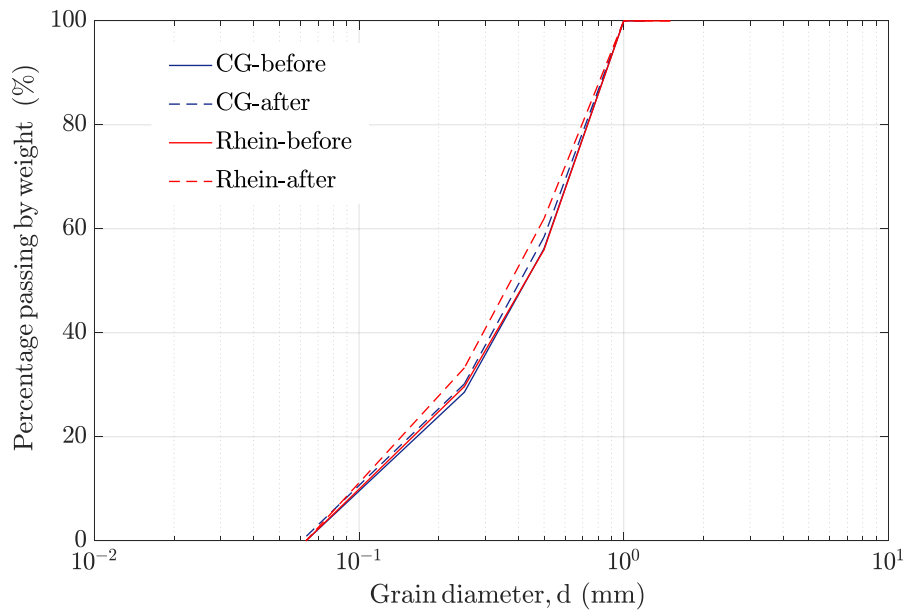
Figure 5.8: Initial and final particle size distributions, determined before and after the whole experimental program was completed

5.3.4 Examination of the effects of rubber (latex) membrane

Several literatures (Kiekbusch & Schuppener 1977; Baldi & Nova 1984) in the past have indicated significant effects of membrane on the results of monotonic triaxial tests. In general, the presence of a membrane has two most notable effects on triaxial test results: membrane penetration and membrane resistance. Membrane penetration occurs due to pressing of the membrane into the voids between the individual soil grains at the boundary of the sample, thereby giving rise to a non-homogenous specimen surface (Fig. 5.9a). Membrane penetration changes with changes in the effective stress acting as pressure difference on the membrane. Such change of effective stress occurs e.g. in drained tests due to an increase of cell pressure, and in undrained tests, due to a change of pore water pressure. Membrane penetration can lead to a falsification of the measured volume changes in drained tests. In undrained cyclic tests the delay in pore water pressure build-up caused by membrane penetration can lead to an overestimation of the liquefaction resistance. This effect becomes more prominent with increasing grain size (Fig. 5.9b), and decreases with an increase in the thickness and elastic modulus of the membrane as well as the sample diameter. For drained conditions this effect is calculated in terms of the volumetric strain change, and can be expressed as Eq. 5.1 (after Baldi & Nova 1984):

(a)

(b)
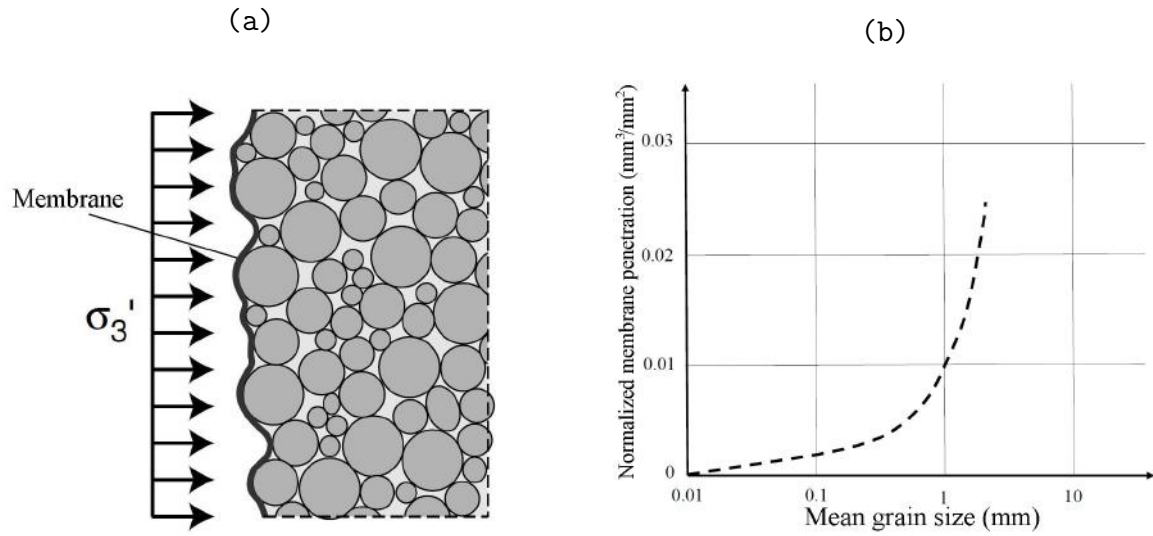
Figure 5.9: (a) Membrane penetration - pressing of the membrane into the voids between the grains due to an increase of the effective lateral stress σ_3' (after Wichtmann 2005); (b) Comparison of relationships for normalized membrane penetration (ratio of unit membrane penetration Δv_m to the mean confining pressure σ_3') versus mean grain size d_{50} (after Baldi & Nova 1984)

$$\frac{\Delta V_m}{V_0} = \frac{1}{2}\frac{d_{50}}{D_s}\left[\frac{\sigma_3' \, d_{50}}{E_m \, t_m}\right]^{1/3} \tag{5.1}$$

ΔV_m denotes the change in volume (measured in mm^3), V_0 is the initial volume after consolidation (mm^3), d_{50} denotes the mean grain size (mm), D_s is the diameter of the specimen (mm), σ_3' is the effective confining stress (kPa), E_m is the elastic modulus of the membrane (generally considered as 1350 kPa in Omar & Sadrekarimi 2014), and t_m is the thickness of the membrane (mm). Using the parameters from the current set of experiments ($d_{50} = 0.45$ mm, $D_s = 100$ mm, $t_m = 0.7$ mm), for the highest confining stress $\sigma_3' = 300$ kPa, the volumetric strain due to membrane penetration is 0.0012 or 0.12% which is very small. It can be concluded that the effects of membrane penetration can be considered negligible for the materials studied in this thesis.

The second problem occurs due to the membrane carrying a part of the load applied in the vertical direction on the specimen. This effect can be particularly significant in measuring the reduced shear strength s_u of loose soils after strain softening and liquefaction (Omar & Sadrekarimi 2014). To correct this effect when analyzing data from consolidated drained triaxial tests, ASTM-D7181 (20) suggests Eq. 5.2 to calculate the deviatoric stress (δq) carried by the membrane:

$$\delta q = 4 \times \frac{E_m \, t_m \, \epsilon_1}{D_c} \tag{5.2}$$

E_m (kPa) is the Young's modulus of the membrane material, t_m (mm) is the thickness of the membrane, and D_c (mm) is the specimen diameter after consolidation. As apparent, membrane resistance increases with increase in the axial strain ϵ_1. For the current set of drained tests, considering the critical case of a loose specimen (I_D=0.386) of crushed glass (CG) under a low effective stress of 80 kPa, the curves of deviatoric stress q versus axial strain with and without considering the effect of membrane resistance are compared in Fig. 5.10. The maximum q with correction for membrane resistance is 230 kPa, whereas the difference δq at ϵ_1=25% is around 9.4 kPa, which is less than the specified 5% limit as suggested by ASTM-D7181 (20). Therefore, the effect of membrane resistance is deemed minimal, and hence can be safely ignored for the other non-critical cases.
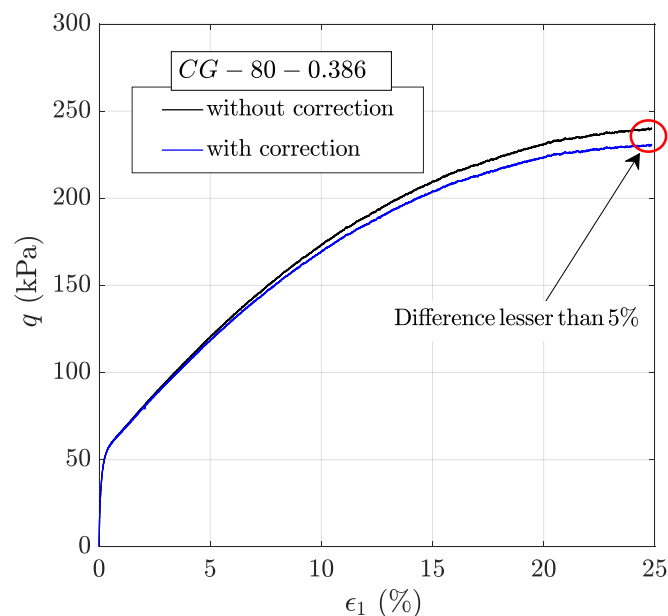
Figure 5.10: Effect of membrane resistance on the stress-strain relationship measured in drained monotonic tests on loose crushed glass at $\sigma_3' = 80$ kPa

5.3.5 Discussion & interpretation within the framework of critical-state soil mechanics

5.3.5.1 Effect of particle characteristics on the slope M

Fig. 5.11 shows the variation of the slope M, i.e. the stress ratio at the steady state in a $q - p'$ diagram, derived from the effective stress paths measured for the three different materials. It can be noticed that the crushed glass (CG) and the Rhein sand show unique

M values of 1.70 and 1.32, respectively, which are independent of density. The difference in the values is in accordance with the results from Yang & Luo (2015), Jiang et al. (2018) and Nguyen et al. (2020a) where angular particles had a higher M value. However, for the round glass beads, two different M values are visible instead of a unique one: the loose specimens with $M = 0.94$ and the dense samples with $M = 1.34$ (also shown in Fig. 5.11c). This may be due to the characteristic features of the glass beads which have a high degree of smoothness that culminated in the 'stick-slip' behavior. The existence of two different M values for the same material is indeed surprising. One related study regarding this issue may be found in Olarte (2008), who performed DEM simulations and biaxial tests with polygonal particles, and showed that for the particles exhibiting stick-slip motion, the slope of the critical state line observed was about 0.9, which is close to that of the loose specimens in the present study. Since they did not use any round materials like glass beads, it was not possible to explicitly confirm the M value for round glass beads.
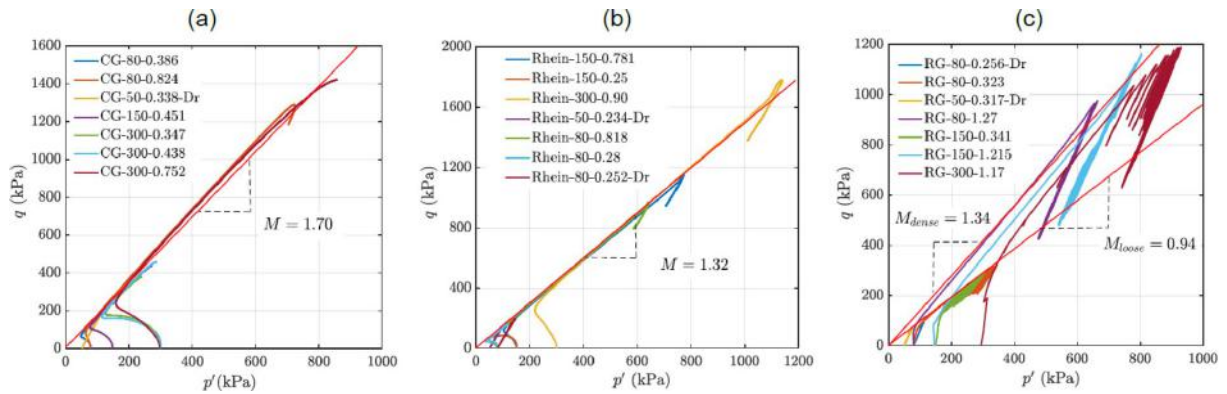
Figure 5.11: M values obtained for the various materials from the effective stress paths measured in the undrained monotonic triaxial tests

5.3.5.2 Effect of confining pressure on the peak friction angle (ϕ_p)

In this study, the peak friction angle mobilized throughout the drained / undrained tests is obtained using the relationship between the friction angle and the slope M:

$$\phi_p = \sin^{-1}\left(\frac{3M}{6+M}\right) \tag{5.3}$$

In case of the drained tests Eq. 5.3 is evaluated with the maximum M value reached during the tests, while for undrained tests the inclinations of the effective stress paths

shown in Fig. 5.11 are used. The values are summarized in Table 5.2. The peak friction angles plotted against the initial effective mean stress are shown in Fig. 5.12. Data for loose and dense samples are plotted separately. One may note that the ϕ_p values from drained tests are slightly lower than those from undrained tests (Table 5.2). However, the drained tests were carried out particularly on loose samples. Evidently, there exists no clear tendency regarding the variation of peak friction angle with the initial effective mean stress although one may note a slight decrease with increasing p'_0 especially for the dense specimens. This is in agreement with Hammad (1991) and Sadrekarimi & Olson (2011) both of which reported a similar observation.
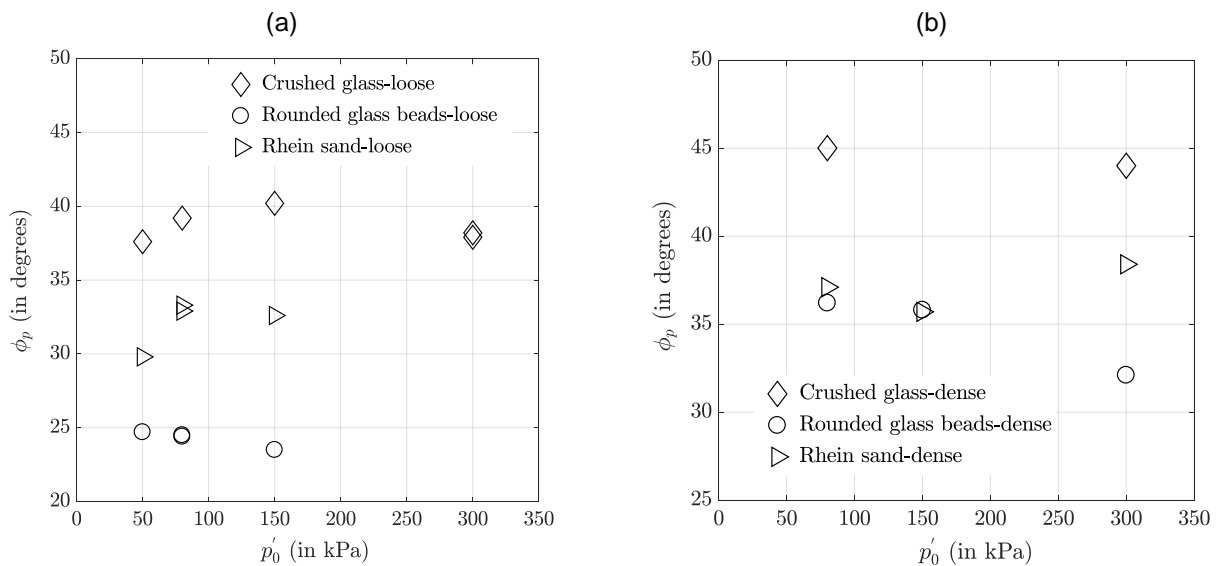
Figure 5.12: Variation of the peak friction angles (ϕ_p) with the initial effective stress (p'_0) for the three different materials: (a) loose specimens ($I_D \leq 0.451$), and (b) dense specimens only ($I_D > 0.451$)

5.3.5.3 Effect of particle characteristics on the peak friction angle (ϕ_p)

Based on the concept of regularity, an attempt was made to relate particle shape with the peak friction angle. The parameters describing grain size and distribution (such as the uniformity coefficient and mean grain size) for the basis of comparison were the same throughout. Plots of the peak friction angle against the regularity are provided in Figs. 5.13a and 5.13b for two cases: (a) undrained tests with same initial mean effective stress (80 kPa) but varying relative densities, and (b) drained and undrained tests with an initial mean effective stress of 50 and 300 kPa and with extreme (loose and dense) relative

densities. In Fig. 5.13a the lower points correspond to loose samples, while the higher ones result from the dense samples. The comparatively high value of ϕ_p in Fig. 5.13(a) for dense glass beads may be explained by the relative density of the specimen being higher than for the other two dense specimens. A steady decrease in the friction angle with an increasing regularity is evident from both diagrams in Fig. 5.13, which is similar to the observation made by Cho et al. (2006). The following equations describe this tendency, where it is distinguished between the two confining pressures 50 and 300 kPa:

$$\phi_{p,300} = A \cdot f(\rho) = A_1 \cdot \rho^{k_1} = A_1 \cdot \rho^{-0.454} \tag{5.4a}$$

$$\phi_{p,50} = A \cdot f(\rho) = A_2 \cdot \rho^{k_2} = A_2 \cdot \rho^{-0.597} \tag{5.4b}$$
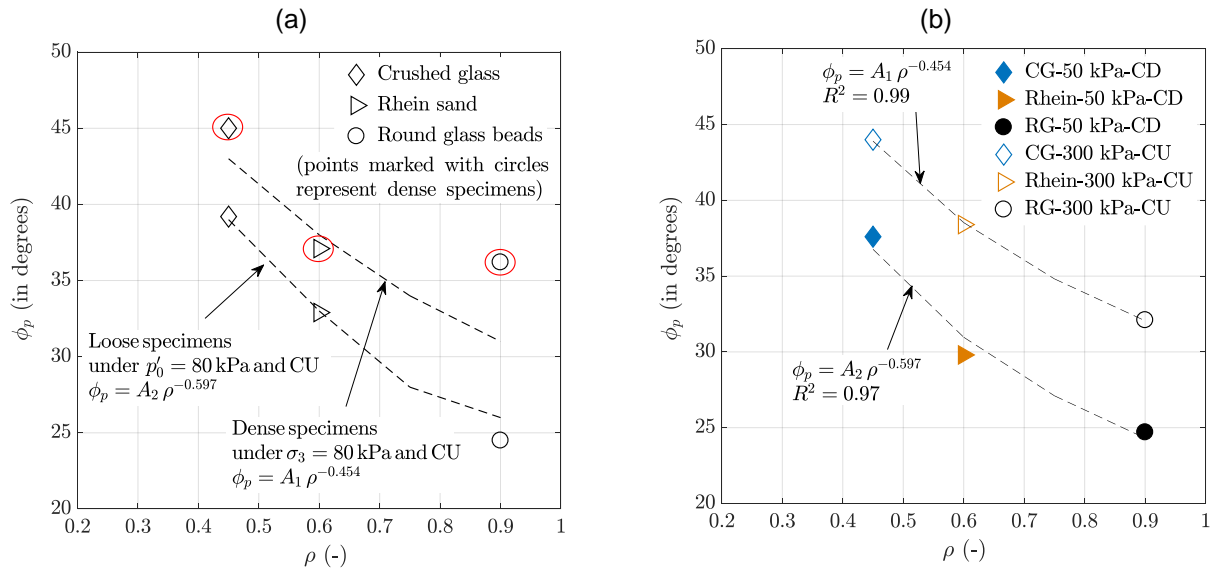
Figure 5.13: Variation of the peak friction angle (ϕ_p) of the three materials against the regularity (ρ) for loose and dense samples from (a) undrained tests under same confining effective stress (80 kPa), and (b) both drained (loose samples) and undrained (dense samples) tests with the maximum and minimum confining stresses (50 and 300 kPa) used for current experiments

The parameter A is a fitting parameter which solely depends on the relative density of the material. For the present case, an average value of the exponent k was chosen considering the maximum and minimum densities and the highest and the lowest effective stresses applied. The average value of k for the current set of experimental data is determined to be -0.526. To determine the effect of relative density, the peak friction angle was

normalized with respect to the regularity, i.e. divided by the function $f(\rho)$ given in Eqs. 5.4, and plotted against the relative density (I_D) of the samples compared in Fig. 5.13b, resulting in the diagram shown in Fig. 5.14(a). Considering all the triaxial experiments, the effect of relative density ($I_D \geq 0.2$) on peak friction angle is shown in Fig. 5.14b.
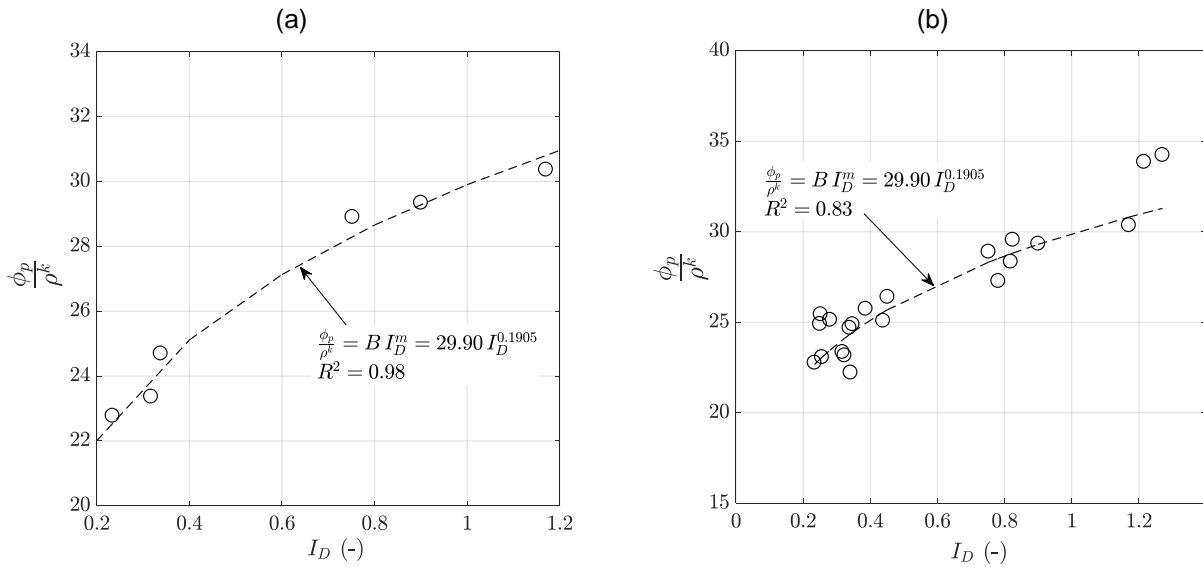
Figure 5.14: Relation between the normalized peak friction angle and the relative density: (a) formulation with selected data from Fig.5.13b, and (b) validation with all current experimental data

As evident, an increase in the normalized friction angle with an increase in the relative density was encountered, which is in good agreement with the observations of Bolton (1986). The normalized data can be fitted by the following equation (Eq. 5.5):

$$\frac{\phi_p}{f(\rho)} = B\, f(I_D) = B\, I_D^m = 29.90\, I_D^{0.1905} \tag{5.5}$$

The final expression describing the combined influence of grain shape and relative density on the peak friction angle therefore reads:

$$\phi_p = f(\rho)\, f(I_D) = 29.90\, \rho^{-0.526}\, I_D^{0.1905} \tag{5.6}$$

For the sake of simplicity and considering relative densities lower than 0.2, Eq. 5.6 can also be expressed as a linear function (ref. Eq. 5.7). In this way, the minimum ($I_D = 0$) and maximum ($I_D = 1$) possible ϕ_p for a perfectly round material ($\rho = 1$) stands at 21.30° and 29.84° respectively, which are values being a bit lower than the experimental data.

$$\phi_p = f(\rho)\,f(I_D) = \rho^{-0.526}\,(8.54\,I_D + 21.30) \tag{5.7}$$

The final expression in Eq. 5.7 shows a good agreement between the measured and the predicted peak friction angles (see Fig. 5.15). In all the tested cases, an error margin of 10% was not exceeded throughout between the measured and the predicted values.
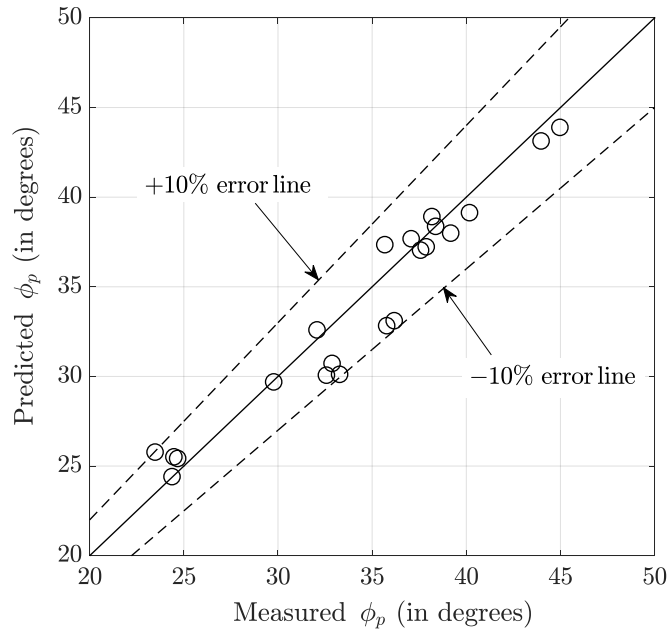
Figure 5.15: Measured versus predicted values of the peak friction angle considering all the current experimental data. The predicted values were obtained from Eq. 5.7

5.3.5.4 Effect of relative density (I_D) on the dilatancy angle (ψ)

The dilatancy angle is typically a characteristic that is derived from drained tests on dense samples using the volumetric strain versus axial strain plot, while loose samples show negligible dilation. For undrained tests, since there is no volume change and no direct method to quantify dilatancy, the dilatancy angle can be estimated using the equation of Schanz & Vermeer (1996) developed originally for drained tests:

$$\sin\psi = \frac{I_R}{6.7 + I_R} \tag{5.8}$$

I_R denotes the relative density index depending on the relative density (I_D) and the applied mean effective stress p' (Schanz & Vermeer 1996). The relation between I_R and I_D is represented as (Bolton 1986):

$$I_R = I_D \left(Q - \ln p^{'}\right) - R \tag{5.9}$$

Q and R are fitting parameters, for which values of 10 and 1 are assumed respectively (Bolton 1986). Fig. 5.16 shows a plot of the dilatancy angles against the relative density. A comparison has been made between the dilation angles obtained from the experiments against the dilation angles computed using the equation suggested by Bolton (1986). Since Bolton's equation for the maximum dilation angle takes into consideration the initial effective confining stress, two specific cases with effective stresses of 80 and 300 kPa were used for the comparison considering plane strain conditions. Evidently, there is a good fit between the experimental dilatancy angles and the angles computed through the model of Bolton. Although a perfect match should ideally have been encountered, the slight deviation is caused due to the test conditions - in Bolton's formulation, the plane strain condition has been used ($0.8\psi = 5I_R$) whereas triaxial conditions have slightly different boundary conditions. In addition, the relative densities for a few specimens of round glass beads are higher than 1, which might also cause the higher scatter at larger I_D values. As expected, dilatancy angle increases with density. The same observation is also supported in Chakraborty & Salgado (2010).
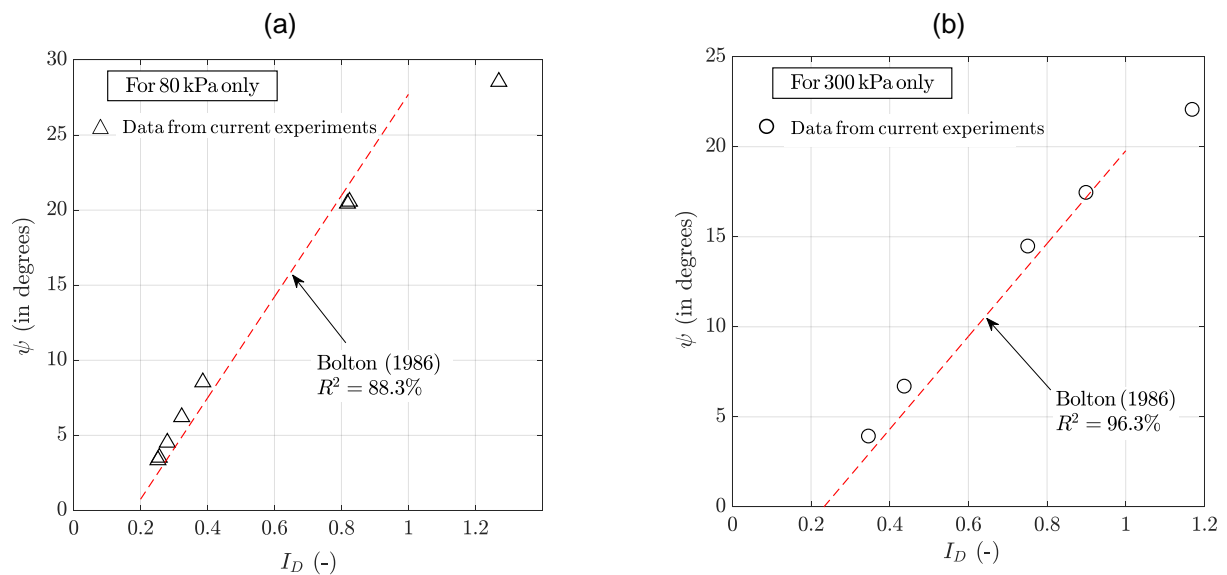
Figure 5.16: Variation of the dilation angle (ψ) against the relative density of all the tested materials under nitial effective confining stress of (a) 80 kPa, and (b) 300 kPa

In Fig. 5.17 the dilatancy angles of all the various tests are plotted against I_D. No specific trend with regards to the influence of grain shape can be noted due to the scatter in

the data. However, the round glass seems to have a slightly larger dilatancy angle at I_D around 0.3-0.35 as compared to the other two materials, although this influence seems negligible. An expected linear trend of increasing ψ with increase in I_D is also visible.
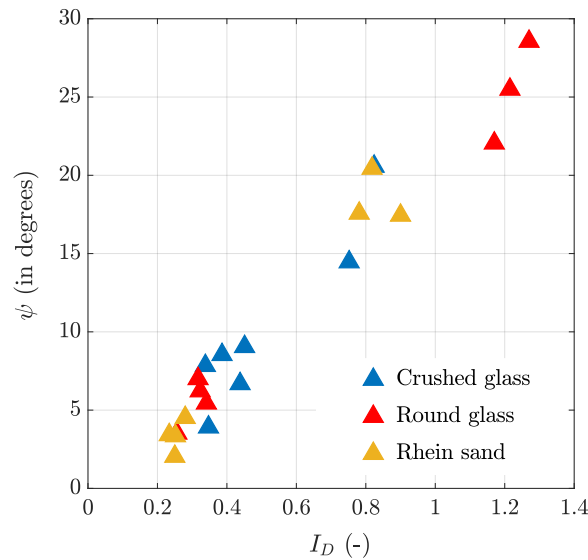
Figure 5.17: Variation of the dilatancyangle (ψ) against the relative density of all the tested materials

5.3.5.5 Effect of confining pressure $p^{'}$ on the dilatancy angle (ψ)

The variation of the dilation angle with the effective confining stress has been plotted for the three materials in Figure 5.18. The results closely match the observations of Strahler et al. (2016) who reported a steady decrease in the dilation angle with an increasing effective stress using a log-linear relationship. The effective stress was normalized with respect to the atmospheric pressure $p^{'}_a = 100$ kPa.

5.3.5.6 Effect of particle shape and density on steady state friction angle ϕ_{cs}

For triaxial tests, the steady state friction angle ϕ_{cs} can be obtained through the relation between the peak friction angle ϕ_p and dilation angle ψ proposed by Bolton (1986):

$$\phi_p - \phi_{cs} = 0.5\,\psi \tag{5.10}$$

The steady state friction angle being a unique parameter for a certain material, is expected to remain constant for any change in relative density, which is confirmed by the
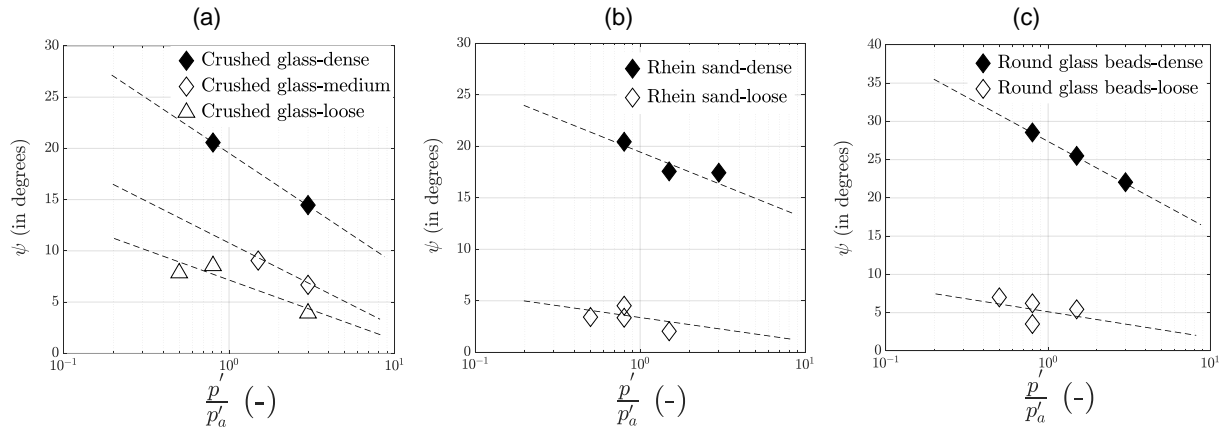
Figure 5.18: Variation of the dilatancy angle against the normalized initial effective stress for the three materials: (a) crushed glass, (b) Rhein sand, and (c) round glass beads (for greater accuracy, the two crushed glass specimens with a relative density of 0.438 and 0.451 have been termed medium)

experimental data in Fig. 5.19(a). The straight horizontal lines represent the arithmetic mean of all the calculated steady state friction angles for a certain material. The scatter between the various values for a certain regularity and different relative densities is much lower than in case of the peak friction angle. Considering the mean value of the steady state angle, a good correlation with the regularity can be observed in Fig. 5.19(b). With an increase in the regularity, the steady state friction angle decreases, which can be represented through the following linear expression (Eq. 5.11):

$$\phi_{cs} = f(\rho) = 47.84 - 29.35\,\rho \tag{5.11}$$

5.3.5.7 Steady state line in the $e - p'$ diagram

Based on the data from the triaxial experiments, an attempt was made to define the steady state line in the $e - p'$ diagram for the three materials. It was assumed that the materials reach steady state after 25% axial strain. The steady state line is determined based on a regression analysis to obtain the best fit of the experimental data, using the well-known Eq. 5.12 (after Schofield & Wroth 1968):

$$e = \tau - \lambda \log\left(\frac{p'}{p_a}\right) \tag{5.12}$$
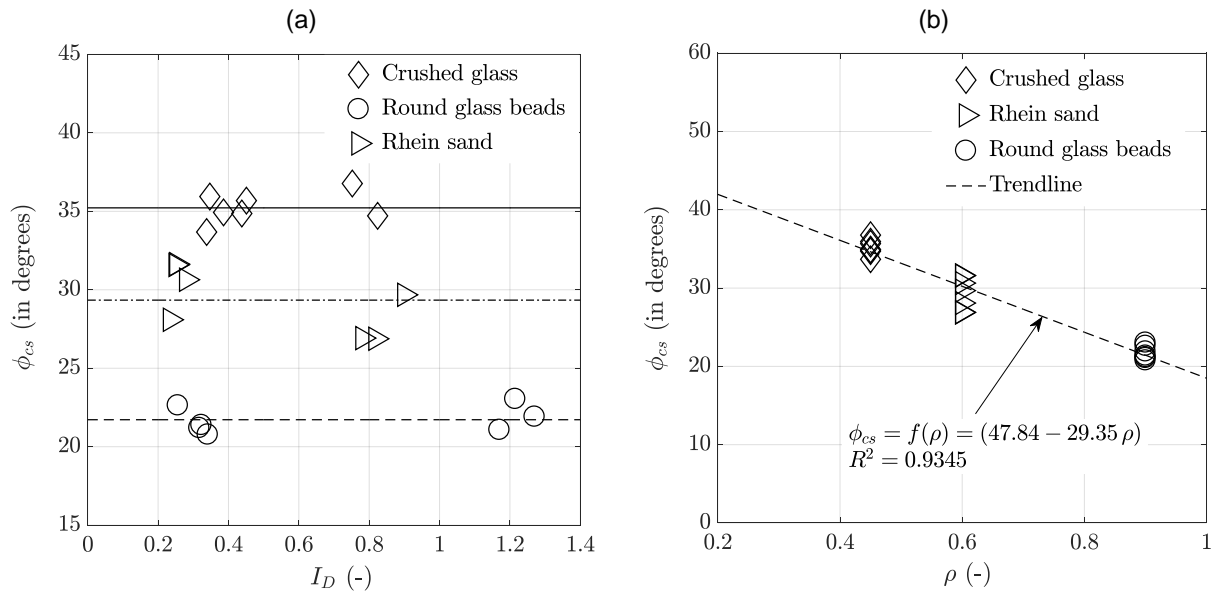
Figure 5.19: Variation of the steady state friction angle (ϕ_{cs}) against the (a) relative density I_D, and (b) regularity ρ

τ and λ represent the intercept and the slope of the steady state line respectively. Fig. 5.20 presents the respective experimental data for the three tested materials. The points marked with open and closed symbols denote the initial and final states of the tests. The red symbols are obtained from the drained tests, while the black symbols denote the undrained tests. However, owing to limitation of the triaxial device and the predominantly dilative response of the tested samples, steady state data at effective stresses below 50 kPa are absent in the present data set. Fig. 5.21a shows the steady state data for all three materials in a single diagram, where on the horizontal axis the mean effective stress is normalized by the atmospheric pressure. The curve-fitting of the above equation to the final states yields the following equations (Eq. 5.13) for the three materials:

$$e = 0.89 - 0.054 \log \left(\frac{p^{'}}{p^{'}_a} \right) \tag{5.13a}$$

$$e = 0.76 - 0.046 \log \left(\frac{p^{'}}{p^{'}_a} \right) \tag{5.13b}$$

$$e = 0.48 - 0.024 \log \left(\frac{p^{'}}{p^{'}_a} \right) \tag{5.13c}$$

These equations are shown as three lines in Fig. 5.21a. The intercepts λ for crushed glass, Rhein sand and round glass beads are 0.89, 0.76 and 0.48, respectively. The decrease of λ with regularity is compared with a previous work (Jerves et al. 2015) and as shown in Fig. 5.21b, can be described by a linear function:

$$\lambda = 0.086 - 0.068\rho \tag{5.14}$$

Assuming the steady state void ratio at an effective stress of 1 kPa to be very close to the maximum void ratio of the material, another common expression of the form of Eq. 5.15 has also been proposed:

$$e = \tau - \lambda \left(\frac{p'}{p'_a} \right)^{\alpha} \tag{5.15}$$

The exponent α represents another fitting parameter. The expressions as obtained after regression analysis are summarized as Eq. 5.16 and plotted individually for each material in Fig. 5.20:

$$e = 0.900 - 0.046 \left(\frac{p'}{p'_a} \right)^{0.89} \tag{5.16a}$$

$$e = 0.790 - 0.041 \left(\frac{p'}{p'_a} \right)^{0.85} \tag{5.16b}$$

$$e = 0.485 - 0.006 \left(\frac{p'}{p'_a} \right)^{1.49} \tag{5.16c}$$

The values of the intercept (τ) and the slope (λ) obtained in the second set of equations for the steady state line are 0.900 and 0.046 for crushed glass, 0.790 and 0.041 for Rhein sand, and 0.485 and 0.006 for round glass beads. The exponent α appears to be lower for the angular and sub-angular materials while being the largest for glass beads.

Furthermore, the intercept τ is the largest for crushed glass, while being the least for glass beads. This can also be attributed to the fact that τ correlates well with the maximum and minimum void ratio, which in turn is a function of grain shape.
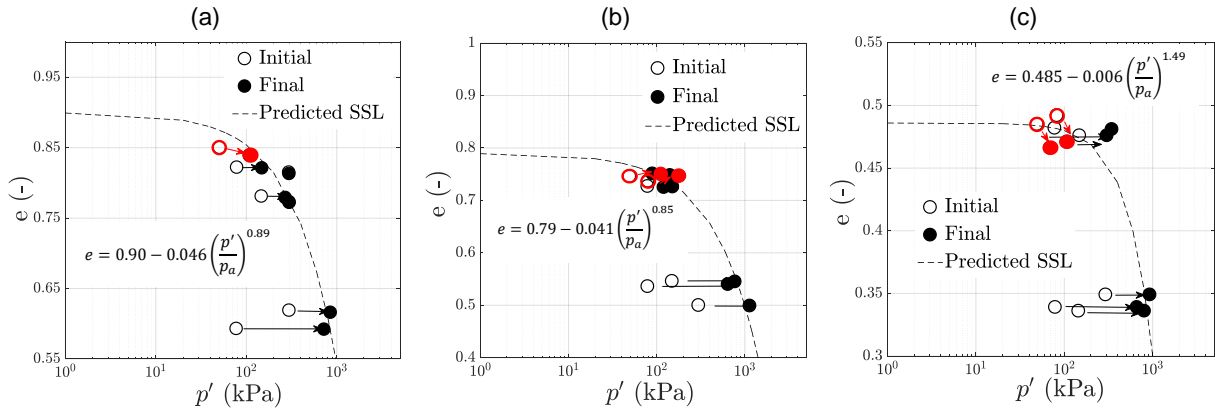
Figure 5.20: Initial and steady states in the $e - p'$ diagram for the three tested materials: (a) crushed glass, (b) Rhein sand, and (c) round glass beads (points marked with red show drained test results, those in black undrained test results). The dashed curves correspond to Eq. 5.16(a-c).
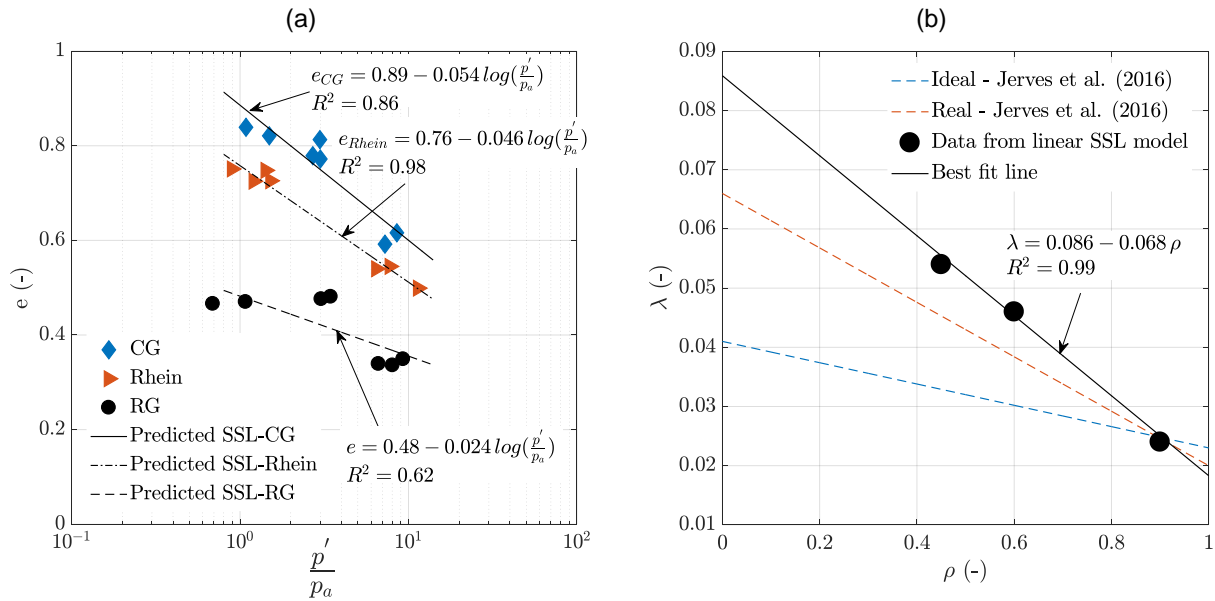
Figure 5.21: (a) Steady state line data for the three tested materials and fitting by Eq. 5.13, and (b) dependence of the slope (λ) of Eq. 5.16 on regularity against the results of Jerves et al. (2015)

5.3.5.8 Comparison of proposed model with various literature

For the purpose of comparison of the steady state friction angles and the parameters obtained from Eq. 5.13, an already existing dataset from Cho et al. (2006) and Alshibli & Cil (2018) has been used, details of which are listed in Table 5.4. For the critical friction

angle in Alshibli & Cil (2018), the average of all the values for a certain material under various densities and stresses has been considered. A good agreement of those data with the current results for the steady state friction angles against the regularity is evident from Fig. 5.22(a). A similar observation is noted in Figures 5.22(b) and (c) for the two fitting parameters of Eq. 5.13 ($\tau - \rho$ and $\lambda - \rho$) where the current data matches the trend as observed in Cho et al. (2006). The small differences in the values may be because of variations in other material parameters such as the uniformity coefficient (C_u), mean grain size (d_{50}) and surface roughness.

Table 5.4: Dataset from literature used for comparison with the current results

Source	Soil name	d_{50}	C_u	ρ	ϕ_{cs}	τ	λ
	Nevada sand	0.15	1.8	0.73	31	1.04	0.071
	Ticino sand	0.58	1.8	0.60	37	1.05	0.053
	Margaret river sand	0.49	1.9	0.70	33	0.84	0.051
	ASTM 20/30	0.6	1.4	0.85	32	0.74	0.053
	Ponte Vedra sand	0.18	1.8	0.58	39	1.01	0.061
	8M8 crushed sand	0.38	3.3	0.45	40	1.16	0.138
Cho et al. (2006)	9C1 crushed sand	0.52	2.3	0.48	39	1.06	0.067
	Jekyll Island sand	0.17	1.7	0.58	40	0.98	0.053
	ASTM graded sand	0.35	1.7	0.85	30	0.869	0.08
	Blasting sand	0.71	1.9	0.43	34	1.099	0.69
	Glass beads	0.32	1.4	1.00	21	0.807	0.039
	Granite powder	0.9	6.2	0.32	34	1.124	0.07
	Ottawa 20/30 sand	0.72	1.2	0.92	27	0.802	0.047
	Ottawa F-110 sand	0.12	1.7	0.70	31	0.937	0.077
	7U7 crushed sand	0.3	3.2	0.50	37	1.06	0.064
	Glass beads	0.36	-	1	27.9	-	-
Alshibli & Cil (2018)	Toyoura sand	0.22	-	0.50	37.1	-	-
	Hostun sand	0.34	-	0.46*	38.8	-	-

* Data obtained from Zheng & Hryciw (2016)

Furthermore, ignoring the effect of surface roughness (which is beyond the scope of the present study), the influence of the uniformity coefficient and mean grain size was also investigated with the documented data from literature. The steady state friction angle was normalized with respect to regularity using Eq. 5.11, and was plotted against the mean grain size in Fig. 5.22d, keeping the variation in C_u minimal ($1.2 \leq C_u \leq 1.8$). A slight increase of ϕ_{cs} with increasing d_{50} can be concluded from the data. However, the
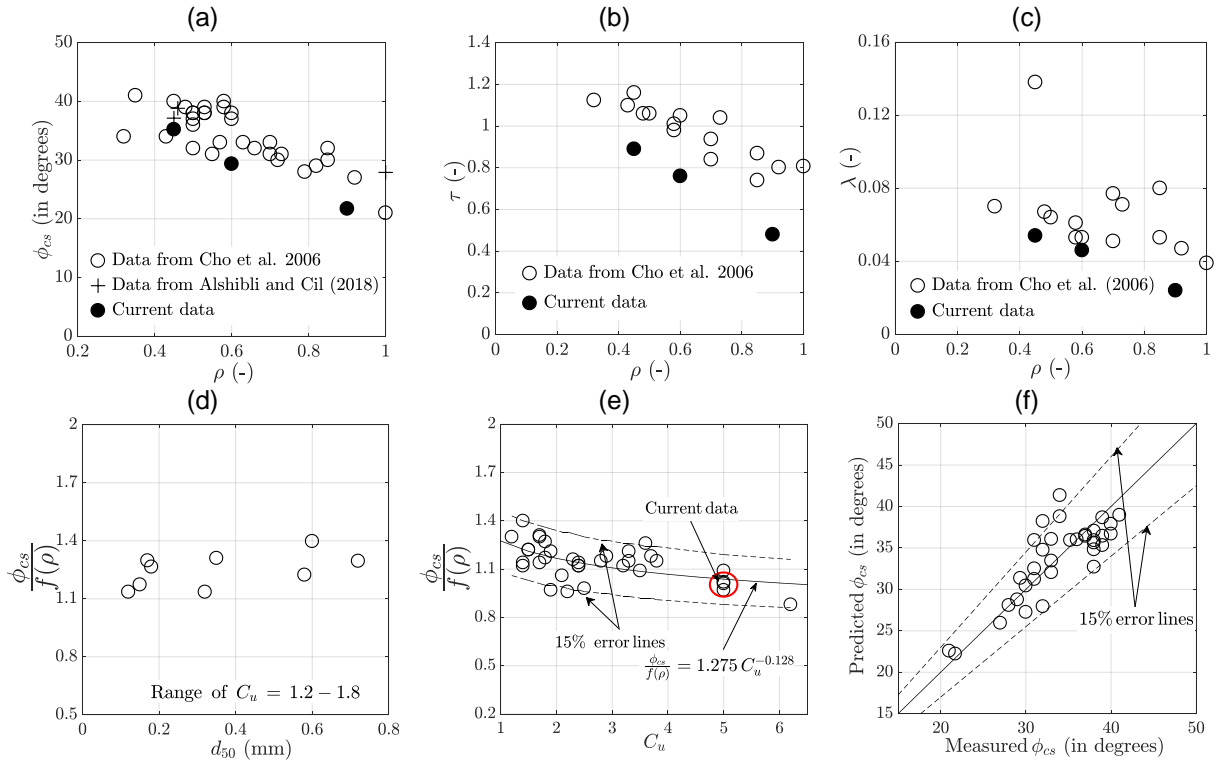
Figure 5.22: Comparison of current results with data obtained from literature: (a) $\phi_{cs} - \rho$, (b) $\tau - \rho$, and (c) $\lambda - \rho$, (d) normalized steady state friction angle versus d_{50}, (e) normalized steady state friction angle versus C_u, and (f) comparison between measured and predicted steady state friction angles

effect of mean grain size is rather small. Therefore, the normalized ϕ_{cs} was plotted against C_u in Fig. 5.22(e). For the purpose of comparison, curves corresponding to an error of 15% were added to take into account various uncertainties and differences between the tests in the data set, e.g. with respect to sample size, rate of loading as well as other morphological factors such as surface roughness. A decent correlation was observed which can be expressed through Eq. 5.17:

$$\frac{\phi_{cs}}{f(\rho)} = 1.275\, C_u^{-0.128} \tag{5.17}$$

A complete formulation incorporating the influence of the particle shape and C_u, but neglecting d_{50}, may be represented as:

$$\phi_{cs} = f(\rho)\, f(C_u) = 1.275\, C_u^{-0.128} \times (47.84 - 29.35\, \rho) \tag{5.18}$$

Fig. 5.22(f) shows a comparison between the measured and the predicted values using Eq. 5.18. Barring a couple of data points, the proposed model performs satisfactorly and predicts the critical friction angle within an error limit of 15%.

5.3.5.9 Influence of gradation on the undrained monotonic behavior

To assess the influence of the particle gradation on the undrained monotonic behavior of granular soils, three more materials (glass beads, natural sand, crushed glass) were tested with a similar d_{50} but with a different $C_u = 1.25$. It is evident from previous studies (refer to Chapter 2) that the shear strength increases with a higher d_{50} but there was no common consensus with respect to C_u. Consequently in the present set of experiments the only variables involved were the grain shape and C_u.

Overall 18 tests were carried out on each of the six materials (three grain shapes $\times$ two uniformity coefficients) among them three tests on each material with three different relative densities. The cell pressure of each test was 300 kPa, while the back pressure was maintained at 200 kPa, thereby signifying an initial effective stress $(p_0^{'})$ of 100 kPa. All the tests performed were consolidated and sheared undrained (CU) tests. The details of these tests are shown in Table 5.5.

i) Loose specimens

The $q - p^{'}$ and $q - \epsilon_1$ curves of two samples of crushed glass with different C_u values and relatively loose initial densities $(0.209 < I_D < 0.315)$ are shown in Fig. 5.23. At first glance from Fig. 5.23a, it is clear that the deviatoric stress q increases significantly faster with increasing axial strain for C_u=1.25 than for C_u=5, with the final q being almost twice larger in the case of the uniform material. It is also interesting to note that the initial part of the effective stress path, including the location of the phase transformation in Fig. 5.23b is very similar for both C_u values. Furthermore, the slope of the $q - p^{'}$ curve during the dilatant phase in Fig. 5.23b does also hardly depend on C_u. Similar conclusions can be drawn from the results for the two gradations of Rhein sand (Fig. 5.24). Such observations were also encountered in the static triaxial tests of Vaid et al. (1990) who tested sub-angular sands having three different gradations but a similar mean grain size. For relative densities around 38%, Vaid et al. (1990) found that the more well-graded mixtures showed lower values of the deviator stress at the end of the test than the more uniform sands.

Table 5.5: Details of the monotonic CU tests conducted on six different materials with three different densities (denoted as decimals in the nomenclature) to study the influence of C_u on the undrained monotonic response

Material	Nomenclature	I_D	e_i	e_0	p_0' (kPa)	e_{cs}	p_{ss}' (kPa)
	CG-Cu=5-ID=0.315	0.315	0.864	0.856	97.86	0.856	141.35
CG-5	CG-Cu=5-ID=0.578	0.578	0.725	0.719	98.18	0.719	254.94
	CG-Cu=5-ID=0.83	0.830	0.592	0.589	98.00	0.589	780.14
	Rhein-Cu=5-ID=0.236	0.236	0.747	0.738	97.59	0.738	83.11
Rhein-5	Rhein-Cu=5-ID=0.581	0.581	0.623	0.618	98.03	0.618	296.21
	Rhein-Cu=5-ID=0.836	0.836	0.531	0.529	97.72	0.529	638.55
	RG-Cu=5-ID=0.228	0.228	0.499	0.495	98.62	0.495	446.8
RG-5	RG-Cu=5-ID=0.578	0.578	0.445	0.442	97.42	0.445	468.78
	RG-Cu=5-ID=0.828	0.828	0.407	0.405	97.64	0.405	466.44
	CG-Cu=1.25-ID=0.269	0.269	1.026	1.019	98.43	1.019	266.83
CG-1.25	CG-Cu=1.25-ID=0.586	0.586	0.877	0.872	97.84	0.872	657.91
	CG-Cu=1.25-ID=0.804	0.804	0.774	0.770	96.64	0.770	770.44
	Rhein-Cu=1.25-ID=0.209	0.209	0.828	0.822	97.78	0.822	144.49
Rhein-1.25	Rhein-Cu=1.25-ID=0.557	0.557	0.714	0.711	97.97	0.711	539.53
	Rhein-Cu=1.25-ID=0.825	0.825	0.626	0.623	97.64	0.623	653.75
	RG-Cu=1.25-ID=0.265	0.265	0.700	0.697	97.93	0.697	444.80
RG-1.25	RG-Cu=1.25-ID=0.551	0.551	0.655	0.652	97.88	0.652	457.58
	RG-Cu=1.25-ID=0.856	0.856	0.606	0.604	98.04	0.604	526.37

Concerning the round glass beads, there is a marked difference. First of all, from Fig. 5.25 showing the data for the loose samples ($0.228 < I_D < 0.265$), it is evident that the shear strength is similar for both the two gradations, implying that the observations from the other two materials are not applicable to round materials. For the round glass beads the deviatoric stress increases rapidly till the first 'stick-slip' point, after which q tends to decrease over ϵ_1. Furthermore, the effective stress paths for both C_u values in Fig. 5.25b do not show a phase transformation point but exhibit a dilative tendency from the beginning of shearing.

ii) Medium dense specimens

A similar tendency is evident for the medium dense samples ($0.551 < I_D < 0.586$) for the six materials, where the influence of gradation for a constant d_{50} for the angular
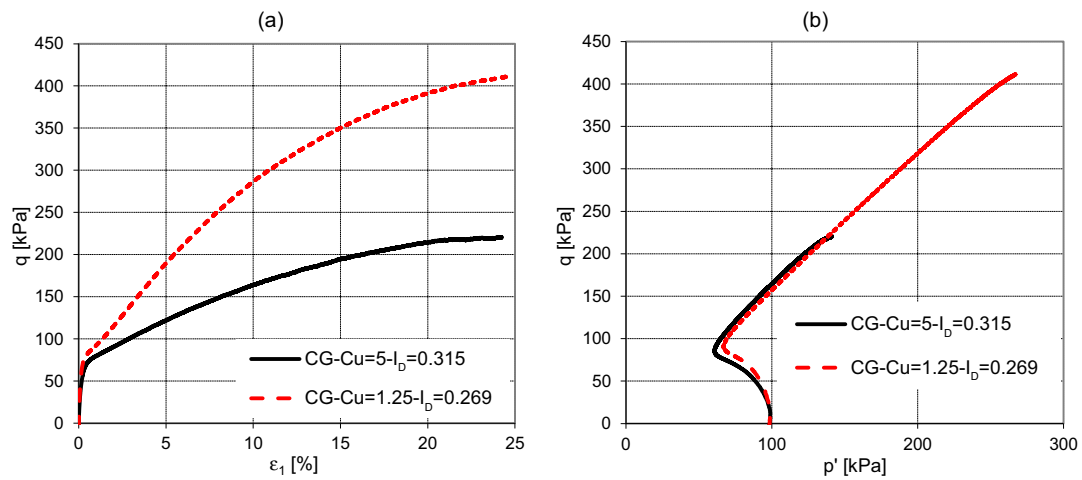
Figure 5.23: Comparison of the (a) $q - \epsilon_1$ and (b) $q - p'$ curves for loose crushed glass with two different gradations
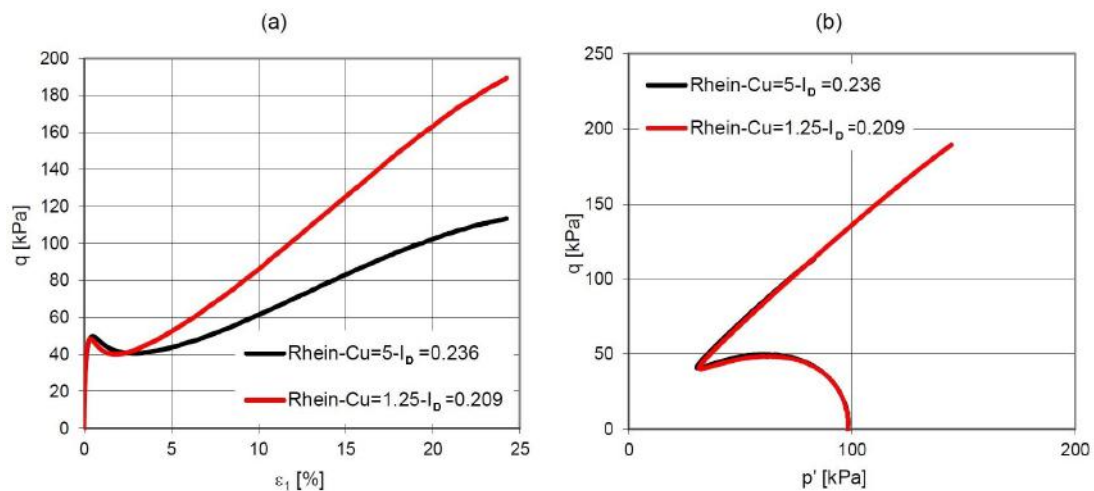
Figure 5.24: Comparison of the (a) $q - \epsilon_1$ and (b) $q - p'$ curves for loose Rhein sand with two different gradations

and sub-angular materials follows the same trend as observed for loose specimens but seems negligible for the round glass beads. An increase in density results in larger shear resistance which is evident from a comparison of Figs. 5.23a and 5.24a with Figs. 5.26a and 5.27a - the maximum value of q for uniform crushed glass increases from nearly 410 kPa to over 1020 kPa while for the uniform Rhein sand, it grows from 190 to 750 kPa. For the well-graded mixtures, the trend was similar although the increment in q was smaller as in the uniform cases. For the round glass beads, this increment was quite small: the peak q increased from approximately 490 kPa in Fig. 5.25a to 550 kPa in Fig. 5.28a. It
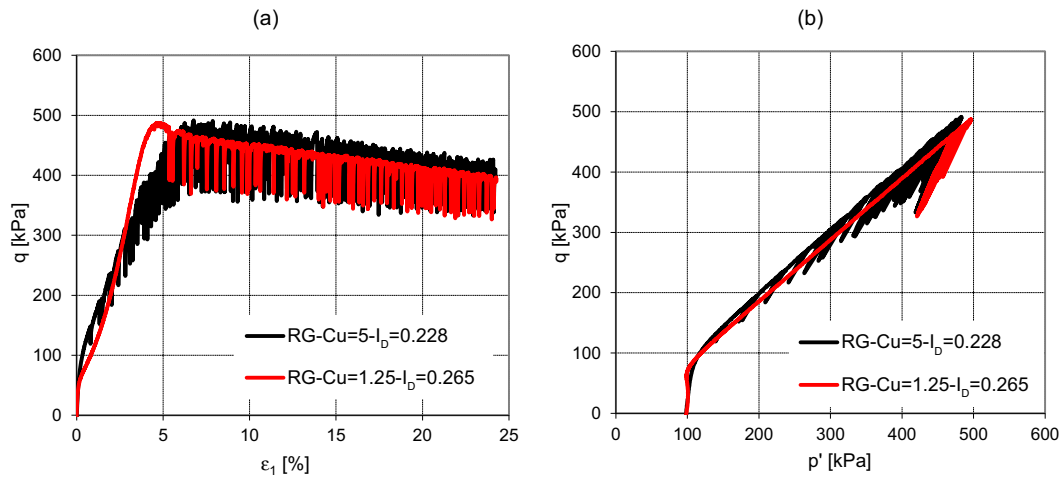
Figure 5.25: Comparison of the (a) $q - \epsilon_1$ and (b) $q - p'$ curves for loose round glass beads with two different gradations
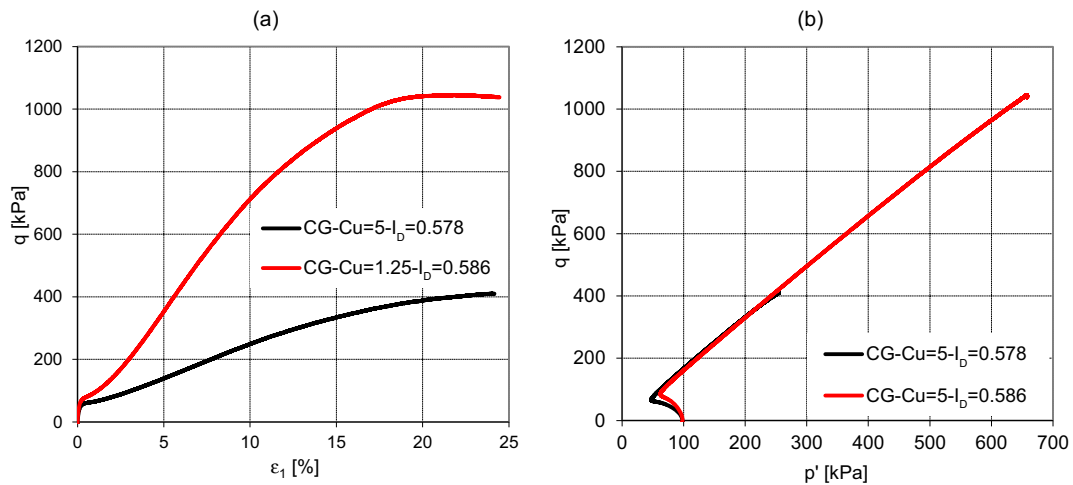
Figure 5.26: Comparison of the (a) $q - \epsilon_1$ and (b) $q - p'$ curves for medium dense crushed glass with two different gradations

must be noted that as the initial back pressure during the start of the test was kept at 200 kPa, the pore pressure rapidly went down to the negative regime after starting the test at an axial strain of 2.6%, and the data might not be reliable anymore afterwards. Thus, evaluating the influence of C_u on shear strength in case of glass beads might not be reliable, and it is thus suggested to perform similar tests with a larger initial back pressure to avoid such issues and investigate the C_u influence further.
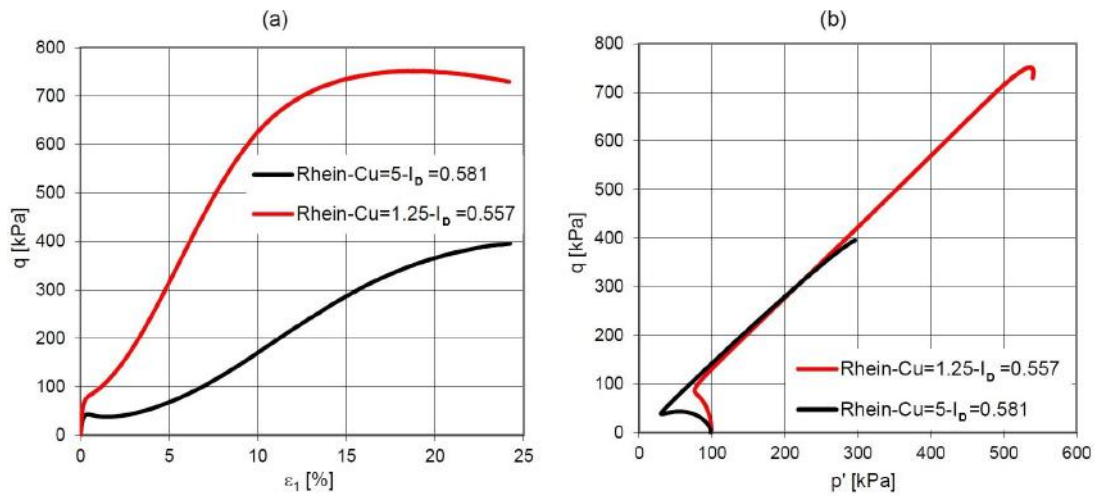
Figure 5.27: Comparison of the (a) $q - \epsilon_1$ and (b) $q - p'$ curves for medium dense Rhein sand constituting two different gradations
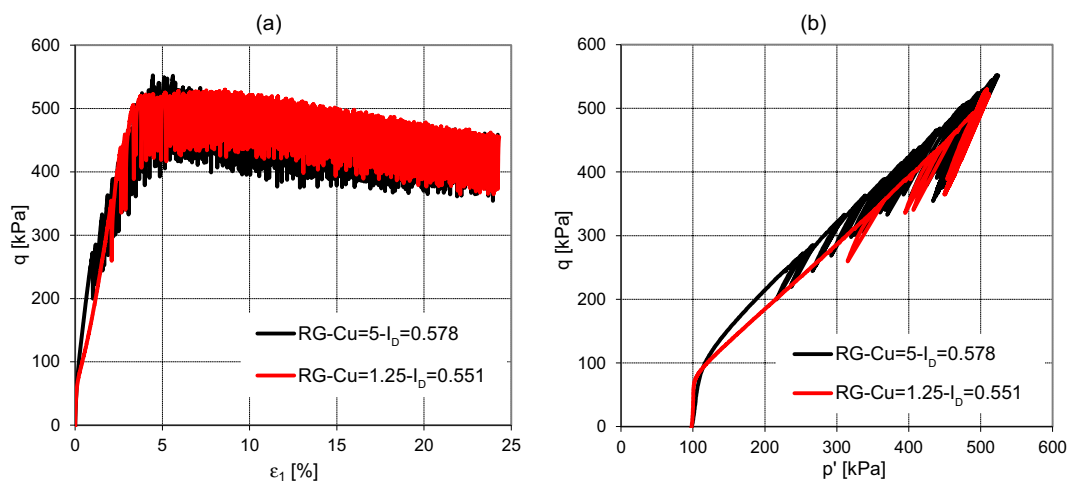
Figure 5.28: Comparison of the (a) $q - \epsilon_1$ and (b) $q - p'$ curves for medium dense round glass beads with two different gradations

iii) Dense specimens

In the dense specimens with $I_D > 0.8$, the differences in the shear strength across various gradations decrease significantly. As evident from Fig. 5.29a, the maximum q for the well-graded angular glass is similar or even slightly larger than that of the uniform angular glass. For the Rhein sand (Fig. 5.30a), the trend is similar to the loose and medium dense cases although the differences are practically negligible at larger axial strains. For the round glass beads (Fig. 5.31a), the uniform mixture shows a rapid increase of strength

in the initial phase of loading, reaching q of 800 kPa, unlike the well-graded mixture, which gains less strength due to an earlier occurence of the numerous 'stick-slip' events. It is interesting to note that the 'stick-slip' effects are more prominent for the well-graded than for the uniform round glass beads. Furthermore, none of the six materials in the dense initial state shows any quasi-steady state behavior throughout, although pronounced phase transformation points are evident for crushed glass (Fig. 5.29b) and Rhein sand (Fig. 5.30b). As was encountered previously in Figs. 5.25b and 5.28b, dense round glass beads also do not display a distinct phase transformation point (Fig. 5.31b). It is interesting to note that the deviatoric stresses at the end of the tests on angular and sub-angular materials are significantly higher (approximately 1300 kPa and 900 kPa for the dense crushed glass and Rhein sand specimens) than for the round glass beads, where the q lies around 520 kPa, similar to the loose and medium dense specimens. This is because for angular materials, the strength gain is mainly governed through interlocking between individual grains which is absent in glass beads, where particle rolling dominates resulting in the 'stick-slip' motion which hampers a steady and continuous increase in q.

Unfortunately, all the dense samples tested were found to have negative pore pressures after a certain axial strain (around 14% for both gradations of crushed glass, 5% for both Rhein sand gradations, and around 2.5-3% for the two gradations of glass beads). Thus, it must be noted that the softening phases at the end of the tests are possibly associated with the negative pore pressure. It will be interesting to repeat some of these tests on dense sands with a higher back pressure to observe their trend at larger axial strains to obtain further results with more confidence.
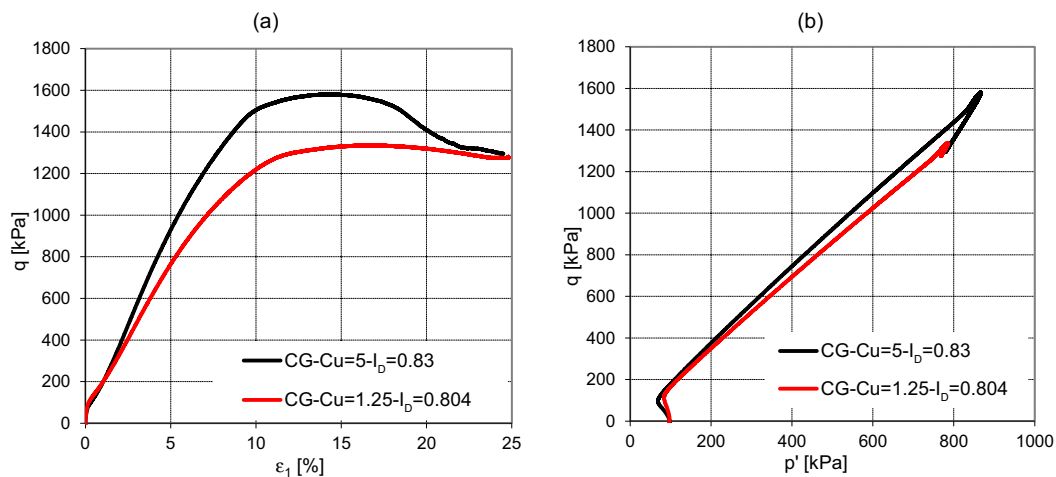
Figure 5.29: Comparison of the (a) $q - \epsilon_1$ and (b) $q - p'$ curves for dense crushed glass with two different gradations
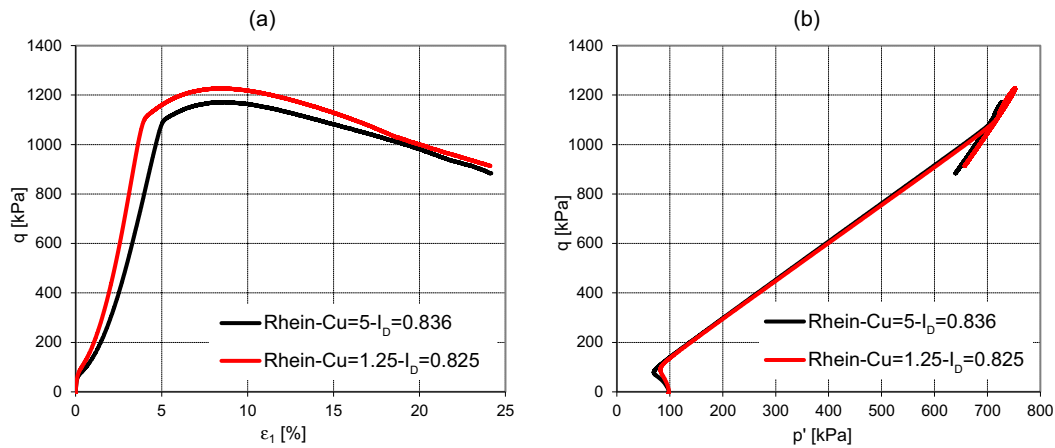
Figure 5.30: Comparison of the (a) $q - \epsilon_1$ and (b) $q - p'$ curves for dense Rhein sand with two different gradations
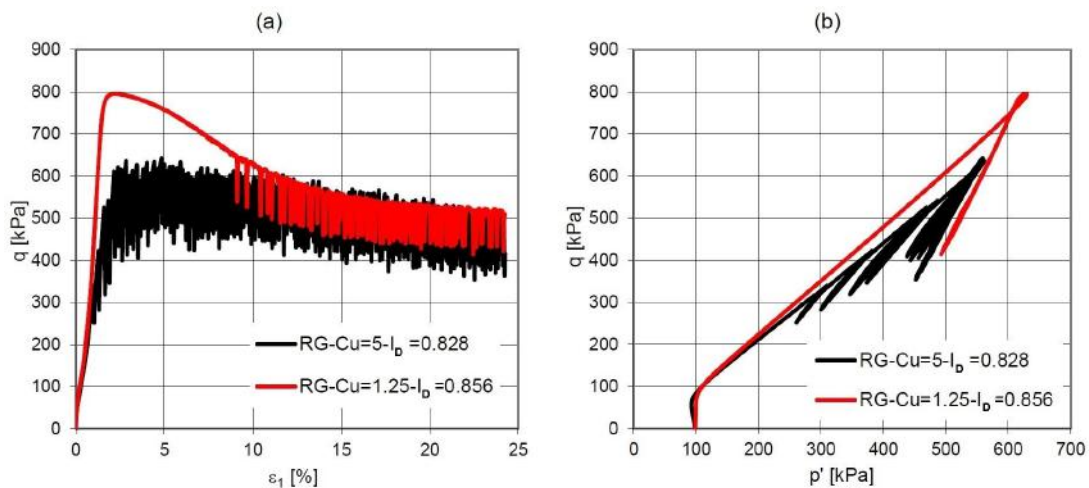
Figure 5.31: Comparison of the (a) $q - \epsilon_1$ and (b) $q - p'$ curves for dense round glass beads with two different gradations

5.4 Cyclic undrained triaxial tests

There are only few studies on granular materials with different uniformity coefficients, particularly more well-graded materials ($C_u > 4$), which partially deliver contradicting results (Kokusho 2007). Furthermore, the combined influence of particle shape and grading on the behaviour of granular soils under cyclic loading, particularly the liquefaction resistance, has not been studied so far. Therefore, one of the major aims of the present study was to investigate the dependence of the undrained cyclic behaviour and the liquefaction resistance of granular materials on both grain shape and grading utilizing a series

of undrained cyclic triaxial tests. The setup used was already explained in Chapter 4. To study the influence of gradation and grain shape, the same six materials as described in Chapter 4 were used: angular crushed glass, sub-angular Rhein sand and glass beads, each tested with the two different uniformity coefficients $C_u = 1.25$ and 5.

5.4.1 Schedule of cyclic undrained triaxial tests

The cyclic undrained triaxial tests were performed under one initial effective confining pressure (p_0'=100 kPa, cell pressure and back pressure were 300 and 200 kPa, respectively) and on two relative densities (loose and medium dense) for each of the materials. For each density, four tests were carried out with different stress amplitudes to obtain the relationship between the cyclic stress ratio CSR and the number of cycles N required for initial liquefaction. Therefore, a total of 48 cyclic undrained tests were performed, 24 for each density. The details of the testing program can be found in Tables 5.6 and 5.7. As mentioned previously, air pluviation was used for sample preparation throughout, assuming that it leads to a similar fabric for all materials and densities.

Typically, B values were 0.96 or higher in all the performed tests. The loading was applied with a constant displacement rate of 0.1 mm/min, which was sufficiently small to enable a uniform distribution of pore water pressure within the sample throughout the test. The loading was applied stress-controlled, which means that the loading direction was reversed once the deviatoric stress reached the pre-defined maximum ($q_{max} = q_{av} + q_{ampl}$) or minimum ($q_{min} = q_{av} - q_{ampl}$) values. One may also refer to this type of loading as a triangular stress-controlled loading. Typically, for the loose specimens, the tests were terminated when an axial strain of 10% was reached or when the magnitude of the effective stress was reduced to zero. For the medium dense specimens, the tests were run until the formation of a 'butterfly-shaped' effective stress path was evident. Generally these tests were stopped when a double axial strain amplitude of 5% was achieved. The number of cycles to liquefaction was noted as the first cycle when the effective stress path passed through $p' = 0$ kPa for the first time.

5.4.2 Test results

a) Loose specimens (0.28 < I_D < 0.37)

Table 5.6 summarizes the various cyclic undrained tests performed on the loose specimens. A total of 24 tests were performed, with each material undergoing four tests with different

Table 5.6: Details of the cyclic undrained tests performed on the loose specimens

Material	C_u	I_D	e_0	q_{ampl} (kPa)	CSR	N_c	C_u	I_D	e_0	q_{ampl} (kPa)	CSR	N_c
Crushed glass	1.25	0.337	0.994	20	0.10	31	5	0.370	0.835	18	0.09	98
		0.326	0.999	22	0.11	5		0.357	0.842	20	0.10	49
		0.342	0.992	25	0.125	5		0.366	0.837	25	0.125	16
		0.335	0.995	30	0.15	1		0.369	0.836	30	0.15	4
Rhein sand	1.25	0.328	0.789	15	0.075	50	5	0.32	0.717	15	0.075	92
		0.302	0.798	18	0.09	5		0.31	0.72	16	0.08	11
		0.298	0.799	20	0.10	2		0.303	0.722	20	0.10	4
		0.306	0.797	25	0.125	1		0.362	0.701	22	0.11	3
Round glass	1.25	0.358	0.685	20	0.10	100	5	0.334	0.483	20	0.10	44
		0.349	0.687	25	0.125	12		0.296	0.488	25	0.125	14
		0.333	0.689	28	0.14	4		0.315	0.485	30	0.15	10
		0.344	0.688	30	0.15	3		0.28	0.491	35	0.175	3

q_{ampl} or CSR $= q_{ampl}/(2p_0')$ values. Furthermore, Table 5.6 provides the relative densities I_D and the post-consolidation void ratios e_0 that were determined at the beginning of the test.

While it was relatively easy to prepare specimens with lower relative densities of 0.28-0.35 for the Rhein sand and the glass beads, this was more difficult for the angular glass, especially for the well-graded mixture where the I_D always varied between 0.35-0.37 post consolidation. To achieve very loose specimens of crushed glass, one could use a different sample preparation method, i.e. moist tamping. However, the present study considers only the air pluviation method to achieve a similar fabric, and it is expected that the small differences in I_D will not affect the interpretation of the test results much.

A typical result from a test on a loose uniform crushed glass specimen ($I_D = 0.337$) subjected to cycles with an amplitude q_{ampl} of 20 kPa is shown in Fig. 5.32. The diagrams represent the deviatoric stress versus the axial strain and the effective stress path in the $q - p'$ plane. Obviously, the cyclic loading leads to an accumulation of excess pore water pressure, which means a decrease of the mean effective stress p' with each further cycle. A significant decrease of effective stress occurs in the last cycle, accompanied by large strains (flow liquefaction). As mentioned previously, the test was terminated at a large axial extension strain fulfilling the failure criterion $|\epsilon_1|=10\%$, which developed as the effective stress path approached the failure line in the extension regime. The formation of 'butterfly' shaped loops were not possible for loose specimens owing to the large sample deformation developing within a single cycle.
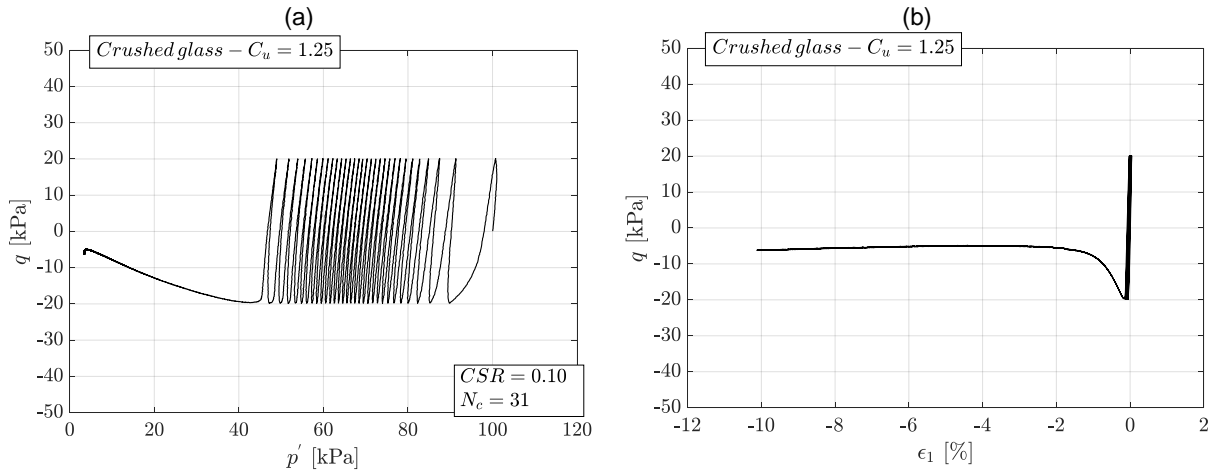
Figure 5.32: (a) $q - p'$ and (b) $q - \epsilon_1$ curves from a test on loose crushed glass with C_u=1.25, $I_D = 0.337$ and CSR=0.10

To compare the cyclic responses for the six tested materials, Figs. 5.33 and 5.34 compile the effective stress paths and stress-strain relationships for a deviatoric stress amplitude q_{ampl} of 20 kPa, corresponding to a CSR value of 0.10. A look at Fig. 5.33a and 5.33b for the two gradations of the crushed glass shows that the number of cycles (N_c) required to obtain a cyclic failure is slightly lower for the uniformly graded specimen (N_c=31) than for the well-graded one (N_c=49). Similar observations are also evident in the case of the Rhein sand (Figs. 5.33c and d) where the number of cycles required for initial liquefaction for the uniformly graded material ($N_c = 2$) is lower than that for the well-graded mixture ($N_c = 4$). Interestingly, it is the other way around for the glass beads, where the poorly graded mixture ($N_c = 100$) needs more cycles to liquefaction than the well-graded one ($N_c = 44$). Looking at the $q - \epsilon_1$ relationships in Fig. 5.34 one can conclude that while the specimens of angular glass and natural sand fail through large deformations developing within a single cycle in the extension regime, the round glass beads of both gradations develop significantly lower axial strains, showing the formation of one wing of the butterfly-shaped loop for the uniform glass beads before reaching $\epsilon_1 = 10\%$ (Fig. 5.34e), and multiple but complete butterfly-shaped loops for the well-graded glass beads (Fig. 5.34f). Under the test condition analyzed in Figs. 5.33 and 5.34 the Rhein sand is the most liquefiable material, while the liquefaction resistance is larger for the crushed glass and the round glass.

Table 5.6 also lists the number of cycles required to achieve initial liquefaction for all the tests performed on loose specimens. In general, the well-graded materials show slightly larger numbers of cycles to initial liquefaction than the uniform ones, especially at larger
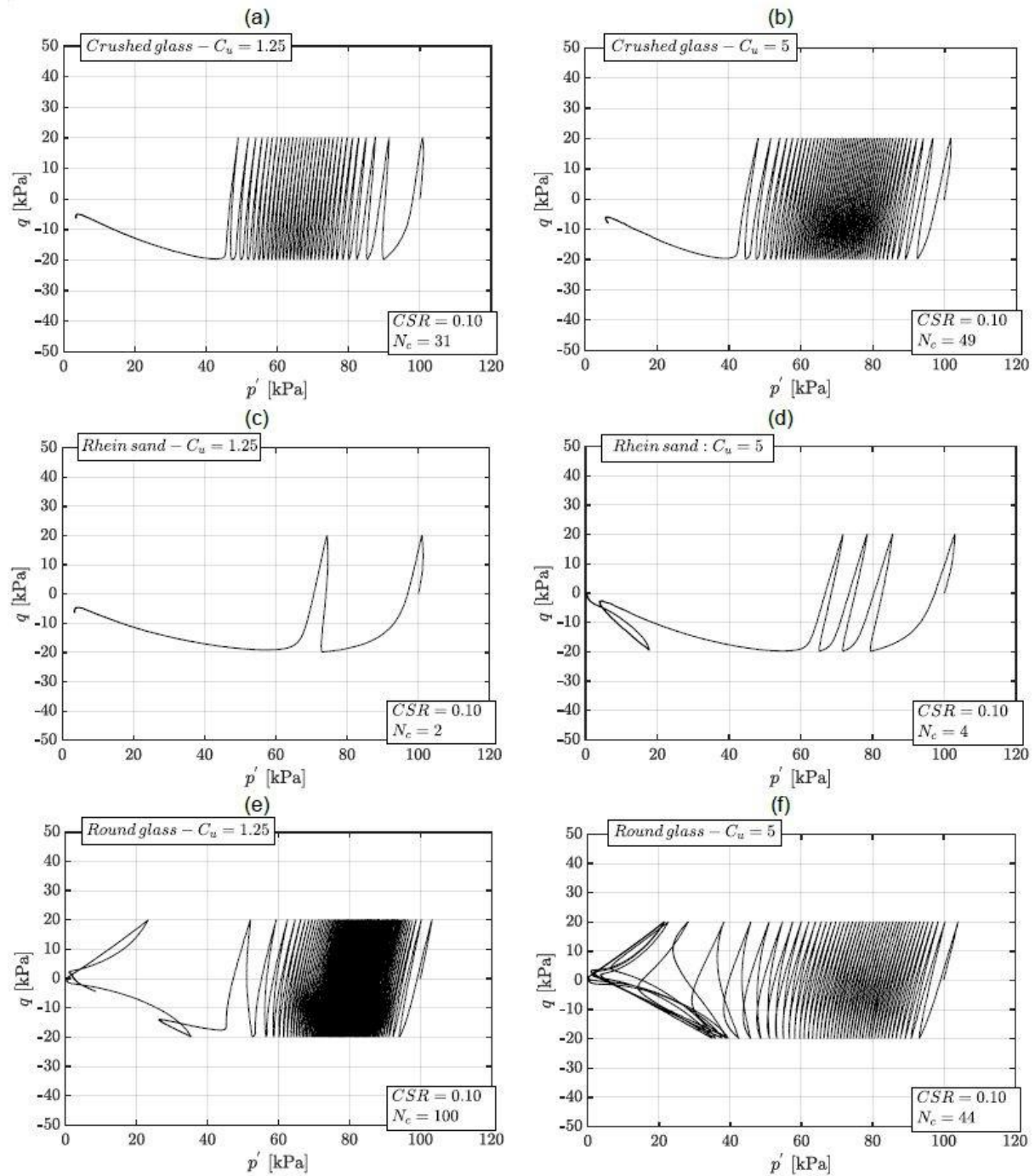
Figure 5.33: Effective stress paths in the $q - p'$ diagram for the six tested materials subjected to a q_{ampl}= 20 kPa corresponding to a CSR=0.10 (loose specimens only)

CSR values. However, at lower CSR values, this trend is opposite for glass beads. For example, for CSRs of 0.10 and 0.125, the well-graded glass beads liquefied earlier than
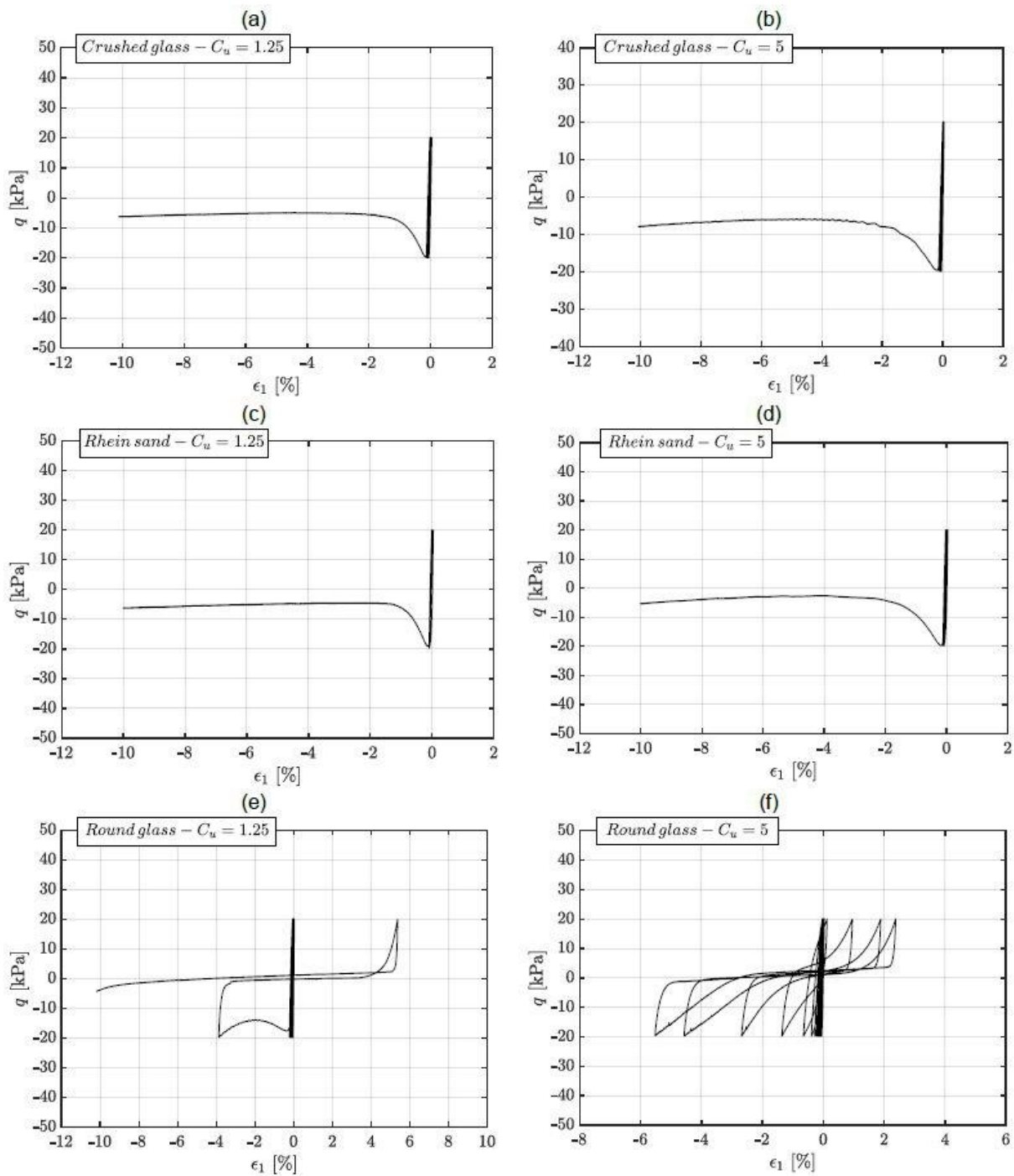
Figure 5.34: Stress-strain relationships in the $q-\epsilon_1$ diagram for the six tested materials subjected to a $q_{ampl}=$ 20 kPa corresponding to a CSR=0.10 (loose specimens only)

the uniformly distributed ones, while at larger CSR values (CSR $\geq$ 0.14), the trend is reversed, with the well-graded mixture requiring larger number of cycles.

Table 5.7: Details of the cyclic undrained tests performed on the medium-dense specimens

Material	C_u	I_D	e_0	q_{ampl} (kPa)	CSR	N_c	C_u	I_D	e_0	q_{ampl} (kPa)	CSR	N_c
Crushed glass	1.25	0.566	0.886	30	0.15	111	5	0.579	0.725	25	0.125	38
		0.541	0.898	35	0.175	9		0.623	0.701	30	0.15	21
		0.554	0.892	38	0.19	6		0.605	0.711	35	0.175	6
		0.563	0.888	40	0.20	1		0.603	0.712	38	0.19	3
Rhein sand	1.25	0.542	0.719	20	0.10	117	5	0.61	0.612	18	0.09	48
		0.588	0.704	25	0.125	45		0.613	0.611	20	0.10	23
		0.56	0.713	30	0.15	7		0.609	0.613	24	0.12	10
		0.564	0.712	40	0.20	1		0.608	0.613	30	0.15	3
Round glass	1.25	0.598	0.647	30	0.15	114	5	0.605	0.441	30	0.15	135
		0.572	0.651	35	0.175	16		0.554	0.449	40	0.20	12
		0.565	0.653	40	0.20	15		0.59	0.443	50	0.25	11
		0.562	0.653	50	0.25	4		0.622	0.438	60	0.30	5

b) Medium-dense specimens ($0.541 < I_D < 0.623$)

Overall 24 tests were performed on the medium-dense specimens of the six different materials (Table 5.7). Different CSRs were employed for the different materials to obtain a wide range of the CSR$-N$ curve.

In Figs. 5.35 and 5.36, the effective stress paths and the stress-strain relationships of the specimens subjected to a stress amplitude q_{ampl} of 30 kPa corresponding to CSR=0.15 are summarized. Since the specimens are relatively denser, all the specimens exhibit butterfly-shaped effective stress loops denoting 'cyclic mobility' which is characterized by an increasing axial deformation with every subsequent stress cycle. For the angular and sub-angular materials, the mode of failure is generally through extension, where the sample undergoes large deformation on the extension side, a characteristic similar to the loose specimens. The only exception is the well-graded Rhein sand where the sample failed under compression (Fig. 5.35d). Also the samples of the glass beads showed a stronger increase of axial strain on the compression side, leading to a failure in compression. The number of cycles for initial liquefaction (defined as the first cycle reaching $p' = 0$ kPa) was larger for the uniformly graded angular and sub-angular specimens (Figs. 5.35a$-$d) than for the corresponding well-graded ones, which is in contrast to the observations for the loose specimens discussed in the previous sub-section. In addition, the number of cycles to initial liquefaction for the round beads increases as one moves from the uniform to the well-graded mixture, again contrasting the observations in the previous case for the
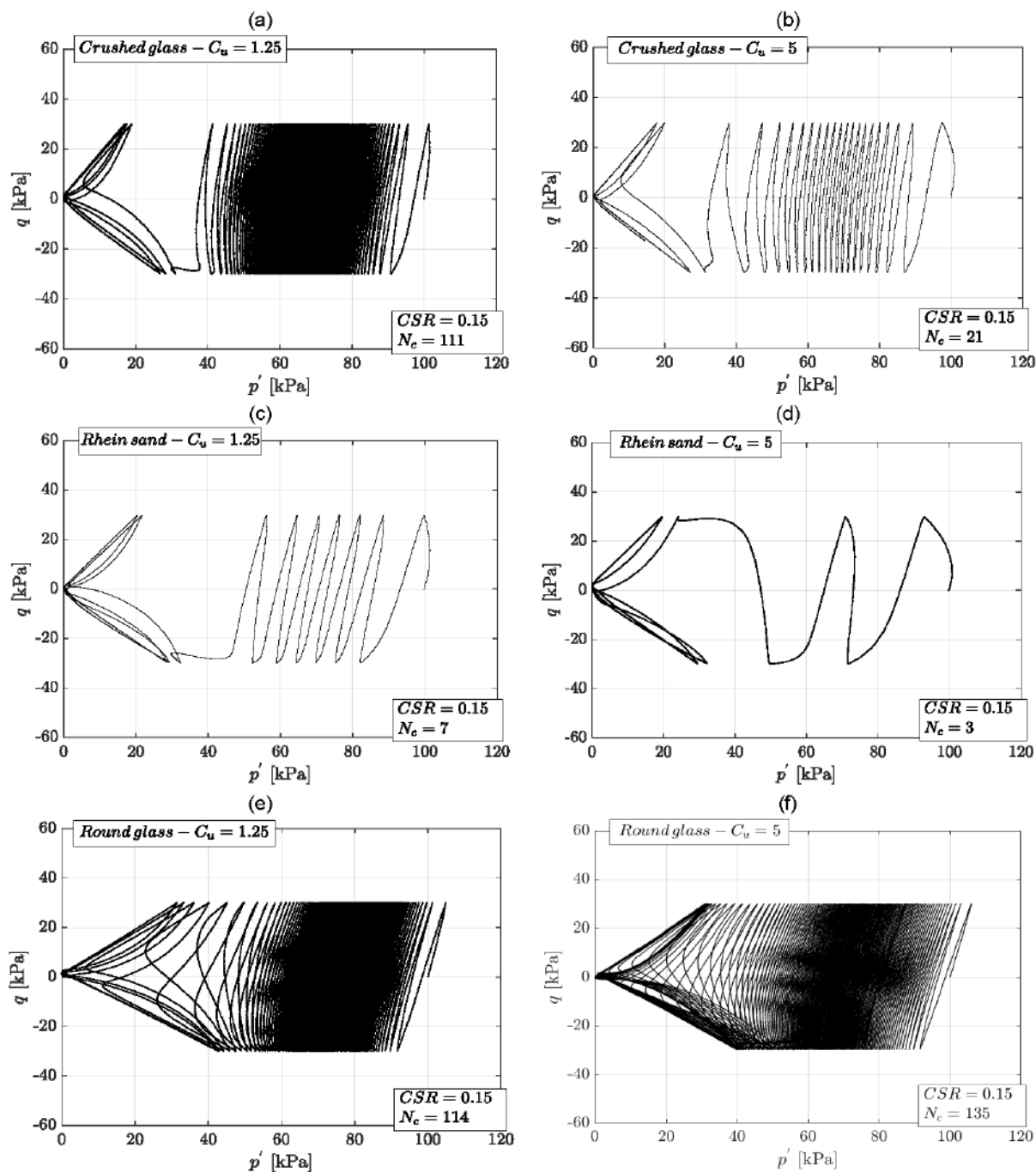
Figure 5.35: Effective stress paths in the $q - p'$ diagram for the six tested materials subjected to a q_{ampl}= 30 kPa corresponding to a CSR=0.15 (medium dense specimens only)

loose specimens. These observations show that the influence of gradation on liquefaction resistance depends on both, relative density and particle shape.
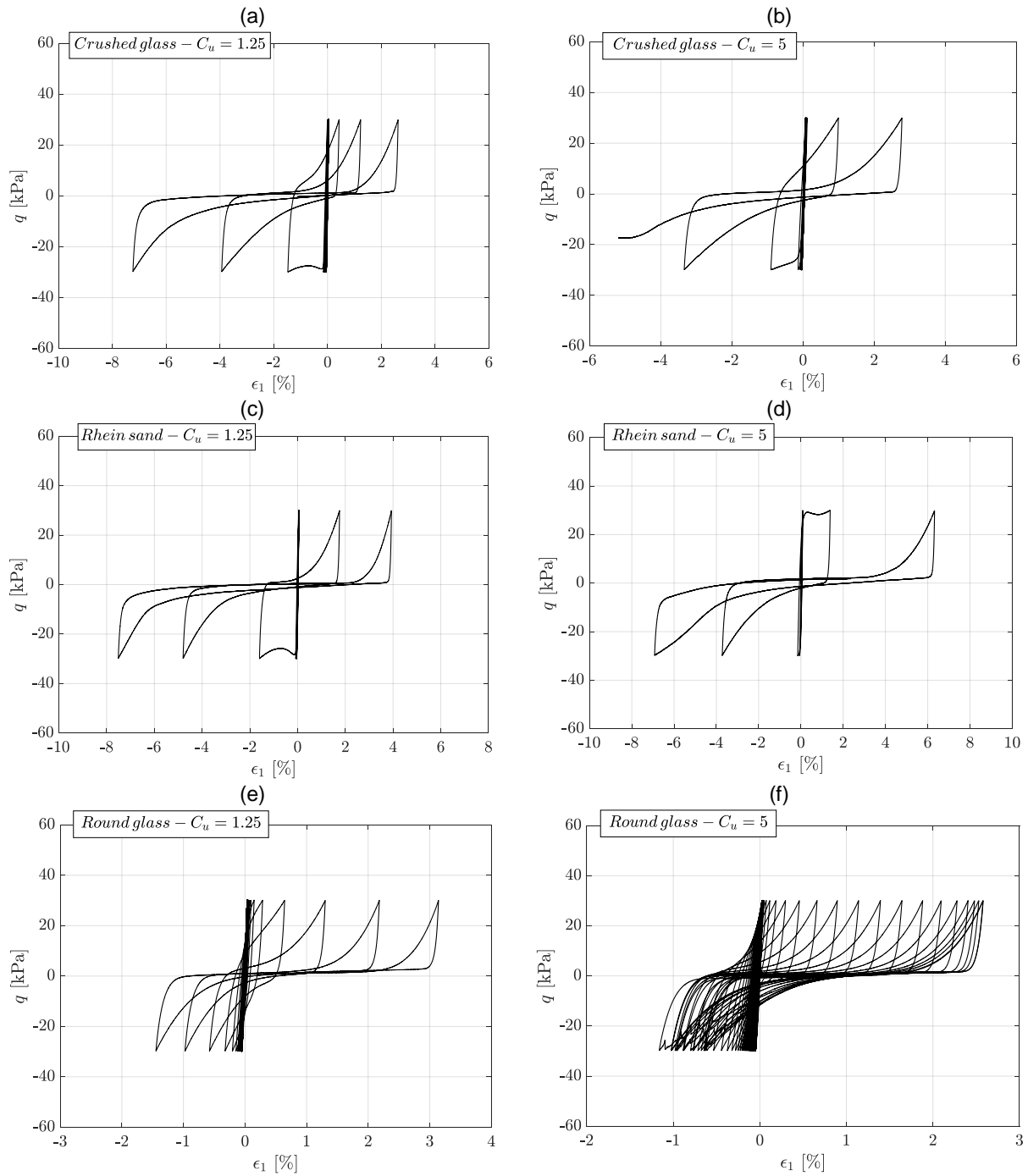
Figure 5.36: Stress-strain relationships in the $q-\epsilon_1$ diagram for the six tested materials subjected to a $q_{ampl}=$ 30 kPa corresponding to a CSR=0.15 (medium dense specimens only)

It is interesting to analyze in more detail the evolution of the axial deformation with subsequent stress cycles after initial liquefaction. Looking at the $q-\epsilon_1$ curves in Fig. 5.36, for the angular glass and sub-angular Rhein sand, the axial deformations develop significantly

faster with increasing number of cycles than for the round beads. Furthermore, in terms of the absolute magnitude the strain loops in extension are larger than the subsequent loops under compression for the uniformly graded crushed glass and Rhein sand, while for the well-graded specimens of these materials, the strain loops are more symmetrical. This means to achieve the maximum and minimum deviatoric stresses within a certain cycle, the deformations in extension and compression are similar. For glass beads, as can be seen from Figs. 5.36e and 5.36f, the build-up of the axial strains is not symmetrical but predominantly compressive with every subsequent cycle post initial liquefaction. This is even more prominent in the well-graded glass beads, where considering the last cycle the maximum ϵ_1 post liquefaction in the extension regime is just over 1%, while in compression, it is more than twice, exceeding 2%. Such larger compressive tendencies in cyclic undrained testing on medium dense to dense specimens were also encountered by other researchers, e.g. Sze & Yang (2014).

Furthermore, one common feature of both the loose and medium dense specimens shown in Figs. 5.33 and 5.35 is the rightward inclination of the effective stress path, which is possibly a result of the inherent anisotropy induced during the process of sample preparation through air pluviation. Past studies (e.g. Kodicherla et al. 2018) have demonstrated that during air pluviation, the preferential particle orientation is in the horizontal direction mainly caused by the gravitational force, resulting in a higher degree of horizontally oriented grains as compared to other preparation methods.

For the other CSRs, the numbers of cycles to initial liquefaction for the six tested materials are also given in Table 5.7. Clearly, the N_c for similar CSR values in the two angular and sub-angular mixtures decreases with increasing uniformity coefficient. For example, at CSR = 0.15, the N_c for angular glass with $C_u = 1.25$ and 5 reads 111 and 21 respectively. Similarly, for the Rhein sand, considering CSR=0.10, the N_c for the uniform and the well-graded materials are 117 and 23 respectively. However, for the glass beads, the trend is opposite: for CSR = 0.15, the N_c for the uniform and well-graded mixtures are 114 and 135 respectively. For higher CSRs, the trend remains similar.

5.4.3 Analysis of cyclic undrained results

5.4.3.1 Effect of particle characteristics on CRR

To analyze the results obtained from the extensive set of cyclic undrained tests with respect to the impact of grain shape and gradation on the liquefaction resistance of loose

granular materials, the number of cycles to initial liquefaction N_c was plotted against the corresponding CSR values in a semi-logarithmic plot as shown in Fig. 5.37. At first glance it is evident that for all three materials the circular points (marked in red) corresponding to the well-graded mixtures generally lie above the black square points representing the uniform mixtures. Thus, generally the cyclic undrained strength of loose well-graded specimens is higher than that of the uniformly graded ones, approximately independent of grain shape.
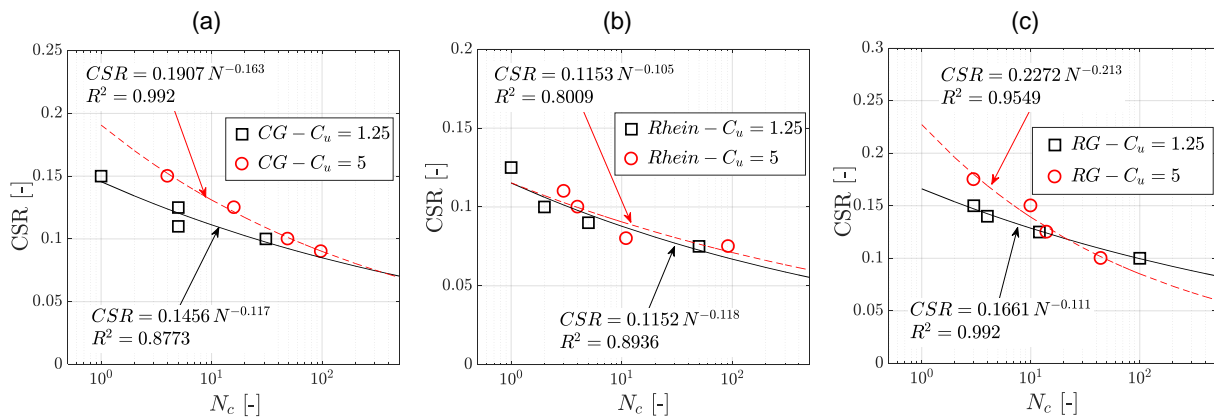
Figure 5.37: CSR against N_c curves for the tested materials considering only the loose specimens: (a) crushed glass, (b) Rhein sand, and (c) glass beads
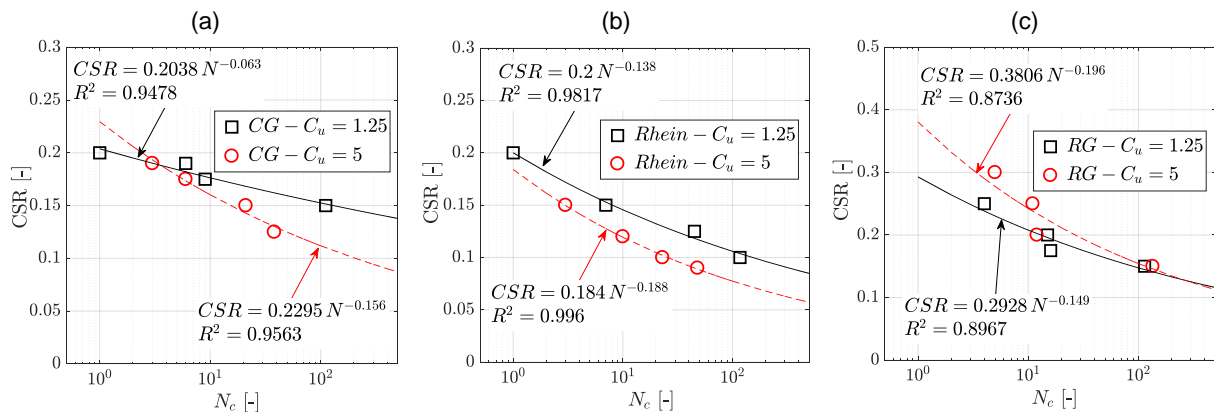
Figure 5.38: CSR against N_c curves for the tested materials considering only the medium-dense specimens: (a) crushed glass, (b) Rhein sand, and (c) glass beads

Similarly, Fig. 5.38 shows the CSR vs N_c curves of the medium-dense samples. The red circular points denoting the well-graded mixtures are observed to lie below the black square points of the uniform mixtures, opposite to the trend found for the loose specimens. One exception to this rule is the case of round beads where the same trend as in the case

of loose specimens is observed (see Fig. 5.38c). Also, it is to be noted that for glass beads at smaller CSR values, the N_c points for the two gradations are closer to each other as compared to higher magnitudes of CSR. Therefore, at smaller CSRs, the particle gradation of the glass beads does not play a significant role in the number of cycles to liquefaction.

For data fitting, the common formulation in the form of Eq. 5.19 was considered following the recommendations of Boulanger & Idriss (2015) and Wei et al. (2020):

$$CSR = a\,(N)^{-b} \qquad\qquad (5.19)$$

where N denotes the number of cycles, while a and b are fitting parameters. The best fit curves are denoted as black solid lines and red dashed lines for the poorly and well-graded materials, respectively, in both Figs. 5.37 and 5.38. The magnitude of the fitting parameters a and b and the R^2 value are also shown in the respective diagrams.

For the purpose of comparison, the cyclic resistance ratio CRR has been generally employed in past studies. The CRR is defined as the CSR causing liquefaction in a given number of cycles (e.g. N=10 or 15) and corresponds to the moment magnitude (M_w) of an earthquake. Usually, the mean number of equivalent uniform cycles of ten is assumed to correspond to an earthquake with M_w= 7 while fifteen cycles are regarded representative for an earthquake of M_w= 7.5 (Idriss 1999; Wei et al. 2020). In the present study, both the CRR values corresponding to $N_c = 10$ and 15 are analyzed. Table 5.8 lists these CRR values obtained from the data in Figs. 5.37 and 5.38 applying Eq. 5.19 with the given fitting parameters.

Table 5.8: Cyclic resistance ratio CRR for the different materials considering the CSR values obtained at N_c=10 and 15 corresponding to moment magnitudes M_w=7 and 7.5 in the event of an earthquake

Density	Material	C_u	$CRR_{N_c=10}$	$CRR_{N_c=15}$	C_u	$CRR_{N_c=10}$	$CRR_{N_c=15}$
Loose	Crushed glass	1.25	0.111	0.106	5	0.131	0.123
	Rhein sand		0.088	0.084		0.091	0.087
	Round glass		0.128	0.123		0.139	0.128
Medium-dense	Crushed glass	1.25	0.176	0.172	5	0.16	0.151
	Rhein sand		0.146	0.138		0.12	0.111
	Round glass		0.208	0.196		0.242	0.224

Fig. 5.39 presents the CRR values for $N_c = 10$ versus the uniformity coefficient for the three different materials. The two diagrams distinguish the loose and the medium dense

samples. For the specimens with the lower density, the CRR values are slightly lower for the uniformly graded materials compared to the well-graded ones. With increasing I_D the trend changes for the angular and sub-angular materials, while it remains unaffected for the grains having a round shape. As a supporting study, one may refer to the work of Vaid et al. (1990), where three different gradations of a natural sand with a common d_{50} and sub-angular shaped grains were tested using samples prepared through water deposition. In that study an increasing cyclic resistance ratio CRR (evaluated as the CSR at $N=10$ in their case) with increasing C_u was reported for loose specimens, whereas for denser specimens with a $I_D > 0.58$, the trend reversed, matching the present observations for angular/sub-angular shaped materials. However, opposite to the current study, the study of Vaid et al. (1990) did not incorporate materials with very angular and very rounded grains.

To the best knowledge of the author, only Hara et al. (2004) made a similar observation in their cyclic tests under a p' of 98 kPa on medium dense ($I_D = 0.50$) samples of rounded river and angular decomposed granite sands having two different C_u values. Considering the CSR at $N = 20$, the CRR for the angular sand was found to decrease with increasing C_u, while the opposite tendency was observed for the round River sand. However, no comment with regards to the influence of grain shape was given: instead it was hypothesized that the undrained cyclic strength is almost independent of particle gradation in contrast to its strong dependency on I_D. Although partially true, their interpretation was incomplete without considering the influence of grain shape as evidenced in the present study.
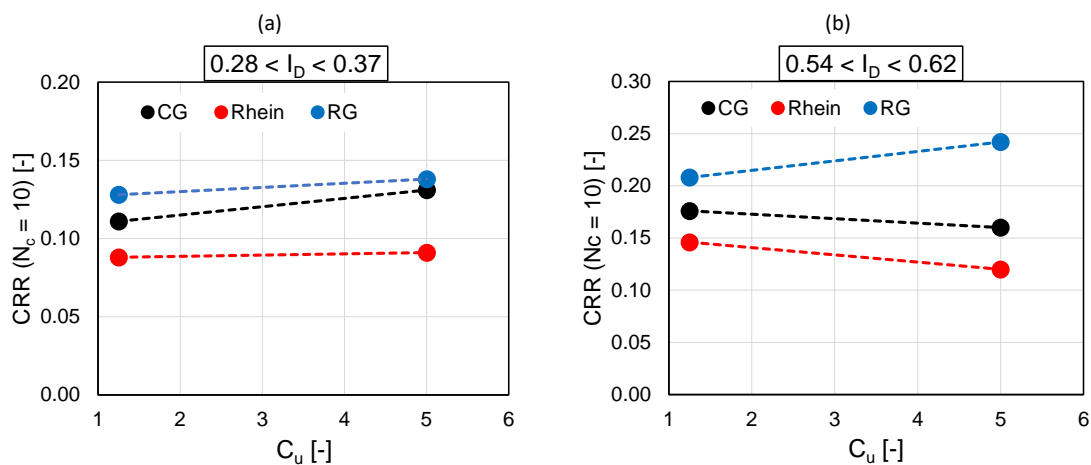
Figure 5.39: Variation of the CRR ($N_c = 10$) against C_u for the tested materials ('CG'= crushed glass; 'Rhein'= Rhein sand; 'RG'= glass beads): (a) loose and (b) medium-dense specimens

Also interesting to note are the different inclinations of the $CSR - N_c$ lines in Figs. 5.37 and 5.38: the curves for the well-graded mixtures are generally steeper than those of the uniform mixtures. This can be also inferred from the differences between the CRR ($N_c = 10$) and CRR ($N_c = 15$) for the tested materials: it generally decreases or remains similar for the loose specimens as one moves from $N_c = 10$ to $N_c = 15$. The parameter b, which denotes the slope of the CSR-N_c curve is generally larger for the well-graded loose specimens except for the Rhein sand (Fig. 5.37b), where the poorly graded sand shows slightly larger values compared to the well-graded one. However, for all the medium dense specimens, the well-graded materials for all the three materials show a larger b compared to the poorly graded ones.

5.4.3.2 Influence of I_D on CRR

In the present study, only two relative densities were studied, corresponding to loose and medium dense specimens. Considering the average post-consolidation I_D for the materials, the variation of the undrained cyclic strengths CRR($N_c = 10$) and CRR($N_c = 15$) with relative density is plotted in Figs. 5.40a and 5.40b, respectively. These diagrams confirm the well-known increase of the liquefaction resistance CRR with increasing relative density, independently of grain shape and gradation.
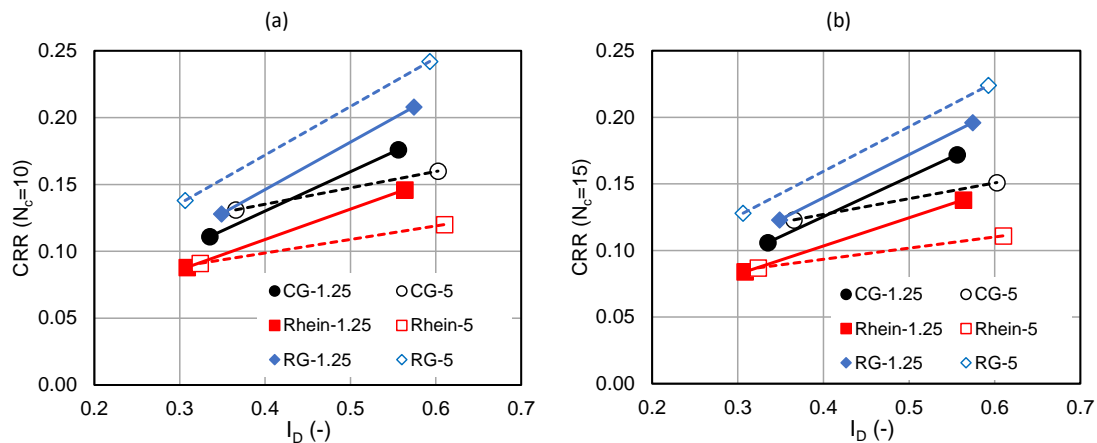
Figure 5.40: Variation of the CRR against I_D for the tested materials ('CG'= crushed glass; 'Rhein'= Rhein sand; 'RG'= glass beads): (a) $N_c = 10$ and (b) $N_c = 15$ referring to $M_w = 7$ and 7.5 respectively. The number next to the material denotes the C_u

Generally, the variation of the CRR against I_D can be considered linear (Vaid et al. 1990). Therefore, considering the two densities for each material, a linear trendline is fitted to the

data in Fig. 5.40. A clockwise rotation of the trendlines for the angular and sub-angular materials can be seen with increasing C_u values (black and red solid and dashed lines). However, the inclination of the trendline remains largely unaffected by variations in C_u in the case of round glass beads (denoted by the blue solid and dashed lines). The inclination of the trendline is denoted as I. The I values obtained from the fitting of the data in Fig. 5.40 are presented in Fig. 5.41 as functions of the uniformity coefficient. Evidently, a decrease in the slope I with increasing C_u occurs for crushed glass and Rhein sand, while it remains practically constant for the glass beads. For increasing M_w, the magnitude of I decreases although the trends remain similar.
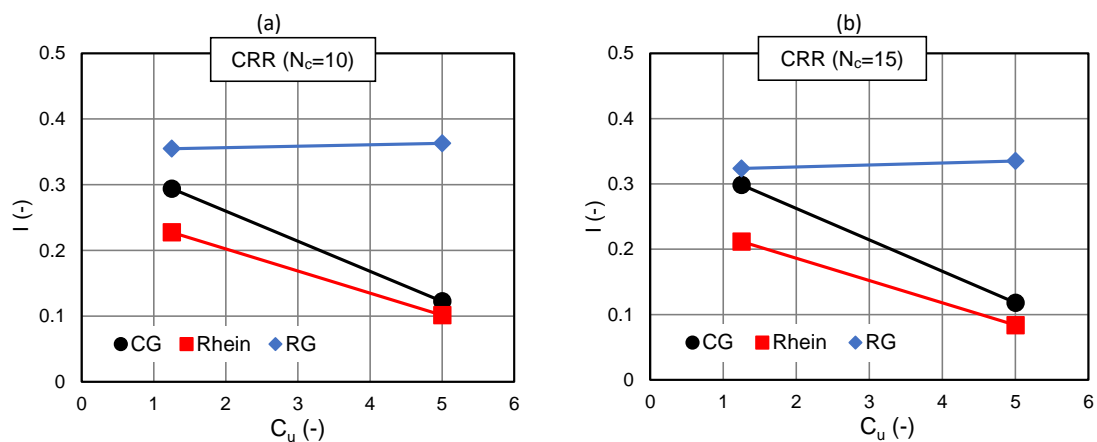
Figure 5.41: Variation of the slope of the CRR$-I_D$ curves shown in Fig. 5.40 against the two C_u values tested in the present study

5.4.3.3 Influence of regularity ρ on $CSR - N_c$ curves and CRR

Fig. 5.42 shows the $CSR - N_c$ curves for the poorly graded materials tested under both loose and medium dense conditions. In case of the loose specimens (Fig. 5.42a), the $CSR-N_c$ curves are almost parallel and do not intersect. The curve for the glass beads lies at the top, suggesting a higher liquefaction resistance, followed by the angular crushed glass. The Rhein sand shows the lowest liquefaction resistance. In a similar way, for the medium dense specimens (Fig. 5.42b), the liquefaction resistance for glass beads is the largest while being the least for Rhein sand. The curve for the crushed sand lies in between but shows a lower inclination. Apparently, the influence of grain shape is not clear since there is no definite trend.

A comparison of the CRR ($N_c = 10$) values against the regularity ρ for the tested materials under loose and medium dense relative densities is presented in Figs. 5.43a and 5.43b,
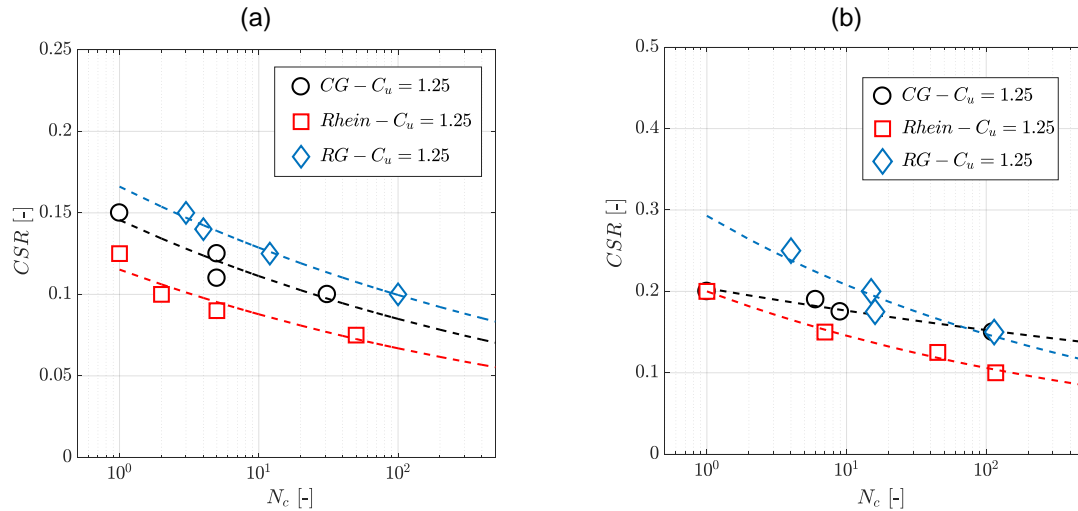
Figure 5.42: Comparison of the CSR values against N_c for the three poorly graded materials ($C_u = 1.25$): (a) loose specimens, and (b) medium dense specimens

respectively. The Rhein sand shows the least CRR for both the poorly and the well graded cases under both relative densities. Furthermore, the influence of gradation on loose Rhein sand seems to be minimal as the CRR ($N_c = 10$) values lie close to each other. However, the difference increases at higher densities, where the poorly graded Rhein sand shows larger liquefaction resistance. For loose crushed glass, a similar trend is observed where the well-graded mixture shows larger liquefaction resistance than the uniform one. However, with increasing density the trend reverses. The glass beads show the largest liquefaction resistance under both densities. Additionally, the loose well-graded mixture shows a larger resistance compared to the poorly graded one, and this difference increases at higher densities. To summarize, the higher the C_u and I_D of glass beads, the larger the liquefaction resistance.

5.5 Correlating the cyclic and monotonic undrained responses

The cyclic loading response has been found to be strongly linked with the monotonic loading response under isotropic conditions (Mohamad & Dobry 1986; Alarcon-Guzman et al. 1988).

It was concluded previously that C_u does not influence the slope M of the steady state lines in the $q - p'$ plane. Therefore, for the two gradations, Fig. 5.44 shows the average slopes
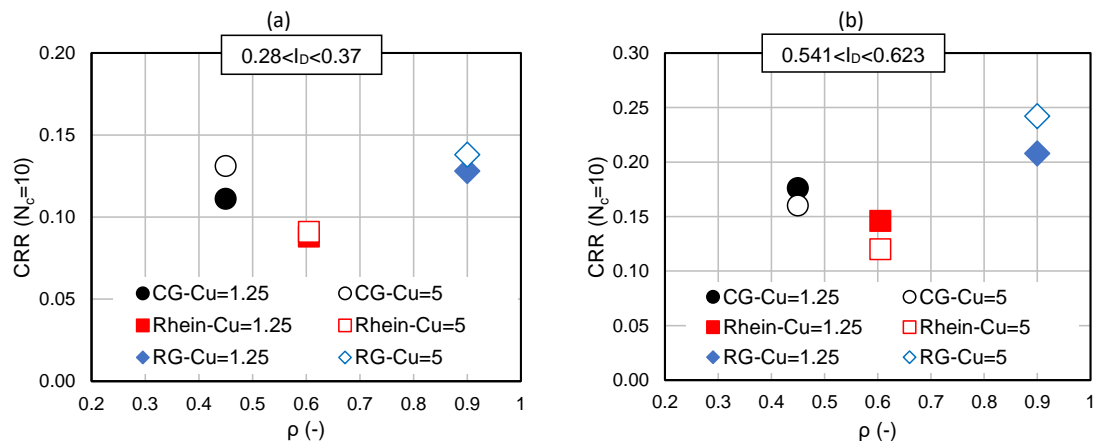
Figure 5.43: Comparison of the CRR ($N_c = 10$) values against regularity ρ for the tested materials ($C_u = 1.25$ and 5): (a) loose specimens, and (b) medium dense specimens

obtained from the monotonic tests superimposed on the $q - p'$ curves of loose specimens in monotonic and cyclic tests, where the latter ones are prone to failure through the mode of extension except the glass beads. The same diagrams are plotted for the medium-dense specimens in Fig. 5.45, where the same slope M is visible for the compression wing of the butterfly-shaped effective stress paths. For the loose specimens, large deformations in the extension regime resulted in sample necking. To assess the failure lines under extension, additional monotonic extension tests must be performed.

It is to be recalled that for both the loose and medium-dense specimens, the monotonic strength was smaller for the well-graded angular/sub-angular materials than for the corresponding uniform mixtures, which was in accordance with Vaid et al. (1990). However, the influence of gradation decreased for the angular/sub-angular materials with increasing I_D, eventually vanishing for $I_D > 0.8$, probably due to development of negative pore water pressures. No influence of gradation was visible for round glass beads under all the three densities tested. In the cyclic tests, the N_c to initial liquefaction for loose specimens increased slightly with an increasing uniformity coefficient irrespective of the grain shape, but for medium-dense specimens, the angular and sub-angular materials showed a strong decrease in N_c with C_u while for glass beads the opposite trend was observed.

Therefore, it can be concluded that under similar boundary conditions, the undrained monotonic response of angular and sub-angular granular materials are affected by the gradation, with this influence decreasing at higher values of I_D. The undrained cyclic response denoted in terms of CRR ($M_w = 7/7.5$) depends on both the gradation as well as the I_D. For round materials, the influence of gradation is insignificant in monotonic
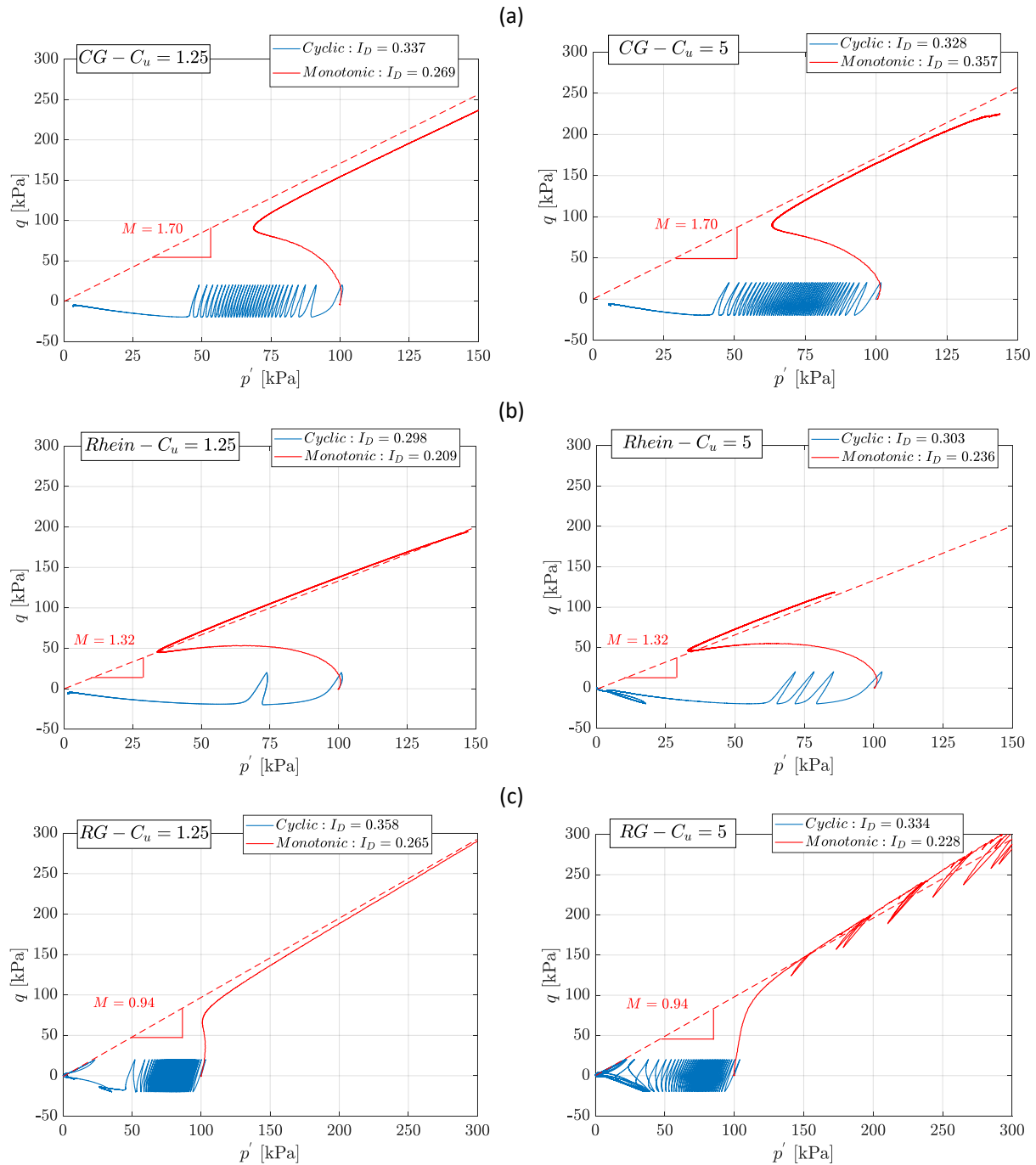
Figure 5.44: Comparing the static and cyclic responses (CSR=0.10) for the loose samples. The dashed line denotes the slope of the steady state obtained from monotonic tests, details of which are provided in Chapter 5.

compression tests, while in the cyclic tests the cyclic undrained strength CRR increases with increasing C_u.
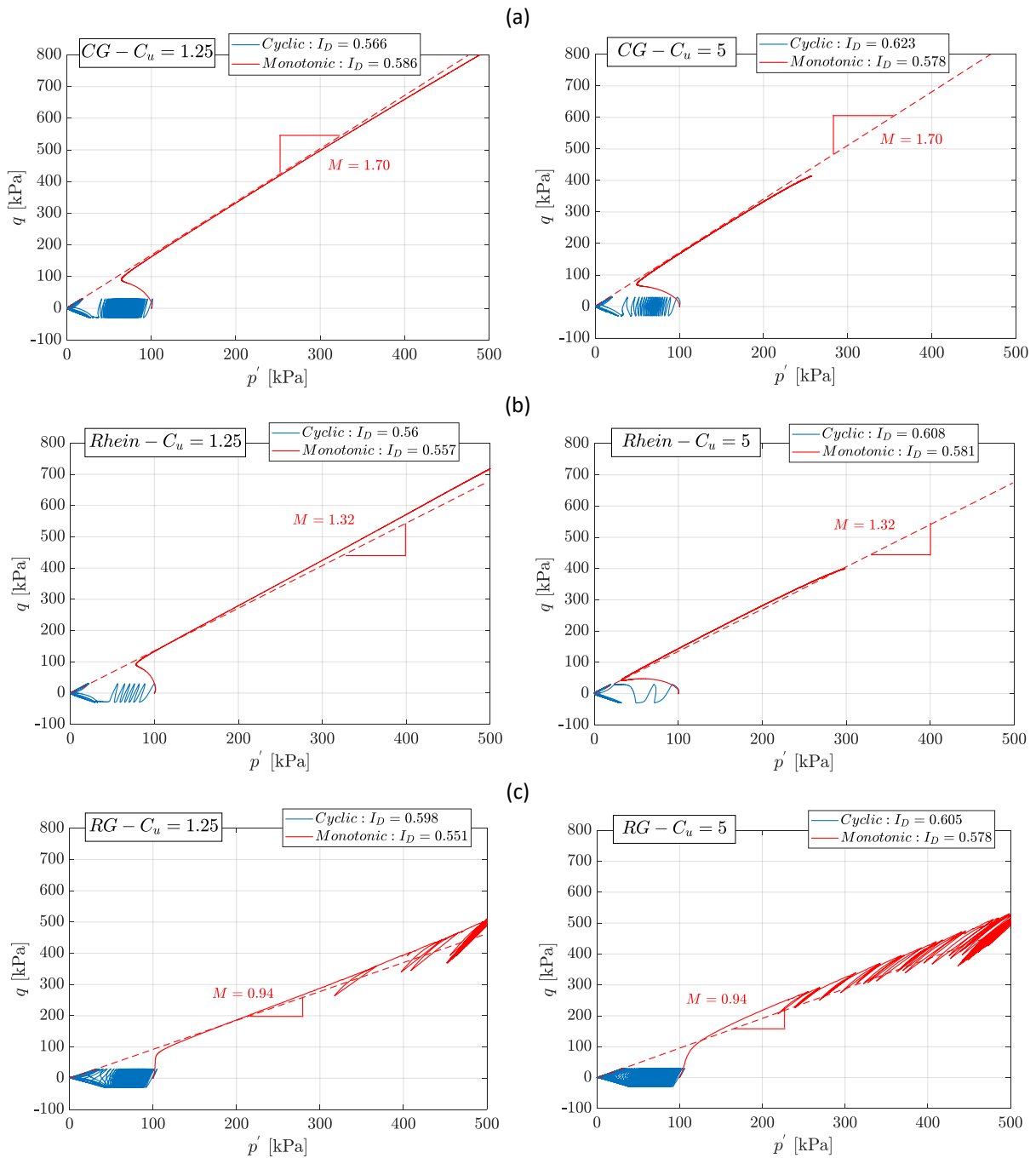
Figure 5.45: Comparing the static and cyclic responses (CSR=0.10) for the medium dense samples. The dashed line denotes the slope of the steady state obtained from monotonic tests, details of which are provided in Chapter 5.

5.6 Summary

The aim of this chapter was to study the effect of the particle shape and gradation on the monotonic drained and undrained behavior as well as the cyclic undrained behavior of granular materials, based on an extensive series of monotonic and cyclic triaxial tests. The main observations can be summarized as follows:

5.6.1 Monotonic behavior

- In general, materials with angular grains (having low values of regularity ρ) exhibit comparatively higher shear strength than the materials with rounded particles. The presence of interlocking in angular materials is one reason for the increased shear strength, which is significantly lower for rounded materials.

- For round glass beads, during drained shear a very small initial contraction is only noticed even for loose samples after which the volume change behaviour becomes dilative. The overall volume changes of glass beads remain small, which correlates with the much smaller difference between the maximum and minimum void ratio for rounded materials as compared to angular ones.

- The peak and steady state friction angles are significantly affected by the particle shape. Crushed glass displays much higher values of both the peak and steady state angles as compared to the Rhein sand and round glass beads. Besides, confirming well-know relations, an increase in relative density causes an increase in the peak friction angle, while the steady state angle remains unaffected by density changes.

- The steady state curves in the $e - p'$ diagram derived from undrained monotonic tests, as well as parameters such as the intercept and the slope of the $e - p'$ curve are dependent on the grain shape. Both the slope and the intercept of the $e - p'$ curve decrease with increasing regularity, which is in line with previous findings in the literature. Besides the particle regularity, the uniformity coefficient (C_u) influences the steady state angle, and a mathematical model for predicting ϕ_{cs} has been presented incorporating both parameters.

- The monotonic undrained strength of angular and sub-angular materials was found to decrease with an increasing C_u, while for round glass beads, it was found C_u-independent. However, with increasing densities, the apparent difference in the shear

strength of materials with subangular or angular particle shape decreases and becomes practically negligible for dense specimens ($I_D > 0.8$). The slope of the steady state line was found to be independent of C_u for all tested materials.

5.6.2 Cyclic behavior

- In the undrained cyclic tests the loose specimens of angular/sub-angular materials failed mainly in the extension regime, undergoing large axial strains within a single cycle eventually leading to $p' = 0$ kPa. For the loose glass beads, the development of axial deformation after initial liquefaction (i.e. reaching $p' = 0$ kPa for the first time) occured slower, leading to some kind of cyclic mobility. Similarly for medium-dense specimens, the strains progressively developing after reaching initial liquefaction were much smaller for glass beads than for the angular/sub-angular materials. However, all medium dense samples showed a cyclic mobility, irrespective of the grain shape.

- The inclination of the $CSR - N_c$ curves are generally larger for the well-graded materials than for the uniformly graded ones.

- Considering two different values of the earthquake magnitude M_w, the CRR is found to increase with an increase in C_u for loose samples of the angular/sub-angular materials, while the trend is reversed in medium-dense specimens. For glass beads, CRR increases with C_u irrespective of the I_D.

- Both gradations of Rhein sand were found to show a lower liquefaction resistance represented in terms of the CRR (CSR at $N_c = 10$) than the corresponding angular glass or glass beads under both tested relative densities. The CRR values were the largest for glass beads for both gradations tested.

- The CRR increases with I_D. Assuming a linear relationship the slope of the CRR$-I_D$ curve is larger for uniform angular/sub-angular materials compared to the corresponding well-graded mixtures, implying a clockwise rotation of the $CRR-I_D$ lines with increasing C_u. In contrast, the inclination of the $CRR-I_D$ curve is independent of C_u for glass beads.

- While the monotonic response depends on the gradation for angular/sub-angular materials, the undrained cyclic response is also dependent on both the gradation as well as the I_D. For round materials, the influence of gradation is insignificant in

monotonic compression tests, while CRR needed to initiate liquefaction increases with increasing C_u.

6 Influence of particle characteristics on dynamic properties

6.1 Introduction

Numerous experimental studies in the past have shown that the mechanical properties of geo-materials subjected to dynamic events, e.g. earthquake, traffic, machine foundations, etc. are strongly dependent on the amplitude of deformation or vibration. The amplitude-dependent "dynamic soil properties", like shear modulus, shear or compression wave velocity and damping play an important role in the design of geotechnical structures subjected to dynamic loading (Payan et al. 2016). This chapter presents the various results obtained from resonant column (RC) tests or compression (CP) and bender (BE) element measurements and discusses the influence of the particle size and shape on the small-strain dynamic properties of granular materials.

6.2 On the effect of particle shape on wave velocity

A comprehensive review of literature did not lead to clear conclusions regarding the suitability of various grain morphology descriptors in characterizing various dynamic soil properties. Therefore, it remains difficult to estimate certain parameters describing dynamic soil behavior considering particle characteristics, particularly grain shape. In this section, an attempt is made in that direction with respect to the shear wave velocity. The three granular materials having the same $C_u = 5$ and $d_{50} = 0.42$ mm with different grain shapes, namely crushed angular glass, sub-angular Rhein sand and round glass beads as described previously (see Table 4.1) are considered for that purpose.

To obtain high quality images, the scanner CanoScan 9000F (Section 3.3.2) was used. Fig. 6.1 shows the obtained raw images for grains falling within the range of sizes 0.315-0.5 mm.
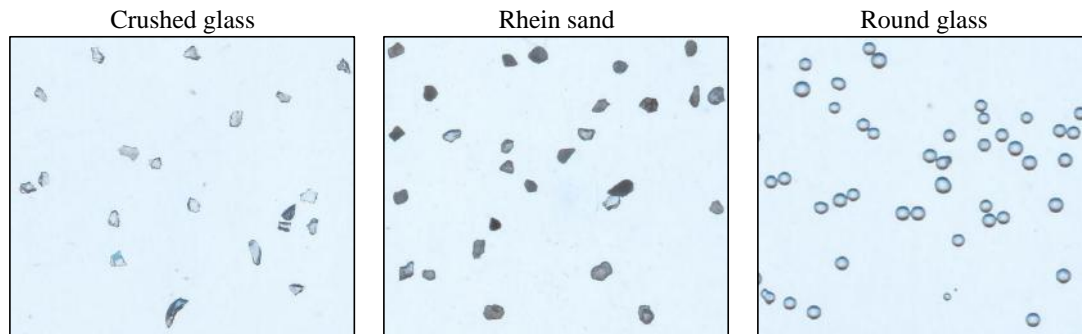
Figure 6.1: Scanner images of the tested materials considering the grains falling between 0.315-0.5 mm only

6.2.1 Quantification of shape parameters through image analysis

In order to obtain the various grain shape parameters through image analysis, the grains were sieved into three fractions: the larger size fraction in the range 0.5-1 mm, the medium size fraction between 0.315-0.5 mm (shown in Fig. 6.1) and the smallest size fraction between 0.063-0.315 mm. This was done to study the variation of grain shape along different grain sizes. The analysis was predominantly performed using the ImageJ approach since a large number of shape parameters can be obtained simultaneously. However, to obtain specific shape parameters (e.g. roundness, different forms of sphericity and regularity), the MATLAB approach was employed. A minimum of 50 grains of each size fraction were analyzed, since no significant difference is expected when using larger numbers of grains (Cox & Budhu 2008). Nevertheless, for the smaller grain sizes, a comparatively larger number of grains were analyzed (more than 70) as more grains were captured using the scanner at once. The values of the shape parameters are listed in Table 6.1.

Influence of grain size on the morphology parameters

Fig. 6.2 shows the variation in the grain shape parameters with varying grain sizes obtained for the crushed angular glass and the Rhein sand only as the shape parameters of round glass beads were similar throughout since they were manufactured by the same method. In general, the shape descriptors do not change significantly with grain size in the adopted materials, although some small variations are evident. For example, from Fig. 6.2a, the aspect ratio of the smallest sized fraction was slightly smaller than for the largest fraction, which consequently implied slightly larger circularity values (Fig. 6.2b). Also, a similar trend for the mean roundness (Fig. 6.2j) is obtained. However, for prac-

tical purposes, the minute differences encountered may be neglected for the majority of the shape descriptors.
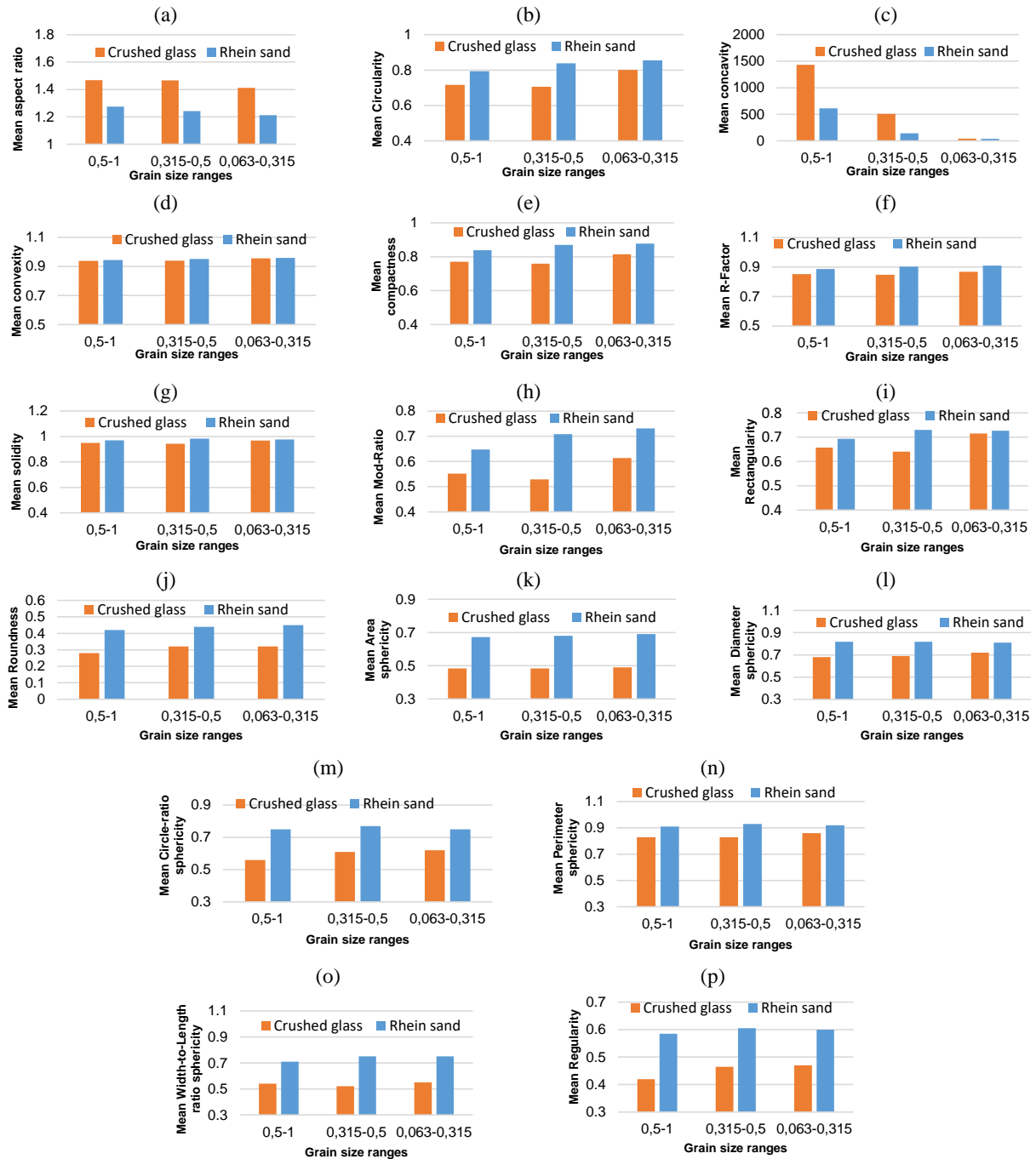
Figure 6.2: Comparison of the grain shape parameters of various grain sizes for the crushed glass and Rhein sand

The only exception refers to the values of concavity (Fig. 6.2c) which shows a large increase in the magnitude with increasing grain size. This is because concavity refers to the area
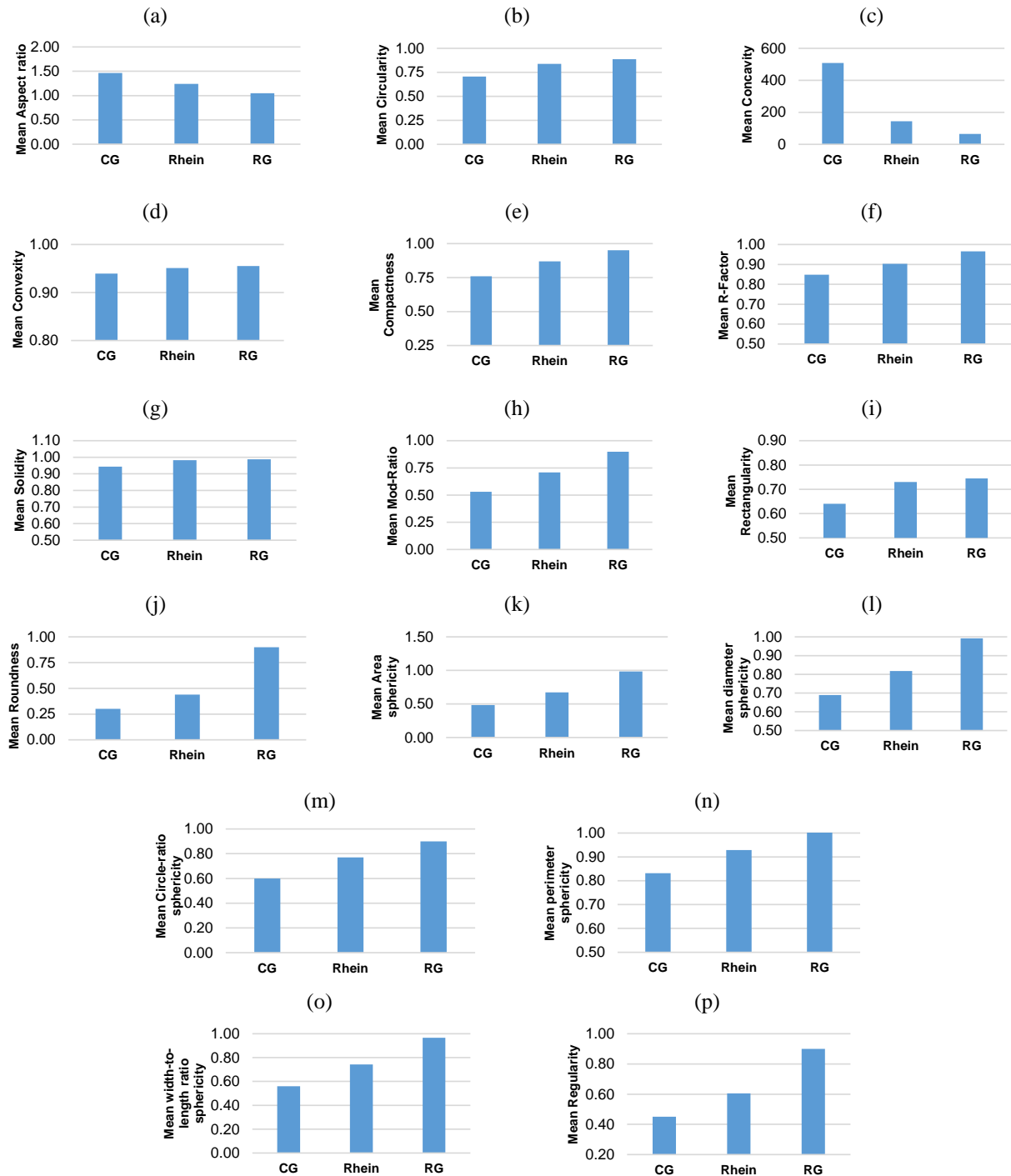
Figure 6.3: Variation of the grain shape parameters of the three materials for the grain sizes in the range 0.315-0.5 mm

between the convex hull and the actual grain area. For analyzing grains under similar magnification, the larger grains have a larger area of the convex hull as well as the grain itself, and the difference between them is also significantly larger. Therefore, it does not

Table 6.1: Different morphological values for the tested materials

Material	Ar	$Circ$	Cv	Cx	$Comp$	RF	So	MR
Crushed glass	1.467	0.706	508.42	0.940	0.759	0.849	0.944	0.529
Rhein sand	1.241	0.839	143.930	0.951	0.870	0.903	0.983	0.709
Glass beads	1.048	0.887	64.993	0.955	0.952	0.965	0.987	0.898
Material	$Rect$	R	S_A	S_D	S_C	S_P	S_{WL}	ρ
Crushed glass	0.640	0.320	0.484	0.690	0.610	0.830	0.520	0.465
Rhein sand	0.730	0.440	0.680	0.818	0.770	0.930	0.750	0.605
Glass beads	0.745	0.900	0.984	0.992	0.900	1.000	0.967	0.900

make sense to compare the concavity values for different grain sizes if not under the same magnification for individual grains.

Variation of the morphology parameters with varying grain shape

Fig. 6.3 compares the shape parameters for the three materials considering the grains lying in the size range 0.315-0.5 mm only. In general, the aspect ratio and the concavity decrease as one moves from crushed angular glass over the natural sand to round glass beads. At the same time, some of the parameters (circularity, compactness, R-Factor, Mod-Ratio, rect-angularity, roundness, area sphericity, diameter sphericity, circle-ratio sphericity, perimeter sphericity, width-to-length ratio sphericity and the regularity) are found to strongly increase, whereas a couple of them (convexity and solidity) show only a slight increasing tendency.

6.2.2 Variation of v_s for the tested materials

Similar to G_{max}, the dependence of the shear wave velocity v_s on void ratio e and the mean confining pressure p' is represented by the model of Hardin (Hardin & Black 1966). For the void ratio function $f(e)$, the popular Jamiolkowski expression is considered with the fitting parameter d while the pressure dependence is indicated using fitting parameters A and n:

$$v_s = A \, p_a \left(\frac{p'}{p_a}\right)^n f(e) \tag{6.1a}$$

$$f(e) = e^{-d} \tag{6.1b}$$

Table 6.2: Fitting parameters of the variation of the shear wave velocity against the void ratio and confining pressure

Material	$d_{i,avg}$ [-]	n [-]	A [-]
Crushed glass	0.53	0.26	1.54
Rhein sand	0.47	0.24	1.77
Glass beads	0.27	0.28	1.79

For each material three to four samples with significantly different relative densities were prepared and tested ($I_{D0} = 0.58 - 0.95$ for crushed glass, $0.52 - 0.96$ for natural sand and $0.51 - 1.06$ for glass beads). Each sample was tested under four different isotropic stresses in succession, with effective mean stresses of $p' = 50, 100, 200$ and 400 kPa. Fig. 6.4 shows the variation of the shear wave velocity against the void ratio and the confining pressure (normalized by atmospheric pressure p_a) for the three materials along with the fitted void ratio and pressure functions. The solid lines in the $v_s - e$ diagrams correspond to the void ratio function with the best-fit d parameters for each pressure. The dashed lines represent the void ratio function evaluated with $d_{i,avg}$, which is the averaged d for the confining pressures of 50, 100, 200 and 400 kPa. The values of the fitting parameters A, n and $d_{i,avg}$ are listed in Table 6.2.

It is known that materials with angular grains have larger void ratios than materials with round grains at similar relative densities (Cho et al. 2006; Sarkar et al. 2019b). Consequently, a sample of angular material has a smaller number of grains in a given volume. At the same time, angular materials are highly irregular in shape, which means a higher number of contacts between grains in a given volume, occasionally having multiple points of contacts between two grains (Tian et al. 2018). Furthermore, for increasing densities in angular materials, the normal contact forces between grains decrease but the number of force chains increases (Liu & Yang 2018) - this results in a faster wave transmission, and consequently, a larger v_s. For round grains, as the magnitudes and the difference between e_{max} and e_{min} are comparatively smaller than the corresponding values for angular materials, there is not a significant change in the number of contacts between a loose and dense specimen, and consequently the magnitude of the normal contact forces. Thus, the variation of v_s with density is comparatively smaller than for an angular material - this results in a flatter slope in the $v_s - e$ curve (refer to Figs. 6.4a-c), which is also evident from the magnitude of the fitting parameter d in Table 6.2.
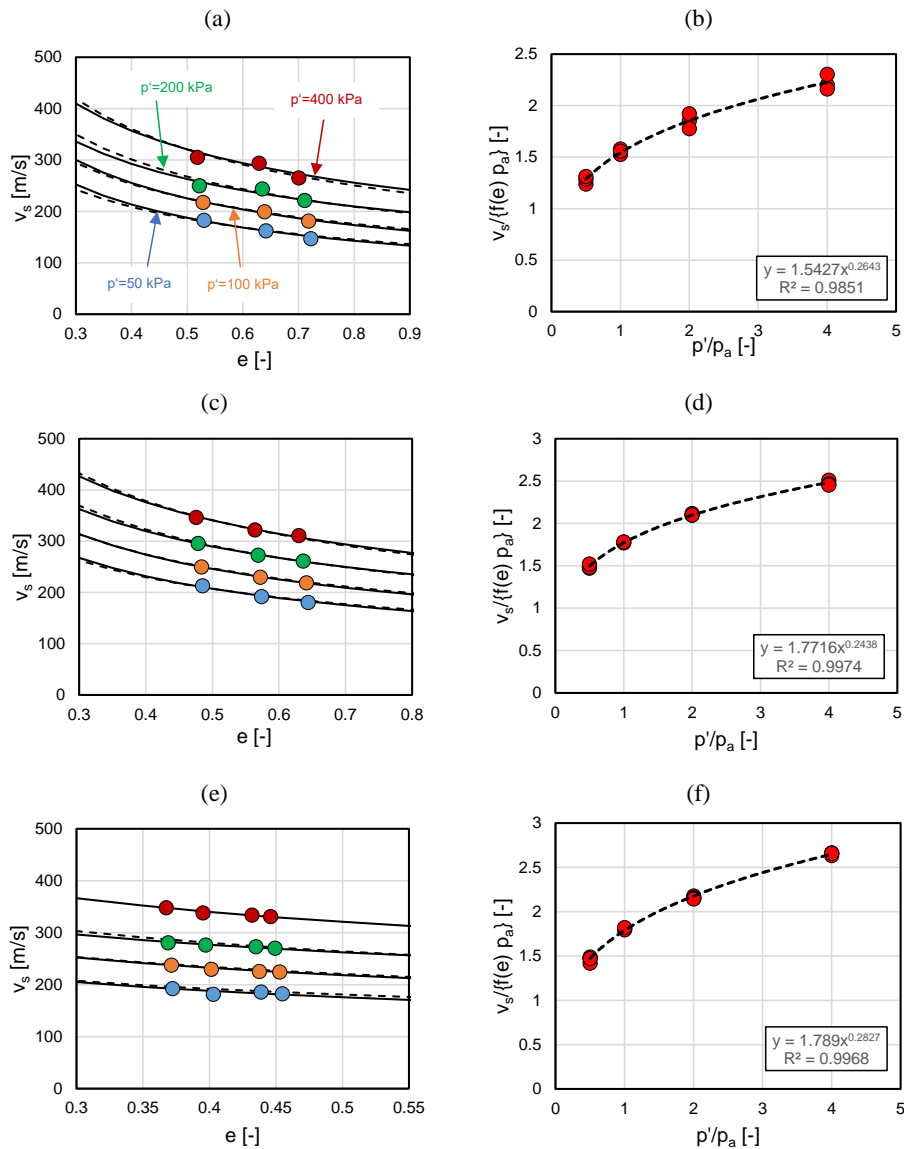
Figure 6.4: v_s vs. e and normalized v_s vs normalized p' curves for the tested materials: (a) and (b) crushed glass, (c) and (d) Rhein sand, and (e) and (f) round glass beads. Solid lines represent the curves from a fitting of Eq. 6.1b with individual d for each pressure step, while dashed lines are drawn using the $d_{i,avg}$ values

In Fig. 6.5, the variation of v_s against the different shape descriptors considering the extreme confining pressures and densities in the range $0.51 - 0.58$ are shown, with the solid circles and squares denoting $p' = 50$ and 400 kPa respectively. The shear wave velocities are lowest for the angular glass, whereas largest for the round glass beads as explained previously. A decreasing trend for v_s with a negative slope was observed for some shape parameters (aspect ratio and concavity) while the others displayed an increase in v_s with increase in the morphological parameter.

Fig. 6.6 shows the variation of the fitting parameter $d_{i,avg}$ against different grain shape descriptors. Comparing the results using a simple regression analysis yields a similar trend throughout, with certain parameters showing a significantly higher R^2 ($R^2 > 0.85$) than the others ($0.50 < R^2 < 0.85$). In particular, the grain roundness (Fig. 6.6j), being a medium scale parameter which considers the various rounded edges and corners, apparently seems to be a contender for one of the best shape parameters to characterize v_s. Generally all other parameters especially the aspect ratio, compactness, R-Factor, Mod-Ratio, circle-ratio, perimeter and width-to-length ratio sphericity are also capable in general to capture the variation of v_s with grain shape. It may be concluded that since the R^2 values are quite high for all the parameters, this implies that the most significant grain shape parameters to describe the shear wave velocities in soils remains vague and no clear recommendation for the choice of certain parameters can be given.

Similarly, the variation of the parameter n against the shape descriptors is shown in Fig. 6.7. A brief look in various past studies on the small-strain shear stiffness of granular materials shows that the relation between n and grain shape is not clear and the influence is thought to be minimal since it randomly varies between 0.44 and 0.67 (Altuhafi et al. 2016). In the present study, it must be stressed upon that the variations result only from the variation in grain shape. Cho et al. (2006) showed a decrease of n with increasing roundness although their study compared two different gradations which may have affected their results. The studies of Payan et al. (2016) on G_{max} suggested a decrease of n with increasing regularity ρ and decreasing C_u. For the case of v_s, it should be considered that the values of n are halved as compared to G_{max}. In the data of the present study (Fig. 6.7), a clear variation of n with the various grain shape parameters is not seen, which is in accordance with the observations of Altuhafi et al. (2016). Therefore, along with the fitting parameter A, the parameter n is not discussed further considering the minimal influence of grain shape. Instead, only the variation of the parameter d of the void ratio function denoting the dependence of v_s on e is discussed henceforth.

6.2.3 Applicability of other shape descriptors on the Krumbein & Sloss (1963) chart

It is well known that the popular chart of Krumbein & Sloss (1963) incorporates only the medium scale parameter roundness and the macro scale parameter sphericity, commonly thought of as the circle-ratio sphericity (Cavarretta 2009). However, other combinations of medium and macro scale parameters can also be similarly assessed. For the macro
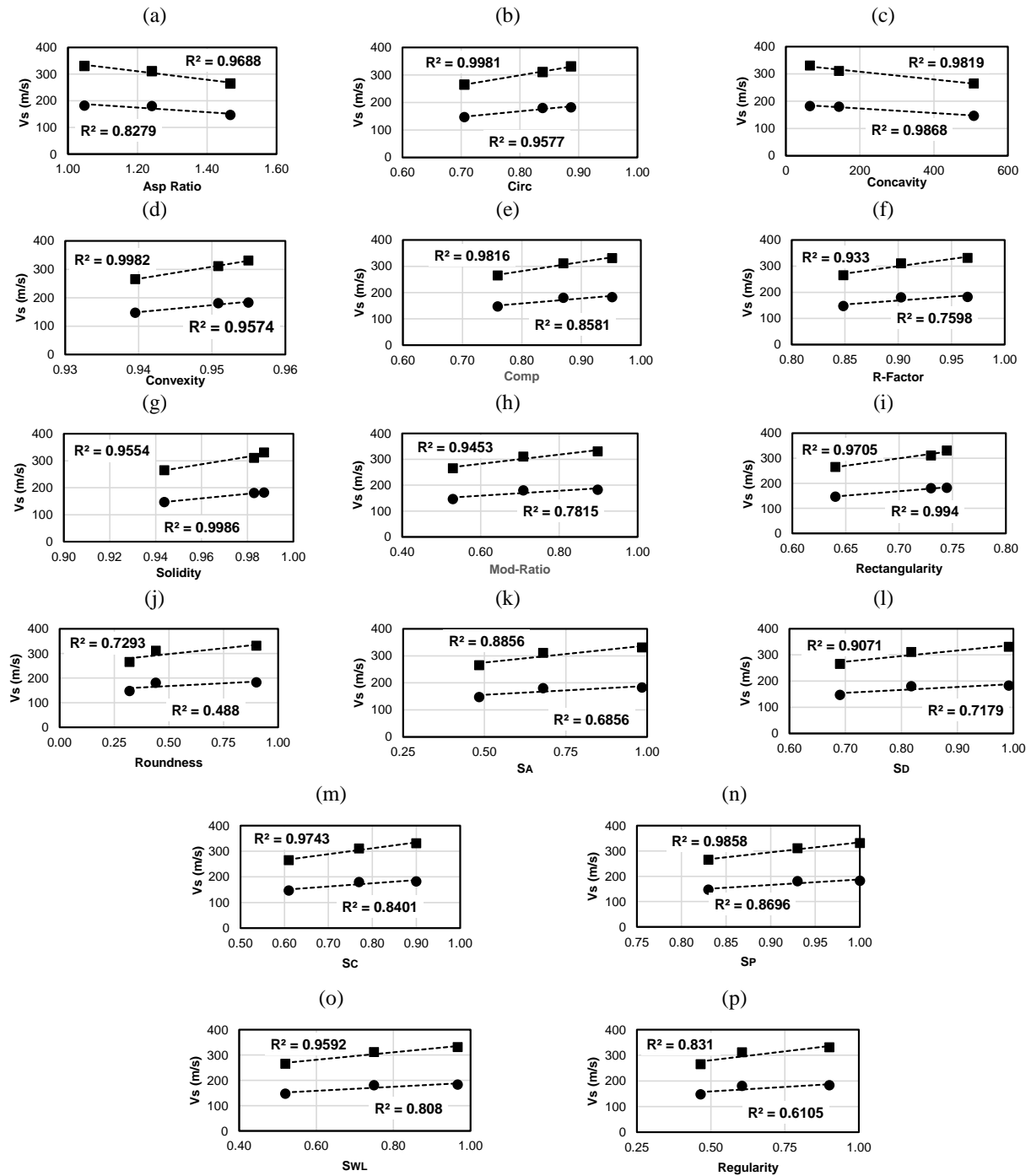
Figure 6.5: Variation of v_s against various shape descriptors considering the minimum and maximum confining pressures tested

scale shape descriptors that assess the grain shape purely based on the overall form, one can use the following parameters: area sphericity (S_A), diameter sphericity (S_D), circle-ratio sphericity (S_C), width-to-length ratio sphericity (S_{WL}), perimeter sphericity (S_P), aspect ratio (Ar), Circularity ($Circ$), Compactness ($Comp$), R-Factor (RF), Mod-ratio
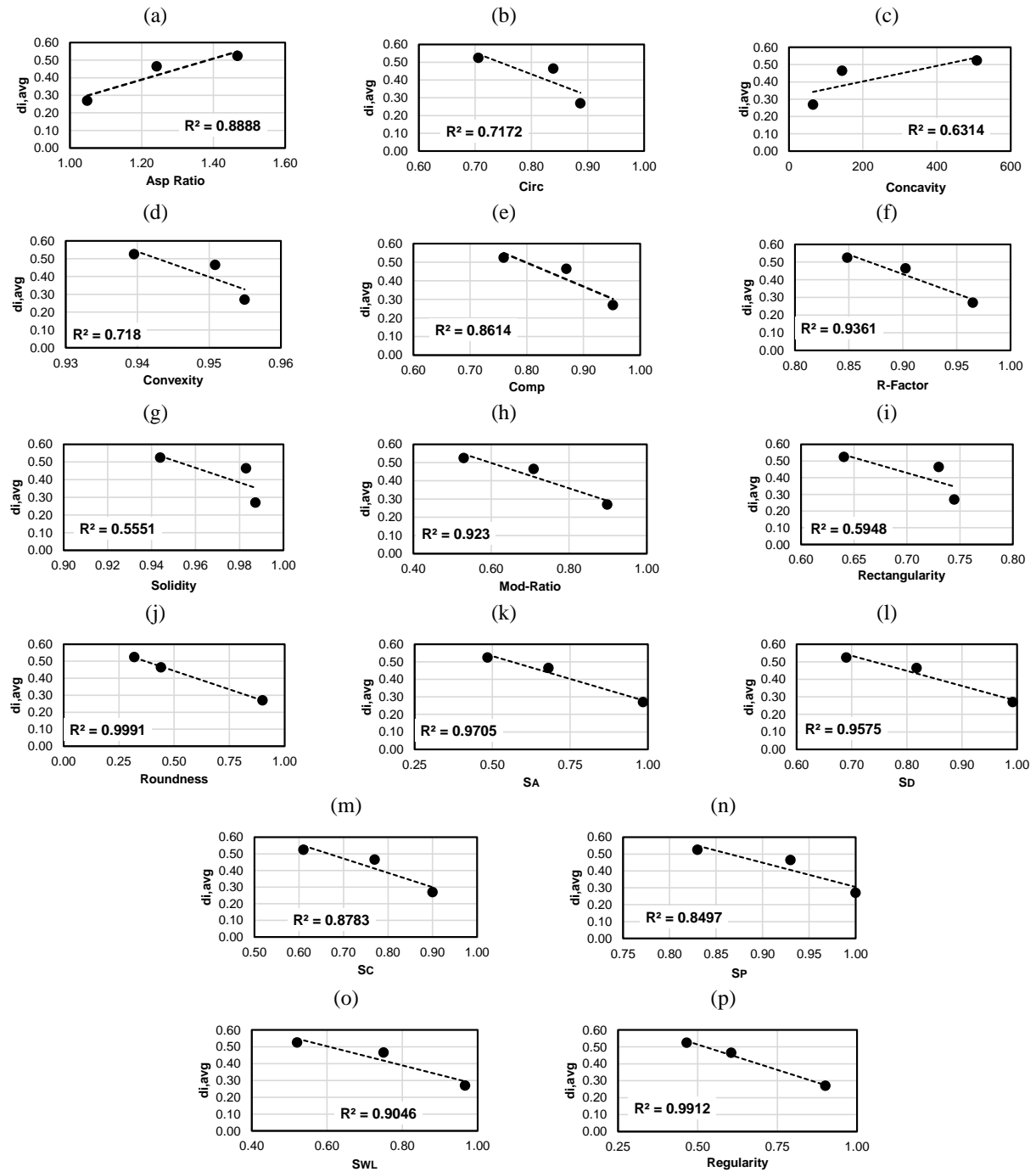
Figure 6.6: Variation of the fitting parameter $d_{i,avg}$ of the void ratio function against various shape descriptors

(MR) and Rectangularity $(Rect)$. The medium scale parameters accounting for the various rounded edges are the roundness (R), solidity (So), concavity (Cv) and convexity (Cx). An attempt was made to characterize the various combinations of grain shape parameters keeping the medium scale parameter on the x-axis and the macro scale parameter on the
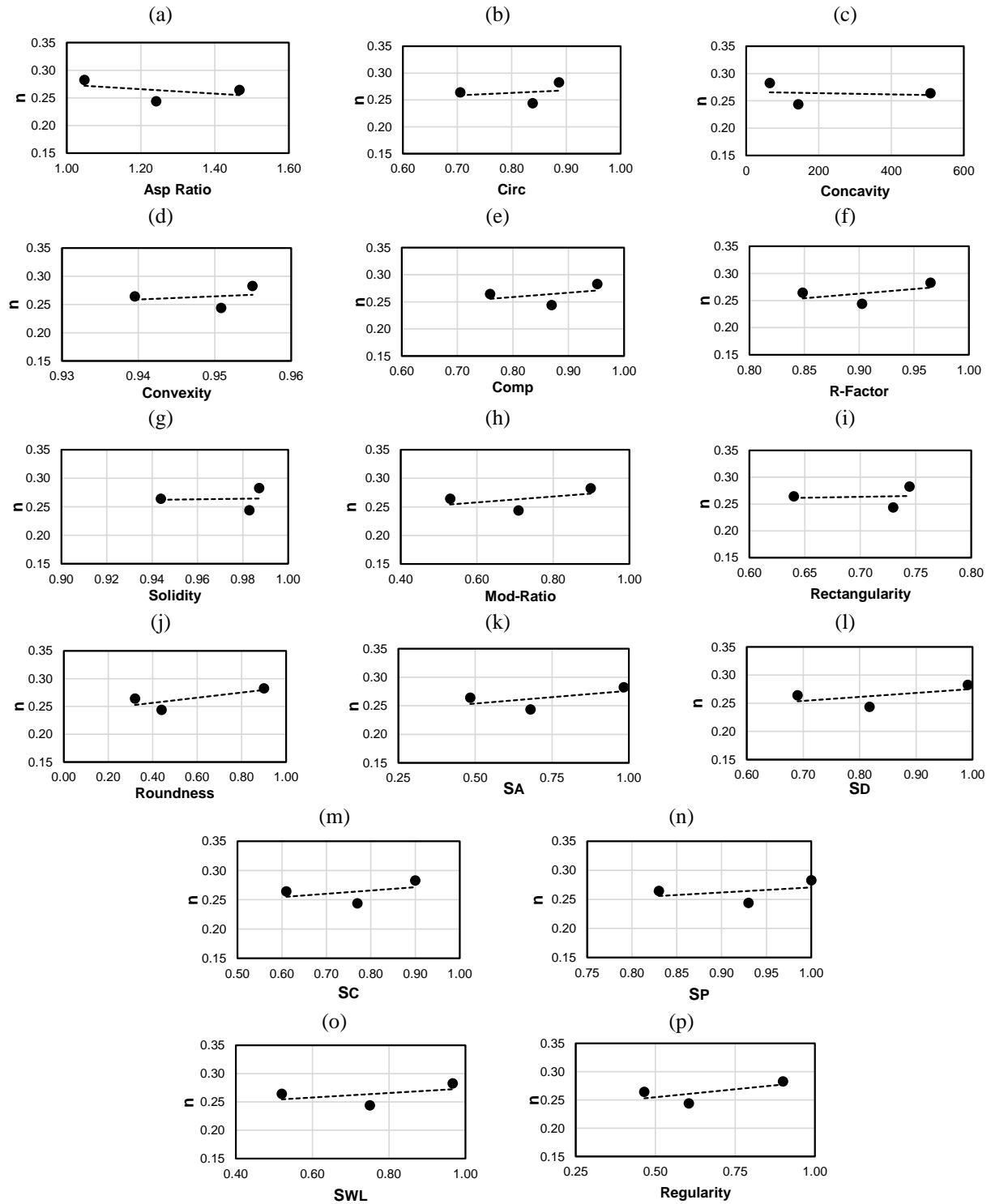
Figure 6.7: Variation of the pressure coefficient n against various shape descriptors

y-axis. At first, the extreme four shapes as denoted previously in Fig. 3.6 are considered. The values of the various parameters are listed in Table 6.3.

Table 6.3: Values of the various grain shape descriptors for the four extreme corner particles in the Krumbein & Sloss (1963) chart

Material	Ar	$Circ$	Cv	Cx	$Comp$	RF	So	MR
A	1.265	0.816	165.5	0.950	0.88	0.926	0.977	0.745
B	1.277	0.853	76.5	0.943	0.881	0.899	0.987	0.745
C	2.078	0.683	121.5	0.954	0.677	0.782	0.954	0.33
D	2.249	0.585	122.0	0.942	0.600	0.74	0.946	0.335

Material	$Rect$	R	S_A	S_D	S_C	S_P	S_{WL}	ρ
A	0.769	0.170	0.830	0.911	0.800	0.962	0.841	0.485
B	0.778	0.900	0.814	0..902	0.780	0.990	0.775	0.840
C	0.749	0.870	0.800	0.708	0.420	0.886	0.433	0.645
D	0.637	0.160	0.399	0.632	0.410	0.834	0.404	0.285

Comparing the values of the various parameters, certain observations are possible: the first is that the bandwidth of certain macro scale parameters namely $Circ$, $Comp$, $Rect$, S_D, S_P falls within 0.5-1 for these four shapes. That means the sensitivity of these parameters is lower than for example in case of S_C (0.41-0.80) or MR ($0.335 - 0.745$), where the bandwidth is larger, thus encompassing a wider range for describing grain shape. Also it is to be noted that instead of having two different parameters Ar and S_{WL}, it is possible to use only one of them, preferably S_{WL}, since the limits are well defined between 0 and 1 unlike Ar which goes upwards from 1 and eventually takes very large values consequently implying a very small S_{WL}. Also, the regularity factor, being a function of R and S_C is not considered as it is not an independent parameter. Furthermore, the medium scale properties except roundness and concavity have a very narrow range, for example, RF and Cx, both of which falls between 0.74 and 1. Furthermore, the Cv values for three grains are similar whereas the grain shapes are obviously distinctly different. Thus, with respect to for the medium scale parameter, roundness seems to be the best choice considering the various advantages mentioned above. Therefore, in the following sections only combinations of R as the medium scale parameter and S_A, S_C, MR and S_{WL} as the macro scale descriptors are considered.

6.2.4 Characterizing the chosen most influencing parameters using the grain shape distribution curve

Generally, in literature, researchers have used the average values of various grain shape parameters (Cox & Budhu 2008; Zheng & Hryciw 2016). However, certain materials have a wider range of grain shapes compared to others. For example, the crushed glass used in this study is well distributed across various grain shapes, with roundness R ranging from values of $0.2 - 0.3$ to $0.5 - 0.6$. Merely considering the average ($R = 0.32$) would imply a generalization of the grain shape without paying any attention to the extreme values. Thus, the contribution of the grains with extreme shape values is possibly not correctly accounted for, which may lead to over- or underestimation of the parameters under investigation. As discussed in the previous section, certain shape parameters in the medium and macro scale are able to capture the grain shapes considered in the chart of Krumbein & Sloss (1963) which are R, S_A, S_C, MR and S_{WL}. In the subsequent sections, a new characterization accounting for the grain shape distribution taking into consideration the parameters selected is demonstrated.

The grain shapes are quantitatively sorted into various classes ranging from the least to the highest value of a certain shape descriptor. For example, for roundness, classes with an interval of 0.1 were defined, starting from 0.2 until 1. The number of grains falling into each category was then determined. Considering the class mean on the horizontal axis, the grain shape distribution curves were further determined, which are shown for the five chosen variables in Fig. 6.8.

From the first glance, a couple of observations are clear: the grain shape parameters vary more widely for the crushed glass and the Rhein sand compared to round glass beads. Thus, using an analogy with the grain-size distribution curve, the shape of the crushed glass and the natural sand is more 'well-graded', while the round glass is uniformly shaped or 'poorly-graded'. Similar to the size distribution charts, shape uniformity coefficient (S_u), defined as the ratio of the shape value at 60% and the shape value at 10%, and mean shape (S_{50}), denoting the shape value at 50%, were determined. These values are listed in Table 6.4. The S_{50} values were found close in magnitude to the average grain shape. It is clear that the S_u values of all considered shape parameters get larger from the round glass over the natural sand to the crushed glass, i.e. the inclination of the grain shape distribution curves increases.

The variation of the fitting parameter $d_{i,avg}$ collected in Table 6.2 against the S_{50} and S_u values of the five chosen shape descriptors has is in Fig. 6.9. In terms of data fitting
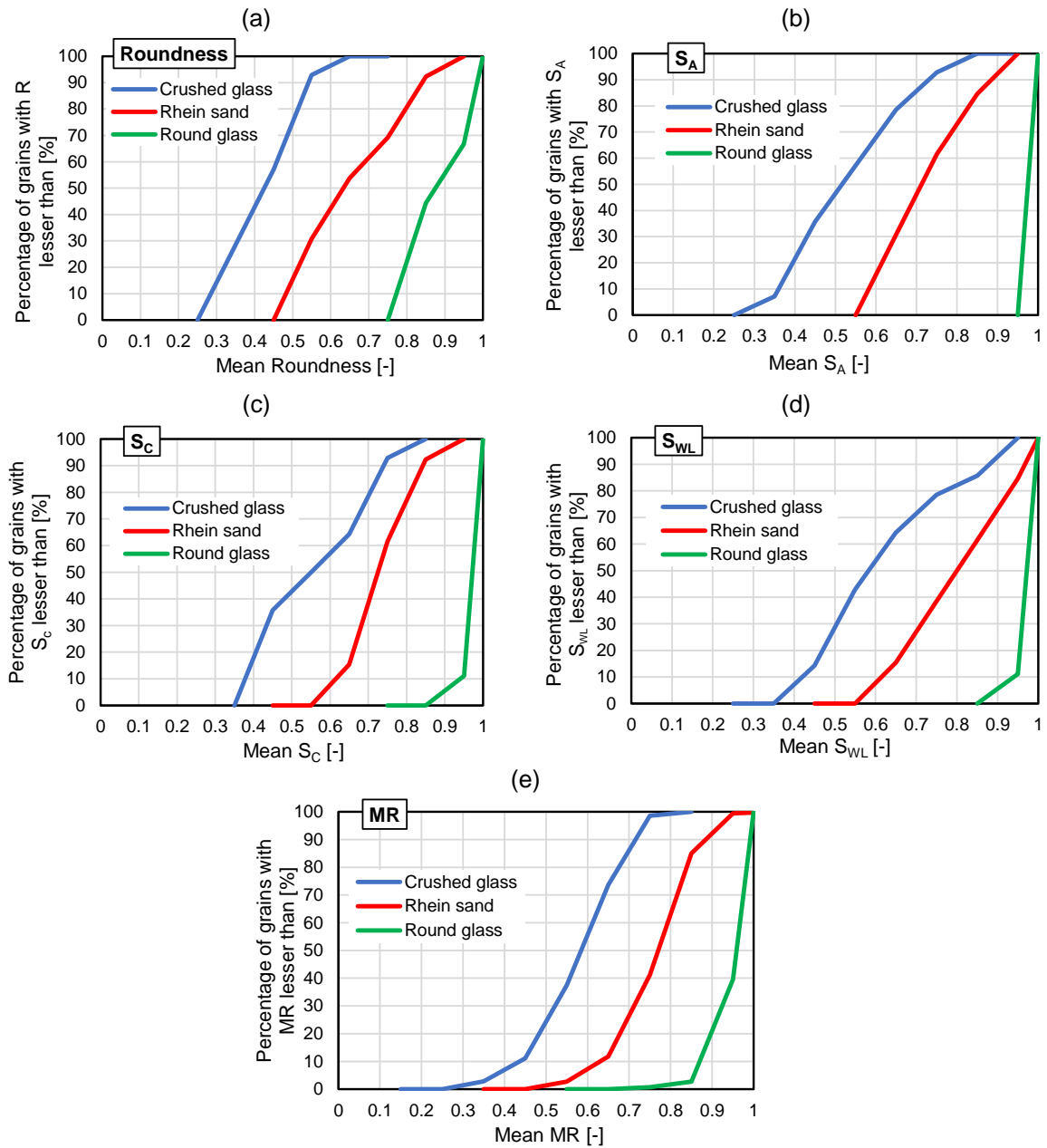
Figure 6.8: Grain shape distribution curves for the three materials considering the five most influencing parameters discussed previously

using linear regression, a strong performance is seen from the chosen parameters. For the medium scale descriptor roundness, the correlation is even better for S_u than for S_{50}. In the macro scale, S_U of S_{WL} provides the best fit out of the four chosen parameters. Thus, the roundness and the width-to-length ratio sphericity may be considered as the most influencing grain shape parameters when considering only the uniformity of the grain shape distribution curve. However, it should be stressed that mean grain shape and shape

Table 6.4: Mean grain shape and shape uniformity coefficient for the five chosen parameters

Parameter	Crushed glass		Rhein sand		Round glass	
	S_u [-]	S_{50} [-]	S_u [-]	S_{50} [-]	S_u [-]	S_{50} [-]
Roundness (R)	1.55	0.43	1.44	0.63	1.18	0.87
Area sphericity (S_A)	1.56	0.52	1.28	0.71	1.02	0.97
Circle-ratio sphericity (S_C)	1.63	0.54	1.21	0.72	1.02	0.98
Width-to-length ratio sphericity (S_{WL})	1.39	0.59	1.27	0.77	1.10	0.95
Mod-Ratio (MR)	1.50	0.58	1.38	0.80	1.03	0.97

uniformity coefficient should be always considered simultaneously, because they describe two different aspects of the grain shape distribution curve.

6.3 Influence of particle characteristics on the stiffness and damping ratio

To assess the influence of grain shape and uniformity coefficient C_u on the small-strain stiffness, modulus degradation and damping ratio of granular soils, the six materials with same d_{50} (=0.42 mm), two different C_u values (1.25 and 5) and three different grain shapes (angular crushed glass, sub-angular Rhein sand and round glass beads) known from previous chapters were studied. RC tests under two modes of vibration, torsional and axial, were performed to measure the shear and elastic stiffnesses respectively. For each mode of vibration a separate sample was necessary. On each material at least three air-pluviated specimens with different densities were tested and each specimen was subjected to four confining pressures in succession, $p' = 50, 100, 200$ and 400 kPa. While the small-strain stiffness was measured at all four pressures, the stiffness and damping at larger strains were tested only for $p' = 100$ and 400 kPa. An overview of all the tests performed is given in Table 6.5.

6.3.1 Maximum shear modulus, G_{max}

Influence of e, p' and C_u on G_{max}

The variation of the maximum shear modulus at small-strains G_{max} against e is shown for the different p' in Fig. 6.10. An increase in e clearly leads to a decrease in the value
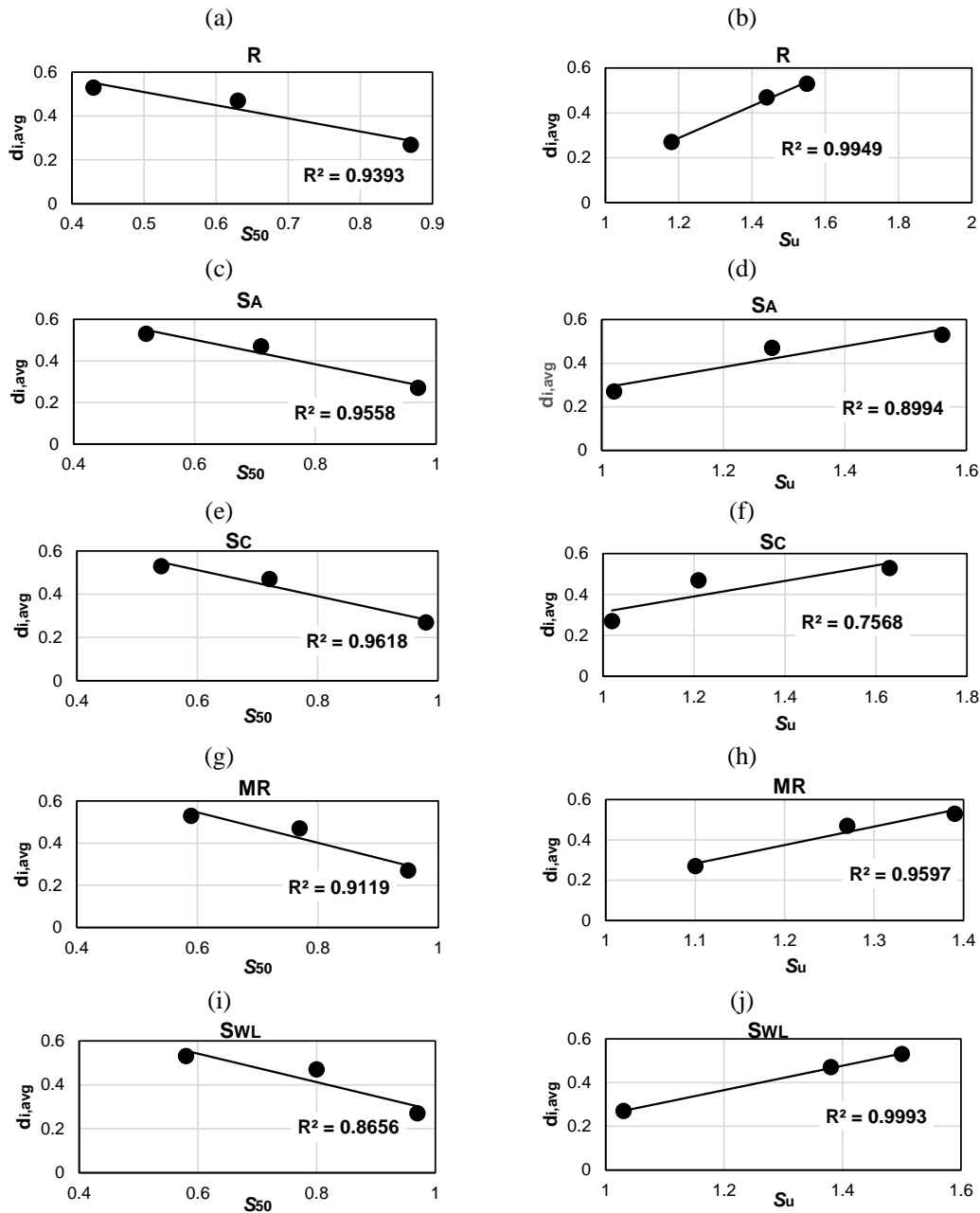
Figure 6.9: Variation of $d_{i,avg}$ against the S_{50} and S_u values of the five selected shape parameters: (a) and (b) Roundness R, (c) and (d) Area sphericity S_A, (e) and (f) circle-ratio sphericity S_C, (g) and (h) Mod-ratio MR, and (i) and (j) width-to-length ratio sphericity S_{WL}

of G_{max} for all the tested materials. Also, increasing p' results in increasing G_{max}. Both measured tendencies are well-known from various past studies. The angular materials have comparatively lower G_{max} as compared to the round glass beads at similar relative densities, possibly due to the fact that the void ratio limits of glass beads are smaller than those of angular glass.

Table 6.5: Details of the RC tests on the six materials including both axial and torsional modes of vibration

Material	C_u	Axial		Torsional		Material	C_u	Axial		Torsional	
		I_D	e	I_D	e			I_D	e	I_D	e
Crushed glass	1.25	0.27	1.025	0.26	1.030	Crushed glass	5	0.30	0.874	0.33	0.858
		0.45	0.939	0.43	0.950			0.46	0.79	0.50	0.722
		0.70	0.823	0.69	0.826			0.62	0.703	0.74	0.642
		0.87	0.742	0.90	0.729			0.92	0.544	0.95	0.530
Rhein sand	1.25	0.29	0.803	0.35	0.781	Rhein sand	5	0.27	0.736	0.28	0.731
		0.53	0.724	0.50	0.734			0.42	0.681	0.52	0.644
		0.73	0.657	0.82	0.628			0.76	0.559	0.72	0.574
		0.91	0.598	0.92	0.596			0.90	0.509	0.96	0.485
Round glass	1.25	0.28	0.697	0.35	0.687	Round glass	5	0.26	0.494	0.19	0.504
		0.31	0.692	0.56	0.654			0.46	0.470	0.51	0.455
		0.33	0.690	0.75	0.623			0.91	0.395	0.62	0.439
		0.48	0.665	0.98	0.586			-	-	0.87	0.403
		0.70	0.631	-	-			-	-	-	-
		0.87	0.605	-	-			-	-	-	-
		0.89	0.600	-	-			-	-	-	-

The influence of C_u on G_{max} is evident from Fig. 6.11. For the same e, the G_{max} values obtained for the well-graded materials are lower than those for the uniform materials. A brief look at literature reveals similar observations, where an increase in C_u resulted in decreasing G_{max} (Iwasaki & Tatsuoka 1977; Hardin & Kalinski 2005; Wichtmann & Triantafyllidis 2009; Senetakis et al. 2012; Payan et al. 2016; Payan 2017).

Influence of grain shape on G_{max}

In Fig. 6.12 a comparison of the G_{max} values for the six materials under two different p' is provided. Clearly, for both stress levels, at similar relative density I_D and C_u, the angular crushed glass has the least magnitude of G_{max} while the glass beads show the largest values. It is interesting to note that although the regularity ρ of Rhein sand is closer to angular glass, the G_{max} values are surprisingly closer (and on occasions larger) to those of glass beads. This might be a result of the surface roughness, the influence of which was not considered in the present research.
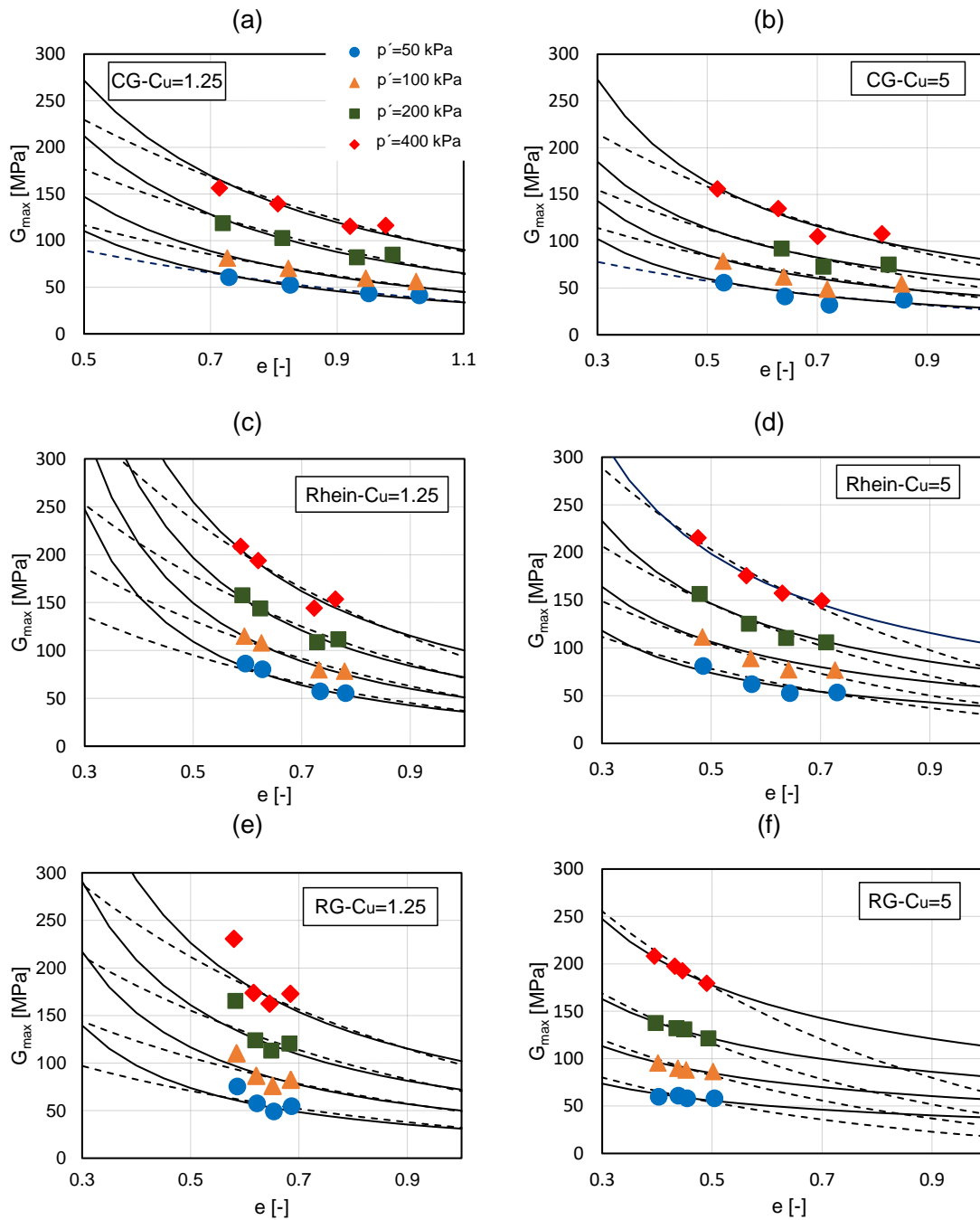
Figure 6.10: Variation of G_{max} against e for the six tested materials. CG, Rhein and RG refers to crushed glass, Rhein sand and glass beads with the number next to them denoting the C_u values. Solid lines are plotted using the Jamiolkowski void ratio formulation while the dashed lines are using the Hardin void ratio formulation using the averaged value of the fitting parameter $\bar{d}_i$ or $\bar{x}_i$
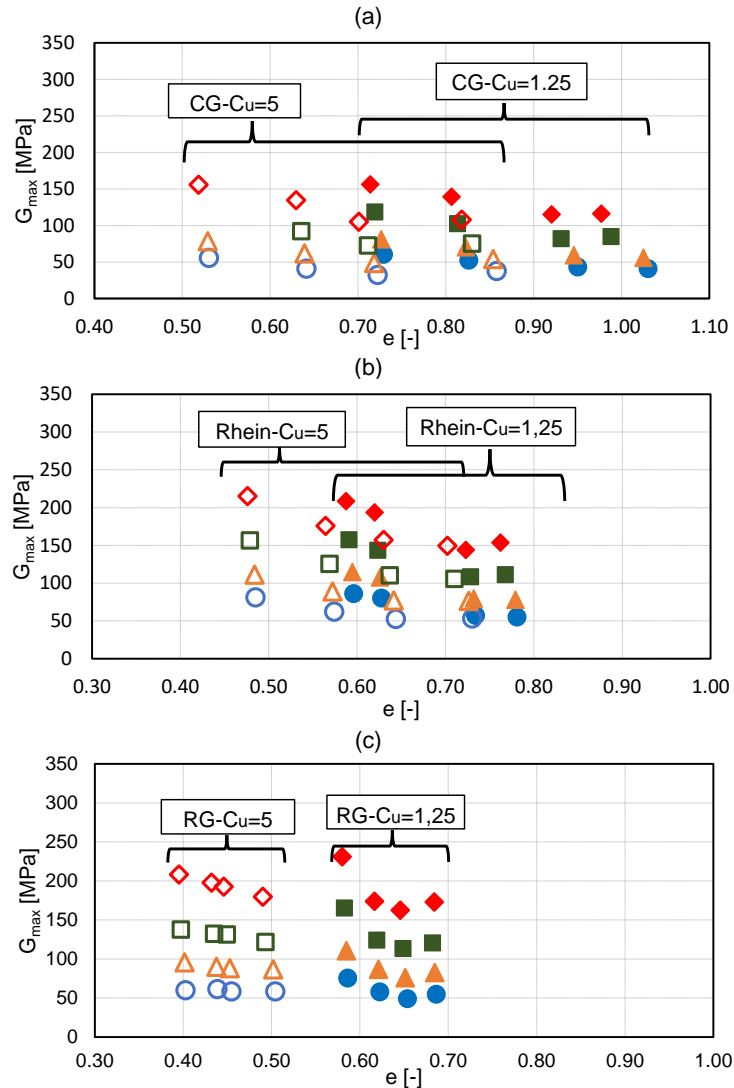
Figure 6.11: Influence of C_u on G_{max}: (a) crushed glass, (b) Rhein sand, and (c) glass beads

6.3.2 Maximum Young's modulus, E_{max}

Influence of e, $p^{'}$ and C_u on E_{max}

Similar to G_{max}, Fig. 6.13 shows the maximum elastic modulus (Young's modulus) E_{max} (strain amplitude $\epsilon_{ampl} < 10^{-6}$) versus the void ratio e. The same $p^{'}$ as in the case of G_{max} were tested. An increase in E_{max} with decreasing e and increasing $p^{'}$ is evident, matching the trends observed for G_{max}. In terms of the absolute magnitude at similar relative densities, the E_{max} for angular glass beads are relatively lower than for the other two materials. Surprisingly, the E_{max} for Rhein sand is slightly larger than that of glass beads for both gradations. Like in the case of G_{max}, the uniform materials show slightly
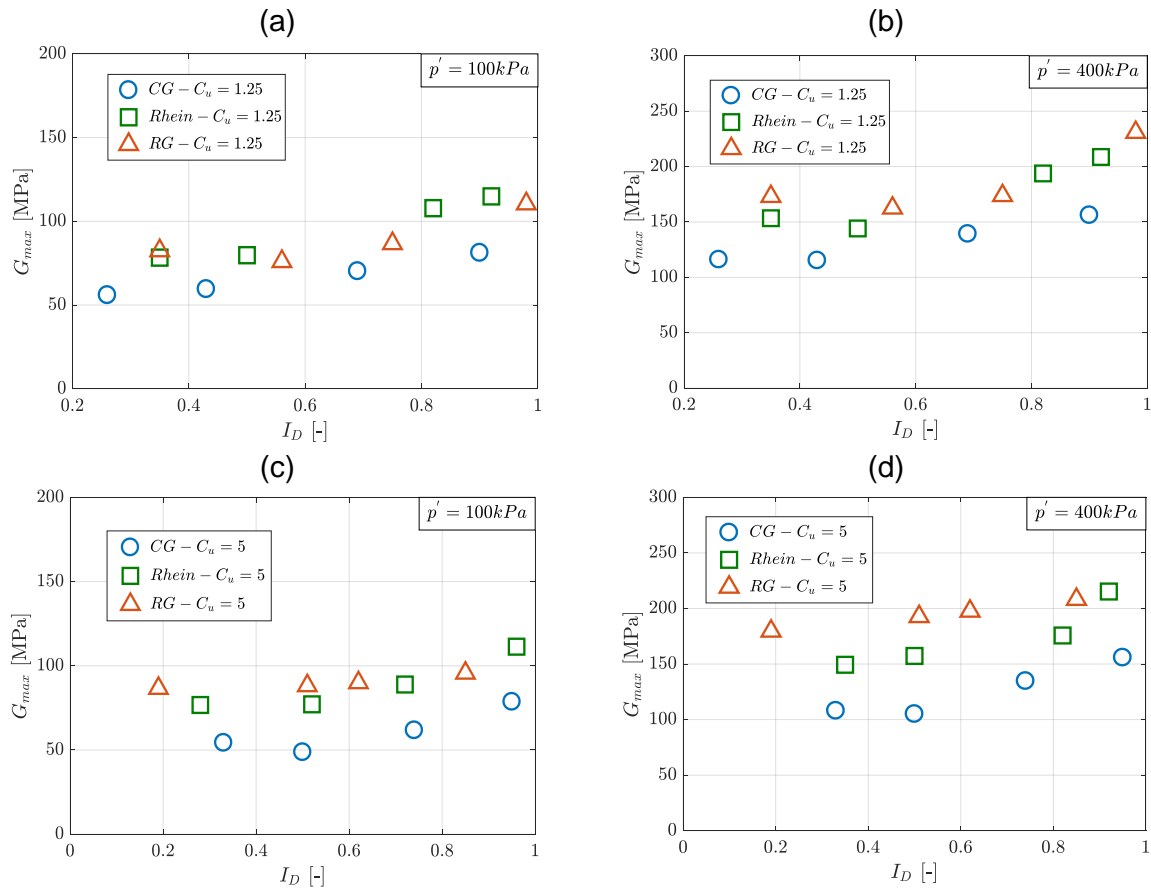
Figure 6.12: Comparison of the G_{max} for the three grain shapes considering both C_u values against I_D for two $p' = 100$ and 400 kPa

larger E_{max} as compared to the well-graded ones, although the differences are quite small for Rhein sand and glass beads, while being larger for angular glass.

Influence of the grain shape on E_{max}

In order to facilitate a direct comparison with respect to the influence of the grain shape on the maximum elastic modulus, the $E_{max} - I_D$ data for the materials with both C_u (=1.25 and 5) and for two different pressures ($p' = 100$ and 400 kPa) are provided in Fig. 6.14. Considering a constant relative density, for both C_u values and both pressure levels, the E_{max} values of the glass beads are the highest (with a few exceptions, e.g. Fig. 6.14a at relative densities greater than 0.70), while those of the crushed glass are the least (also with some exceptions, e.g. Fig. 6.14a at relative densities lower than 0.40). The values of the natural sand lie in between, but much closer to the glass beads. Generally, the difference between the E_{max} values for the three different grain shapes is larger for the
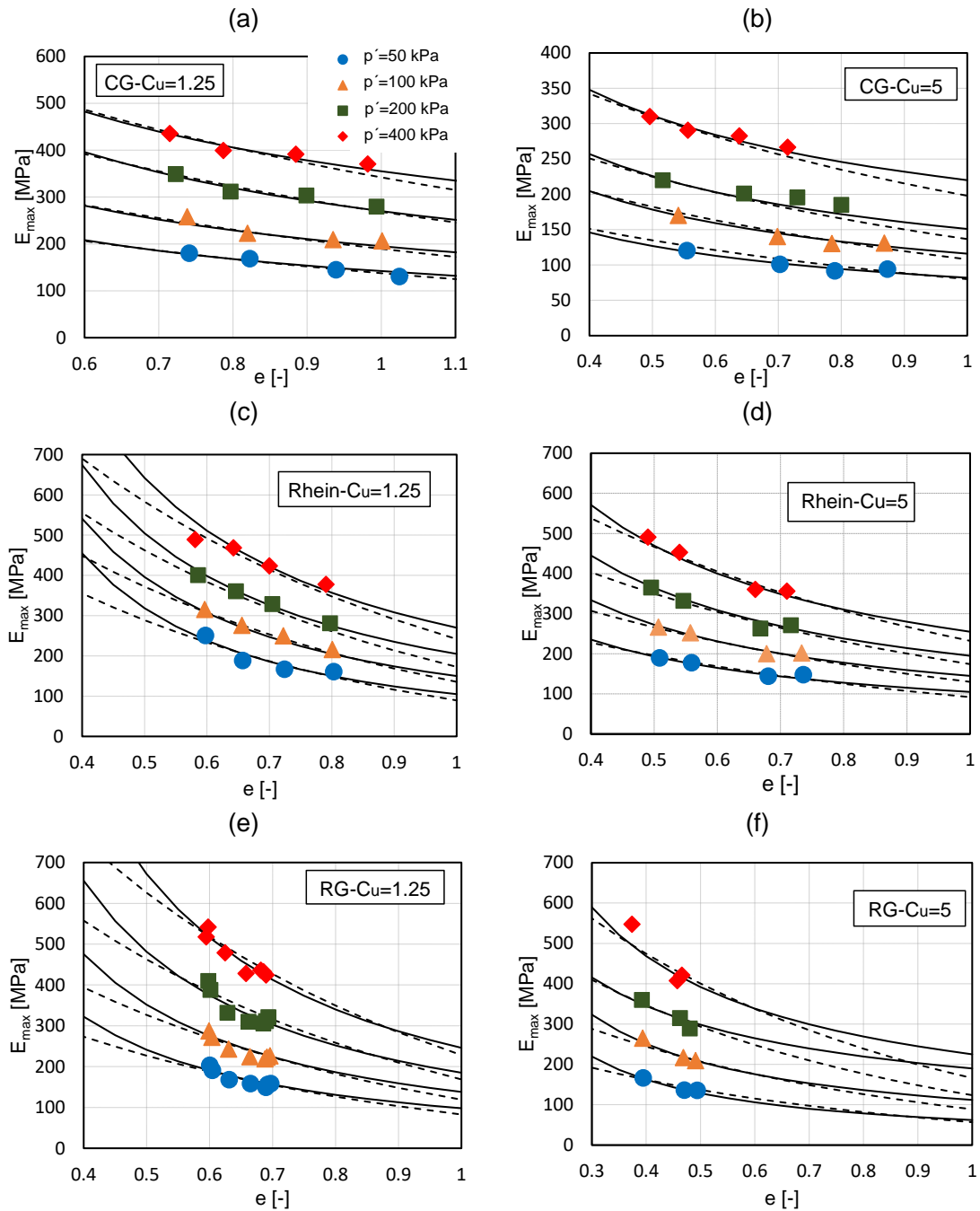
Figure 6.13: Variation of E_{max} against e for the tested materials. CG, Rhein and RG refers to crushed glass, Rhein sand and glass beads with the number next to them denoting the C_u values. Solid lines are plotted using the Jamiolkowski void ratio formulation while the dashed lines are using the Hardin void ratio formulation using the averaged value of the fitting parameter $\bar{d}_i$ or $\bar{x}_i$

well-graded materials ($C_u = 5$) than for the uniform ones ($C_u = 1.25$). The results show

that at a certain stress level, the change in the magnitude of E_{max} for crushed glass across various relative densities is the least as compared to the other materials, especially for the well-graded crushed glass, thereby yielding a flatter curve.
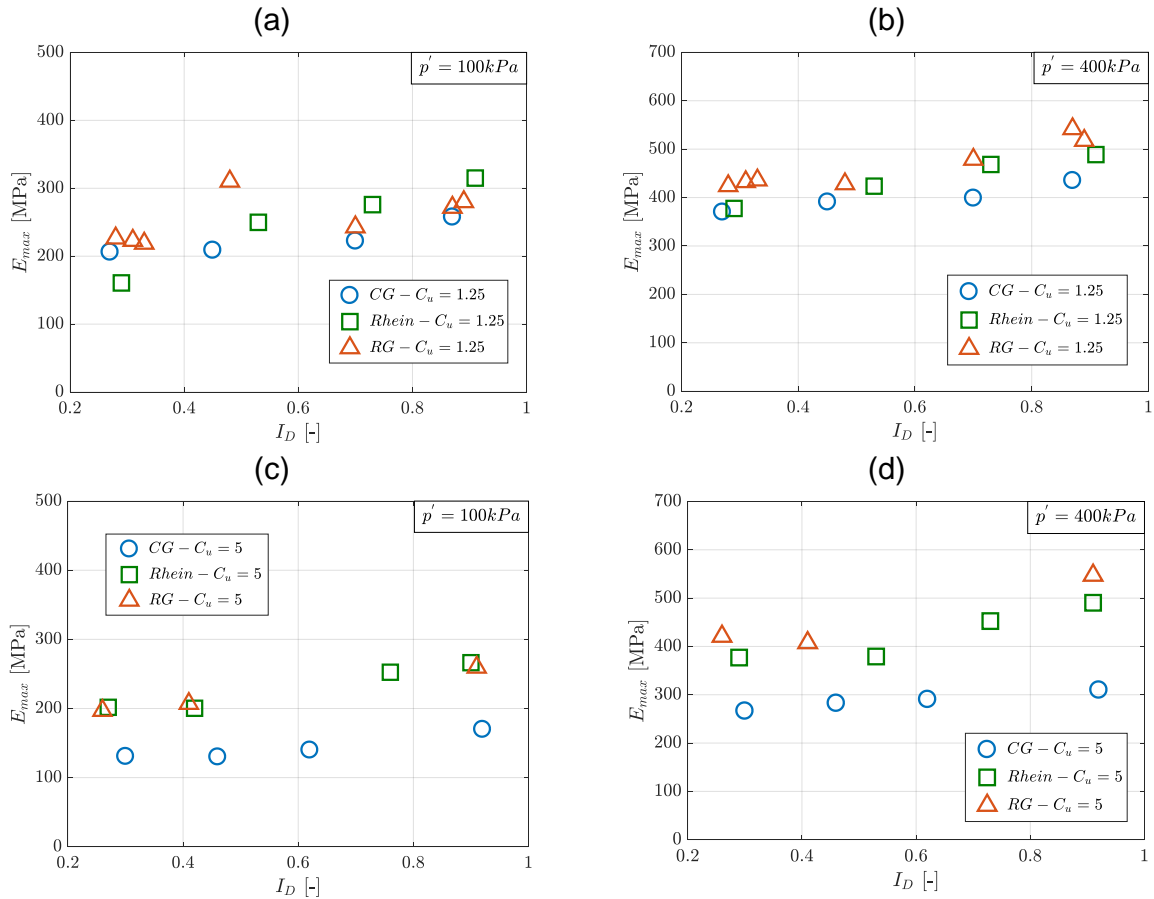
Figure 6.14: Comparison of E_{max} versus relative density for the three different grain shapes and two C_u values for $p' = 100$ and 400 kPa

Table 6.6: Fitting parameters of the empirical equations for G_{max} and E_{max} respectively for the six materials using either Hardin or Jamiolkowski void ratio functions

Material	p' [kPa]	$G_{max} - Hardin$					$G_{max} - Jamiolkowski$				
		K_i	x_i	$\bar{x}_i$	A_i	n_i	K_i	d_i	$\bar{d}_i$	A_i	n_i
Crushed glass ($C_u = 1.25$)	50	26.50	2.75				42.00	1.50			
	100	34.50	2.75	2.71	37.57	0.46	55.00	1.50	1.48	54.85	0.46
	200	60.00	2.60				80.00	1.50			
	400	68.00	2.75				107.00	1.40			
Rhein sand ($C_u = 1.25$)	50	45.00	2.28				36.00	1.60			
	100	60.00	2.31	2.32	59.04	0.44	51.00	1.55	1.38	54.79	0.44
	200	78.00	2.35				72.00	1.45			
	400	107.00	2.32				100	1.35			

Table 6.6 continued from previous page

Material	p' [kPa]	$E_{max} - Hardin$					$E_{max} - Jamiolkowski$				
		K_i	x_i	$\bar{x}_i$	A_i	n_i	K_i	d_i	$\bar{d}_i$	A_i	n_i
Round glass ($C_u = 1.25$)	50	21.00	2.75				31.00	1.25			
	100	29.00	2.84	2.80	30.45	0.55	50.00	1.22	1.20	50.41	0.55
	200	46.00	2.75				72.00	1.16			
	400	58.00	2.84				102	1.15			
Crushed glass ($C_u = 5$)	50	15.00	2.90				29.00	1.05			
	100	22.00	2.90	2.85	21.33	0.52	42.00	1.02	1.01	39.55	0.52
	200	35.00	2.70				59.00	0.95			
	400	42.00	2.88				81.00	1.01			
Rhein sand ($C_u = 5$)	50	37.00	2.28				39.00	0.92			
	100	48.00	2.31	2.32	47.67	0.48	59.00	0.85	0.90	54.64	0.49
	200	64.00	2.35				78.00	0.91			
	400	92.00	2.32				105	0.92			
Round glass ($C_u = 5$)	50	36.00	2.00				38.00	0.55			
	100	47.00	2.12	2.10	47.27	0.56	57.00	0.57	0.59	55.15	0.56
	200	67.00	2.11				81.00	0.58			
	400	97.00	2.15				113	0.65			

Material	p' [kPa]	$E_{max} - Hardin$					$E_{max} - Jamiolkowski$				
		K_i	x_i	$\bar{x}_i$	A_i	n_i	K_i	d_i	$\bar{d}_i$	A_i	n_i
Crushed glass ($C_u = 1.25$)	50	15.60	5.20				142	0.75			
	100	20.50	5.30	5.88	16.25	0.44	195	0.72	0.71	196.5	0.44
	200	21.50	6.00				270	0.75			
	400	19.00	7.00				355	0.60			
Rhein sand ($C_u = 1.25$)	50	221	1.90				105	1.60			
	100	205	2.15	2.18	195.71	0.39	150	1.40	1.39	151.06	0.38
	200	240	2.20				205	1.30			
	400	230	2.45				270	1.25			
Round glass ($C_u = 1.25$)	50	125	2.15				98	1.30			
	100	180	2.15	2.15	175.59	0.48	138	1.35	1.37	132.39	0.48
	200	255	2.15				185	1.38			
	400	345	2.15				246	1.45			
Crushed glass ($C_u = 5$)	50	10.00	5.00				82	0.63			
	100	13.50	5.00	5.63	9.87	0.42	116	0.62	0.58	113.67	0.43
	200	13.50	5.50				151	0.58			
	400	11.00	7.00				220	0.50			
Rhein sand ($C_u = 5$)	50	51.00	2.90				105	0.88			
	100	59.00	3.10	3.10	58.58	0.42	145	0.91	0.89	143.76	0.42
	200	72.00	3.20				195	0.90			
	400	96.00	3.20				255	0.88			
Round glass ($C_u = 5$)	50	54.00	2.45				62.00	1.05			
	100	74.00	2.55	2.49	107.03	0.46	112	0.88	0.85	155.09	0.46
	200	110	2.50				190	0.65			
	400	158	2.45				225	0.80			

6.3.3 Analysis of results for small strains

The well-known formula of Hardin & Black (1966) (refer Eq. 2.21) is used along with the two void ratio functions of Hardin & Black (1966) (Eq. 2.22) and Jamiolkowski et al. (1991) (Eq. 2.24) to describe the variation of G_{max} and E_{max} with respect to e and $p^{'}$. The parameters obtained by curve-fitting to the data in Figs. 6.10 and 6.13 are summarized in Table 6.6. The dashed and solid lines in Figs. 6.10 and 6.13 denote the predictions given by the empirical equations using the Hardin or Jamiolkowski void ratio functions respectively. The averaged values of x_i or d_i (denoted as $\bar{x}_i$ and $\bar{d}_i$) obtained for the four different pressures $p^{'}$ was considered in the subsequent analysis for obtaining the pressure dependency parameters A_i and n_i. For that purpose G_{max} or E_{max} were normalized with respect to the void ratio function $f(e)$ using $\bar{x}$ and $\bar{d}$. Only results using the Jamiolkowski $f(e)$ function are discussed further.

Variation of $\bar{d}_i$ and n_i against grain shape and gradation for G_{max} and E_{max}

As evident from Table 6.6, for the two different C_u values, the magnitude of $\bar{d}$, describing the variation of G_{max} and E_{max} with void ratio e, generally decreases as the grains become more round. To facilitate a direct comparison, the variation of $\bar{d}$ and n_i against the regularity factor ρ for G_{max} in uniformly-graded materials ($C_u = 1.25$) is shown in Fig. 6.15. A decrease of $\bar{d}$ with regularity is evident for the materials with a $C_u = 1.25$ in Fig. 6.15a. Likewise, the same trend is also seen for the case of $C_u = 5$ (refer Table 6.6). Also, going by the trendline, an increase of the stress exponent n_i with regularity is visible from Fig. 6.15b although this is debatable since n_i of Rhein sand is the least. Therefore, it is difficult to draw a definitive conclusion in this regard unlike the case of $\bar{d}$. The trend of these two fitting parameters for E_{max} are in lines with those observed for G_{max} as evident from Figs. 6.16a and b.

To assess the influence of gradation on G_{max}, Figs. 6.15c and d show the fitting parameters against C_u. A decrease of $\bar{d}$ with increasing C_u in Fig. 6.15c is evident, while the trend is less clear in the case of n_i. It seems that the n_i for G_{max} remains almosts constant for glass beads (Fig. 6.15d), but slightly increases with C_u for the other two materials. For E_{max} (Fig. 6.16c), d shows a similar decreasing trend with increasing uniformity as in case of G_{max}, although the inclination is less for crushed glass. The parameter n_i for E_{max} (Fig. 6.16d) decreases with C_u for glass beads, remains practically same for Rhein sand, but increases for angular glass. Thus, from the present set of observations, it is not possible
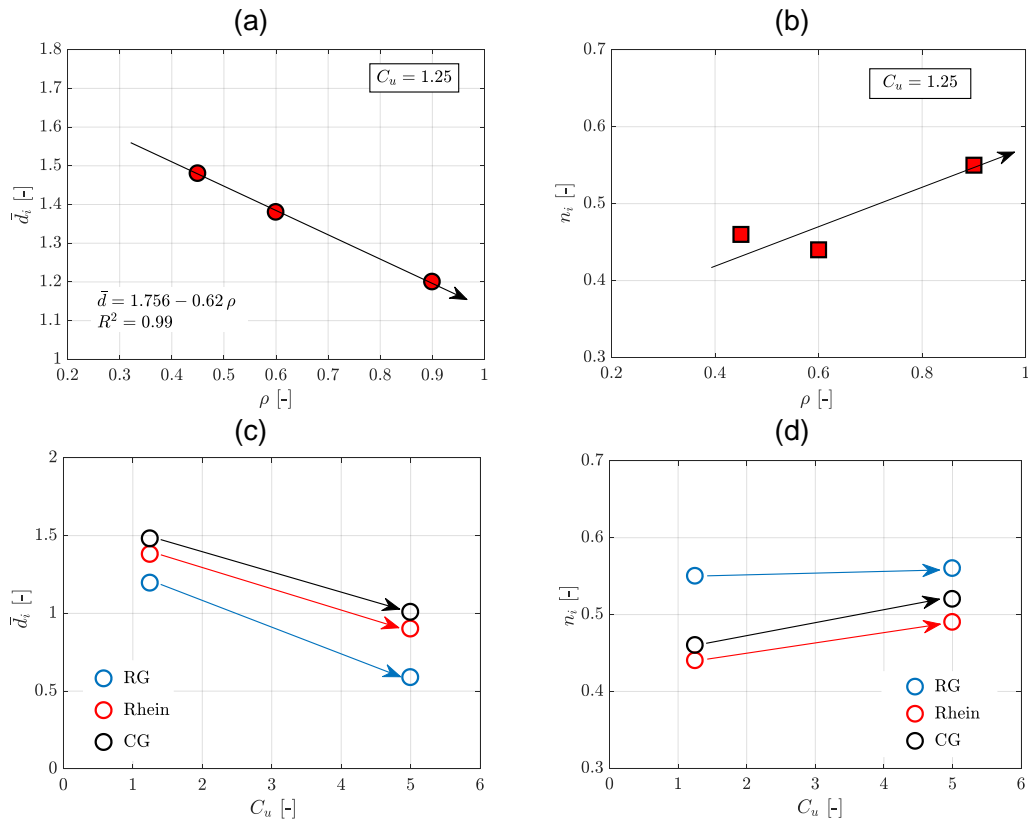
Figure 6.15: Variation of the fitting parameters $\bar{d}_i$ and n_i for G_{max} with regularity and uniformity coefficient, considering only $C_u = 1.25$ (a, b) or $C_u = 1.25$ and 5 (c, d)

to draw a definite conclusion regarding the influence of grain shape and gradation on the pressure exponent n.

6.3.4 Analysis of results for small to intermediate strains

To assess the influence of grain shape and gradation at small to intermediate strains in both the torsional and axial modes of vibrations, the model of Stokoe et al. (1999) (refer Eq. 2.31) has been used to capture the variation of G/G_{max} or E/E_{max} against the shear or axial strains γ and ϵ, respectively. For the damping, the formulation adopted by Goudarzy et al. (2018) (Eq. 2.34) is applied. As previously mentioned, the reference shear strain γ_r is defined as the γ at $G/G_{max} = 0.5$. The second fitting parameter α defines the transition point denoting the elastic limit shear strain γ_{el}: a higher value of α at a constant γ_r would push the elastic strain limit to the right resulting in higher values of γ. The fitting parameters M and N in Eq. 2.34 play a similar role, both together defining the slope of the $D(\gamma) - \gamma$ curve. The same equations can be applied for the case of E as
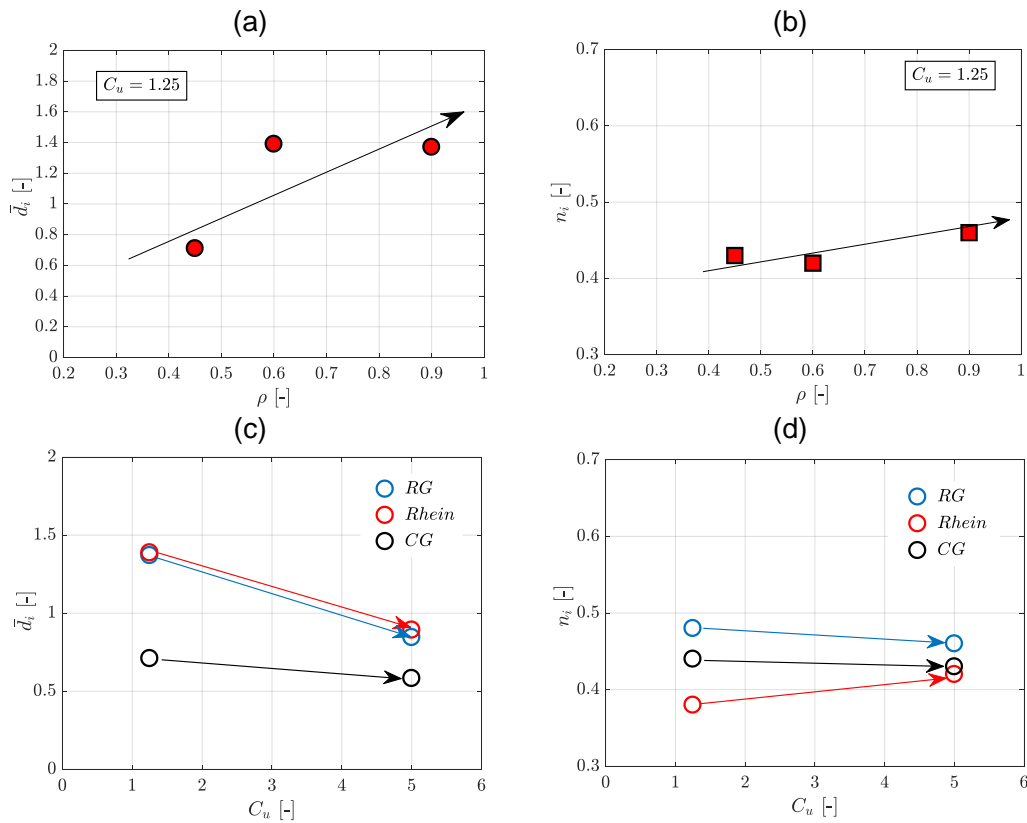
Figure 6.16: Variation of the fitting parameters $\bar{d}_i$ and n_i for E_{max} with regularity and uniformity coefficient, considering only $C_u = 1.25$ (a, b) or $C_u = 1.25$ and 5 (c, d)

well after suitable modifications. Therefore, the following sub-sections discuss the shear modulus degradation, elastic modulus degradation and damping curves obtained from the tests with torsional and axial modes of vibration.

Influence of e, p' and gradation on $G(\gamma)/G_{max}$ and $D(\gamma)$

The influence of the void ratio e or relative density I_D on the G/G_{max} curves was observed to be minimal for a certain material as discussed previously for a given p' based on the experimental data using glass beads in Rüscher (2019). This is confirmed once more by the data for the round glass beads ($C_u = 5$) in Fig. 6.17a, where all the G/G_{max} curves for varying I_D fall together at $p' = 400$ kPa. However, a change in p' has a significant influence as observed in Fig. 6.17b: an upwards shift of the G/G_{max} curve with increasing p' for similar γ is visible. Similarly, the influence of e and I_D on damping ratio D seems negligible for a certain material at a given p', which was already demonstrated in Rüscher (2019). For a $p' = 400$ kPa, Fig. 6.17c confirms no influence of varying I_D on D, whereas

an increase in p' in Fig. 6.17d results in a decrease in D. The dashed and solid lines show the predictions by the Stokoe and Goudarzy models for $G(\gamma)/G_{max}$ and $D(\gamma)$ respectively, with the fitting parameters listed at a later section.
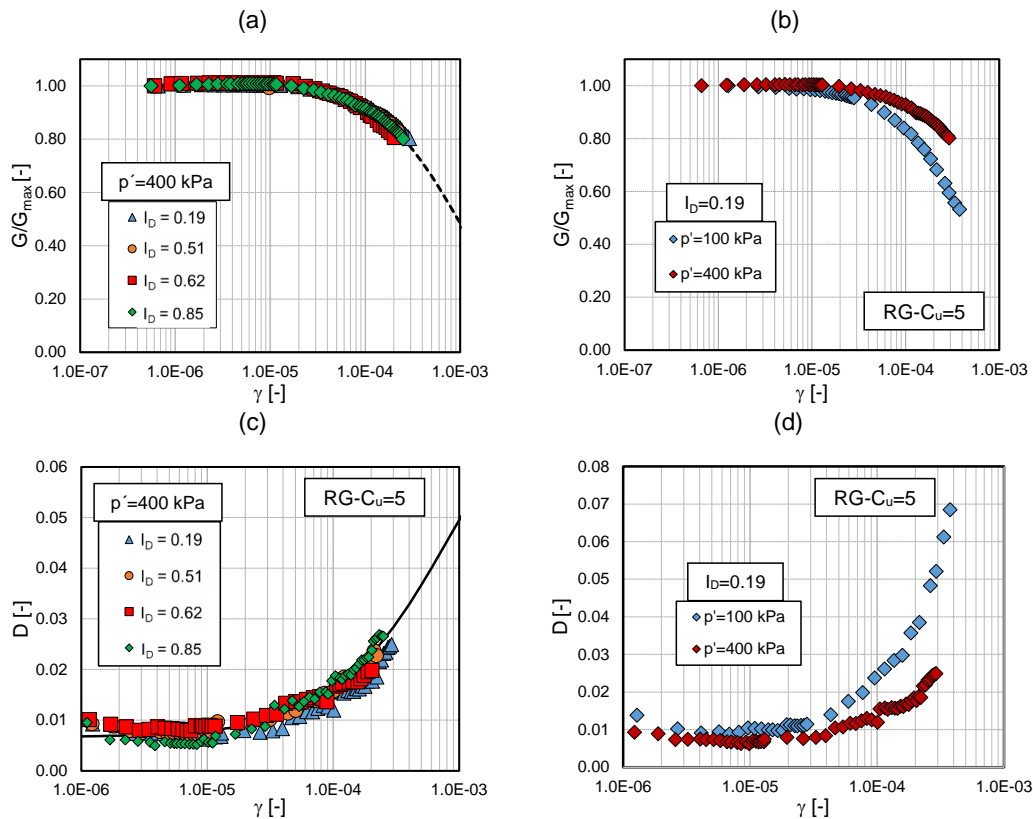
Figure 6.17: Influence of the void ratio e / relative density I_D and mean effective stress p' on (a) and (b) $G(\gamma)/G_{max}$, and (c) and (d) $D(\gamma)$ curves for well-graded glass beads. The same observations are equally applicable for the other materials

Regarding the influence of gradation, Fig. 6.18 shows the variation of the $G/G_{max} - \gamma$ and $D - \gamma$ curves for two dense specimens of the tested materials with either $C_u = 1.25$ or 5 subjected to a p' of 100 kPa. The decrease in the G/G_{max} for the well-graded mixture of angular glass (Fig. 6.18a) is slightly faster as compared to the uniform one. The same trend can be found for Rhein sand and glass beads (Fig. 6.18c and e). For the damping of angular glass and round glass (Figs. 6.18b,f), the uniform mixture shows slightly higher damping at a similar γ compared to the well-graded material. However, for Rhein sand, the opposite trend was noted (ref. Fig. 6.18d), which could again be due to the influence of surface roughness.
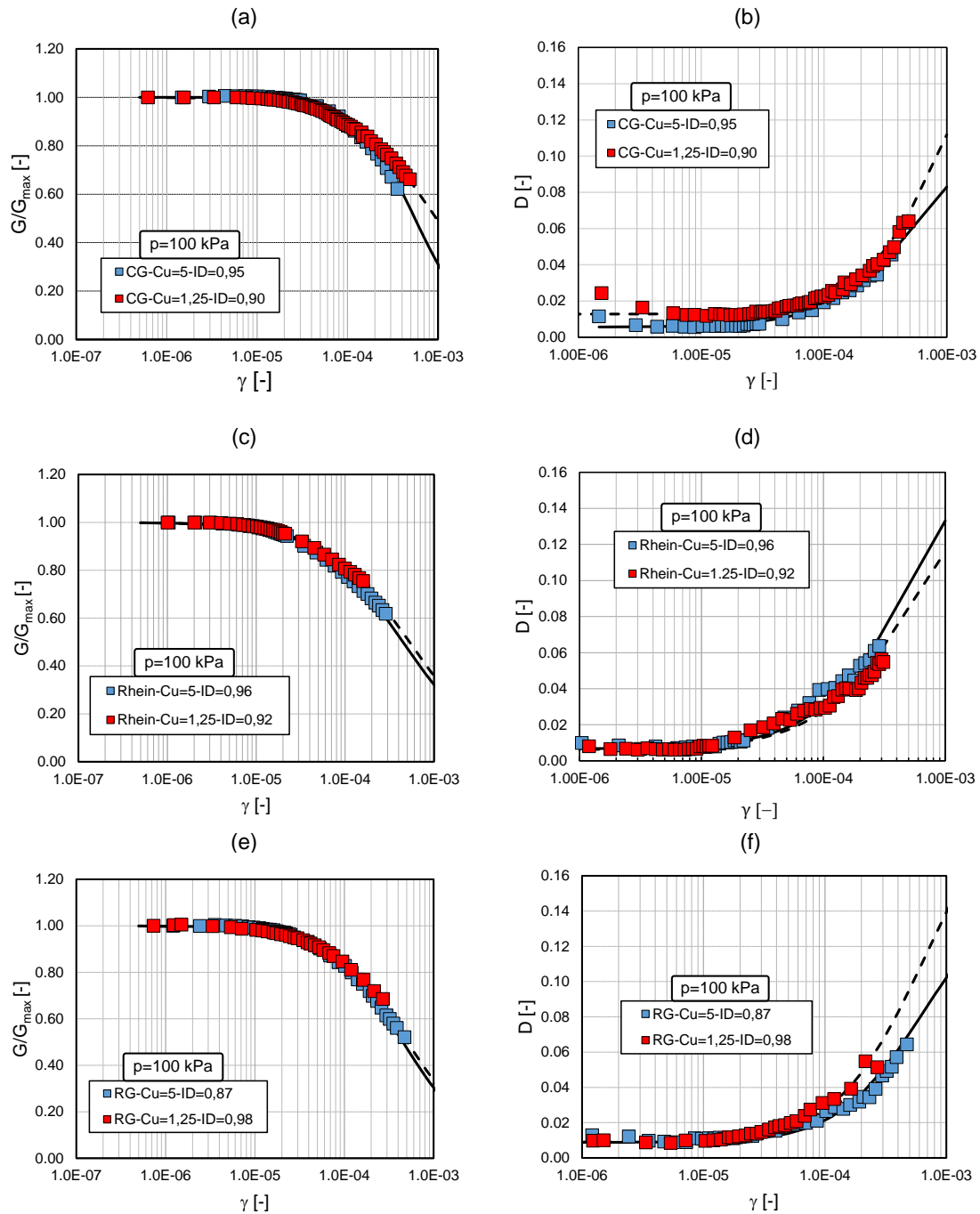
Figure 6.18: Influence of the gradation on (a) $G(\gamma)/G_{max}$ and (b) $D(\gamma)$ curves for all materials compared under a $p^{'} = 100$ kPa

Influence of grain shape on $G(\gamma)/G_{max}$ and $D(\gamma)$

Using the best-fit parameters of the Stokoe and Goudarzy models to describe $G(\gamma)/G_{max}$ and $D(\gamma)$ variation in granular soils, a comparison on the influence of grain shape is

provided in Fig. 6.19 for $p' = 100$ kPa. In Fig. 6.19a, only the uniformly graded materials are considered. It is clear that the variation in the G/G_{max} with shear strain for the crushed glass is visibly different from that of the others, generally showing higher values at larger strains in the range between $\gamma = 10^{-5}$ and 10^{-3}. For the Rhein sand and glass beads, the reduction of G/G_{max} with increasing γ is similar. A similar observation is noted for the well-graded mixtures in Fig. 6.19b, with the reduction of $G(\gamma)/G_{max}$ being slowest in case of angular glass. This implies that the reference shear strains γ_r for such angular materials are larger than for more rounded materials.
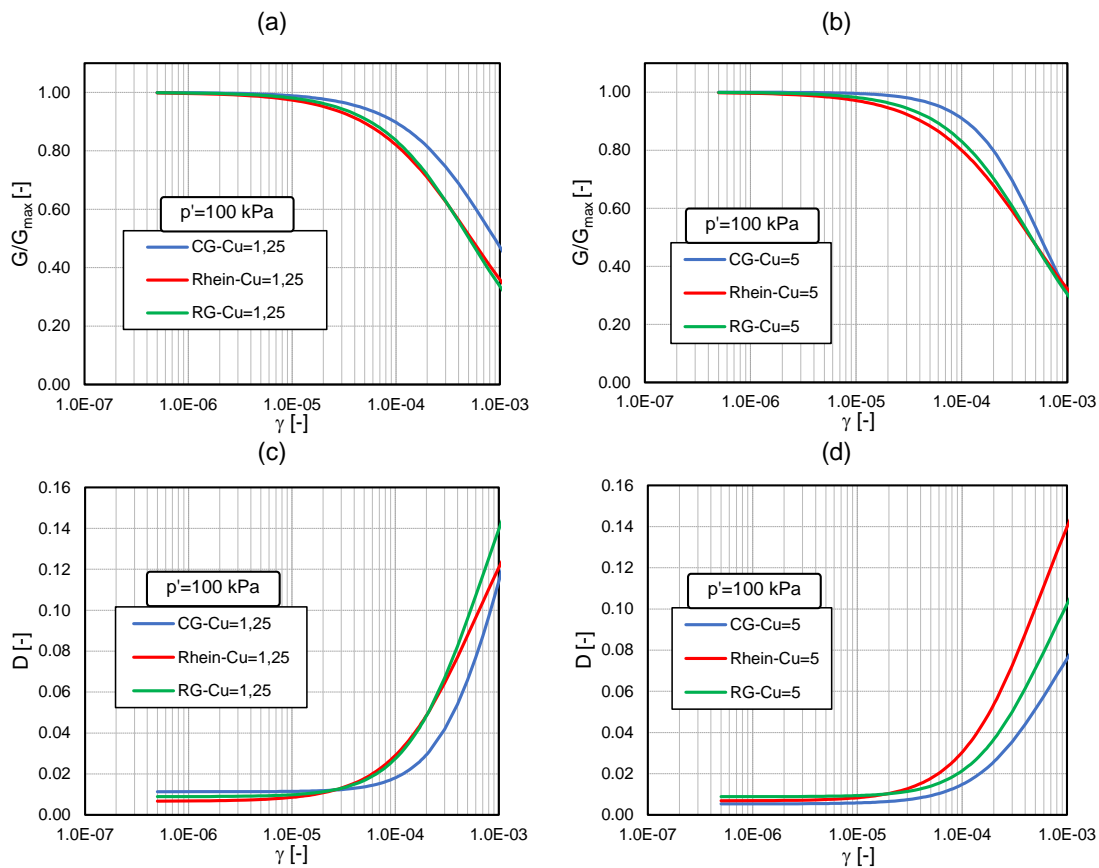
Figure 6.19: Influence of the grain shape on (a) and (b) $G(\gamma)/G_{max}$, and (c) and (d) $D(\gamma)$ curves for the six materials compared at $p' = 100$ kPa. The curves are generated by Eqs. 2.31 and 2.34 using the fitting parameters in Table 6.6

The variation of D with γ using the fitting parameters of the Goudarzy damping model leads to similar conclusions as for G/G_{max}: although the initial minimum damping is similar for the tested materials, at increasing γ, the damping increases faster for the Rhein sand and glass beads compared to the angular glass. It is interesting to note that the increase of D particularly for the well-graded Rhein sand is faster than for glass beads
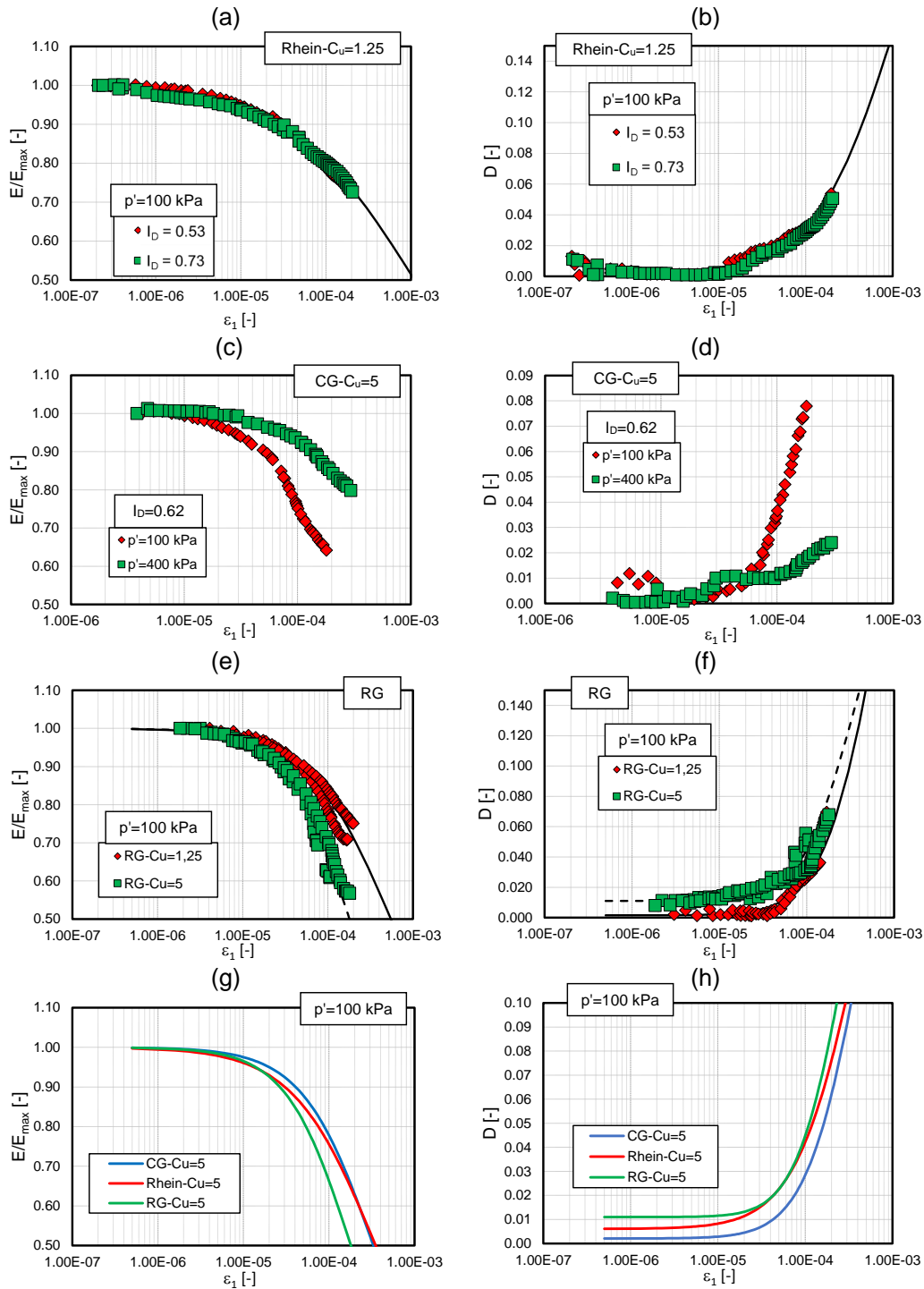
Figure 6.20: Influence of the (a) and (b) I_D for Rhein sand ($C_u = 1.25$), (c) and (d) p' for crushed glass ($C_u = 5$), (e) and (f) gradation for glass beads under a constant $p' = 100$ kPa, and (g) and (h) different grain shapes on the $E/E_{max} - \epsilon$ and $D - \epsilon$ curves obtained from the various RC tests with axial excitation

although for the uniform mixtures (Fig. 6.19c), the predicted D at $\gamma = 10^{-3}$ for glass beads is slightly larger.

Influence of e, p' and gradation on $E(\epsilon)/E_{max}$ and axial damping ratio $D(\epsilon)$

Following a similar trend to the results for the torsional mode of vibration, Fig. 6.20 shows the influence of various parameters on the elastic modulus degradation and damping curves. The influence of the void ratio (or relative density) is negligible on both the $E/E_{max} - \epsilon$ and $D - \epsilon$ curves as in the case of the torsional tests, being evident in the results for the uniformly graded Rhein sand subjected to $p' = 100$ kPa shown in Fig. 6.20a and b. In accordance with the data for the torsional mode of vibration, the reduction in E/E_{max} and the increase in D with increasing axial strain ϵ is lower at higher p', leading to a considerably higher E/E_{max} and lower D at similar ϵ as can be seen for the angular glass specimen with a relative density of 0.62 in Figs. 6.20c and d). It must be mentioned that the small fluctuations observed for D at $p' = 100$ kPa for very small ϵ are a result of noises arising from the device, and with increasing p', the noises become lesser, which is why the same is not observed for a $p' = 400$ kPa.

Regarding the influence of gradation in Figs. 6.20e and f, the reduction in E/E_{max} with increasing axial strain is larger for the well-graded glass beads than for the uniform glass beads, implying that at a similar ϵ, the E/E_{max} for the well-graded material at larger axial strains are lower than for the poorly graded one. However, for the variation of damping, at smaller ϵ, the D for the well-graded beads seems to be slightly larger than for the uniform beads, but as axial strain increases, both curves become closer, although in general the damping for the well-graded material seems slightly higher than for the uniform one. This observation seems contrasting to the variation of D observed in the case of torsional mode for glass beads although the variation of E/E_{max} follows a similar trend as G/G_{max}.

Influence of grain shape on $E(\epsilon)/E_{max}$ and axial damping ratio $D(\epsilon)$

The trend for the variation of the elastic modulus degradation and damping curves with varying grain shape for the well-graded materials seems clearer (see Figs. 6.20g and h), with the angular material showing the maximum E/E_{max} at a given ϵ as well as the minimum D. The data for round glass beads show a reverse trend, with the least E/E_{max} and maximum D at a given ϵ, generally matching well with the observations from torsional tests.

Table 6.7: Fitting parameters to describe the variation of the shear and elastic modulus with shear or axial strain for the torsional (under both $p' = 100$ and 400 kPa) and axial (only under $p' = 100$ kPa) modes of vibration applying the models of Stokoe (Stokoe et al. 1999) and Goudarzy (Goudarzy et al. 2018)

Material	C_u	p' [kPa]	Torsional mode: $G(\gamma)/G_{max}$ and $D(\gamma)$				
			Stokoe model		Goudarzy model		
			α [-]	γ_r [-]	D_{min} [-]	M [-]	N [-]
Crushed glass			0.99	8.90×10^{-4}	0.0113	25.75	1.64
Rhein sand	1.25		0.91	5.29×10^{-4}	0.0066	28.00	1.15
Round glass		100	1.00	5.07×10^{-4}	0.0089	26.00	1.40
Crushed glass			1.35	5.55×10^{-4}	0.0053	24.50	1.40
Rhein sand	5		0.93	4.47×10^{-4}	0.0068	31.50	1.30
Round glass			1.05	4.53×10^{-4}	0.0088	18.50	1.50
Crushed glass			1.05	1.63×10^{-3}	0.0078	31.50	1.51
Rhein sand	1.25		0.94	1.10×10^{-3}	0.0065	18.33	1.10
Round glass		400	0.98	1.06×10^{-3}	0.0053	20.75	1.03
Crushed glass			1.32	9.43×10^{-4}	0.0062	16.25	1.28
Rhein sand	5		0.97	8.16×10^{-4}	0.0067	20.00	1.15
Round glass			1.06	9.40×10^{-4}	0.0066	11.75	0.90
			Axial mode: $E(\epsilon)/E_{max}$ and $D(\epsilon)$				
			Stokoe model		Goudarzy model		
			α [-]	ϵ_r [-]	D_{min} [-]	M [-]	N [-]
Crushed glass			1.00	1.45×10^{-3}	0.0170	120.00	1.60
Rhein sand	1.25		0.60	1.10×10^{-3}	0.0021	150.00	0.95
Round glass		100	0.90	5.50×10^{-4}	0.0015	350.00	1.65
Crushed glass			1.00	3.78×10^{-4}	0.0030	150.00	1.87
Rhein sand	5		0.95	3.50×10^{-4}	0.0059	75.00	1.58
Round glass			1.07	2.80×10^{-4}	0.0113	19.00	1.50

Based on the fitting parameters for the torsional (both under $p' = 100$ and 400 kPa) and axial modes (only under $p' = 100$ kPa) of vibration representing the G/G_{max} or E/E_{max} and D versus γ or ϵ curves (Table. 6.7), the main observations are as follows:

1. The magnitude of the reference shear or axial strain γ_r and ϵ_r increases with increasing angularity irrespective of gradation.

2. The slope of the degradation curves represented by α is also dependent on the grain size, and can be inferred from the degradation of G or E curves for the tested materials.

3. A clear trend with respect to the influence of grain shape or gradation on the minimum damping D_{min} is not apparent with the present set of results.

4. The variation of M for differing grain shapes seems random, while the N generally takes larger values for angular materials.

5. The reference shear or axial strains are generally larger for uniformly graded soils than for well-graded ones. With respect to α, no definite trend is seen. Initial D_{min} values for uniformly graded materials are slightly larger than for the well-graded ones. Also, the value of N generally decreases with increasing C_u, while no specific variation of M is presently noticeable.

6.4 Summary

In this chapter, the influence of grain shape and gradation on the dynamic properties of granular soils was thoroughly analyzed and discussed. The main conclusions are as listed below:

- An attempt was made to investigate the efficiency of various grain shape parameters both in medium and macro scale to capture the variation of the shear wave velocity of granular materials. The shape distribution curve to capture the variation of grain shapes accurately, particularly in well-graded materials was proposed, and its effectiveness was validated through strongly capturing the influence of void ratio e (represented by the fitting parameter d) on v_s.

- At similar values of void ratio and mean effective stress, G_{max} is comparatively higher for uniformly graded materials as compared to well-graded materials. The G_{max} and E_{max} for round materials are larger than for angular materials. No influence of void ratio e on the modulus degradation and damping curves was encountered presently, while modulus degradation is less and damping ratio is lower for higher pressures p'.

- The reference shear or axial strains are larger for angular materials compared to round materials, as well as for poorly-graded (uniform) materials compared to well-graded ones. The influence of grain shape on D_{min} is insignificant based on the

results of the present study. In addition, the influence of grain shape and gradation on certain fitting parameters was assessed.

7 Micro- and macromechanical outlook: DEM and SANISAND

While the previous chapters predominantly focused on the analysis of soil behavior observed in various laboratory tests, the present chapter considers the micro- and macromechanical implications using the experimental results. To facilitate the micro-mechanical interpretations, the discrete element method (also referred to as distinct element method and usually abbreviated as DEM) is employed, while the elastoplastic SANISAND constitutive model considers the macromechanical (continuum) point of view. Finally, based on the experimental results from the RC device, a ground response analysis considering ground composed of granular soils with different particle shape subjected to earthquake motion was performed.

7.1 Discrete Element Method

First introduced by Cundall & Strack (1979), the discrete element method represents a numerical tool capable of describing the mechanical behavior of assemblies of discs and spheres. The biggest advantage of DEM is that the interaction of the particles is monitored contact by contact and the motion of the particles is modelled particle by particle. Thus, with DEM, it is possible to decribe the properties of granular materials considering their microscopic physical properties such as grain size, surface friction and rigidity. One of the biggest drawbacks of DEM is that simulations are time-consuming since every single particle is treated individually, and the soil is not considered as a continuum unlike in finite element models. This issue intensifies when simulating different grain shapes. Therefore, most studies have used round grains with varying surface friction to simulate different grain shapes, with a higher friction denoting angular materials (Lee et al. 2012).

Nevertheless, in recent years certain advancements have been made to take into consideration the influence of varying grain shapes (Jensen et al. 2001; Nouguier-Lehon et al.

2003; De Bono & Mcdowell 2016; Chang et al. 2017; Zhao et al. 2018; Nguyen et al. 2020a; Nguyen et al. 2020b). One of the most recent studies by Zhao & Zhao (2021) presents a novel open-source discrete element code, SudoDEM, for efficient modeling of both 2D and 3D non-spherical particles. Their code is built upon the popular open-source code YADE, and offers the possibility of generating a rich library of prime particle shapes, including poly-superellipsoids, superellipsoids, cylinders, cones, polyhedrons for 3D and disks and superellipses for 2D. More complex particle shapes can also be generated through clumping. Therefore, for it's ease of usage, in the present study, the author has adopted this code for simulating monotonic drained and undrained triaxial tests.

7.1.1 Simulating the three different grain shapes

To simulate the three grain shapes, the simplest approach using SudoDEM is the option of considering the grain aspect ratio Ar to model various angularity. As mentioned in the previous chapter (Chapter 6), the values of Ar calculated using ImageJ for the crushed glass, Rhein sand and glass beads were 1.467, 1.241 and 1.048 (refer Table 6.1). For the sake of simplicity, in the simulations these values are considered as 1.50, 1.25 and 1.00 for the angular glass, Rhein sand and round beads respectively. Thus, the largest Feret dimension (L) for an angular grain is 1.50 times the Feret breadth (B) measured perpendicular to the length axis. As a representative volume (RV), a total of 5000 grains are randomly generated for each simulation. The pictorial representation of the three materials is shown in Fig. 7.1.

To reduce the complexity of calculation during simulating the triaxial tests, a simple bidisperse distribution with the mean grain size $d_{50} = 0.45$ mm is achieved taking equal proportions of grains by number having diameters of 0.40 and 0.50 mm. This means that the grain size distribution was closer to the uniformly graded material used in the experiments. However, the same gradation has also been used for studying the drained behavior, while only well-graded mixtures were tested in the experiments. This is assumed acceptable since certain past studies have shown no or relatively small influence of the grain size distribution on the $q/p' - \epsilon_1$ curves analyzed in the following (e.g. Latha & Sitharam 2008; Harehdasht et al. 2019). Thus, although the consolidated undrained tests performed in the scope of the present work show some influence of gradation on the deviatoric stress response, the influence of gradation was neglected for the comparison of the drained test data just for the sake of simplicity and to reduce computational time. The density of the simulated particles is considered as 2650 kg/m^3. The grains were simulated using identical values of normal contact ($k_n = 3 \times 10^4$ kN/m) and tangential contact
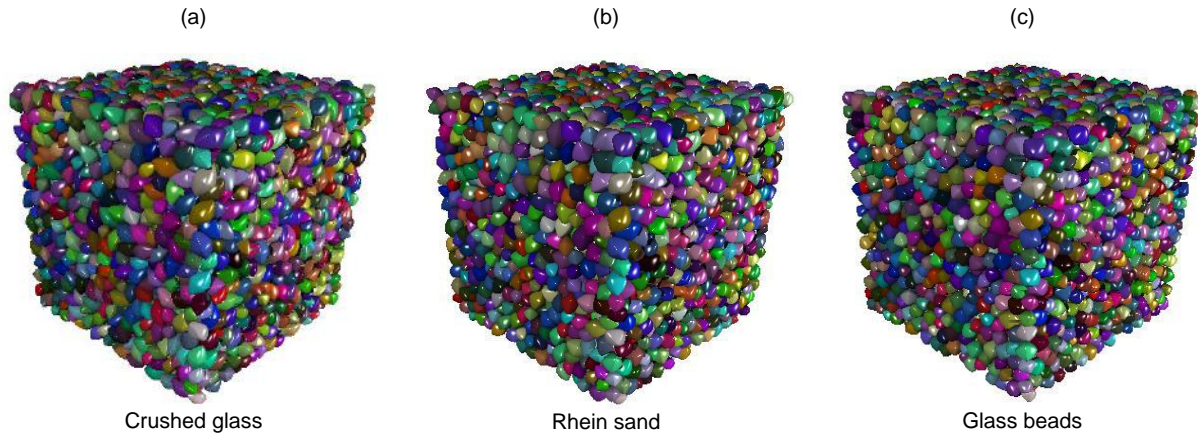
Figure 7.1: Schematic representation of the three grain shapes considering different aspect ratios: (a) crushed glass ($Ar = 1.50$), (b) Rhein sand ($Ar = 1.25$) and (c) glass beads ($Ar = 1.00$) simulated using SudoDEM

($k_s = 3 \times 10^4$ kN/m) stiffnesses, implying a ratio $k_s : k_n$ equal to 1 as commonly used in many previous studies (Kwok & Bolton 2013; Jiang et al. 2018; Zhao & Guo 2013; Nguyen et al. 2020b). The friction between the grains was varied to obtain different densities, with a low μ (=0.01-0.1 as an example) corresponding to dense specimens, while higher μ (=0.3 onwards) would imply a loose packing. Since the concept of periodic boundary conditions is not implemented in SudoDEM at present, rigid frictionless walls ($k_n = 1 \times 10^6$ N/m; $k_s = 0$; $\mu = 0$) were considered as boundaries.

The process of performing a triaxial test through DEM consists of two major steps: consolidation to the required void ratio, and the actual process of shearing under drained or undrained (constant volume) boundary conditions. After the particles are generated in random, they are isotropically compressed from the initial gas state with the predefined μ to reach a certain void ratio under a certain confining pressure. The consolidation process is considered to be completed once the ratio of the unbalanced forces (defined as the ratio of the kinetic to the potential energy) is lower than 0.01 while also maintaining the dimensionless inertial number I (a function of the mean grain size, shear rate, effective stress and grain density) lower than 10^{-3} (Zhao & Zhao 2021).

Afterwards, the state of the granular soil is saved, and it is subjected to monotonic drained or undrained triaxial loading. For drained tests, the displacement in the vertical direction is controlled by a predefined strain rate while keeping constant the lateral stresses. The volumetric strain ϵ_v is calculated as a function of the axial and lateral strains ϵ_1 and ϵ_3 (Eq. 7.1). In the case of undrained tests, the test is controlled by strains only, with no change

permitted in the ϵ_v, resulting in Eq. 7.2. The tests are continued till an axial strain of 25% is reached, similar to the experiments. A schematic representation for the undrained triaxial test on the glass beads showing the transformation from the post-consolidation cubic lattice to the final stage at $\epsilon_1 = 25\%$ is shown in Fig. 7.2.

$$\epsilon_v = \epsilon_1 + 2\epsilon_3 \tag{7.1}$$

$$\epsilon_v = 0 \tag{7.2a}$$

$$\epsilon_1 = -2\epsilon_3 \tag{7.2b}$$
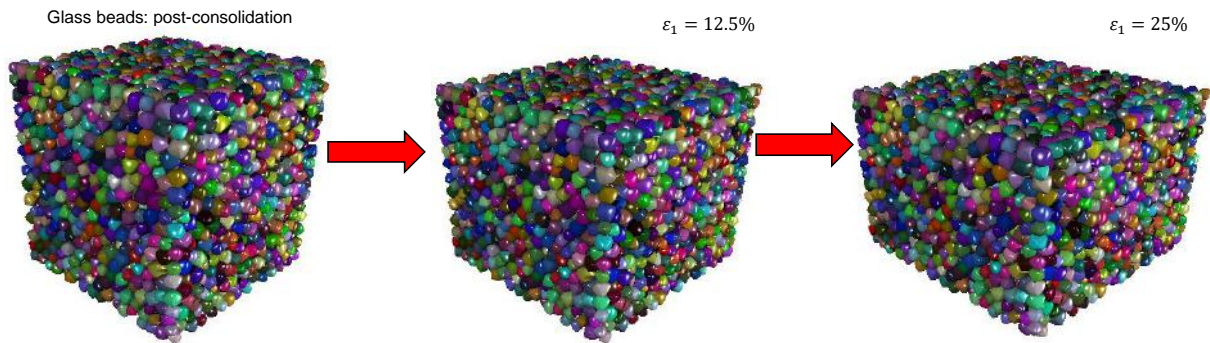
Figure 7.2: Schematic representation of the transformation of the glass beads from the post-consolidation state to the final end-of-shear state attained at $\epsilon_1 = 25\%$ after undrained shearing

Table 7.1: Details of the simulations performed using DEM considering similar I_D. The consolidated drained and undrained tests have been simulated for the well-graded and uniform specimens respectively

Material	Aspect ratio Ar	e_{max}	e_{min}	e	I_D	I_D-**Exp** (**CU**) $p' = 100$ **kPa**	I_D-**Exp.** (**CD**) $p' = 50$ **kPa**	μ_i	μ_f
				0.697	0.426	–	0.338	0.30	0.55
Crushed glass	1.50	0.902	0.423	0.501	0.84	0.804	–	0.05	0.55
				0.717	0.376	–	0.234	0.28	0.48
Rhein sand	1.25	0.881	0.545	0.545	0.77	0.825	–	0.08	0.40
				0.703	0.417	–	0.317	0.28	0.45
Round glass	1.00	0.848	0.498	0.568	0.80	0.856	–	0.08	0.30

7.1.2 Results from DEM

To simulate the monotonic undrained tests and to compare the results to the data for both uniform and well-graded specimens, DEM simulations were conducted. It is to be noted that varying the particle gradation does not have any major influence on the inclination $M = q/p^{'}$ of the steady state line as evidenced from the experimental results using two different C_u values (refer to Chapter 5). As a start, the maximum and minimum void ratios of the granular materials simulated through DEM are calculated under similar confining stresses since it is known that the limit void ratios considering extreme values of μ (=0 and 1) vary with stress (Nguyen et al. 2020b). Thus, for the purpose of comparison, the post-consolidation I_D in the experiments was considered as the reference based on which the I_D from DEM simulations was assessed. The maximum and minimum possible values of the void ratios achievable for the three simulated materials using the limit μ values are listed in Table 7.1. In addition, different I_D were obtained by varying the initial friction (denoted as μ_i), with a larger value for loose specimens, but a smaller one for achieving larger I_D. Therefore, the initial friction value is also the friction between grains used during consolidation. During triaxial compression, different end friction coefficients μ_f were used to achieve similar ranges of q and $p^{'}$ corresponding to the test completion.

The experimental results were presented in the $q - p^{'}$ and $q - \epsilon_1$ spaces. However, most studies in DEM prefer to use the stress ratio $q/p^{'}$ instead of q; therefore, the same approach has been adopted here for the stress-strain relationships.

Consolidated undrained (CU) tests

Fig. 7.3 compares the results obtained from the triaxial tests against the predictions by DEM considering dense specimens ($I_D > 0.75$) for the uniformly distributed samples. The M for the angular glass for the dense sample simulated via DEM is around 1.45, while for the Rhein sand and glass beads, the values are 1.40 and 1.00, respectively. As the ϵ_1 increases, the $q - p^{'}$ curves show a slight reduction of inclination, which is in contrast to the experimental data, where the M is almost constant and does not show any change of inclination even at higher axial strains. In agreement with the experiments the DEM model shows a slight strain softening behavior at larger strains for all the specimens. However, even with relative high friction coefficients during shearing, the DEM model predicts peak $q/p^{'}$ (i.e. M) values being lower than what is observed in the experiments, especially for materials having larger Ar values. This observation has also been encountered previously in the works of Nguyen et al. (2020a) and Nguyen et al. (2020b) employing different
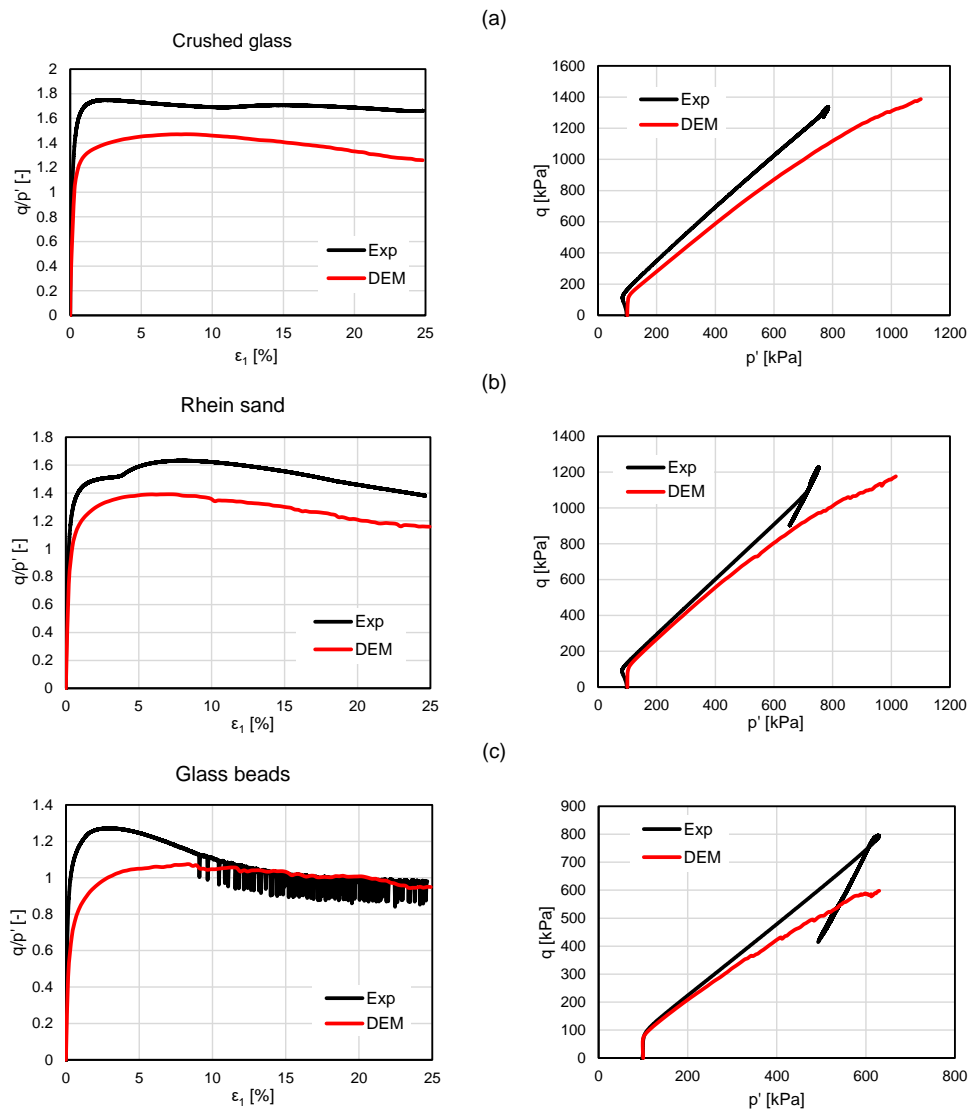
Figure 7.3: Comparison of the $q/p' - \epsilon_1$ and $q - p'$ responses from the undrained experiments with those predicted by DEM for the uniformly distributed test materials subjected to initial $p' = 100$ kPa

particle shapes where the maximum value of q/p' was found to be 1.20 for the most irregular-shaped samples. In the present case, the M values observed at the end of test (assumed to correspond to the steady state) read 1.25, 1.18 and 0.94 for the crushed glass, Rhein sand and glass beads, respectively.

Consolidated drained (CD) tests

In the DEM simulations the consolidated drained tests on loose samples of the well-graded materials under an initial $p^{'}$ of 50 kPa were considered. Fig. 7.4 shows the predicted $q/p^{'} - \epsilon_1$ and volumetric-axial strain ($\epsilon_v - \epsilon_1$) curves in comparison to the experimental data.
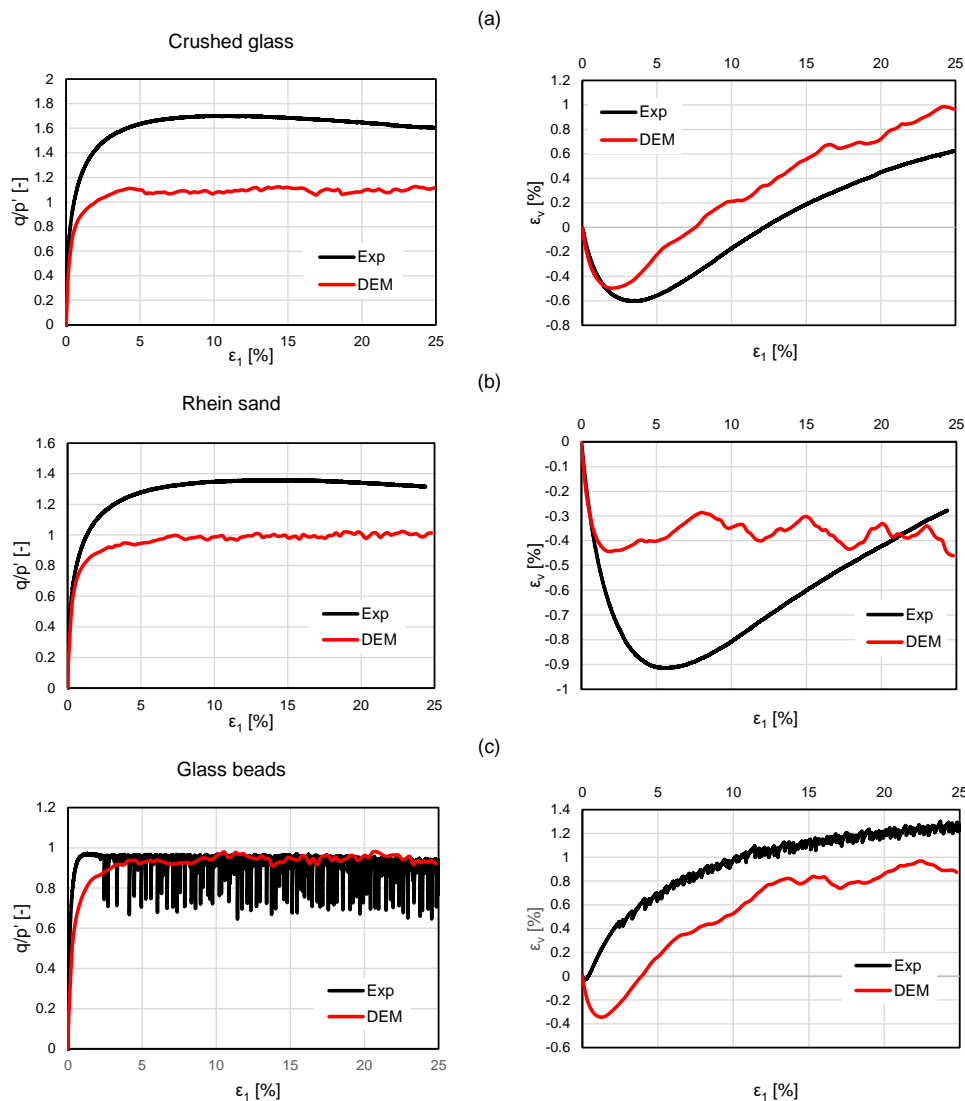
Figure 7.4: Comparison of the $q/p^{'} - \epsilon_1$ and $q - p^{'}$ responses from the drained experiments on well-graded materials with those predicted by DEM for the uniformly distributed materials subjected to initial $p^{'} = 50$ kPa

For the change in the volumetric strain ϵ_v against ϵ_1, the experimental results show a dilation behavior from the beginning of shearing for glass beads, while contraction followed

by dilatancy was measured for the other two materials. However, the DEM simulations on the three different materials all show initial compaction followed by dilatancy. Comparing the variation of the magnitude of ϵ_v between the experiments and DEM, a good agreement is seen for the crushed glass and glass beads, while the congruence was less satisfying for Rhein sand without following a specific trend. Nevertheless, the final magnitude of ϵ_v at the end of the test obtained in the simulations was close to the experimental observation. As in the undrained case, the maximum and final values of the stress ratio q/p measured in the experiments on the angular glass and the Rhein sand were significantly underestimated in the DEM simulations.

The biggest difference between the loose drained and dense undrained simulations is the value of M at the end of the test ($\epsilon_1 = 25\%$). While in the case of the undrained tests on dense specimens of angular glass and Rhein sand the M values evaluated at $\epsilon_1 = 25\%$ are 1.45 and 1.40, respectively, much lower values were obtained for the loose specimens under drained conditions, namely, 1.10 and 1.01, respectively. However, the final experimental M values are reproduced quite well in the simulations for glass beads in both the cases.

7.1.3 Influence of grain shape in both CU and CD tests

To assess the influence of grain shape, the $q/p' - \epsilon_1$ and $q - p'$ curves from the simulations on the samples with the three different grain shapes are plotted together for the drained and undrained cases in Fig. 7.5. Comparing the plots for both the undrained (Fig. 7.5a) and drained (Fig. 7.5b) tests, in both cases the q/p' against ϵ_1 for crushed glass lies above the curves for Rhein sand, which is again above glass beads, implying a similar sequence of the residual strength values at the steady state. Furthermore, this observation is supported by the magnitudes of the deviator stress reached at $\epsilon_1 = 25\%$, as visible from the $q - p'$ diagrams. The differences between the varying grain shapes are smaller for the drained case owing to the rather loose initial state of the specimens.

The variations of the peak friction angle ϕ_p against the grain shape parameters aspect ratio Ar and regularity is plotted in Figs. 7.6a and 7.6b respectively. As in the case of the experiments, the angular crushed glass shows the highest ϕ_p and the glass beads the least. It should be noted that the ϕ_p increases with increasing Ar but decreases with increasing ρ. The trend of the present set of results is in agreement with the observations from the recent studies by Nguyen et al. (2020b) who pursued a similar goal: to assess the influence of four different grain shapes (spheres, ellipsoids and two types of clusters) corresponding to a certain grain size distribution via DEM using the software OVAL.
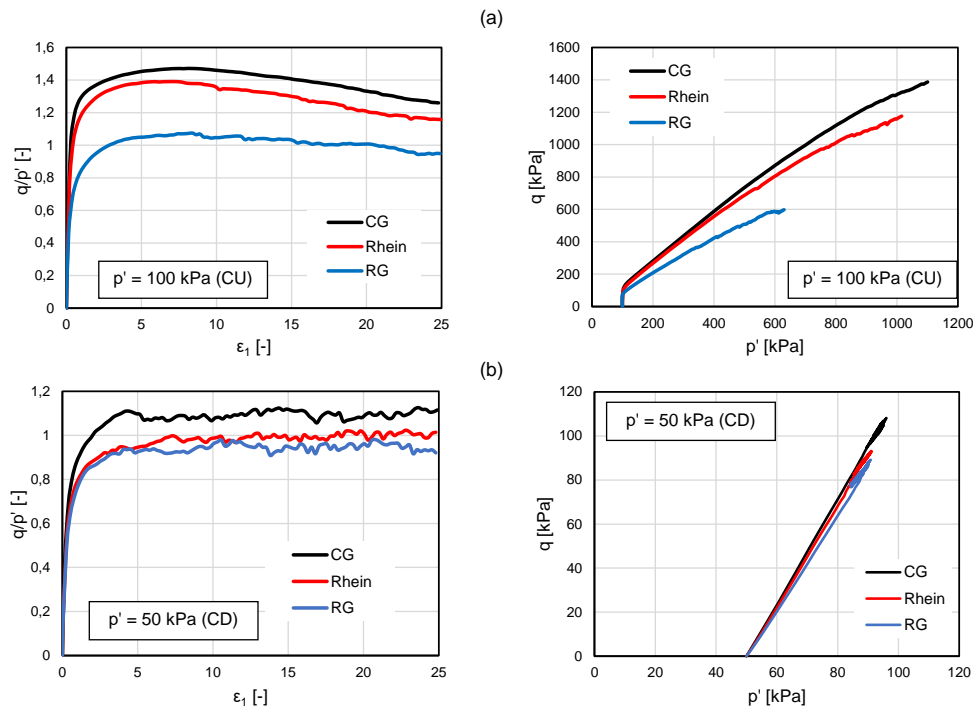
Figure 7.5: Comparison of the $q/p' - \epsilon_1$ and $q - p'$ responses from the two sets of DEM simulations isolating the influence of grain shape

The spheres showed the least magnitude of M with a value around 0.80 followed by the ellipsoids with $M = 0.90$. The clusters, comprising of a combination of seven spheres with two different degrees of overlap, displayed the maximum, with M ranging between 1.10 and 1.20.

7.1.4 Fabric orientation within the specimens

To understand the influence of different grain shapes on the fabric of the specimens tested in this research, it is imperative to analyze the average normal and tangential forces measured between individual grains at the end of the test, i.e. at an axial strain ϵ_1 of 25%. Fig. 7.7 shows the contact force chain diagram for the dense round glass beads in the CU simulations at $\epsilon_1 = 25\%$.

The particle-to-particle contact information which lists down the three components of the normal and shear forces was further analyzed. It is to be noted that the particle-wall contacts were eliminated since periodic condition was not guaranteed. The average normal
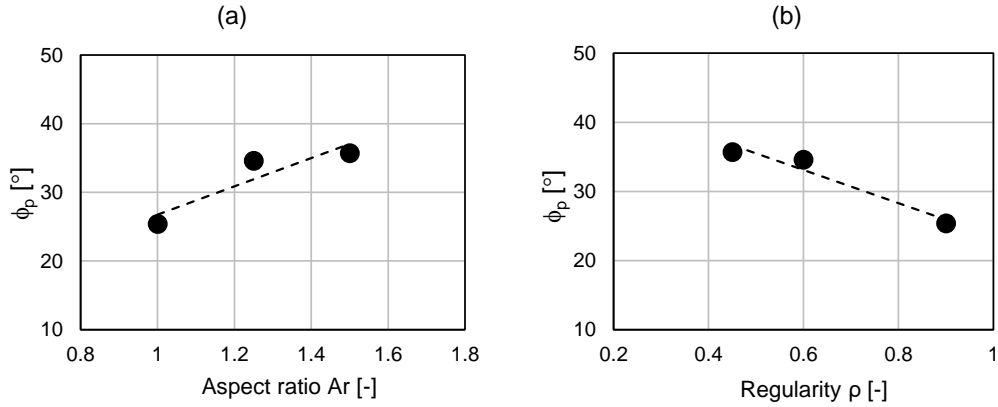
Figure 7.6: Comparison of the peak friction angle ϕ_p from the results of the DEM simulations on the dense samples against (a) the aspect ratio Ar and (b) the regularity factor
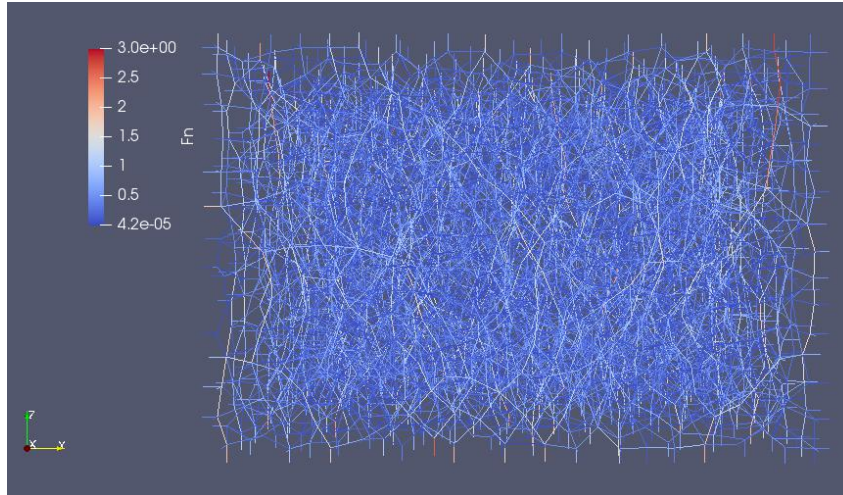
Figure 7.7: Contact force chain network for dense glass beads at an axial strain $\epsilon_1 = 25\%$ sheared undrained under an initial p' of 100 kPa

(F_n) and tangential/shear (F_t) forces for each particle contact were calculated from the following equations:

$$F_n = \sqrt{F_n(x)^2 + F_n(y)^2 + F_n(z)^2} \tag{7.3a}$$

$$F_t = \sqrt{F_t(x)^2 + F_t(y)^2 + F_t(z)^2} \tag{7.3b}$$

$F_n(x)$, $F_n(y)$ and $F_n(z)$ denote the normal force components while $F_t(x)$, $F_t(y)$ and $F_t(z)$ are the shear force components in the x, y and z directions, respectively.

For the specimens sheared under the consolidated undrained conditions, the value of the average normal forces at ϵ_1=25% are 0.698, 0.627 and 0.338 for the angular glass, Rhein sand and glass beads respectively. At the same time, the average shear forces measured are 0.216, 0.181 and 0.067 in decreasing order of aspect ratio. Therefore, it is clear that the magnitude of the shear force in comparison to the normal contact force is larger for angular materials than for round ones, and this aspect results in larger shear strengths. The ratio of the average F_n to the average F_t is 3.226, 3.464 and 5.044 with the highest magnitude determined for the glass beads. The fabric tensor (a symmetric second rank tensor which characterizes the geometric arrangement of the porous material microstructure, refer Cowin 1985) orientation for the three undrained tests is shown in Fig. 7.8. Similarly, for the loose drained specimens discussed previously, the average normal contact forces at 25% axial strain are calculated as 0.089, 0.080 and 0.077 while the shear forces measure 0.031, 0.025 and 0.027 respectively in decreasing order of the aspect ratio. A visualization of the fabric tensor for the loose samples is presented in Fig. 7.8.
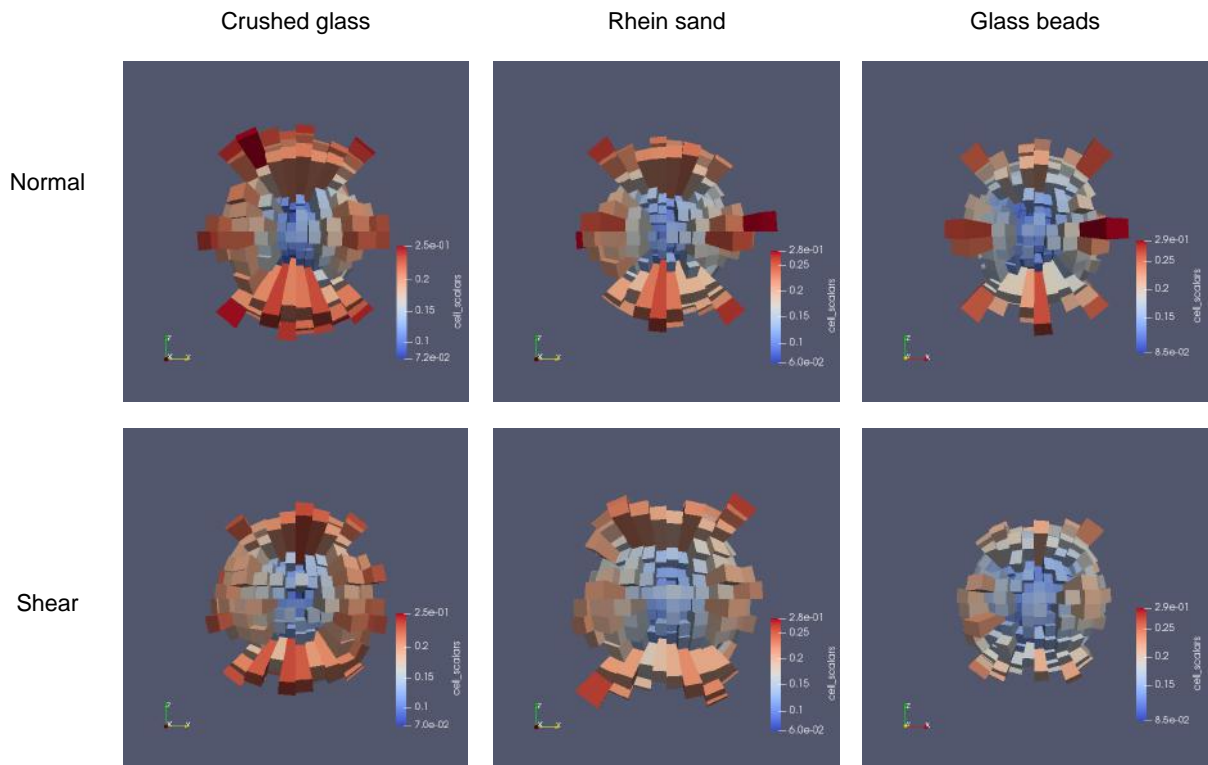
Figure 7.8: Fabric tensor at an axial strain $\epsilon_1 = 25\%$ for the dense specimens sheared under an initial p' of 100 kPa under undrained conditions

This can also be inferred from the magnitude of the coordination number (CN_0) which is defined in terms of the number of contacts C and the number of particles N. However,

Thornton (2000) pointed out that there are possibly some particles with zero contacts and some particles that have a contact with only one neighbour, therefore, these particles make no contribution to the stable state. Thus, the mechanical coordination number (denoted presently as CN) was recommended as follows:

$$CN = \frac{2C - N_1}{N - N_0 - N_1} \tag{7.4}$$

N_1 and N_0 are the number of particles with one and zero contacts respectively. For the dense specimens studied under undrained loading, at $\epsilon_1 = 25\%$, the CN for the material with the highest aspect ratio was 6.78, while for the intermediate specimen, it was 6.18. The least angular material had a CN of 6.08. All of these values are larger than 6 which is the value for a dense assembly of spheres compressed isotropically at 100 kPa. In case of the drained tests on the loose specimens, the values of the CN are determined as 4.92, 4.73 and 3.98 in decreasing order of the aspect ratio. A higher CN translates to a larger force carrying capacity, resulting in larger deviatoric stresses, which was evident from both sets of experimental and numerical observations.
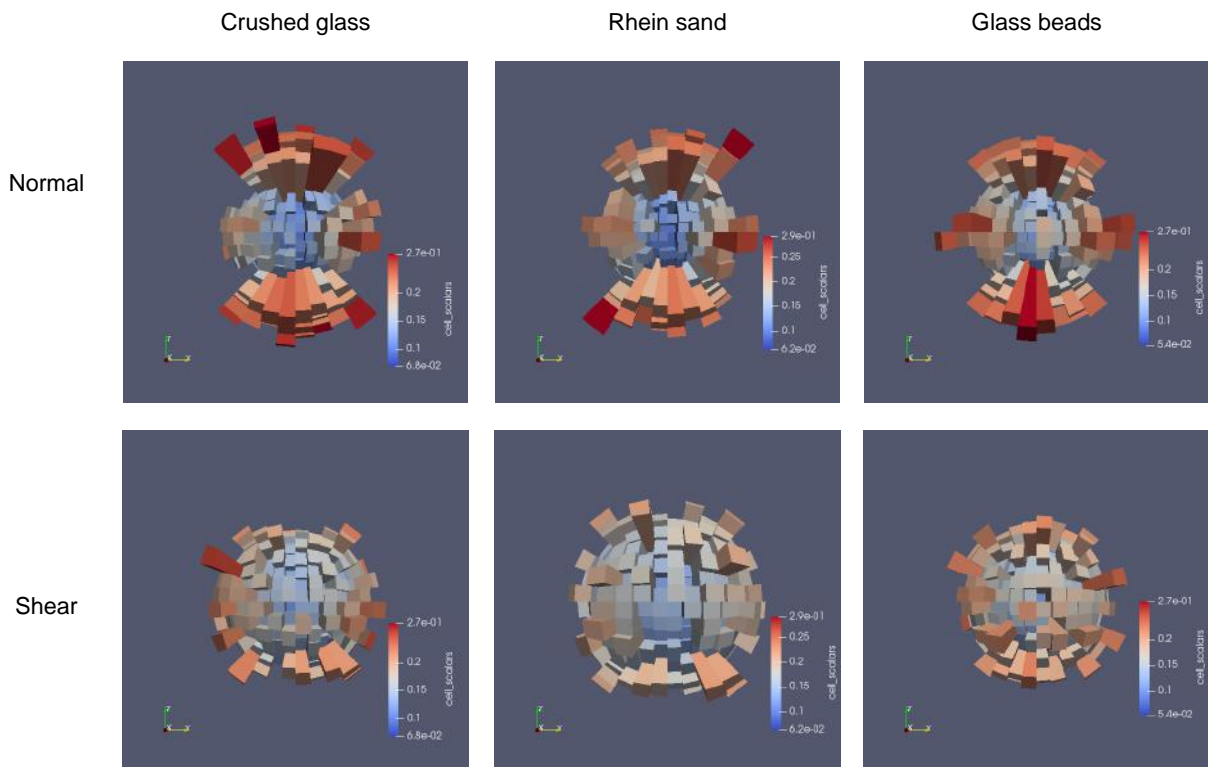
Figure 7.9: Fabric tensor at an axial strain $\epsilon_1 = 25\%$ for the loose specimens sheared under an initial p' of 50 kPa under drained conditions

7.2 Calibration of the parameters of SANISAND model

7.2.1 Brief introduction to SANISAND

Originally introduced by Manzari & Dafalias (1997) and later modified to include fabric change effects (Dafalias & Manzari 2004), SANISAND stands for a simple anisotropic model for sands. SANISAND is defined within the framework of critical state soil mechanics and bounding surface plasticity. It uses a narrow open cone-type yield surface with apex at the origin obeying rotational hardening, which implies that only changes of the stress ratio can cause plastic deformations, while constant stress-ratio loading induces only elastic response. The model has been widely used in simulating various stress-strain responses of granular materials over the years particularly due to its foundation on concepts and data which are well established and understood by the geotechnical engineering community. In the present study, one of the aims is to determine the material parameters of SANISAND for granular materials with different grain shape and to analyze the effect of grain shape on these parameters. For that purpose the parameters of the SANISAND model are calibrated using optimization techniques, with the ultimate goal of being able to provide certain recommendations for the choice of the values of the constitutive parameters that consider particle characteristics. This procedure is visualized in Fig. 7.10.
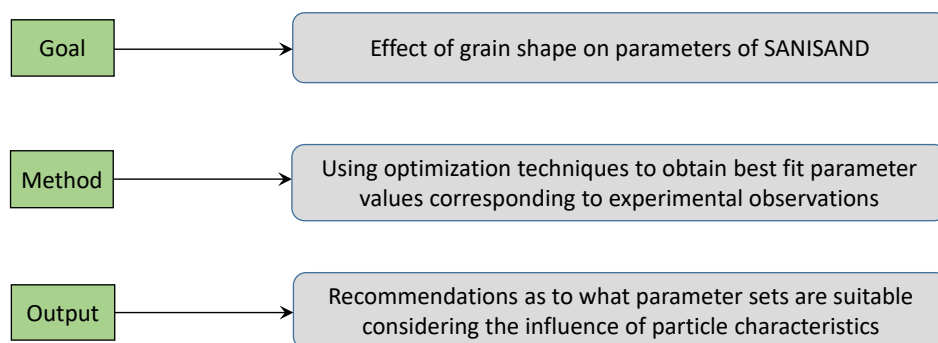
Figure 7.10: Flowchart outlining a schematic representation of the working sub-package

7.2.2 The parameters of the SANISAND model

The SANISAND model uses 15 parameters, some of which are obtained from experiments while others are numerical constitutive parameters which lack physical meaning. The parameters are listed in Table 7.2 along with their definition. The parameters that are

Table 7.2: Parameters of the SANISAND (2004) model

Parameter		Definition
CSL	$e_{cr,0}$	Critial void ratio corresponding to an effective stress $p^{'} = 1$ kPa
	λ	Slope of the critical state line in the $e - p'$ diagram
	ζ	Fitting parameter to account for the curvature of the critical state line
	M_c	Slope of the critical state line in the $q - p'$ diagram in compression regime
	$M_{e/c}$	Ratio of the critical state slopes under extension and compression regime
Yield surface	m	Tangent of half the opening angle of the yield surface
Elasticity	G_0^{el}	Dimensionless shear stiffness parameter
	ν	Poisson's ratio
Kinematic hardening	h_0	Positive material constant 1 to define the hardening modulus
	c_h	Positive material constant 2 to define the hardening modulus
	n_b	Material constant to calculate the stress image on the bounding surface
Dilatancy	A_0	Dilatancy material constant
	n_d	Material constant to calculate the stress image on the dilatancy surface
Fabric dilatancy	z_{max}	Maximum value that z can attain
	c_z	Control of the evolution of z

unique for each material and to be determined from experimental data are $e_{cr,0}$, λ, ζ, M_c and $M_{e/c}$. The other 10 parameters are constitutive parameters and must be determined by variation until the best fit of experimental data is achieved.

7.2.3 Some previous studies utilizing the SANISAND model

Since the early 2000s, the SANISAND model has gained popularity. A host of studies have focused on calibrating the material constants of the SANISAND model based on experimental results. Table 7.3 summarizes the parameters determined in the previous studies, along with information about the grain size distribution of the considered material and the available e_{max} and e_{min} data. CU and CD refers to consolidated undrained and drained monotonic tests, respectively, while Cyc denotes cyclic undrained tests. The typical ranges of the various fitting parameters as observed from Table 7.3 are listed in Table 7.4.

Table 7.3: Values of the various parameters in SANISAND model as obtained from certain studies in literature: A= Wichtmann et al. (2019c); B= Ramirez et al. (2018); C= Yang et al. (2018); D= Golchin & Lashkari (2014); E= Lashkari (2010); F= Shahir & Pak (2010); G= Taiebat & Dafalias (2008)

References		A	B		C	D		E	F		G	
Sands		KFS	Monterey 0/30	Ottawa F-65	Monterey 0/30	Toyoura	Hostun	Nevada	Toyoura	Fuji	Toyoura	Sacramento
Properties		$d_{50}=0.14$mm $C_u=1.4$	$d_{50}=0.4$mm $C_u=1.3$	$d_{50}=0.15$mm $C_u=1.45$	$d_{50}=0.3$mm $C_u=1.4$	$d_{50}=0.17$mm $C_u=1.32$	$d_{50}=0.35$mm $C_u=1.4$	-	$d_{50}=0.3$mm $C_u=1.4$	$d_{50}=0.38$mm $C_u=2.21$	$d_{50}=0.17$mm $C_u=1.7$	-
		$e_{max}=1.054$ $e_{min}=0.677$	$e_{max}=0.84$ $e_{min}=0.54$	$e_{max}=0.82$ $e_{min}=0.53$	$e_{max}=0.848$ $e_{min}=0.577$	$e_{max}=0.977$ $e_{min}=0.597$	$e_{max}=1.023$ $e_{min}=0.671$	-	$e_{max}=0.977$ $e_{min}=0.597$	$e_{max}=1.08$ $e_{min}=0.53$	$e_{max}=0.977$ $e_{min}=0.597$	-
Test type		CU/CD/Cyc	-	CD/Cyc	CU/Cyc	CU/Cyc	CU/Cyc	CD/CU/Cyc	CU/Cyc	Cyc	CU/CD	CU/CD
Elasticity	G_0/G_0^{el}	150	130	125	101	50	80	150	125	75	125	200
	ν	0.05	0.05	0.05	0.039	0.17	0.105	0.05	0.05	0.05	-	-
CSL	M_c	1.34	1.27	1.26	1.32	1.25	1.3	1.14	1.25	1.45	1.2	1.3
	$M_{e/c}$	0.938	0.712	0.735	0.718	0.712	0.81	0.78	0.89	1.0875	0.712	0.65
	$e_{cr,0}$	1.103	0.858	0.78	0.849	0.934	0.955	0.83	0.934	0.9	0.934	0.96
	λ	0.122	0.02	0.0287	0.01	0.019	0.094	0.027	0.019	0.0356	0.019	0.028
	ζ	0.205	0.69	0.7	0.7	0.7	0.3	0.45	0.7	0.7	0.7	0.7
Yield surface	m	0.05	0.02	0.02	0.03	0.001	0.001	0.02	0.01	0.01		
Dilatancy	n_d	2	2.5	2.5	2	2.1	3.3	1.05	3.5	3.25	2.1	2
	A_0	0.9	0.6	0.55	0.213	0.6	0.55	0.81	0.704	0.75	0.4	0.8
Kinematic hardening	n_b	1.2	1.05	2.3	2.5	1	0.65	2.56	1.1	0.65	1.25	1.3
	h_0	10.5	8.05	5	7.93	249.2	325	9.7	881.25-1300	99.8	36.96	22.75
	c_h	0.75	0.968	0.968	1.14	0.92	0.97	1.02	0.968-1.02	0	0.987	1.03
Fabric dilatancy	z_{max}	20	4	11	25	-	-	5	3	3.3	-	-
	c_z	1000-10000	50	500	1000	-	-	800	1500-3500	2500	-	-

Table 7.4: Typical ranges of the constitutive parameters of SANISAND (2004) model as observed in Table 7.3

Property	From Table 7.3	
	Min	Max
Elasticity	50	200
	0.039	0.17
Yield surface	0.001	0.05
Dilatancy	1.05	3.5
	0.213	0.9
Kinematic hardening	0.65	2.56
	5	1300
	0	1.14
Fabric dilatancy	3	25
	50	10000

It is expected that different sands will have different magnitudes of the CSL (critical state line) parameters. From the above information, it is clear that the constitutive parameters resulting from curve-fitting (excluding the CSL parameters) range within certain values, some of which have a smaller range (for example, dilatancy parameters A_0, n_d), while others have a significantly larger range (G_0^{el} and h_0). Therefore, selecting parameter values that fit for the materials under investigation need to be obtained by rigorously following an optimization procedure, thus ensuring the best possible fit of the experimental data by the numerical predictions.

Although the critical state parameters could have been adopted from the results of the experiments listed in 5, it was not done intentionally owing to a couple of points. The first reason is the limitation of the experimental setup: it was assumed that the critical / steady state was achieved at a strain of 25%, which was unfortunately not always the case, and therefore might induce errors during the optimization process. The second point was that the robustness of the optimization algorithm was also tested, to observe if the values predicted via optimization were representative or close to what is expected from the experimental observations. Also, a previous study has recommended and shown that using non-rigid steady state and elasticity parameters, a better fit to experimental data can be achieved otherwise employing the hypoplastic soil model (see Machaček et al. 2022).

Various optimization techniques

There are different optimization strategies that are used for multi-objective optimization depending upon the problem under investigation. Some of them are listed below:

- Strength Pareto Evolutionary Algorithm - II (SPEA - II)

- Multi-objective Evolutionary Algorithm by Decomposition (MOEAD)

- Covariance Matrix Adaption Evolution Strategy (CMAES)

- Indicator Based Evolution Algorithm (IBEA)

- Generalized Differential Evolution Algorithm - III (GDE - III)

- Optimized Multi-Objective Particle Swarm Optimization (OMOPSO)

- Non-Dominated Sorting Genetic Algorithm - II (NSGA - II) (Platypus 2015)

- Non-Dominated Sorting Genetic Algorithm - III (NSGA - III)

In the scope of the present optimization scheme, the Non-Dominated Sorting Genetic Algorithm - II (NSGA - II) has been employed since it was proven to be very efficient and as reliable as the NSGA - III Algorithm for 2 objective functions, further details of which may be found in Deb & Jain (2013) and Vallurupalli (2020). There are five stages and procedures for the NSGA - II Algorithm:

1. **Stage I:** Within the parameter space, the initial population of a certain size is generated. The ranking and crowding distribution is done where the initial population produces the same number of child population following the procedures: tournament selection, crossover and mutation.

2. **Stage II:** After crossover and mutation, the initial and child population are combined together.

3. **Stage III:** The ranking of these combined individuals is evaluated and the non-domination levels or rank fronts are designated to this combined population.

4. **Stage IV:** In case the need of sorting the individuals from the same rank front arises, the crowding distance is calculated for the individuals in that non-domination level and the better distanced individuals are refined and forwarded to fill the leftover size.

5. **Stage V:** The new population of pre-defined size is generated - the new population becomes initial population (parent population) which again produces the child population (crossover) depending on the number of generations assigned.

7.2.4 Sensitivity of various SANISAND model parameters

The input parameters of a system (e.g. SANISAND) do not have the same share of effect on the response of the system. Thus, changes in a certain parameter have a more pronounced influence on the system output as compared to other parameters. Since there are 15 parameters that are needed for the SANISAND model, it is imperative to perform a sensitivity analysis (SA) to isolate the more influential parameters from the lesser or non-influential ones. In this way, one can reduce the dimension of the problem without affecting the accuracy. Thus, some of the parameters can be eliminated from the optimization routine (or fixed with standardized values from literature) while the major influencing parameters can be determined with more accuracy.

Practically, there are two sensitivity analysis techniques: global and local SA. In local SA, the impact of a small variation in one variable on the model prediction is studied while the other parameters are kept constant. The global SA is more robust since it varies all the parameters within their specified ranges to investigate their effects on the system response as well as capturing coupled and non-linear phenomena. Therefore, compared to local SA, the global SA uses more computational power.

In the given problem, global SA was used to identify the most influential parameters. The results of the SA were denoted in the form of sensitivity indices which are calculated based on the procedure outlined in Sobol$'$ (2001). The SA has been performed at present only for the undrained monotonic tests on the three well-graded materials ($C_u = 5$). Two objective functions q and p' were checked for their sensitivity to the variation of the various model parameters. Therefore, the main objective of the SA is to isolate parameters that influence both q and p' so that only these parameters are taken forward for the optimization procedure.

In order to further simplify the optimization procedure, some trial runs for different values of the yield function parameter m were performed for the tested materials, where m was always found to converge within the range 0.042-0.050. Therefore, based on this observation, the variation of m was deemed insignificant, and was not included in the sensitivity analysis to speed up the computational time. As can be seen from Fig. 7.11, certain parameters have a higher sensitivity score, measured in the form of sensitivity indices (SI) while some others do not harbor any influence on the monotonic undrained responses of the tested materials. Take for example, the elastic parameter G_0^{el} has a high sensitivity score, which means its effect is significant: a variation in G_0^{el} can significantly change the material response. In a similar way, the steady state parameters e_{c0}, λ and
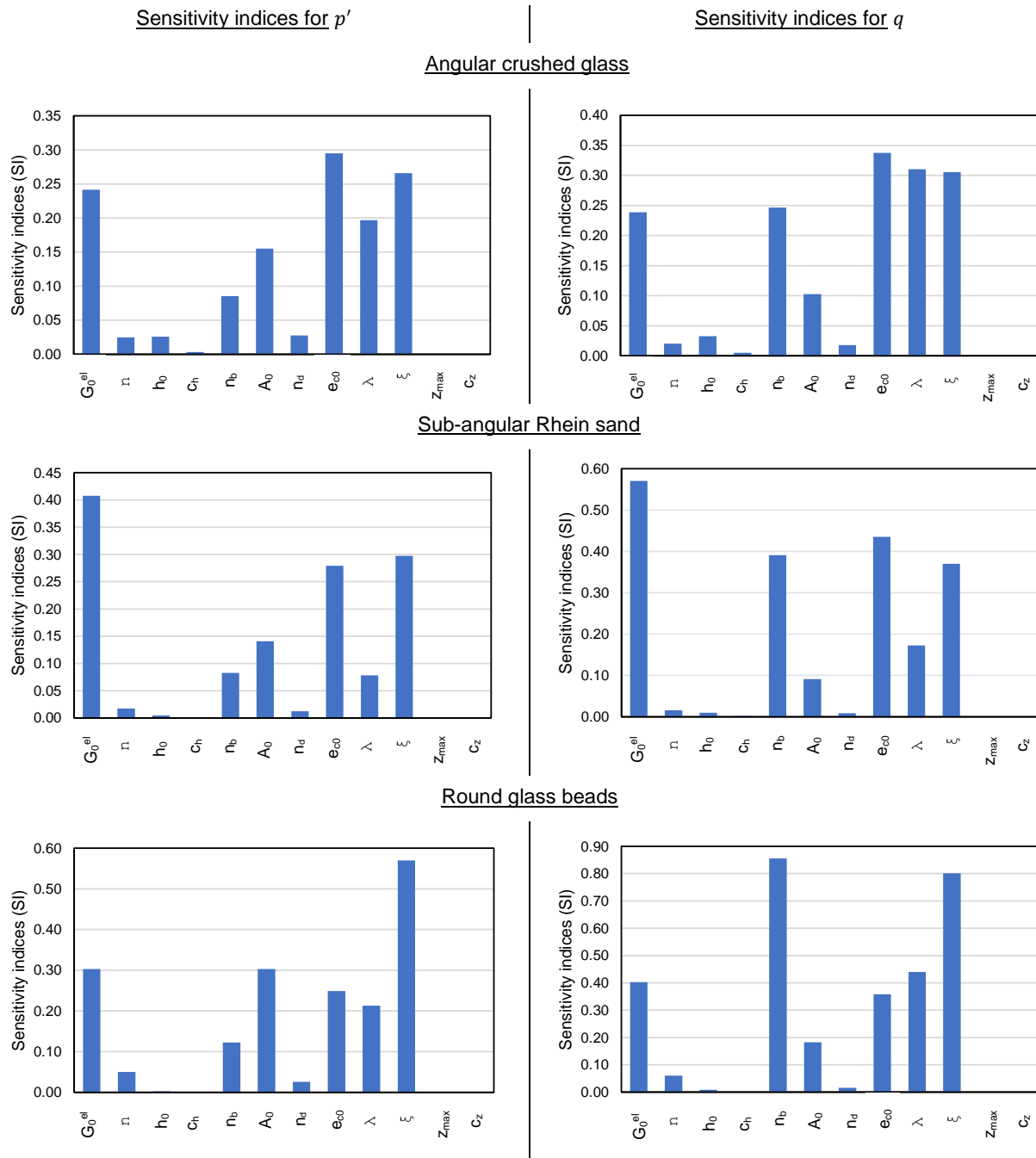
Figure 7.11: Sensitivity analysis for the objective functions $p^{'}$ and q considering the undrained tests under an initial $p^{'} = 300$ kPa for the dense samples of the three materials

ξ in addition to the slope of the steady state line M_c and $M_{e/c}$ (presently not shown) as was demonstrated in Chapter 5 also have quite large sensitivity indices denoting their significant influences. However, the influence of certain other constitutive parameters such

as ν, h_0, c_h, n_b, A_0 and n_d is also significant. In contrast, the SI values for the fabric parameters c_z and z_{max} are zero, which means that any variation of these parameters will not affect the material response as they are designed for capturing cyclic behavior. Therefore, for the optimization procedure, these two parameters are eliminated further to reduce the dimension of the optimization algorithm and to reduce computational time.

7.2.5 Optimization of SANISAND model parameters

The optimization procedure involves calibrating the input parameters in a way that the numerical predictions by the SANISAND model fit the experimental results as good as possible. The initial ranges of the constitutive parameters have already been presented in Table 7.4, which have been carried forward as the search domain that is fed as input to the optimization algorithm. Only the influential parameters which are to be varied (all parameters including the CSL parameters except m denoting the slope of the yield surface) have been chosen.

Since it is affirmative that the objective functions for optimization and the parameter ranges are significant in achieving effective results, the two objective functions have been developed which calculate the error between the experimental data and the numerical prediction with respect to the mean effective stresses and the deviatoric stresses at given axial strains. The R-squared score has been considered for the calculation of the mentioned error. With the genetic algorithm (NSGA-II) parameters of population (p = 100), generations (g = 50), crossover (uniform crossover) and mutation (m = 0.1%), this calibration procedure has been performed through minimizing these objective functions (automatically minimizing the error between the curves). The corresponding results will be presented for the monotonic test results only (both drained and undrained). Special emphasis is laid on the behavior in the elastic region for $q - \epsilon_1$ curves. In order to develop the fit, several other investigations concerning the effect of strain increment on numerical outputs, Poisson's ratio ν variation (local sensitivity analysis), etc. have also been carried out, details of which are presented in the upcoming sections.

As a first step, the calibration procedure was applied to crushed glass with a C_u of 5 to obtain the best fit parameters delivering numerical predictions being as close to the experimental observations as possible. Two extreme cases of the monotonic experiments performed presently were simulated: the first one was a drained test with an initial confining pressure $p' = 50$ kPa, while the second one was an undrained experiment with $p' = 300$ kPa. Two different end-of-consolidation void ratios e_0 were used. The compar-

ison between the experimental data and the SANISAND prediction was made up to an axial strain ϵ_1 of 15% since at higher strains, there is significant sample inhomogeneity associated. Using the best-fit parameters for the calibration, the comparison between the $q - p^{'}$ and $q - \epsilon_1$ curves is shown below in Fig. 7.12. It must be mentioned that the fitting parameters employed are the best-fit values as obtained from the two sets of experiments conducted. Therefore, only 1 set of parameters is obtained at the final stage, and not a range.
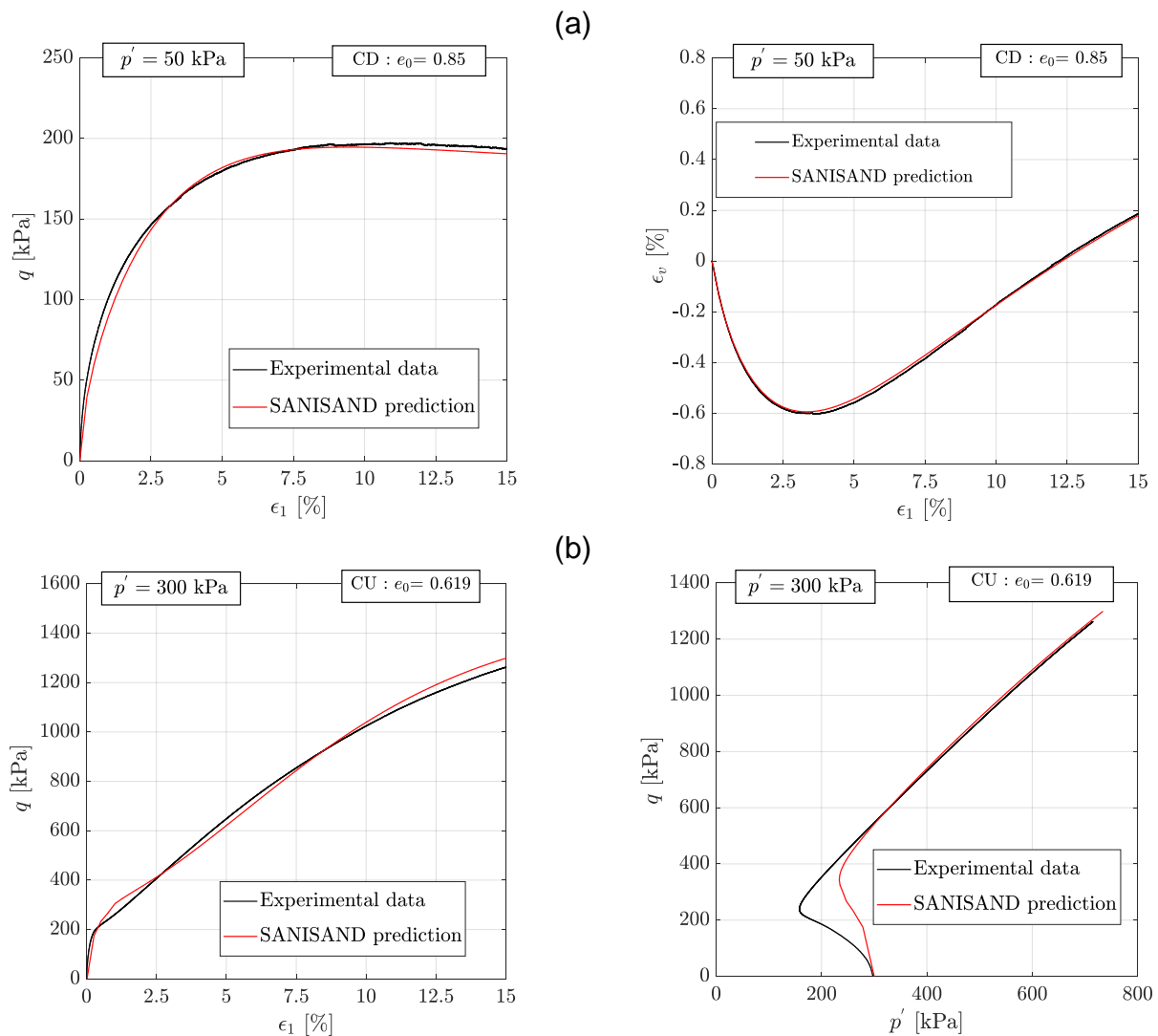
Figure 7.12: Comparison between the experimental data and SANISAND predictions for crushed glass under (a) drained and (b) undrained conditions subjected to two different initial $p^{'}$ values and different initial void ratios / relative densities
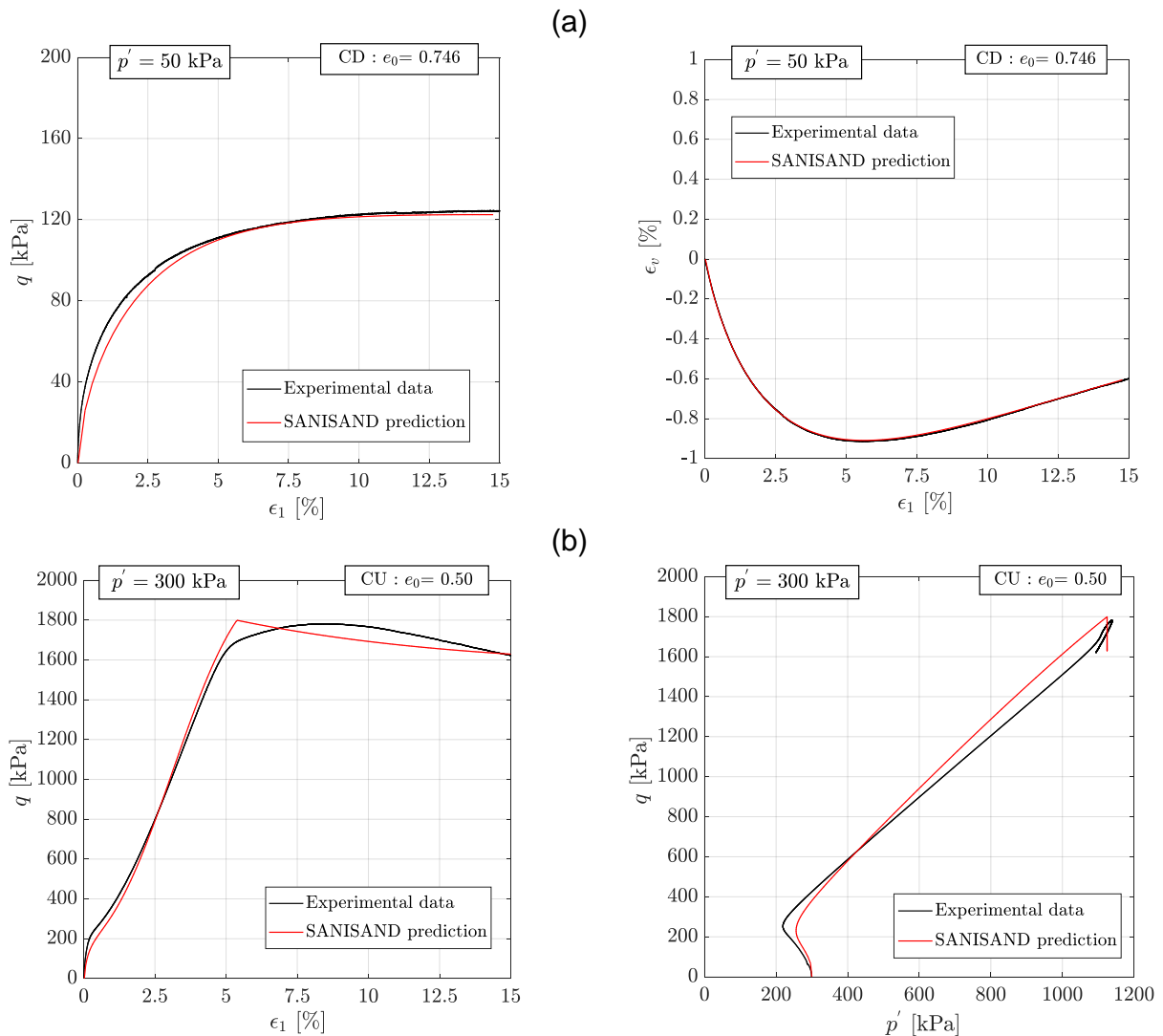
Figure 7.13: Comparison between the experimental data and SANISAND predictions for Rhein sand under (a) drained and (b) undrained conditions subjected to two different initial $p^{'}$ values and different initial void ratios / relative densities

It is clear that the fit between the experimental and numerical datasets is quite strong considering both drained and undrained cases. The only issue with the undrained case in Fig. 7.12b for the $q - p^{'}$ curve is that the predicted reduction in $p^{'}$ in the initial phase of the test (or till a q of around 400 kPa) is not as large as observed in the experiment. However, this in general is one of the backdraws of the SANISAND model as Wichtmann et al. (2019c) also encountered such differences in the effective stress path.

In a similar manner, the calibration procedure has been applied to the well-graded Rhein sand (Fig. 7.13) and glass beads (Fig. 7.14) under similar conditions as the crushed glass

(a)

(b)
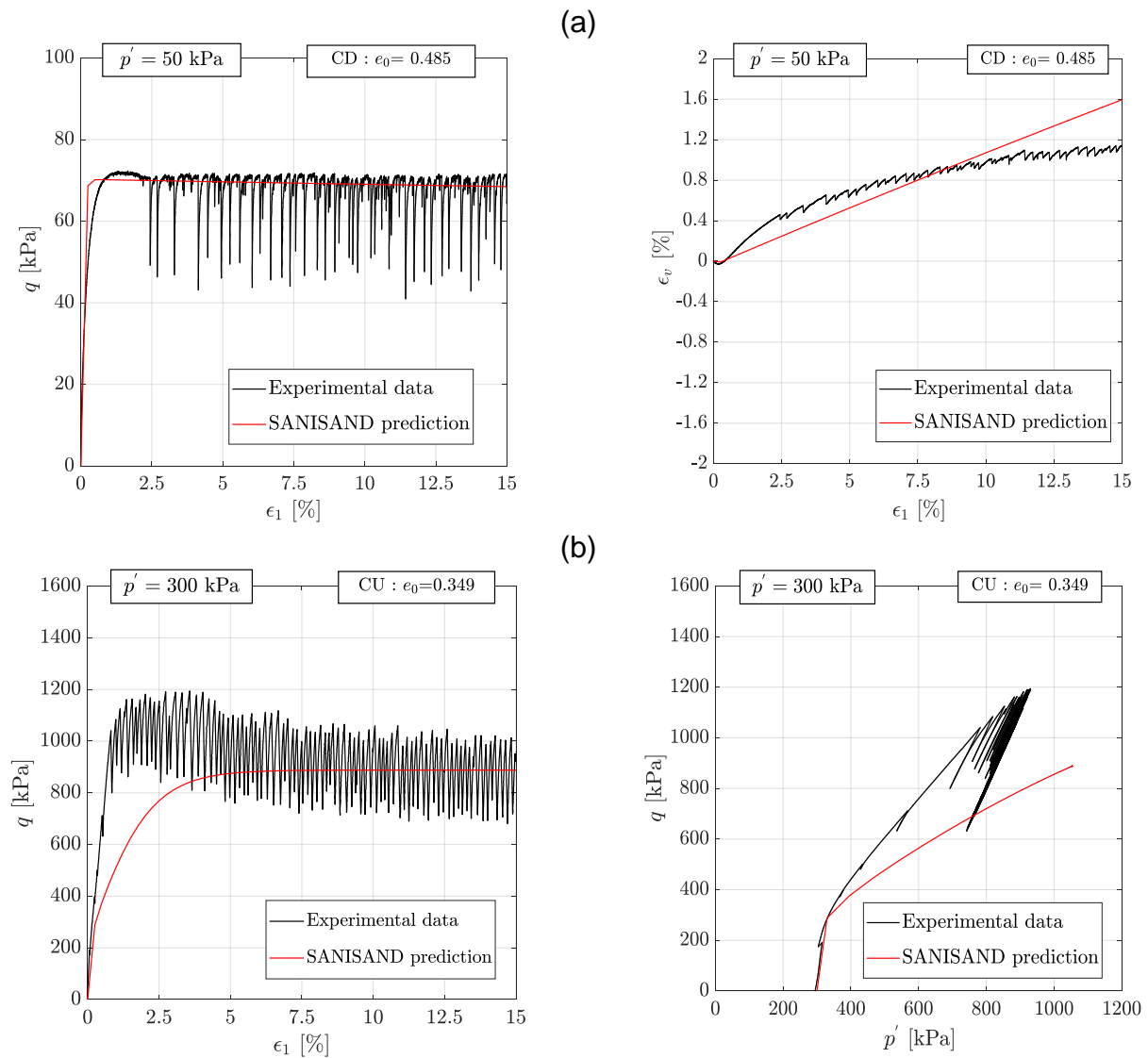
Figure 7.14: Comparison between the experimental data and SANISAND predictions for glass beads under (a) drained and (b) undrained conditions subjected to two different initial $p^{'}$ values and different initial void ratios / relative densities

($p^{'} = 50$ and 300 kPa) considering both drained and undrained cases and using two different e_0 values. The results for Rhein sand show a good agreement between the predicted and measured curves for both the drained and undrained cases. Clearly, the $q - \epsilon_1$ and $\epsilon_v - \epsilon_1$ curves for the drained test show a relatively better fitting compared to the undrained test, an observation similar to that noted for crushed glass. It is also noted that in the undrained case, the fitting of the $q - p^{'}$ at lower $p^{'}$ values is relatively better as compared to angular glass. However, the slope of the $q - p^{'}$ line obtained from the

prediction is slightly larger than that from the experiment. Unlike in the case of angular glass where the phase transformation point as predicted by SANISAND laid close to a q of nearly 340 kPa and p' of 250 kPa (q around 230 kPa and p' of 180 kPa were observed in experiment), the phase transformation point for Rhein sand from model prediction was around $q = 220$ kPa as against 230 kPa from experimental data, while the p' was around 250 kPa as against 215 kPa from experimental observation. For the glass beads, the SANISAND model is unable to reproduce the stick-slip motions since it only predicts a flat linear curve after achieving maximum q. Therefore, a compromised data set was employed to capture the general trend as well as the magnitudes of the q and ϵ_v as obtained from experiments. While a satisfying fit can be concluded for the drained case, the fitting is somehow worse for the undrained case. While the initial phase of the effective stress path in the CU test is captured well, the slope of the path is significantly underestimated afterwards. Furthermore, as visible from the stress-strain relationship also the stiffness in the initial phase of the test is predicted too low.

The fitting parameters that were employed for the best fit considering both monotonic drained (CD) and undrained (CU) cases are collected for the three different mateirals in Table 7.5.

Table 7.5: Fitting parameters for the SANISAND model obtained via optimization for the well-graded materials tested in the present study

Property	Parameter	Crushed glass	Rhein sand	Round glass
Elasticity	G_0^{el}	100.00	82.00	237.00
	ν	0.05	0.04	0.16
CSL	M_c	1.64	1.36	0.86
	$M_{e/c}$	0.646	0.687	0.778
	e_{c0}	0.981	0.755	0.728
	λ	0.058	0.030	0.045
	ξ	0.957	0.871	0.905
Yield surface	m	0.050	0.050	0.050
Dilatancy	n_d	1.053	3.000	2.306
	A_0	0.64	0.89	0.34
Kinematic hardening	n_b	0.70	2.50	0.70
	h_0	1.30	2.50	6.70
	c_h	0.49	1.07	0.86
Fabric dilatancy	z_{max}	4	4	4
	c_z	600	600	600

7.2.6 Analysis of the typical ranges of the fitting parameters

From Table 7.5, certain features can be observed. The magnitude of G_0^{el} apparently seems to increase with increasing grain roundness although the values for Rhein sand seem out of place. This might be hypothesized to be a result of the variation in surface roughness: while angular glass was expected to have higher roughness, one must realize it is a product of crushing smooth glass beads, and certain uncrushed surfaces are therefore expected to be relatively smoother than some others which might result in a higher G_0^{el}. Furthermore, the Poisson's ratio ν seems to slightly increase with increasing roundness.

For the steady state parameters, the M_c for angular materials is comparatively higher than for glass beads, while the ratio of the extension to compression slope $M_{e/c}$ increases with increasing degree of roundness. In agreement with the experimental observations listed in Chapter 5, a noticeable decrease in $e_{cr,0}$ and decreasing trend in λ and ξ with increasing grain roundness is also evident. Also in general, glass beads show significantly higher values of the hardening parameter h_0, while the values of the dilatancy parameter n_d show no definite trend with respect to grain shape. For the other parameters, the influence of grain shape is not clear with the limited experimental data used for calibration. Therefore, more tests with different boundary conditions are recommended as a part of future work. Furthermore, one may consider more grain shape combinations in further work packages.

7.3 Ground response analysis

To simulate ground motions resulting from earthquakes, the well-known ground response analysis software ProShake was adopted. ProShake is a computer program for one dimensional, equivalent linear ground response analysis. The original program for ground response analysis of layered sites was developed in the early 1970s, and was known as SHAKE (after Schnabel et al. 1972). For commercial usage, it was later renamed to ProShake. Some of the major advantages of ProShake is that user-defined modulus degradation and damping ratio curves can be provided as input parameters instead of using some standard existing models.

Therefore, in the present study, a 20 m deep soil profile directly resting upon a bedrock is considered with the water table located at the ground surface. To consider the stress-dependence of the soil properties the soil profile is further divided into 5 layers, each layer being 4 m in thickness. The layers are named from 1-5, with the 1st layer being the topmost layer and the 5th layer directly situated above the bedrock. The stresses

are calculated at the middle of each layer to consider the average effective stress in the particular layer. The same material is assigned to all five layers. The small-strain shear modulus G_{max} is calculated from Eq. 2.21 (Hardin & Black 1966) and the void ratio function of Jamiolkowski et al. (1991) is adopted. The fitting parameters previously listed in Table 6.6 are applied. The properties of the soil layers are derived directly from the test results for the three well-graded materials ($C_u = 5$) with differing grain shapes (angular glass, sub-angular Rhein sand and round glass beads) as highlighted previously in Chapter 6. Only fully water-saturated loose soil states ($0.19 < I_D < 0.33$) are considered since they represent the most critical conditions for soil liquefaction and subsequently, larger ground deformations. Thus, for the soil profile using angular glass, the dry unit weight was 13.47 kN/m^3, while for the Rhein sand and glass beads, these values were 15 kN/m^3 and 16.59 kN/m^3 respectively. Therefore, the corresponding I_D values were 0.33, 0.28 and 0.19 respectively, corresponding to the experimental relative densities. The bedrock was considered to be rigid with a unit weight of 23.56 kN/m^3 and a G_{max} of 1395.18 MPa in accordance with the ProShake tutorial (EduPro Civil Systems 2020).
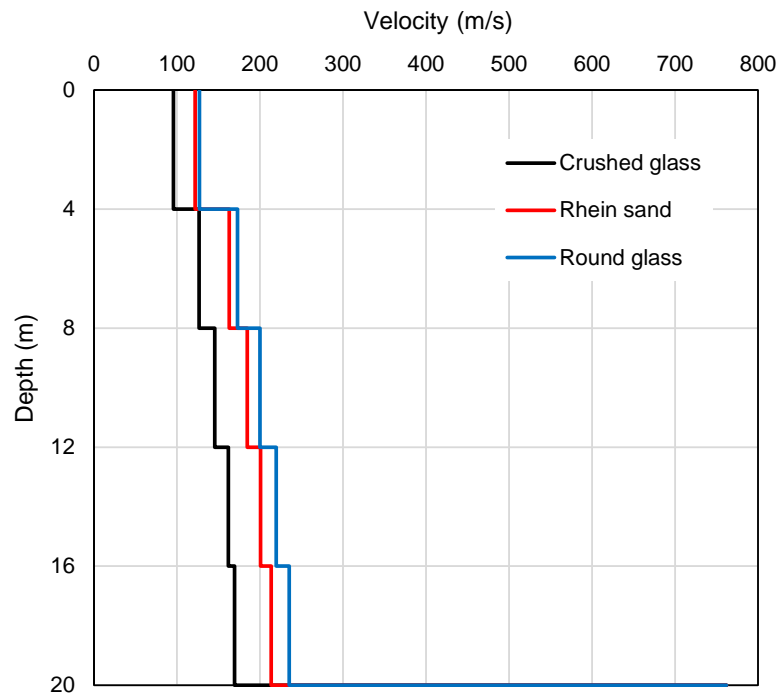
Figure 7.15: Variation of the shear wave velocity v_s against depth for the three materials

Fig. 7.15 shows the variation of the shear wave velocity v_s against the profile depth for the three considered materials. As evident from the previous chapter, the v_s for the round glass was measured to be larger than that of the more angular materials which can be

partially attributed to the larger void ratios in the latter ones. Similarly, at a given soil depth considering a similar I_D, the unit weight and correspondingly the mean effective stress p' are also lower for more angular soils. This leads to lower v_s and G_{max}.
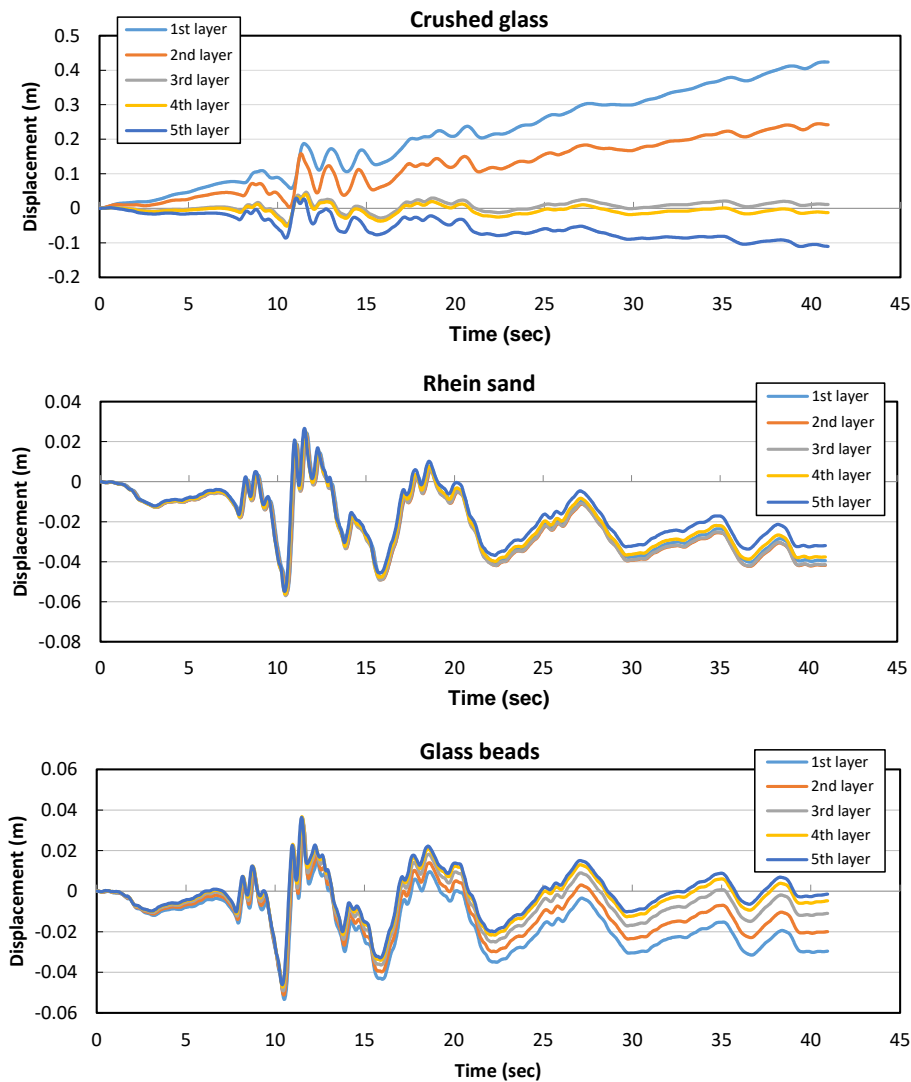
Figure 7.16: Horizontal displacement time history calculated at the middle of each of the five layers for the three materials subjected to the Loma Prieta earthquake

The damping properties of the bottom bedrock layer were adopted from the in-built rock model which was already provided in ProShake (Schnabel et al. 1972; Idriss & Sun 1992). For the other three materials, the modulus degradation and damping curves were obtained using the fitting parameters for the mean effective stress $p' = 100$ kPa, details of which are listed in Table 6.7. This value of the confinement was chosen since it represents the stress conditions in the adopted soil profile closer than $p' = 400$ kPa. The dynamic earthquake

motion applied to the soil profile is the Loma Prieta earthquake of 1989 which had a moment magnitude $M_w = 6.9$ and occured in and around the San Francisco Bay area. The motion with a peak ground acceleration of 0.113 g was applied at the top of the bedrock from which the waves propagate upwards along the soil layers.
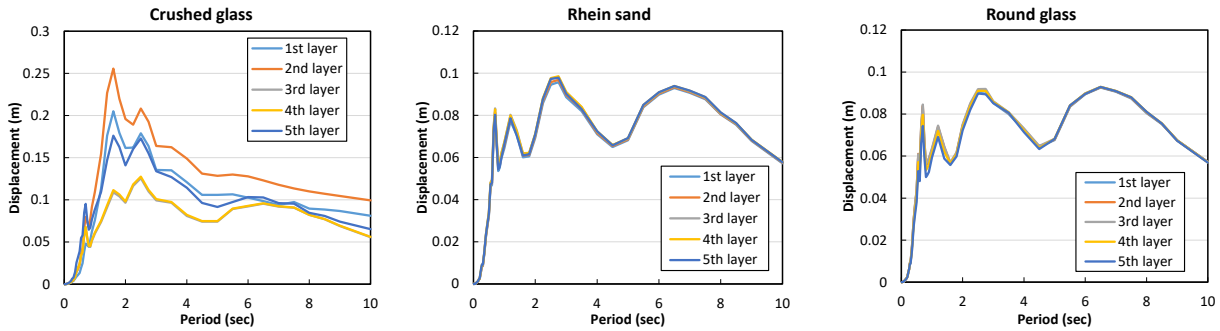
Figure 7.17: Spectral horizontal displacement calculated at the middle of each of the five layers for the three materials subjected to the Loma Prieta earthquake

The ground horizontal displacements were analyzed for the three soil conditions as shown in Fig. 7.16. The results for round glass beads and Rhein sand show no significant ground deformation, although some displacements can be noted at the end of the simulations. In contrast, the soil profile composed of angular crushed glass develops large horizontal deformations, with values higher than 0.4 m in the top soil layer at the end of the simulation. From the spectral displacement curves highlighting the maximum displacements (Fig. 7.17) which are important in case of high rise buildings to estimate the displacements caused due to the ground motion, the soil profile with angular glass likewise shows the largest values (0.25 m) reached at 2 seconds, while the values are much smaller (around 0.1 m for Rhein sand and 0.08 m for glass beads) for the other two materials. The peaks are encountered almost simultaneously for the three materials.

Similarly, from the horizontal acceleration time histories (Fig. 7.18), the magnitude of the peak accelerations obtained for the three materials are different: the peak accelerations for the angular crushed glass soil profile measure between 0.15 and -0.25g, while they range between 0.19 and -0.22g for the Rhein sand. For the glass beads, the peak accelerations are almost symmetrical, with the values lying between 0.2 and -0.2g. However, considering the spectral acceleration (SA) denoting the acceleration felt by a building as modeled by a particle mass on a massless vertical rod having the same natural period of vibration as the building (as defined by the US Geological Survey), the values are within similar range, varying between 0.7 and 0.8g (refer Fig. 7.19). Also, the magnitude of spectral acceleration for angular glass reduces with decreasing soil depth - thus, the maximum
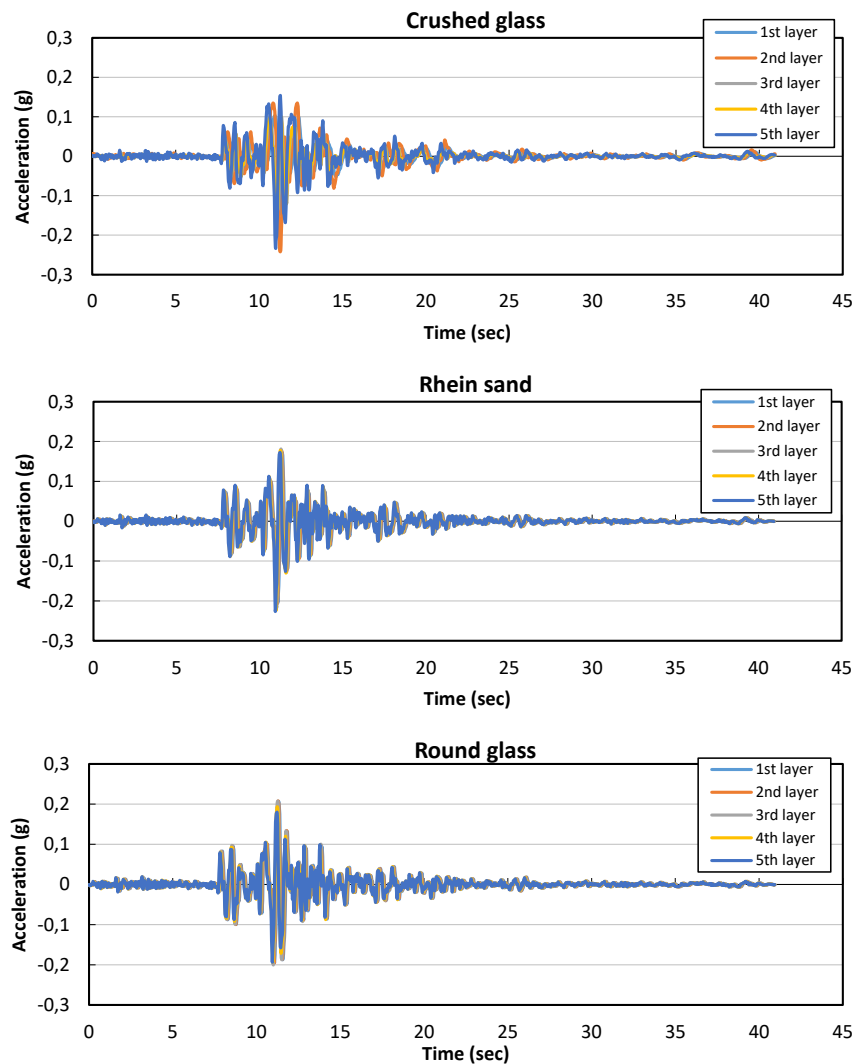
Figure 7.18: Acceleration time history calculated at the middle of each of the five layers for the three materials subjected to the Loma Prieta earthquake

magnitude of spectral acceleration at the topmost layer is 0.4g, half of the value in the layer above the bedrock. Such a variation was not observed for the other two materials, where the with-time variation in spectral acceleration was similar throughout the depth.

7.4 Summary

This chapter introduces the micromechanical interpretation of the experimental results using the discrete element simulations as well as the macromechanical outlook through a rigorous calibration procedure for the popular SANISAND model to capture soil behav-
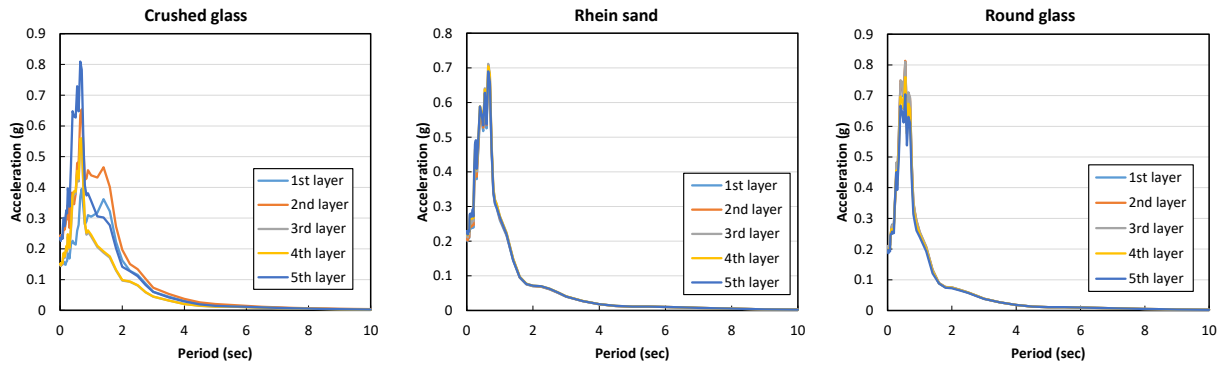
Figure 7.19: Spectral acceleration calculated at the middle of each of the five layers for the three materials subjected to the Loma Prieta earthquake

ior. In addition, as a practical application a ground response analysis under a specified dynamic motion highlighting the influence of grain shape captured via the dynamic parameters obtained in Chapter 6 is also discussed. The major findings are summarized as follows:

- The discrete element simulations of drained and undrained monotonic triaxial tests for three materials with different aspect ratios showed that for angular materials (i.e. larger aspect ratio), the deviatoric stress q at same relative densities and same strain is larger compared to rounded materials. Similarly, the slope of the effective stress path in the $q - p'$ diagram for undrained monotonic shearing is also higher for granular materials with larger aspect ratio. These observations agree with an analysis of the coordination number (CN) and the average contact force distribution within the specimens: a higher CN and larger shear and tangential forces are evident for more angular materials while being the least for rounded ones. It is interesting to note that the ratio of the normal to shear forces in the contacts is least for materials having a larger angularity which means the contribution of shear forces to the shear strength is comparatively larger and can be physically explained by an increased interlocking between individual grains as was already discussed previously in Chapter 5.

- With respect to the macromechanical analysis, certain parameters in the SANISAND model (such as the fabric parameters) are insignificant while simulating the monotonic soil behavior as determined by sensitivity analysis. In addition, certain parameters (such as elastic parameter G_0^{el}, the critical state parameters M_c, $M_{e/c}$, e_{c0}, λ, ξ, dilatancy parameter n_d, hardening parameter h_0) seem to be affected by grain shape as seen from the best-fit parameters obtained by optimization procedure. The

trends for the other remaining parameters with grain shape are not clear, therefore, one may conduct further investigations along this direction in the future.

- As obtained from the ground response analysis, the horizontal deformation under ground shaking in the angular materials especially at the top layers with water level at ground surface are significantly higher compared to the more rounded materials since the shear modulus of angular materials is significantly smaller. However, the magnitude of the maximum acceleration encountered at the middle of the soil layers at effective confining pressures of around and lesser than 100 kPa is larger for angular materials possibly due to a lower damping ratio at higher strains as shown in Fig. 6.19 of Chapter 6.

8 Summary, conclusions and recommendations

8.1 Summary and conclusions

In this research, the influence of the grain characteristics on the various intrinsic, static, cyclic and dynamic properties of granular materials was studied in detail with special attention to the influence of grain morphology in the medium/meso and macro scales. The influence of grain shape, size and mineralogy (denoted using the specific gravities) on the limit void ratios in granular materials was studied. Later, the influence of grain shape on the response of granular soils to monotonic loading, in particular shear strength and steady state characteristics, was investigated in drained and undrained triaxial tests on three granular materials with significantly different grain shape (glass beads, natural sand, crushed glass) but identical grain size distribution curve. A similar investigation was done with respect to the liquefaction resistance determined from undrained cyclic triaxial tests. Resonant column tests and shear wave velocity measurements with bender elements were performed to obtain stiffness and damping properties at small to intermediate strains. The influence of particle gradation on the static, cyclic and dynamic properties of granular materials was also examined in detail. At the end through discrete element simulations, the significant influence of grain shape on the fabric orientation in granular materials under triaxial compression was validated with the observations from experiments. Also, the influence of grain shape on the fitting parameters of the popular elastoplastic constitutive model SANISAND was demonstrated. The main outcomes derived from the study are categorized and listed as follows.

Effect of particle characteristics on the limit void ratios

1. For poorly graded glass beads, the mean grain size d_{50} was found to be a suitable parameter to predict the maximum and minimum void ratios rather than the

uniformity coefficient C_u. Significant particle segregation may be encountered for well-graded glass beads which would induce errors in the determination of the limit void ratios.

2. For sands, the influence of the mean grain size d_{50} on the limit void ratios e_{max} and e_{min} was negligible. Instead, the major influence resulted from the gradation (denoted by the uniformity coefficient C_u) and the grain shape (denoted by the regularity factor ρ which is an average of the medium scale roundness R and the macro scale circle-ratio sphericity S_c). An increase of C_u and ρ results in decreasing values of e_{max} and e_{min}.

3. The influence of the mineralogy considered by the specific gravities was minimal and can be ignored for practical purposes.

Effect of particle shape and size on the static and cyclic (large strain) properties

1. Generally, angular materials like crushed glass (having low values of ρ) exhibit comparatively higher strength in the monotonic tests than rounded materials like glass beads owing to interlocking between grains, especially at larger relative densities I_D. For well-graded glass beads, the difference between the limit void ratios is very small which results in dilation occuring earlier compared to angular materials. The variation of the stress-strain responses and the fabric orientation with different grain shapes were also confirmed by the results obtained from DEM simulations considering similar boundary conditions.

2. The peak and steady state friction angles are significantly affected by the particle shape with angular materials having much higher values as compared to round materials. The steady state line in the $e - p'$ diagram and its parameters such as the intercept and slope are dependent on the grain shape, too. The curves show a downward shift in the $e - p'$ diagram if the grains become rounder.

3. For round materials, the influence of the uniformity coefficient C_u on the $q - \epsilon_1$ response under monotonic loading seems negligible, while uniform angular/sub-angular materials typically show larger q values at same ϵ_1 compared to their well-graded counterparts. This difference decreases with increasing I_D.

4. In the cyclic tests loose angular or sub-angular materials typically undergo large axial deformation in extension representing a flow liquefaction type failure. At larger

relative densities, the more angular materials show a cyclic mobility type failure, with axial strains usually developing faster on the extension than on the compression side. Round glass beads show a different behaviour, with cyclic mobility already at loose states and a rather symmetrical development of axial strains which remain comparatively small.

5. In most studied cases well-graded angular/sub-angular materials liquefy faster than uniform ones at similar boundary conditions. The cyclic resistance ratio CRR (defined as the cyclic stress ratio corresponding to a certain number of cycles) is larger for medium dense uniformly graded specimens but slightly smaller for loose uniform materials when compared to the results from well-graded materials. However, the liquefaction resistance CRR for round materials is independent of gradation, or may even be seen to increase slightly with the uniformity coefficient.

Effect of particle shape and gradation on the dynamic (small and intermediate strain) properties

1. Recommendations were provided regarding the choice of the grain shape descriptors in both the meso and macro scale to capture the variation of the shear wave velocity of granular materials with grain shape. A new methodology to capture the variation of grain shapes within a material more accurately, particularly in well-graded materials, using a grain shape distribution curve in analogy to the grain size distribution curve was proposed along with the introduction of parameters describing the mean value and slope of the curves.

2. At similar void ratio the small-strain shear modulus G_{max} is comparatively higher for uniformly graded materials as compared to well-graded ones. The G_{max} and E_{max} values for round materials were found larger than for angular materials. No influence of void ratio e or relative density I_D on the modulus degradation and damping curves was noted.

3. The reference shear or axial strains are larger for angular materials as well as poorly-graded (uniform) materials, while the influence of grain shape on D_{min} seems insignificant.

8.2 Recommended future works

Although an exhaustive experimental study was carried out during the course of this research, certain recommendations may be made for future work building up on the results, some of which are as follows:

1. For the purpose of material characterization, the influence of surface roughness (micro scale parameter) on the limit void ratios can be studied. In addition, correlations can be explored between the other meso/medium/macro scale parameters and the limit void ratios. The shape of the particles of the non-plastic fines can also be included in the formulation of new empirical models for binary mixtures.

2. While the primary focus was on the influence of grain shape and gradation in the present study, the influence of mean grain size d_{50} on the monotonic and cyclic undrained response of granular soils can be investigated in future. It will be particularly of interest to study the combined influence of d_{50}, C_u and grain shape.

3. One can also consider performing triaxial tests with bender elements mounted at the sample boundary to measure shear wave propagation in the horizontal direction. This would allow to study the influence of grain shape on the v_s in the horizontal direction, and thus the anisotropy of the small-strain properties of the samples for different grain shapes. Besides, studies can also be extended to assess the influence of grain shape and size on dynamic small and intermediate strain properties of sand-silt mixtures.

4. Discrete element simulations were carried out considering the mean grain size of the test materials only and not replicating the gradation for the sake of simplicity. Thus in a future work, variations of the particle gradation can also be added to ensure more accurate results. Furthermore, to simulate different grain shapes, a variation of the aspect ratio was applied. The shape of the grains can be modelled more realistically in the future, incorporating other morphology parameters to bring the simulation results closer to the experimental data.

5. Results of monotonic triaxial tests on materials having different grain shapes other than the ones considered in this study may be employed as additional datasets to validate and improve the output of the sensitivity analysis and optimization algorithm for the calibration of the SANISAND model. Furthermore, one may also perform sensitivity analysis and calibrate the constitutive parameters via optimization for the cyclic undrained triaxial results presented in this research.

Bibliography

Abbireddy, C. O. R. & Clayton, C. R. I. (2015), 'The impact of particle form on the packing and shear behaviour of some granular materials: an experimental study', *Granular Matter* **17**, 427–438.

Agarwal, S. L., Malhotra, A. K. & Banerjee, R. (1977), Engineering properties of calcareous soils affecting the design of deep penetration piles for offshore structures, *in* 'Proceedings of the 9th Offshore Technology Conference', Vol. 1, pp. 503–512.

Alarcon-Guzman, A., Leonards, G. A. & Chameau, J. L. (1988), 'Undrained monotonic and cyclic strength of sands', *Journal of Geotechnical Engineering* **114**(10), 1089–1109.

Alshibli, K. A. & Cil, M. B. (2018), 'Influence of particle morphology on the friction and dilatancy of sand', *Journal of Geotechnical and Geoenvironmental Engineering* **144**(3). 04017118.

Altuhafi, F., Coop, M. R. & Georgiannou, V. N. (2016), 'Effect of particle shape on the mechanical behavior of natural sands', *Journal of Geotechnical and Geoenvironmental Engineering* **142**(12), 04016071.

Altuhafi, F., O'Sullivan, C. & Cavarretta, I. (2013), 'Analysis of an image-based method to quantify the size and shape of sand particles', *Journal of Geotechnical and Geoenvironmental Engineering* **139**(8), 1290–1307.

Amini, F. & Qi, G. Z. (2000), 'Liquefaction testing of stratified silty sands', *Journal of Geotechnical and Geoenvironmental Engineering* **126**(3), 208–217.

Aschenbrenner, B. C. (1956), 'A new method of expressing particle sphericity', *Journal of Sedimentary Research* **26**(1), 15–31.

ASTM-D1557(07) (2012), 'Standard test methods for laboratory compaction characteristics of soil using modified effort', *ASTM International* (West Conshohocken, PA,). www.astm.org.

ASTM-D2049(69) (1969), 'Test method for relative density of cohesionless soils', *ASTM International* (West Conshohocken, PA,). www.astm.org.

ASTM-D4015 (2000), 'Standard test methods for modulus and damping of soils by fixed-base resonant column devices', *ASTM International* (West Conshohocken, PA,). www.astm.org.

ASTM-D4253 (2002), 'Standard test methods for maximum index density and unit weight of soils using a vibratory table', *ASTM International* (West Conshohocken, PA,). www.astm.org.

ASTM-D4254 (2002), 'Standard test methods for minimum index density and unit weight of soils and calculation of relative density', *ASTM International* (West Conshohocken, PA,). www.astm.org.

ASTM-D4767(11) (2020), 'Standard test method for consolidated undrained triaxial compression test for cohesive soils', *ASTM International* (West Conshohocken, PA,). www.astm.org.

ASTM-D5311/D5311M-13 (2013), 'Standard test method for load controlled cyclic triaxial strength of soil', *ASTM International* (West Conshohocken, PA,). www.astm.org.

ASTM-D7181(20) (2020), 'Standard test method for consolidated drained triaxial compression test for soils', *ASTM International* (West Conshohocken, PA,). www.astm.org.

Baldi, G. & Nova, R. (1984), 'Membrane penetration effects in triaxial testing', *Journal of Geotechnical Engineering (ASCE)* **110**(3), 403–420.

Barrett, P. J. (1980), 'The shape of rock particles, a critical review', *Sedimentology* .

Bartake, P. P. & Singh, D. N. (2007), 'Studies on the determination of shear wave velocity in sands', *Geomechanics and Geoengineering* **2**(1), 41–49.

Baxter, C. D. P. & Mitchell, J. K. (2004), 'Experimental study on the aging of sands', *Journal of Geotechnical and Geoenvironmental Engineering* **130**(10), 1051–1062.

Been, K. & Jefferies, M. G. (1985), 'A state parameter for sands', *Géotechnique* **35**(2), 99–112.

Bellotti, R., Jamiolkowski, M., Lo Presti, D. C. F. & O'Neill, D. A. (1996), 'Anisotropy of small strain stiffness in ticino sand', *Géotechnique* **46**(1), 115–131.

Bhushan, B. (2001), 'Nano- to microscale wear and mechanical characterization using scanning probe microscopy', *Wear* **251**(1-12), 1105–1123.

Bolton, M. D. (1986), 'The strength and dilatancy of sands', *Géotechnique* **36**(1), 65–78.

Boulanger, R. W. & Idriss, I. M. (2015), 'Magnitude scaling factors in liquefaction triggering procedures', *Soil Dynamics and Earthquake Engineering* **79**, 296–303.

Bowden, F. P. & Tabor, D. (1950), *The Friction and Lubrication of Solids*, Oxford Univ. Press.

Bowels, J. E. (1986), *Engineering properties of soils and their measurement*, McGraw-Hill Book Company.

Brandes, H. G. (2011), 'Simple shear behavior of calcareous and quartz sands', *Geotechnical and Geological Engineering* **29**, 113–126.

Bray, J. D., Sancio, R. B., Riemer, M. & Durgunoglu, H. T. (2005), Liquefaction susceptibility of fine-grained soils, *in* 'Proceedings of the 11th International Conference on Soil Dynamics and Earthquake Engineering', pp. 655–662.

BS-1377(1) (2002), 'Methods of test for soils for civil engineering purposes - part 1: General requirements and sample preparation', *British Standards Institution* (389 Chiswick High Road, London, W4 4AL). UK.

Bui, M. T. (2009), Influence of some particle characteristics on the small strain response of granular materials, PhD thesis, School of Civil Engineering and the Environment, University of Southampton.

Burmister, D. M. (1938), Study of physical characteristics of soils, with special reference to earth structures, Technical report, Bulletin of Columbia University Civil Engineering Res. Lab.

Cabalar, A. F., Dulundu, K. & Tuncay, K. (2013), 'Strength of various sands in triaxialand cyclic direct shear tests', *Engineering Geology* **156**, 92–102.

Calvarano, L. S., Palamara, R., Leonardi, G. & Moraci, N. (2017), 3D-FEM analysis on geogrid reinforced flexible pavement roads, *in* 'IOP Conference Series: Earth and Environmental Science', Vol. 95.

Campanella, R. G. & Lim, B. S. (1981), Liquefaction characteristics of undisturbed soils, *in* 'Proceedings of 1981 - First International Conference on Recent Advances in Geotechnical Earthquake Engineering & Soil Dynamics', St. Louis, Missouri, USA.

Casagrande, A. (1975), 'Liquefaction and cyclic deformation of sands: a critical review', *Harvard Soil Mechanics Series No. 88* .

Cascante, G., Santamarina, J. C. & Yassir, N. (1998), 'Flexural excitation in a standard torsional-resonant column', *Canadian Geotechnical Journal* **35**, 478–490.

Castro, G. C. (1969), Liquefaction of sands, PhD thesis, Division of Engineering and Applied Physics, Harvard University, Cambridge, USA.

Castro, G. & Poulos, S. J. (1977), 'Factors affecting liquefaction and cyclic mobility', *Journal of the Geotechnical Engineering Division (ASCE)* **103**(6), 501–506.

Cavarretta, I. (2009), The influence of particle characteristics on the engineering behaviour of granular materials, PhD thesis, Department of Civil and Environmental Engineering, Imperial College London, London.

Cavarretta, I., Coop, M. R. & O'Sullivan, C. (2010), 'The influence of particle characteristics on the behaviour of coarse grained soils', *Géotechnique* **60**(6), 413–423.

Cavarretta, I. & O'Sullivan, C. (2012), 'The mechanics of rigid irregular particles subject to uniaxial compression', *Géotechnique* **62**(8), 681–692.

Chakraborty, T. & Salgado, R. (2010), 'Dilatancy and shear strength of sand at low confining pressures', *Journal of Geotechnical and Geoenvironmental Engineering* **136**(3), 527–532.

Chang, C. S., Wang, J. Y. & Ge, L. (2015), 'Modeling of minimum void ratio for sand-silt mixtures', *Engineering Geology* **196**, 293–304.

Chang, N. Y. & Ko, H. Y. (1982), Effect of grain size distribution on dynamic properties and liquefaction potential of granular soils, Technical report, Research Report R82-103, University of Colorado at Denver. 132(5).

Chang, X., Wang, Y. T., Zhou, W., Ma, G. & Liu, J. Y. (2017), The influence of rotational resistance on critical state of granular materials, *in* 'Proceedings of the 7th International Conference on Discrete Element Methods', Springer (Singapore), pp. 225–233.

Chen, Y. P. (1985), Liquefaction potential of coral sand, Master's thesis, Department of Civil Engineering, Colorado State University, Fort Collins, Colorado.

Cherif Taiba, A., Mahmoudi, Y., Belkhatir, M. & Schanz, T. (2018), 'Experimental investigation into the influence of roundness and sphericity on the undrained shear response of silty sand soils', *Geotechnical Testing Journal* **41**(3), 619–633.

Cho, G. C., Dodds, J. & Santamarina, J. C. (2006), 'Particle shape effects on packing density, stiffness, and strength: Natural and crushed sands', *Journal of Geotechnical and Geoenvironmental Engineering* **132**(5), 591–602.

Cho, G. C. & Santamarina, J. C. (2001), 'Unsaturated particulate materials- particle-level studies', *Journal of Geotechnical and Geoenvironmental Engineering* **127**(1), 84–96.

Choo, J., Jung, Y. H., Cho, W. & Chung, C. K. (2013), 'Effect of pre-shear stress path on nonlinear shear stiffness degradation of cohesive soils', *Geotechnical Testing Journal (ASTM)* **36**(2). 20120116.

Choobbasti, A. J., Ghalandarzadeh, A. & Esmaeili, M. (2014), 'Experimental study of the grading characteristic effect on the liquefaction resistance of various graded sands and gravelly sands', *Arabian Journal of Geosciences* **7**, 2739–2748.

Chung, R., Yokel, F. & Drnevich, V. (1984), 'Evaluation of dynamic properties of sands by resonant column testing', *Geotechnical Testing Journal* **7**(2), 60–69.

Clayton, C. R. I. (2011), 'Stiffness at small strain: research and practice', *Géotechnique* **61**(1), 5–37.

Corey, A. T. (1949), Influence of shape on the fall velocity of sand grains, Unpublished M.S. thesis, Colorado A&M College, USA.

Cowin, S. C. (1985), 'The relationship between the elasticity tensor and the fabric tensor', *Mechanics of Materials* **4**(2), 137–147.

Cox, M. R. & Budhu, M. (2008), 'A practical approach to grain shape quantification engineering', *Engineering Geology* **96**(1), 1–16.

Cresswell, A., Barton, M. E. & Brown, R. (1999), 'Determining the maximum density of sands by pluviation', *Geotechnical Testing Journal (ASTM)* **22**(4), 324–328.

Cubrinovski, M. & Ishihara, K. (2002), 'Maximum and minimum void ratio characteristics of sands', *Soils and Foundations* **42**(6), 65–78.

Cundall, P. A. & Strack, O. D. L. (1979), 'A discrete numerical model for granular assemblies', *Géotechnique* **29**(1), 47–65.

Dafalias, Y. F. & Manzari, M. T. (2004), 'Simple plasticity sand model accounting for fabric change effects', *Journal of Engineering Mechanics* **130**(6), 622–634.

De Bono, J. P. & Mcdowell, G. R. (2016), 'Investigating the effects of particle shape on normal compression and overconsolidation using DEM', *Granular Matter* **18**(3), 1–10.

Deb, K. & Jain, H. (2013), 'An evolutionary many-objective optimization algorithm using reference-point-based nondominated sorting approach, part I: solving problems with box constraints', *IEEE Transactions on Evolutionary Computation* **18**(4), 577–601.

DeJong, J. T. & Christoph, G. G. (2009), 'Influence of particle properties and initial-specimen state on one-dimensional compression and hydraulic conductivity', *Journal of Geotechnical and Geoenvironmental Engineering* **135**(3), 449–454.

DIN-18123 (2011), 'Baugrund, Untersuchung von Bodenproben - Bestimmung der Korngrößenverteilung', *Deutsches Institut für Normung* (Germany), in German.

DIN-18124 (2011), 'Baugrund, Untersuchung von Bodenproben - Bestimmung der Korndichte - Kapillarpyknometer, Weithalspyknometer, Gaspyknometer', *Deutsches Institut für Normung* (Germany), in German.

DIN-18126 (1996), 'Baugrund, Untersuchung von Bodenproben - Bestimmung der Dichte nichtbindiger Böden bei lockerster und dichtester Lagerung', *Deutsches Institut für Normung* (Germany), in German.

DIN-EN13286-7 (2004), 'Ungebundene und hydraulisch gebundene Gemische- teil 7: Dreiaxialprüfung mit zyklischer belastung für ungebundene gemische', *Deutsches Institut für Normung* (Germany).

DIN-EN17892-9 (2018), 'Geotechnische Erkundung und Untersuchung- Laborversuche an Bodenproben - Teil 9: Konsolidierte triaxiale Kompressionsversuche an wassergesättigten Böden', *Deutsches Institut für Normung* (Germany).

Doanh, T., Hoang, M. T., Roux, J.-N. & Dequeker, C. (2013), 'Stick-slip behaviour of model granular materials in drained triaxial compression', *Granular Matter* **15**(1), 1–23.

Drnevich, V. P. (1967), Effects of strain history on the dynamic properties of sand, PhD thesis, University of Michigan, USA.

Drnevich, V. P. (1978), Resonant-column testing: Problems and solutions, Technical report, Dynamic Geotechnical testing. Pages 384-398.

Drnevich, V. P., Hall Jr, J. R. & E., R. J. F. (1967), Effects of amplitude of vibration on the shear modulus of sand, *in* 'International Symposium on Wave Propagation and Dynamic Properties of Earth Materials', Albuquerqe, New Mexico, USA, pp. 189–199.

Drnevich, V. P. & Richart, F. E. (1970), 'Dynamic prestraining of dry sand', *Journal of Soil Mechanics and Foundation Division, ASCE* **96**(2), 453–467.

Druckerey, A. M., Alshibli, K. A. & Al-Raoush, R. I. (2016), '3D characterization of sand particle-to-particle contact and morphology', *Computers and Geotechnics* **74**, 26–35.

EduPro Civil Systems, I. (2020), 'Proshake 2.0', 5141 189th Avenue NE, Sammamish, WA, USA.

Ehrlich, R. & Weinberg, B. (1970), 'An exact method for characterization of grain shape', *Journal of Sedimentary Research* **40**(1), 205–212.

Enomoto, T. (2016), 'Effects of grading and particle characteristics on small strain properties of granular materials', *Soils and Foundations* **56**(4), 745–750.

Evans, M. D. & Zhou, S. (1995), 'Liquefaction behavior of sand-gravel composites', *Journal of Geotechnical Engineering (ASCE)* **121**(3), 287–298.

Ferreira, T. A. & Rasband, W. (2012), 'The ImageJ user guide'. Tech. Rep. IJ 1.46.

Fonseca, J., O'Sullivan, C., Coop, M. R. & Lee, P. D. (2012), 'Non-invasive characterization of particle morphology of natural sands', *Soils and Foundations* **52**(4), 712–722.

Freeman, H. (1961), 'On the encoding of arbitrary geometric configurations', *IRE Transactions on Electronic Computers* pp. 260–268.

Friel, J. J. & Pande, C. S. (1993), 'A direct determination of fractal dimension of fracture surfaces using scanning electron microscopy and stereoscopy', *Journal of Materials Research* **8**(1), 100–104.

Georgiannou, V. N. & Konstadinou, M. (2013), 'Torsional shear behavior of anisotropically consolidated sands', *Journal of Geotechnical and Geoenvironmental Engineering* **140**(2). 04013017.

Giang, P. H. H., Van Impe, P. O., Van Impe, W. F., Menge, P. & Haegeman, W. (2017), 'Small-strain shear modulus of calcareous sand and its dependence on particle characteristics and gradation', *Soil Dynamics and Earthquake Engineering* **100**, 371–379.

Golchin, A. & Lashkari, A. (2014), 'A critical state sand model with elastic-plastic coupling', *International Journal of Solids and Structures* **51**, 2807–2825.

Goudarzy, M. (2015), Micro and Macro Mechanical Assessment of Small and Intermediate Strain Properties of Granular Material, PhD thesis, Faculty of Civil and Environmental Engineering, Ruhr-Universitat Bochum, Germany.

Goudarzy, M., König, D., Santamarina, J. C. & Schanz, T. (2018), 'The influence of the anisotropic stress state on the intermediate strain properties of granular material', *Géotechnique* **68**(3), 221–232.

Goudarzy, M., Rahman, M. M., König, D. & Schanz, T. (2016), 'Influence of non-plastic fines content on maximum shear modulus of granular materials', *Soils and Foundations* **56**(6), 973–983.

Goudarzy, M., Viefhaus, H., König, D. & Schanz, T. (2014), Micro and macro mechanical response of granular packing containing fine materials, *in* 'Geomechanics from Micro to Macro-IS Cambridge'.

Goudarzy, M. & Wichtmann, T. (2019), Influence of particle characteristics on the dynamic characteristics of granular materials, *in* 'Fachsektionstage Geotechnik, 2. Bodenmechanik-Tagung', Wurzburg, Germany.

Greenwood, J. A. & Tripp, J. H. (1967), 'The elastic contact of rough spheres', *Journal of Applied Mechanics. Transactions of the American Society of Mechanical Engineers* **34**(1), 153–159.

Greenwood, J. A. & Williamson, J. B. P. (1966), 'Contact of nominally flat surfaces', *Proceedings of the Royal Society of London. Series A, Mathematical and Physical Sciences* **295**(1442), 300–319.

Gu, X., Yang, J. & Huang, M. (2013), 'Laboratory measurements of small strain properties of dry sands by bender element', *Soils and Foundations* **53**(5), 735–745.

Hammad, W. I. (1991), Modelisation non lineare et etude experimentale des bandes de cisaillement dans les sable, PhD thesis, Universite Grenoble Alpes, France.

Hara, T., Kokusho, T. & Hiraoka, R. (2004), Undrained strength of gravelly soils with different particle gradations, *in* '13th World Conference on Earthquake Engineering', Vancouver, Canada. Paper No. 144.

Hardin, B. O. (1965), 'Dynamic vs. static shear modulus for dry sand', *Materials Research and Standards, American Society for Testing and Materials* **5**(5), 232–235.

Hardin, B. O. (1978), The nature of stress-strain behavior for soils, *in* 'Proceedings of the ASCE Geotechnical Engineering Division Specialty Conference', Pasadena, California.

Hardin, B. O. & Black, W. L. (1966), 'Sand stiffness under various triaxial stresses', *Journal of the Soil Mechanics and Foundation Division, ASCE* **92**(2), 27–42.

Hardin, B. O. & Black, W. L. (1968), 'Vibration modulus of normally consolidated clay', *Journal of the Soil Mechanics and Foundation Division, ASCE* **92**(2), 27–42.

Hardin, B. O. & Black, W. L. (1969), 'Closure to: Vibration modulus of normally consolidated clay', *Journal of the Soil Mechanics and Foundation Division, ASCE* **95**(6), 1531–1537.

Hardin, B. O. & Drnevich, V. P. (1972a), 'Shear modulus and damping in soils: Measurement and parameter effects', *Journal of the Soil Mechanics and Foundation Division, ASCE* **98**, 603–624.

Hardin, B. O. & Drnevich, V. P. (1972b), 'Shear modulus and damping in soil: equations and curves', *Journal of the Soil Mechanics and Foundation Division, ASCE* **98**, 667–692.

Hardin, B. O. & Kalinski, M. E. (2005), 'Estimating the shear modulus of gravelly soils', *Journal of Geotechnical and Geoenvironmental Engineering* **131**(7), 867–875.

Hardin, B. O. & Richart, E. F. J. (1963), 'Elastic wave velocities in granular soils', *Journal of the Soil Mechanics and Foundation Division, ASCE* **89**(1), 33–65.

Harehdasht, S. A., Hussien, M. N., Karray, M., Roubtsova, V. & Chekired, M. (2019), 'Influence of particle size and gradation on shear strength-dilation relation of granular materials', *Canadian Geotechnical Journal* **56**, 208–227.

Harehdasht, S. A., Karray, M., Hussien, M. N. & Chekired, M. (2017), 'Influence of particle size and gradation on the stress-dilatancy behavior of granular materials during drained triaxial compression', *International Journal of Geomechanics* **17**(9). 04017077.

Hassanlourad, M., Rasouli, M. R. & Salehzadeh, H. (2014), 'A comparison between the undrained shear behavior of carbonate and quartz sands', *International Journal of Civil Engineering* **12**(4), 338–350.

Hayman, N. W., Ducloué, L., Foco, K. L. & Daniels, K. E. (2011), 'Granular controls on periodicity of stick-slip events: kinematics and forcechains in an experimental fault', *Pure and Applied Geophysics* **168**, 2239–2257.

He, H., Li, W. & Senetakis, K. (2019), 'Small strain dynamic behavior of two types of carbonate sands', *Soils and Foundations* **59**, 571–585.

He, H., Senetakis, K. & Ranjith, P. G. (2017), 'The behavior of a carbonate sand subjected to a wide strain range of medium-frequency flexural excitation', *Geomechanics and Geophysics for Geo-Energy and Geo-Resources* **3**(1), 51–60.

Horn, H. M. & Deere, D. U. (1962), 'Frictional characteristics of minerals', *Géotechnique* **12**(4), 319–335.

Hryciw, R. D., Zheng, J. & Penn, R. (2016), An update of Robert M. Koerner's models for the packing densities of sands using image-based intrinsic soil properties, *in* 'Geosynthetics, forging a path to bona fide engineering materials', pp. 83–94.

Hyodo, M., Aramaki, N., Itoh, M. & Hyde, A. F. L. (1996), 'Cyclic strength and deformation of crushable carbonate sand', *Soil Dynamics and Earthquake Engineering* **15**(5), 331–336.

Hyodo, M., Yoshomoto, N., Kuwajima, K. & Okabayashi, T. (2002), Effect of fines on liquefaction of a volcanic soil Shirasu, *in* 'Proceedings of the Japan Earthquake Engineering Symposium', pp. 671–676.

Idriss, I. M. (1999), An update to the Seed-Idriss simplified procedure for evaluating liquefaction potential, TRB workshop on new approaches to liquefaction, Federal Highway Administration, Washington DC, USA.

Idriss, I. M. & Sun, J. I. (1992), SHAKE91: A computer program for conducting equivalent linear seismic response analyses of horizontally layered soil deposit, User's guide, University of California, Davis, California, US.

Igathinathane, C., Pordesimo, L. O., Columbus, E. P., Batchelor, W. D. & Methuku, S. R. (2008), 'Shape identification and particles size distribution from basic shape parameters using ImageJ', *Computers and Electronics in Agriculture* **63**(2), 168–182.

Iida, K. (1937), The velocity of elastic wave in sands, Technical report, Earthquake research institute. pages 132-145.

Ishihara, K. (1993), 'Liquefaction and flow failure during earthquakes', *Géotechnique* **43**(3), 351–451.

Ishihara, K. (1996), *Soil Behaviour in Earthquake Geotechnics*, Clarendon Press, Oxford, UK.

Islam, M. N., Siddika, A., Hossain, M. B., Rahman, A. & Asad, M. A. (2011), 'Effect of particle size on the shear strength behavior of sands', *Australian Geomechanics Journal* **46**(3), 75–86.

ISO-9276(6) (2006), *Representation of results of particle size analysis- Part 6: Descriptive and quantitative representation of particle shape and morphology*, ISO/DIS 9276, Geneva.

Iwasaki, T. & Tatsuoka, F. (1977), 'Effects of grain size and grading on dynamic shear moduli of sands', *Soils and Foundations* **17**(3), 19–35.

Iwasaki, T., Tatsuoka, F. & Takagi, Y. (1978), 'Shear moduli of sands under cyclic torsional shear loading', *Soils and Foundations* **18**(1), 39–56.

Jamiolkowski, M., Leroueil, S. & Lo Priesti, D. C. (1991), Design parameters from theory to practice, *in* 'International conference on geotechnical engineering for coastal development: GeoCoast', Coastal Development Institute of Technology, Yokohama, Japan, pp. 877–917.

Jensen, R. P., Edil, T. B., Bosscher, P. J., Plesha, M. E. & Kahla, N. B. (2001), 'Effect of particle shape on interface behavior of DEM-simulated granular materials', *International Journal of Geomechanics* **1**(1), 1–19.

Jerves, A. X., Kawamoto, R. Y. & Andrade, J. E. (2015), 'Effects of grain morphology on steady state: a computational analysis', *Acta Geotechnica* **11**, 493–503.

JGS-0161 (2015), 'Test method for the maximum and minimum density of sands', *Japanese Geotechnical Society* .

Jiang, M. D., Yang, Z. X., Barreto, D. & Xie, Y. H. (2018), 'The influence of particle-size distribution on critical state behavior of spherical and non-spherical particle assemblies', *Granular Matter* **20:80**.

Jovicic, V. & Coop, M. R. (1988), 'The measurement of stiffness anisotropy in clays with bender element tests in the triaxial apparatus', *Geotechnical Testing Journal (ASTM)* **21**, 3–10.

Kabai, I. (1968), Grading entropy of soils, PhD thesis, Technical Sciences, TU of Budapest.

Kang, X., Xia, Z., Chen, R., Ge, L. & Liu, X. (2019), 'The critical state and steady state of sand: A literature review', *Marine Georesources and Geotechnology* **37**(9), 1105–1118.

Keramatikerman, M. & Chegenizadeh, A. (2017), 'Effect of particle shape on monotonic liquefaction: Natural and crushed sand', *Experimental Mechanics* **57**, 1341–1348.

Kiekbusch, M. & Schuppener, B. (1977), 'Membrane penetration and its effects on pore pressures', *Journal of the Geotechnical Engineering Division (ASCE)* **103**(11), 1267–1280.

Kirkpatrick, W. M. (1965), Effects of grain size and grading on the shearing behavior of granular materials, *in* 'Proceedings of 6th International Conference on Soil Mechanics and Foundation Engineering', pp. 273–277.

Kodicherla, S. P. K., Gong, G., Fan, L., Moy, C. K. S. & He, J. (2018), 'Effects of preparation methods on inherent fabric anisotropy and packing density of reconstituted sand', *Cogent Engineering* **5**(1), 1–14.

Koerner, R. M. (1969), 'Limiting density behavior of quartz powders', *Powder Technology* **3**(1), 208–212.

Koerner, R. M. (1970), 'Effect of particle characteristics on soil strength', *Journal of the Soil Mechanics and Foundation Division, ASCE* **96**(4), 1221–1234.

Kokusho, T. (1980), 'Cyclic triaxial test dynamic soil properties for wide strain range', *Soils and Foundations* **20**(2), 45–60.

Kokusho, T. (2007), *Liquefaction Strengths of poorly-graded and well-graded granular soils investigated by lab tests*, Earthquake Geotechnical Engineering, Springer, chapter 8, pp. 159–184. K. D. Pitilakis (Ed.).

Kokusho, T., Hara, T. & Hiraoka, R. (2004), 'Undrained shear strength of granular soils with different particle gradations', *Journal of Geotechnical and Geoenvironmental Engineering* **130**(6), 621–629.

Kolbuszewski, J. & Frederick, M. R. (1963), The significance of particle shape and size on the mechanical behavior of granular materials, *in* 'European Conference on Soil Mechanics and Foundation Engineering (Wiesbaden)', pp. 253–263.

Kolbuszewski, J. J. (1948), An experimental study of the maximum and minimum porosities of sand, *in* 'Proceedings of the 4th International Conference on Soil Mechanics and Foundation Engineering', Rotterdam, pp. 158–165.

Konrad, J. M. (1990), 'Minimum undrained strength versus steady-state strength of sands', *Journal of Geotechnical Engineering* **116**(6), 948–963.

Kramer, S. L. (1996), *Geotechnical Earthquake Engineering*, Pearson Education.

Krumbein, W. C. (1941), 'Measurement and geological significance of shape and roundness of sedimentary particles', *Journal of Sedimentary Petrology* **11**(2), 64–72.

Krumbein, W. C. & Sloss, L. L. (1963), *Stratigraphy and Sedimentation*, W. H. Freeman and Company, San Francisco, California, USA.

Kumar, J. & Madhusudhan, B. N. (2011), 'On determining the elastic modulus of a cylindrical sample subjected to flexural excitation in a resonant column apparatus', *Canadian Geotechnical Journal* **47**, 1288–1298.

Kumara, J., Hayano, K. & Ogiwara, K. (2012), 'Image analysis techniques on evaluation of particle size distribution of gravel', *International Journal of GEOMATE* **3**(1), 290–297.

Kuwano, R. & Jardine, R. J. (2004), 'On the applicability of cross-anisotropic elasticity to granular materials at very small strains', *Géotechnique* **52**(10), 727–749.

Kwok, C. Y. & Bolton, M. D. (2013), 'DEM simulations of soil creep due to particle crushing', *Géotechnique* **63**(16), 1365–1376.

Lade, P. V. & Hernandez, S. B. (1977), 'Membrane penetration effects in undrained testing', *Journal of the Geotechnical Engineering Division (ASCE)* **103**(2), 109–125.

Lade, P. V. & Ibsen, L. B. (1997), A study of the phase transformation and the characteristic lines of sand behavior, *in* 'Proceedings of the International Symposium on Deformation and Progressive Failure in Geomechanics', Nagoya, Japan.

Lambe, T. W. & Whitman, R. V. (1979), *Soil Mechanics*, John Wiley and Sons, New York, USA.

Landini, G. (2008), Advanced shape analysis with ImageJ, *in* 'Proceedings of the Second ImageJ User and Developer Conference', Luxembourg. https://blog.bham.ac.uk/intellimic/g-landini-software/.

Lashkari, A. (2010), 'A SANISAND model with anisotropic elasticity', *Soil DynamicsandEarthquakeEngineering* **30**, 1462–1477.

Latha, G. M. & Sitharam, T. G. (2008), 'Effect of particle size and gradation on the behaviour of granular materials simulated using DEM', *Indian Geotechnical Journal* **38**(1), 68–88.

Lee, N. J. (1993), Experimental Study of Body Wave Velocities in Sand Under Anisotropic Conditions, PhD thesis, The University of Texas at Austin, USA.

Lee, S. J., Hashash, Y. M. A. & Nezami, E. G. (2012), 'Simulation of triaxial compression tests with polyhedral discrete elements', *Computers and Geotechnics* **43**, 92–100.

Lees, G. (1964), 'The measurement of particle shape and its influence in engineering materials', *Journal of the British Granite and Whinestone Federation, London* pp. 1–22.

Li, X. S. & Dafalias, Y. F. (2000), 'Dilatancy for cohesionless soils', *Géotechnique* **50**(4), 449–460.

Li, X. S. & Wang, Y. (1998), 'Linear representation of steady-state line for sand', *Journal of Geotechnical and Geoenvironmental Engineering* **124**(12), 1215–1217.

Liu, X. & Yang, J. (2018), 'Shear wave velocity in sand: effect of grain shape', *Géotechnique* **68**(6), 742–748.

Lo Presti, D. C., Jamiolkowski, M., Pallara, O., Cavallaro, A. & Pedroni, S. (1997), 'Shear modulus and damping of soils', *Géotechnique* **47**(3), 603–617.

Lontou, P. B. & Nikolopoulou, C. P. (2004), 'Effect of grain size on dynamic shear modulus of sands: An experimental investigation'. Univ. of Patras, Greece (in Greek).

Machaček, J., Staubach, P., Tavera, C. E. G., Wichtmann, T. & Zachert, H. (2022), 'On the automatic parameter calibration of a hypoplastic soil model', *Acta Geotechnica* **17**, 5253–5273.

Mandelbrot, B. B. (1977), *Fractals: Form, Chance and Dimension*, W. H. Freeman and Company, San Francisco, USA.

Manzari, M. T. & Dafalias, Y. F. (1997), 'A two-surface critical plasticity model for sand', *Géotechnique* **47**(2), 255–272.

Martin, G. R., Seed, H. B. & Finn, W. D. L. (1978), 'Effects of system compliance on liquefaction tests', *Journal of the Geotechnical Engineering Division (ASCE)* **104**(4), 463–479.

Mate, C. M. (2008), *Tribology on the Small Scale - A Buttom Up Approach to Friction, Lubrication, and Wear*, Oxford University Press.

MathWorks (2014), 'MATLAB image processing toolbox'.

Menq, F. Y. (2003), Dynamic properties of sandy and gravelly soils, PhD thesis, The University of Texas at Austin, USA.

Menq, F. Y. & Stokoe, K. H. I. (2003), Linear dynamic properties of sandy and gravelly soils from large-scale resonant tests, *in* L. Swets & Zeitlinger, ed., 'Deformation characteristics of geomaterials', H. Di Benedetto, T. Doanh, H. Geoffroy, and C. Sauzeat, pp. 63–71.

Mitchell, J. K. & Soga, K. (2005), *Fundamentals of Soil Behavior*, 3rd edn, John Wiley and Sons, Inc.

Miura, K., Maeda, K., Furukawa, M. & Toki, S. (1997), 'Physical characteristics of sands with different primary properties', *Soils and Foundations* **37**(3), 53–64.

Mohamad, R. & Dobry, R. (1986), 'Undrained monotonic and cyclic strength of sand', *Journal of Geotechnical Engineering (ASCE)* **112**(10), 941–958.

Monkul, M. M., Etminan, E. & Senol, A. (2017), 'Coupled influence of content, gradation and shape characteristics of silts on static liquefaction of loose silty sands', *Soil Dynamics and Earthquake Engineering* **101**, 12–26.

Morioka, B. T. & Nicholson, P. (2000), Evaluation of the liquefaction potential of calcareous sand, *in* 'Proceedings of the 10th International Offshore and Polar Engineering Conference', pp. 494–500.

Moroto, N. & Ishii, T. (1990), 'Shear strength of uni-sized gravels under triaxial compression', *Soils and Foundations* **30**(2), 23–32.

Nakagawa, K., Soga, K. & Mitchell, J. K. (1997), 'Observation of Biot compressional wave of the second kind in granular soils', *Géotechnique* **47**(1), 133–147.

Nguyen, H. B. K., Rahman, M. M. & Fourie, A. B. (2018), 'Characteristic behavior of drained and undrained triaxial compression tests: DEM study', *Journal of Geotechnical and Geoenvironmental Engineering* **144**(9). 04018060.

Nguyen, H. B. K., Rahman, M. M. & Fourie, A. B. (2020a), 'Effect of particle shape on constitutive relation: DEM study', *Journal of Geotechnical and Geoenvironmental Engineering* **146**(7). 04020058.

Nguyen, H. B. K., Rahman, M. M. & Fourie, A. B. (2020b), 'How particle shape affects the critical state and instability triggering of granular material: results from a DEM study', *Géotechnique* . https://doi.org/10.1680/jgeot.18.P.211.

Nicholson, P. G. (2006), 'Liquefaction evaluation discrepancies in tropical lagoonal soils', *Journal of Geotechnical and Geoenvironmental Engineering* **124**(5), 1259–1269.

Noorany, I. (1989), 'Classification of marine sediments', *Journal of Geotechnical Engineering (ASCE)* **115**(1), 23–37.

Nouguier-Lehon, C., Cambou, B. & Vincens, E. (2003), 'Influence of particle shape and angularity on the behaviour of granular materials: a numerical analysis', *International Journal for Numerical and Analytical Methods in Geomechanics* **27**, 1207–1226.

Olarte, A. A. P. (2008), Influence of Particle Shape on the Global Mechanical Response of Granular Packings: Micromechanical Investigation of the Critical State in Soil Mechanics, PhD thesis, University of Stuttgart, Germany.

Olson, S. M. & Mattson, B. B. (2008), 'Mode of shear effects on yield and liquefied strength ratios', *Canadian Geotechnical Journal* **45**(4), 574–587.

Omar, T. & Sadrekarimi, A. (2014), 'Effects of multiple corrections on triaxial compression testing of sands', *Journal of GeoEngineering* **9**(2), 33–40.

Otsubo, M. & O'Sullivan, C. (2018), 'Experimental and DEM assessment of the stress-dependency of surface roughness effects on shear modulus', *Soils and Foundations* **58**(3), 602–614.

Otsubo, M., O'Sullivan, C., Sim, W. W. & Ibraim, E. (2015), 'Quantitative assessment of the influence of surface roughness on soil stiffness', *Géotechnique* **65**(8), 694–700.

Patel, A., Bartake, P. P. & Singh, D. N. (2008), 'An empirical relationship for determining shear wave velocity in granular materials accounting for grain morphology', *Geotechnical Testing Journal (ASTM)* **32**(1), 1–10.

Payan, M. (2017), Study of Small Strain Dynamic Properties of Sands and Silty Sands, PhD thesis, School of Civil and Environmental Engineering, UNSW Sydney, Australia.

Payan, M., Senetakis, K., Khoshghalb, A. & Khalili, N. (2016), 'Influence of particle shape on small-strain damping ratio of dry sands', *Géotechnique* **66**(7), 610–616.

Phan, V. T., Hsiao, D. & Nguyen, P. T. (2016), Effects of fine contents on engineering properties of sand-fines mixtures, *in* 'Procedia Engineering- Sustainable Development of Civil, Urban and Transportation Engineering Conference', Vol. 142, pp. 213–220.

Platypus (2015), 'Multi objective optimization in python'. https://platypus.readthedocs.io/en/latest/.

Poulos, S. J. (1981), 'The steady state of deformation', *Journal of Geotechnical Engineering, ASCE* **107**(5), 553–562.

Powers, M. C. (1953), 'A new roundness scale for sedimentary particles', *Journal of Sedimentary Research* **23**(2), 117–119.

Rahemi, N. (2017), Evaluation of Liquefaction Behavior of Sandy Soils Using Critical State Soil Mechanics and Instability Concept, PhD thesis, Faculty of Civil and Environmental Engineering, Ruhr-Universität Bochum, Germany.

Rahman, M. M. (2009), Modelling the influence of fines on liquefaction behaviour, PhD thesis, School of Engineering and Information Technology, The University of New South Wales at Australian Defence Force Academy, Australia.

Ramirez, J., Barrero, A. R., L., C., Dashti, S., Ghofrani, A., Taiebat, M. & Arduino, P. (2018), 'Site response in a layered liquefiable deposit: Evaluation of different numerical tools and methodologies with centrifuge experimental results', *Journal of Geotechnical and Geoenvironmental Engineering* **144**(10), 04018073.

Rangasamy, K., Boominathan, A. & Rajagopal, K. (2010), 'Influence of initial conditions on liquefaction resistance of silty sands', *Geomechanics and Geoengineering: An International Journal* **5**(3), 199–211.

Rasband, W. S. (2004), *ImageJ*, National Institutes of Health, Bethesda, Maryland, USA.

Rees, S. (2010), Effects of fines on the undrained behaviour of Christchurch sandy soils, PhD thesis, University of Canterbury, New Zealand.

Reynolds, J. M. (2011), *An Introduction to Applied and Environmental Geophysics*, Wiley Blackwell.

Richardson, L. F. (1961), *The problem of contiguity: an appendix of statistics of deadly quarrels*, 3rd edn, Taylor and Francis. In General Systems Yearbook 6, pp. 139-187.

Richart, E. F., Hall, J. R. & Woods, R. D. (1970), *Vibrations of soils and foundations*, Theoretical and Applied Mechanics series, Prentice-Hall International, Englewood Cliffs, New Jersey, USA.

Rittenhouse, G. (1943), 'A visual method of estimating two dimensional sphericity', *Journal of Sedimentary Petrology* **13**, 79–81.

Rodriguez, J., Johannson, J. & Edeskär, T. (2012), Particle shape determination by two-dimensional image analysis in geotechnical engineering, *in* 'Proceedings of Nordic Conference on Soil Mechanics and Geotechnical NGM', Danish Geotechnical Society, Copenhagen, Denmark, pp. 207–218.

Roscoe, K. H., Schofield, A. N. & Wroth, C. P. (1958), 'On the yielding of soils', *Géotechnique* **8**(1), 22–53.

Rothenburg, L. & Bathurst, R. J. (1992), 'Effects of particle shape on micromechanical behavior of granular materials', *Studies in Applied Mechanics* **31**, 343–352.

Rousé, P. C., Fannin, R. J. & Shuttle, D. A. (2008), 'Influence of roundness on the void ratio and strength of uniform sand', *Géotechnique* **58**(3), 227–231.

Rüscher, T. L. (2019), Einfluss der partikelgröße auf Dynamische Kennwerte von granularem Material (in German), Master's thesis, Ruhr-Universität Bochum.

Russell, R. D. & Taylor, R. E. (1937), 'Roundness and the shape of Mississippi River sands', *The Journal of Geology* **45**(3), 225–267.

Sadrekarimi, A. & Olson, S. M. (2011), 'Effect of sample-preparation method on critical-state behavior of sands', *Geotechnical Testing Journal (ASTM)* **35**(4). Paper ID GTJ104317.

Sandoval, E. & Pando, M. A. (2012), 'Experimental assessment of the liquefaction resistance of calcareous biogenous sands', *Earth Sciences Research Journal* **16**(1), 55–63.

Santamarina, J. C. & Cascante, G. (1998), 'Effect of surface roughness on wave propagation parameters', *Géotechnique* **48**(1), 129–136.

Santamarina, J. C. & Cho, G. C. (2004), Soil behaviour: The role of particle shape, *in* 'Skempton Conference', London.

Sarkar, D., Goudarzy, M. & König, D. (2019b), 'An interpretation of the influence of particle shape on the mechanical behavior of granular material', *Granular Matter* **21:53**, 1–24.

Sarkar, D., Goudarzy, M., König, D. & Wichtmann, T. (2020), 'Influence of particle shape and size on the threshold fines content and the limit index void ratios of sands containing non-plastic fines', *Soils and Foundations* **60**(3), 621–633.

Sarkar, D., König, D. & Goudarzy, M. (2019a), 'The influence of particle characteristics on the index void ratios in granular materials', *Particuology* **46**, 1–13.

Saxena, S. K. & Reddy, K. R. (1989), 'Dynamic moduli and damping ratios for Monterey No. 0 sand by resonant column tests', *Soils and Foundations* **29**(2), 37–51.

Schanz, T. & Vermeer, P. A. (1996), 'Angles of friction and dilatancy of sand', *Géotechnique* **46**(1), 145–151.

Schnabel, P. B., Lysmer, J. & Seed, H. B. (1972), SHAKE: A computer program for earthquake response analysis of horizontally layered site, Report EERC 72 -12, University of California, Berkeley. Earthquake Engg. Research Center.

Schofield, A. & Wroth, C. P. (1968), *Critical State Soil Mechanics*, McGraw-Hill.

Seed, H. B. (1981), Earthquake resistance design of earth dams, *in* 'International Conference on Recent Advances in Geotechnical Earthquake Engineering and Soil Dynamics III', St. Louis, MO, USA, pp. 1157–1173.

Seed, H. B., Wong, R. T., Idriss, I. M. & Tokimatsu, K. (1986), 'Moduli and damping factors for dynamic analyses of cohesionless soils', *Journal of Geotechnical Engineering* **112**(11), 1016–1032.

Senetakis, K., Anastasiadis, A. & Pitilakis, K. (2012), 'The small-strain shear modulus and damping ratio of quartz and volcanic sands', *Geotechnical Testing Journal* **35**(6), 964–980.

Shahir, H. & Pak, A. (2010), 'Estimating liquefaction-induced settlement of shallow foundations by numerical approach', *Computers and Geotechnics* **37**, 267–279.

Sharifipour, M., Dano, C. & Hicher, P. Y. (2004), Wave velocities in assemblies of glass beads using bender-extender elements, *in* 'Proceedings of the 17th ASCE Conference on Engineering Mechanics (EM2004)', University of Delaware, USA.

Shen, C., Liu, S., Xu, S. & Wang, L. (2019), 'Rapid estimation of maximum and minimum void ratios of granular soils', *Acta Geotechnica* **14**, 991–1001.

Sherif, M. A. & Ishibashi, I. (1976), 'Dynamic shear moduli for dry sands', *Journal of Geotechnical and Geoenvironmental Engineering* **102**(11), 1171–1184.

Sherif, M. A., Tsuchiya, C. & Ishibashi, I. (1977), 'Saturation effect on initial soil liquefaction', *Journal of the Geotechnical Engineering Division (ASCE)* **103**(8), 914–917.

Shin, H. & Santamarina, J. C. (2013), 'Role of particle angularity on the mechanical behavior of granular mixtures', *Journal of Geotechnical and Geoenvironmental Engineering* **139**(2), 353–355.

Short, A. D. (2005), 'Carbonate sandy beaches', *Encyclopedia of Coastal Science* .

Skinner, A. E. (1969), 'A note on the influence of interparticle friction on the shearing strength of a random assembly of spherical particles', *Géotechnique* **19**(1), 150–157.

Sladen, J. A., D'Hollander, R. D. & Krahn, J. (1985), 'The liquefaction of sands, a collapse surface approach', *Canadian Geotechnical Journal* **22**(4), 564–578.

Smalley, I. J. (1966), 'The properties of glacial loess and the formation of loess deposits', *Journal of Sedimentary Research* **36**(3), 669–676.

Sneed, E. D. & Folk, R. L. (1958), 'Pebbles in the lower Colorado River, Texas: A study in particle morphogenesis', *Journal of Geology* **66**, 114–150.

Sobol', I. M. (2001), 'Global sensitivity indices for nonlinear mathematical models and their Monte Carlo estimates', *Mathematics and Computers in Simulation* **55**, 271–280.

Stark, N., Hay, A. E., Cheel, R. & Lake, C. B. (2014), 'The impact of particle shape on the angle of internal friction and the implications for sediment dynamics at a steep, mixed sand-gravel beach', *Earth Surface Dynamics* **2**, 469–480.

Stokoe, K. H., Darendeli, M. B., Andrus, R. D. & Brown, L. T. (1999), Dynamic soil properties: laboratory, field and correlation studies, *in* 'Second International Conference on Earthquake Geotechnical Engineering', Vol. 3, A. A. Balkema, pp. 811–845.

Strahler, A., Stuedlin, A. W. & Arduino, P. W. (2016), 'Stress-strain response and dilatancy of sandy gravel in triaxial compression and plane strain', *Journal of Geotechnical and Geoenvironmental Engineering* **142**(4). 04015098.

Stremler, F. G. (1982), *Introduction to Communication Systems*, 2nd edn, Massachusetts: Addison-Wesley.

Sukumaran, B. & Ashmawy, A. K. (2001), 'Quantitative characterisation of the geometry of discrete particles', *Géotechnique* **51**(7), 619–627.

Sze, H. Y. & Yang, J. (2014), 'Failure modes of sand in undrained cyclic loading: Impact of sample preparation', *Journal of Geotechnical and Geoenvironmental Engineering* **140**(1), 152–169.

Taiebat, M. & Dafalias, Y. F. (2008), 'SANISAND: Simple anisotropic sand plasticity model', *International Journal for Numerical and Analytical Methods in Geomechanics* **32**, 915–948.

Tanaka, Y., Kudo, K., Yoshida, Y. & Ikemi, M. (1987), A study on the mechanical properties of sandy gravel-dynamic properties of reconstituted sample, Research rep. No. u87019, Central Research Institute of Electric Power Industry, Abiko, Japan. In Japanese.

Tatsuoka, F., Molenkamp, F., Torii, T. & Hino, T. (1984), 'Behavior of lubrication layers in platens in element tests', *Soils and Foundations* **24**(1), 113–128.

Tatsuoka, F., Toki, S., Miura, S., Kato, H., Okamoto, M., Yamada, S., Yasuda, S. & Tanizawa, F. (1986), 'Some factors affecting cyclic triaxial strength of sand', *Soils and Foundations* **26**(3), 99–116.

Terzaghi, K., Peck, R. & Mesri, G. (1996), *Soil Mechanics in Engineering Practice*, 3rd edn, John Wiley and Sons, New York.

Thevanayagam, S. (1998), 'Effect of fines and confining stress on undrained shear strength of silty sands', *Journal of Geotechnical and Geoenvironmental Engineering* **124**(6), 479–491.

Thevanayagam, S., Shenthan, T., Mohan, S. & Liang, J. (2002), 'Undrained fragility of clean sands, silty sands, and sandy silts', *Journal of Geotechnical and Geoenvironmental Engineering* **128**(10), 849–859.

Thomann, T. G. (1990), Stiffness and strength changes in cohensionless soils due to stress history and dynamic disturbance, PhD thesis, University of Michigan, USA.

Thornton, C. (2000), 'Numerical simulations of deviatoric shear deformation of granular media', *Géotechnique* **50**(1), 43–53.

Tian, J., Lui, E., Jiang, L., Jiang, X., Sun, Y. & Xu, R. (2018), 'Influence of particle shape on the microstructure evolution and the mechanical properties of granular materials', *Comptes Rendus Méchanique* **346**(6), 460–476.

Tordesillas, A., Hilton, J. E. & Tobin, S. T. (2014), 'Stick-slip and force chain evolution in a granular bed in response to a grain intruder', *Physical Review E* **89**(4). 042207.

Tordesillas, A., Walker, D. M. & Lin, Q. (2010), 'Force cycles and force chains', *Physical Review E* **81**(1). 011302.

Towhata, I. (2008), *Geotechnical Earthquake Engineering*, Springer Series in Geomechanics and Geoengineering.

Tsomokos, A. & Georgiannou, V. N. (2010), 'Effect of grain shape and angularity on the undrained response of fine sands', *Canadian Geotechnical Journal* **47**(5), 539–551.

Uchida, K., Sawada, T. & Hasegawa, T. (1980), Dynamic properties of sand subjected to initial shear stress, *in* 'Proceedings of the International Symposium on soils under cyclic and transient loading', Swansea, UK, pp. 121–132.

Vaid, Y. P., Fischer, J. M., Kuerbis, R. H. & Negussey, D. (1990), 'Particle gradation and liquefaction', *Journal of Geotechnical Engineering (ASCE)* **116**(4), 698–703.

Vaid, Y. P., Sivathalayan, S. & Stedman, D. (1999), 'Influence of specimen reconstituting method on the undrained response of sand', *Geotechnical Testing Journal (ASTM)* **22**(3), 187–195.

Vallejo, L. E. (1996), 'Fractal analysis of the fabric changes in a consolidating clay', *Engineering Geology* **43**(4), 281–290.

Vallurupalli, S. S. H. (2020), Optimizing the design of retaining wall systems using multi-objective optimization strategies, Master's thesis, Ruhr-Universität Bochum, Bochum, Germany.

Verdugo, R. & Ishihara, K. (1996), 'The steady state of sandy soils', *Soils and Foundations* **36**(2), 81–91.

Vernese, F. L. & Lee, K. L. (1977), Effect of frictionless caps and bases in the cyclic triaxial test, Final report s-77-1, Mechanics and Structures Department, University of California, Los Angeles, USA.

Wadell, H. (1932), 'Volume, shape, and roundness of rock particles.', *The Journal of Geology* **40**(443-451).

Wadell, H. (1933), 'Sphericity and roundness of rock particles', *The Journal of Geology* **41**(3), 310–331.

Wadell, H. (1935), 'Volume, shape, and roundness of quartz particles.', *The Journal of Geology* **43**(3), 250–280.

Wang, J., Zhang, H., Tang, S. & Liang, Y. (2013), 'Effects of particle size distribution on shear strength of accumulation soil', *Journal of Geotechnical and Geoenvironmental Engineering* **139**(11), 1994–1997.

Wang, Y. & Mok, C. (2008), 'Mechanisms of small strain shear modulus anisotropy in soils', *Journal of Geotechnical and Geoenviromental Engineering* **134**(10), 1516–1530.

Wei, L. M. & Yang, J. (2014), 'On the role of grain shape in static liquefaction of sand-silt mixtures', *Géotechnique* **64**(9), 740–745.

Wei, X., Yang, J., Zhou, Y. & Chen, Y. (2020), 'Influence of particle-size disparity on cyclic liquefaction resistance of silty sands', *Géotechnique Letters* **10**, 1–7.

Wen, R., Tan, C., Wu, Y. & Wang, C. (2018), 'Grain size effect on the mechanical behavior of cohesionless coarse-grained soils with the discrete element method', *Advances in Civil Engineering* **2018**. 4608930.

Whitehouse, D. J. & Archard, J. F. (1970), 'The properties of random surfaces of significance in their contacts', *Proceedings of the Royal Society of London. Series A, Mathematical and Physical Sciences* **316**, 97–121.

Wichtmann, T. (2005), Explicit accumulation model for non-cohesive soils under cyclic loading, PhD thesis, Institute of Soil Mechanics and Foundation Engineering, Ruhr-University Bochum, Germany. Volume 38.

Wichtmann, T. (2016), *Soil behaviour under cyclic loading - experimental observations, constitutive description and applications*, Karlsruher Institut für Technologie (KIT). Habilitation thesis.

Wichtmann, T., Fuentes, W. & Triantafyllidis, T. (2019c), 'Inspection of three sophisticated constitutive models based on monotonic and cyclic tests on fine sand: Hypoplasticity vs. SANISAND vs. ISA', *Soil Dynamics and Earthquake Engineering* **124**, 172–183.

Wichtmann, T., Sonntag, T. & Triantafyllidis, T. (2001), 'Über das Erinnerungsvermögen von Sand unter zyklischer Belastung', *Bautechnik* **78**(12), 852–865.

Wichtmann, T. & Triantafyllidis, T. (2009), 'On the influence of the grain size distribution curve of quartz sand on the small strain shear modulus G_{max}', *Journal of Geotechnical and Geoenvironmental Engineering* **135**(10), 1404–1418.

Wichtmann, T. & Triantafyllidis, T. (2010), 'On the influence of the grain size distribution curve on p-wave velocity, constrained elastic modulus M_{max} and Poisson's ratio of quartz sands', *Soil Dynamics and Earthquake Engineering* **30**(8), 757–766.

Wichtmann, T. & Triantafyllidis, T. (2013), 'Effect of uniformity coefficient on G/G_{max} and damping ratio of uniform to well-graded quartz sands', *Journal of Geotechnical and Geoenvironmental Engineering* **139**(1), 59–72.

Wichtmann, T., Triantafyllidis, T. & Späth, L. (2019a), 'On the influence of grain shape on the cumulative deformations in sand under drained high-cyclic loading', *Soils and Foundations* **59**(1), 208–227.

Wong, R. T., Seed, H. B. & Chan, C. K. (1975), 'Cyclic loading liquefaction of gravelly soils', *Journal of Geotechnical Engineering (ASCE)* **101**(6), 571–583.

Wu, Y., Yamamoto, H. & Izumi, A. (2016), 'Experimental investigation on crushing of granular material in one-dimensional test', *Periodica Polytechnica Civil Engineering* **60**(1), 27–36.

Xia, H. & Hu, T. (1991), 'Effects of saturation and back pressure on sand liquefaction', *Journal of Geotechnical Engineering (ASCE)* **117**(9), 1347–1362.

Yamamuro, J. A. & Lade, P. V. (1993), 'Effects of strain rate on instability of granular soils', *Geotechnical Testing Journal (ASTM)* **16**(3), 304–313.

Yamamuro, J. A. & Lade, P. V. (1998), 'Steady-state concepts and static liquefaction of silty sands', *Journal of Geotechnical and Geoenvironmental Engineering* **124**(9), 868–877.

Yamashita, S., Kawaguchi, T., Nakata, Y., Mikami, T., Fujiwara, T. & Shibuya, S. (2009), 'International parallel test on the measurement of G_{max} using Bender elements', *Soils and Foundations* **49**(4), 631–650.

Yang, H., Baudet, B. A. & Yao, T. (2016), 'Characterization of the surface roughness of sand particles using an advanced fractal approach', *Proceedings of the Royal Society of London. Series A, Mathematical and Physical Sciences* **472**.

Yang, J. & Dai, B. B. (2011), 'Is the quasi-steady state a real behaviour? A microme-chanical perspective', *Géotechnique* **61**(2), 175–184.

Yang, J. & Gu, X. Q. (2013), 'Shear stiffness of granular material at small strains: Does it depend on grain size?', *Géotechnique* **63**(2), 165–179.

Yang, J. & Luo, X. D. (2015), 'Exploring the relationship between critical state and particle shape for granular materials', *Journal of the Mechanics and Physics of Solids* **84**, 196–213.

Yang, J., Savidis, S. & Roemer, M. (2004), 'Evaluating liquefaction strength of par-tially saturated sand', *Journal of Geotechnical and Geoenvironmental Engineering* **130**(9), 975–979.

Yang, J. & Wei, L. M. (2012), 'Collapse of loose sand with the addition of fines: the role of particle shape', *Géotechnique* **62**(12), 1111–1125.

Yang, M., Seidalinov, G. & Taiebat, M. (2018), 'Multidirectional cyclic shearing of clays and sands: Evaluation of two bounding surface plasticity models', *Soil Dynamics and Earthquake Engineering* **124**, 230–258.

Yasin, S. J. M. & Safiullah, A. M. M. (2003), 'Effect of particle characteristics on the strength and volume change behavior of sand', *Journal of Civil Engineering* **31**(2), 127–148.

Yoshimi, Y., Tanaka, K. & Tokimatsu, K. (1989), 'Liquefaction resistance of partially saturated sand', *Soils and Foundations* **29**(3), 157–162.

Youd, T. L. (1973), 'Factors controlling maximum and minimum density of sands', *ASTM STP 523* pp. 98–112.

Yu, P. & Richart, F. E. (1984), 'Stress ratio effects on shear modulus of dry sands', *Journal of Geotechnical Engineering, ASCE* **110**(3), 331–345.

Zelasko, J. S., Krizek, R. J. & Edil, T. B. (1975), Shear behavior of sands as a function of grain characteristics, *in* 'Proceedings of the Istanbul Conference on Soil Mechanics and Foundation Engineering', pp. 55–64.

Zhang, H. & Garga, V. K. (1997), 'Quasi-steady state: a real behaviour?', *Canadian Geotechnical Journal* **34**, 749–761.

Zhang, J. (1994), 'Transient shear strength of saturated sand under cyclic loading considering strain-rate effect', *Soils and Foundations* **34**(4), 51–65.

Zhang, X. J., Andrus, R. D. & Juang, C. H. (2005), 'Normalized shear modulus and material damping ratio relationships: damping determination of sands under different loadings.', *Journal of Geotechnical and Geoenviromental Engineering* **131**(4), 453–464.

Zhao, J. & Guo, N. (2013), 'Unique critical state characteristics in granular media considering fabric anisotropy', *Géotechnique* **63**(8), 695–704.

Zhao, S., Evans, T. M. & Zhou, X. (2018), 'Shear-induced anisotropy of granular materials with rolling resistance and particle shape effects', *International Journal of Solids and Structures* **150**, 268–281.

Zhao, S. & Zhao, J. (2021), 'SudoDEM: Unleashing the predictive power of the discrete element method on simulation for non-spherical granular particles', *Computer Physics Communications* **259**. 107670.

Zhao, Y. & Liu, Z. (2018), 'Study of material composition effects on the mechanical properties of soil-rock mixtures', *Advances in Civil Engineering* **2018**(3854727). Rock Mechanics in Energy Resources Exploitation.

Zheng, J. & Hryciw, R. D. (2015), 'Traditional soil particle sphericity, roundness and surface roughness by computational geometry', *Géotechnique* **65**(6), 494–506.

Zheng, J. & Hryciw, R. D. (2016), 'Index void ratios of sands from their intrinsic properties', *Journal of Geotechnical and Geoenvironmental Engineering* **142**(12). 06016019.

Zhou, B., Wang, J. & Wang, H. (2018), 'A novel particle tracking method for granular sands based on spherical harmonic rotational invariants', *Géotechnique* **68**(12), 1116–1123.

Zhou, W., L., Y., Ma, G., Xu, K., Lai, X. & Chang, X. (2017), 'DEM modeling of shear bands in crushable and irregularly shaped granular materials', *Granular Matter* **19**(25).

Zingg, T. (1935), Beitrag zur Schotteranalyse, PhD thesis, ETH Zurich, Switzerland.

Zolkov, E. & Wiseman, G. (1965), Engineering properties of dune and beach sands and the influence of stress history, *in* 'Proceedings of the Sixth International Conference on Soil Mechanics and Foundation Engineering', Vol. 1, pp. 134–138.

Schriftenreihe des Instituts für Grundbau, Wasserwesen und Verkehrswesen der Ruhr-Universität Bochum

Herausgeber: H.L. Jessberger

15 (1991) **Mahmud Thaher**
Tragverhalten von Pfahl-Platten-Gründungen im bindigen Baugrund,
Berechnungsmodelle und Zentrifugen-Modellversuche

Schriftenreihe des Instituts für Grundbau der Ruhr-Universität Bochum

Herausgeber: H.L. Jessberger

16 (1992) **Rainer Scherbeck**
Geotechnisches Verhalten mineralischer Deponieabdichtungsschichten
bei ungleichförmiger Verformungswirkung

17 (1992) **Martin M. Bizialiele**
Torsional Cyclic Loading Response of a Single Pile in Sand

18 (1993) **Michael Kotthaus**
Zum Tragverhalten von horizontal belasteten Pfahlreihen aus langen Pfählen in Sand

19 (1993) **Ulrich Mann**
Stofftransport durch mineralische Deponieabdichtungen:
Versuchsmethodik und Berechnungsverfahren

20 (1992) **Festschrift anlässlich des 60. Geburtstages von**
Prof. Dr.-Ing. H. L. Jessberger
20 Jahre Grundbau und Bodenmechanik an der Ruhr-Universität Bochum

21 (1993) **Stephan Demmert**
Analyse des Emissionsverhaltens einer Kombinationsabdichtung im Rahmen der
Risikobetrachtung von Abfalldeponien

22 (1994) **Diethard König**
Beanspruchung von Tunnel- und Schachtausbauten in kohäsionslosem Lockergestein
unter Berücksichtigung der Verformung im Boden

23 (1995) **Thomas Neteler**
Bewertungsmodell für die nutzungsbezogene Auswahl von Verfahren zur Altlastensanierung

24 (1995) **Ralph Kockel**
Scherfestigkeit von Mischabfall im Hinblick auf die Standsicherheit von Deponien

25 (1996) **Jan Laue**
Zur Setzung von Flachfundamenten auf Sand unter wiederholten Lastereignissen

26 (1996) **Gunnar Heibrock**
Zur Rissbildung durch Austrocknung in mineralischen Abdichtungsschichten
an der Basis von Deponien

27 (1996) **Thomas Siemer**
Zentrifugen-Modellversuche zur dynamischen Wechselwirkung zwischen Bauwerken
und Baugrund infolge stoßartiger Belastung

28 (1996) **Viswanadham V. S. Bhamidipati**
Geosynthetic Reinforced Mineral Sealing Layers of Landfills

29 (1997) **Frank Trappmann**
Abschätzung von technischem Risiko und Energiebedarf bei Sanierungsmaßnahmen
für Altlasten

30 (1997) **André Schürmann**
Zum Erddruck auf unverankerte flexible Verbauwände

31 (1997) **Jessberger, H. L. (Herausgeber)**
Environment Geotechnics, Report of ISSMGE Technical Committee TC 5
on Environmental Geotechnics

Schriftenreihe des Instituts für Grundbau und Bodenmechanik der Ruhr-Universität Bochum

Herausgeber: Th. Triantafyllidis

32 (2000) **Triantafyllidis, Th. (Herausgeber)**
Boden unter fast zyklischer Belastung: Erfahrung und Forschungsergebnisse (Workshop)

33 (2002) **Christof Gehle**
Bruch- und Scherverhalten von Gesteinstrennflächen mit dazwischenliegenden Materialbrücken

34 (2003) **Andrzej Niemunis**
Extended hypoplastic models for soils

35 (2004) **Christiane Hof**
Über das Verpressankertragverhalten unter kalklösendem Kohlensäureangriff

36 (2004) **René Schäfer**
Einfluss der Herstellungsmethode auf das Verformungsverhalten von Schlitzwänden
in weichen bindigen Böden

37 (2005) **Henning Wolf**
Zur Scherfugenbänderung granularer Materialien unter Extensionsbeanspruchung

38 (2005) **Torsten Wichtmann**
Explicit accumulation model for non-cohesive soils under cyclic loading

39 (2008) **Christoph M. Loreck**
Die Entwicklung des Frischbetondruckes bei der Herstellung von Schlitzwänden

40 (2008) **Igor Arsic**
Über die Bettung von Rohrleitungen in Flüssigböden

41 (2009) **Anna Arwanitaki**
Über das Kontaktverhalten zwischen einer Zweiphasenschlitzwand und nichtbindigen Böden

Schriftenreihe des Lehrstuhls für Grundbau, Boden- und Felsmechanik der Ruhr-Universität Bochum

Herausgeber: T. Schanz

42 (2009) **Yvonne Lins**
Hydro-Mechanical Properties of Partially Saturated Sand

43 (2010) **Tom Schanz (Herausgeber)**
Geotechnische Herausforderungen beim Umbau des Emscher-Systems
Beiträge zum RuhrGeo Tag 2010

44 (2010) **Jamal Alabdullah**
Testing Unsaturated Soil for Plane Strain Conditions: A New Double-Wall Biaxial Device

45 (2011) **Lars Röchter**
Systeme paralleler Scherbänder unter Extension im ebenen Verformungszustand

46 (2011) **Yasir Al-Badran**
Volumetric Yielding Behavior of Unsaturated Fine-Grained Soils

47 (2011) **Usque ad finem**
Selected research papers

48 (2012) **Muhammad Ibrar Khan**
Hydraulic Conductivity of Moderate and Highly Dense Expansive Clays

49 (2014) **Long Nguyen-Tuan**
Coupled Thermo-Hydro-Mechanical Analysis: Experimental and Back Analysis

50 (2014) **Tom Schanz (Herausgeber)**
Ende des Steinkohlenbergbaus im Ruhrrevier: Realität und Perspektiven für die
Geotechnik Beiträge zum RuhrGeo Tag 2014

51 (2014) **Usque ad finem**
Selected research papers

52 (2014) **Houman Soleimani Fard**
Study on the Hydro-Mechanical Behaviour of Fiber Reinforced Fine Grained Soils
with Application to the Preservation of Historical Monuments

53 (2014) **Wiebke Baille**
Hydro-Mechanical Behavior of Clays - Significance of Mineralogy

54 (2014) **Qasim Abdulkarem Jassim Al-Obaidi**
Hydro-Mechanical Behavior of Collapsible Soils

55 (2015) **Veselin Zarev**
Model Identification for the Adaption of Numerical Simulation Models - Application
to Mechanized Shield Tunneling

56 (2015) **Meisam Goudarzy**
Micro and Macro Mechanical Assessment of Small and Intermediate Strain Properties
of Granular Material

57 (2016) **Oliver Detert**
Analyse einer selbstregulierenden interaktiven Membrangründung für Schüttkörper auf geringtragfähigen Böden

58 (2016) **Yang Yang**
Analyses of Heat Transfer and Temperature-induced Behaviour in Geotechnics

59 (2016) **Alborz Pourzargar**
Application of suction stress concept to partially saturated compacted soils

60 (2017) **Hanna Haase**
Multiscale analysis of clay-polymer composites for Geoenvironmental applications

61 (2017) **Kavan Khaledi**
Constitutive modeling of rock salt with application to energy storage caverns

62 (2017) **Nina Silvia Müthing**
On the consolidation behavior of fine-grained soils under cyclic loading

63 (2017) **Elham Mahmoudi**
Probabilistic analysis of a rock salt cavern with application to energy storage systems

64 (2017) **Negar Rahemi**
Evaluation of liquefaction behavior of sandy soils using critical state soil mechanics and instability concept

65 (2018) **Chenyang Zhao**
A contribution to modeling of mechanized tunnel excavation

66 (2019) **Tom Schanz (Herausgeber)**
Innovationen im Spezialtiefbau und in der Umweltgeotechnik
Geotechnik Beiträge zum RuhrGeo Tag 2014

67 (2019) **Linzhi Lang**
Hydro-Mechanical Behaviour of Bentonite-Based Materials Used for Disposal of Radioactive Wastes

68 (2019) **Usama Al-Anbaki**
Hydraulic Interaction of Soil and Nonwoven Geotextiles under Unsaturated Conditions

69 (2019) **Abhishek Rawat**
Coupled Hydro-mechanical Behavior of a Compacted Bentonite-Sand Mixture:
Experimental and Numerical Investigations

Schriftenreihe des Lehrstuhls für Bodenmechanik, Grundbau und Umweltgeotechnik der Ruhr-Universität Bochum

Herausgeber: T. Wichtmann